U.PORTO

DOUTORAMENTO

CIÊNCIAS BIOMÉDICAS

Mucoadhesive camptothecin polymeric micelles as nanodelivery systems for oral chemotherapy to treat colorectal cancer

Andreia Almeida

D

2021

U.PORTO

Andreia Almeida: Mucoadhesive camptothecin polymeric micelles as nanodelivery systems for oral chemotherapy to treat colorectal cancer

D.ICBAS 2021

Mucoadhesive camptothecin polymeric micelles as nanodelivery systems for oral chemotherapy to treat colorectal cancer

Andreia Almeida

INSTITUTO DE CIÊNCIAS BIOMÉDICAS ABEL SALAZAR

Andreia Marina de Sousa Almeida

MUCOADHESIVE CAMPTOTHECIN POLYMERIC MICELLES AS NANODELIVERY SYSTEMS FOR ORAL CHEMOTHERAPY TO TREAT COLORECTAL CANCER

Tese de Candidatura ao grau de Doutor em Ciências Biomédicas submetida ao Instituto de Ciências Biomédicas Abel Salazar da Universidade do Porto

Orientador
Doutor Bruno Filipe Carmelino Cardoso Sarmento
Categoria – Investigador Principal & Professor Associado Convidado Afiliação – i3S - Instituto de Investigação e Inovação em Saúde, INEB - Instituto de Engenharia Biomédica, Universidade do Porto & IUCS - Instituto Universitário de Ciências da Saúde

Co-orientadora
Doutora Marlene Susana Dionísio Lúcio
Categoria – Investigadora Auxiliar/Professora Associada Convidada
Afiliação – Centro de Física das Universidades do Minho e Porto (CF-UM-UP) e Centro de Biologia Molecular e Ambiental da Universidade do Minho (CBMA)

Co-orientador
Doutor Simó Schwartz Navarro
Categoria – Diretor do CIBBIM-Nanomedicine
Afiliação – Molecular Biology and Biochemistry Research Center for Nanomedicine (CIBBIM-Nanomedicine), Hospital Universitari Vall d'Hebron e Vall d'Hebron Institut de Recerca (VHIR)

DECLARAÇÃO DE HONRA

Eu, Andreia Marina de Sousa Almeida, declaro que a presente tese é de minha autoria e não foi utilizada previamente noutro curso ou unidade curricular, desta ou de outra instituição. As referências a outros autores (afirmações, ideias, pensamentos) respeitam escrupulosamente as regras da atribuição, e encontram-se devidamente indicadas no texto e nas referências bibliográficas, de acordo com as normas de referenciação. Tenho consciência de que a prática de plágio e auto-plágio constitui um ilícito académico.

Porto, 31 de Maio de 2021

_____

Andreia Marina de Sousa Almeida

Aos meus Pais, ao meu Irmão e Cunhada, à minha princesa Joana e ao meu Javier...

The work presented in this thesis was developed at:

Nanomedicines & Translational Drug Delivery Group
i3S - Instituto de Investigação e Inovação em Saúde and
INEB - Instituto de Engenharia Biomédica
Universidade do Porto, Porto, Portugal
Rua Alfredo Allen, 208
4200-135 Porto, Portugal
www.i3s.up.pt | www.ineb.up.pt

And

CF-UM-UP – Centro de Física das Universidades do Minho e Porto e
CBMA – Centro de Biologia Molecular e Ambiental da Universidade do Minho
Universidade do Minho, Braga, Portugal
Campus de Gualtar
4710-057 Braga, Portugal

And

CIBBIM-Nanomedicine – Molecular Biology and Biochemistry Research Center for Nanomedicine
Vall d'Hebron University Hospital
VHIR – Vall d'Hebron Research Institute
Passeig Vall d'Hebron, 119-129
08035 Barcelona, Spain

And

Department of Pharmacy and Pharmaceutical Technology
University of Seville
Calle San Fernando, 4
41004 Seville, Spain

And

MyBiotech GmbH – Products for biotech and pharma
Industriestraße 1b,
66802 Überherrn, Germany

And

IINFACTS – Institute of Research and Advanced Training in Health Sciences and Technology
Rua Central de Gandra, 1317
4585-116 Gandra, Paredes, Portugal

And

ESA – European Space Agency

ESTEC - European Space Research and Technology Centre

Keplerlaan 1,

2201 AZ Noordwijk, Netherlands

FINANCIAL SUPPORT

Andreia Almeida was supported by a national PhD grant (SFRH/BD/118721/2016) from Fundação para a Ciência e Tecnologia (FCT), Portugal; three short term scientific missions (STSMs) granted by European Cooperation in Science & Technology (COST); Associação Empresarial de Portugal (AEP) in the scope of the program Norte Empreendedor; Spin Your Thesis! 2020 program, organized by European Space Agency (ESA) Education Office and Pharmaceutics 2020 Travel Awards organized by MDPI Open Access Journal. This work was financed by the project NORTE-01-0145-FEDER-000012, supported by Norte Portugal Regional Operational Programme (NORTE 2020), under the PORTUGAL 2020 Partnership Agreement, through the Europe and Regional Development Fund (ERDF), by FEDER - Fundo Europeu de Desenvolvimento Regional funds through the COMPETE 2020 - Operacional Programme for Competitiveness and Internationalisation (POCI), Portugal 2020, and by Portuguese funds through FCT/Ministério da Ciência, Tecnologia e Ensino Superior in the framework of the project "Institute for Research and Innovation in Health Sciences" (UID/BIM/04293/2019), and also Partnership Agreement PT2020 UID/QUI/50006/2013 -POCI/01/0145/FEDER/007265. This work was also funded by the Project PI4AC 2017, “Establishment of new muco-interactive nanomicelles as oral delivery systems of camptothecin for colorectal cancer”, MicelCampt-CESPU-2017. Finally, this work was also supported by Merck, the Spin Your Thesis! 2020 program organized by ESA Education Office, COST and by Instituto Ciências Biomédicas de Abel Salazar (ICBAS).

PUBLICATIONS

Ao abrigo do disposto do n.º 2, alínea a) do artigo 31° do Decreto-Lei n.° 115/2013 de 7 de Agosto, fazem parte integrante desta tese de doutoramento os seguintes trabalhos já publicados ou submetidos para publicação:

- Silva, D. S., **Almeida, A**., Azevedo, C., Campana-Filho, S. P. & Sarmento, B, 2018. Synthesis and Applications of Amphiphilic Chitosan Derivatives for Drug Delivery Applications. In *Nanoparticles in Life Sciences and Biomedicine* (45-73), Pan Stanford.
- Andrade, F., **Almeida, A**., Rafael, D., Schwartz, S. & Sarmento, B., 2018. Micellar-Based Nanoparticles for Cancer Therapy and Bioimaging. In *Nanooncology*, (211-238), Springer, Cham.
- **Almeida, A**., Macedo, M.H., das Neves, J. & Sarmento, B, 2018. Thermo-responsive Nanomedicines for Drug Delivery in the Gastrointestinal Tract. In *Stimuli-responsive Drug Delivery Systems* (83-108), Royal Society of Chemistry.
- **Almeida, A**.*, Azevedo, C.*, Macedo, M.H.* & Sarmento, B., 2020. 3D intestinal models towards a more realistic permeability screening. In *Nanotechnology for Oral Drug Delivery* (389-417), Academic Press. (*equal contribution)
- **Almeida, A**., Araújo, M., Novoa-Carballal, R., Andrade, F., Gonçalves, H., Reis, L. R., Lúcio, M., Schwartz Jr, S. & Sarmento, B, 2020. Novel amphiphilic chitosan micelles as carriers for hydrophobic anticancer drugs. *Materials Science and Engineering: C:* 110920.
- **Almeida, A**. & Sarmento, B., 2021. Chitosan polymeric micelles as oral delivery platform of hydrophobic anticancer drugs. In *Chitosan for Biomaterials IV: Biomedical Applications*, Advances in Polymer Science, Springer.
- Azevedo C.*, Macedo M.H.*, **Almeida A**.*, Pinto S.*, van Loon J. & Sarmento B, 2021. The effect of hypergravity in intestinal permeability of nanoformulations and molecules. *European Journal of Pharmaceutics and Biopharmaceutics*, 163: 38-48. (*equal contribution)
- **Almeida, A.***, Fernandes, E.*, Sarmento, B. & Lúcio, M., 2021. A biophysical insight of camptothecin biodistribution: towards a molecular understanding of its pharmacokinetic issues, *Pharmaceutics,* 13(6), 869. (*equal contribution)

- **Almeida, A.***, Linares, V.*, Mora-Castaño, G., Casas, M., Caraballo, I. & Sarmento, B., 2021. 3D printed systems for specific colonic delivery of chitosan micelles for a better intestinal absorption, *European Journal of Pharmaceutics and Biopharmaceutics*. (*equal contribution)
- **Almeida, A.**, Günday-Türeli, N. & Sarmento, B., 2021. A scale-up strategy for the synthesis of chitosan derivatives used in micellar nanomedicines, *submitted*.
- **Almeida, A.**, Castro, F., Resende, C., Lúcio, M., Schwartz Jr, S. & Sarmento, B., 2021. Oral delivery of camptothecin-loaded in chitosan-based micelles is effective in reducing colorectal cancer, *submitted.*

ACKNOWLEDGMENTS

I use to joke that I did a PhD in Biomedical Sciences while also did a PhD in Life. Although these four years have been one of the most difficult and complex of my life, I am really grateful because everything happens for a reason and adversity is a necessary evil for us to grow, learn, and evolve. And, indeed, I grew, learned, and evolved both personally and professionally during this PhD. There were many people who came into, passed through, and stayed in my life during these four years and who, in some way or another, helped me in the course of this work and left a positive impression on me. For this reason, I would like to thank some of these people:

To my supervisor, Professor Bruno Sarmento, for the opportunity to join his research group and for supporting me in successfully completing this PhD thesis. Thank you for all of your friendship, for always demonstrating that there is always a way out, and for always being present, even when physically absent. Thank you for all of your guidance, for broadening my horizons, for all of your advices, and for your commitment and understanding. Thank you for believing in me (even when I did not) and teaching me that there is a life beyond the PhD that must not be forgotten to be lived. All of your teachings will live on in my memory and in my heart.

To my co-supervisor, Dr. Marlene Lúcio, for always supporting me throughout the PhD process, and for her dedication to commitment even when the time was short. Eduarda Fernandes, one of her students, for all the assistance in carrying out the experimental work. Both were always available to help me with whatever I needed and always welcomed me with kindness in Braga.

To my co-supervisor, Dr. Simó Schwartz, who welcomed me so warmly in Barcelona, I am grateful for all of your availability and enthusiasm for this project. To his entire research team, especially Fernanda Andrade, for the hours spent in the laboratory and on the streets of Barcelona with a cup of hot chocolate in hand.

To Dr. Alejandro Sosnik and his students, thank you for making me feel so welcome in your laboratory in Israel and for the opportunity to learn new techniques. To Shaked Eliyahu, who came from Israel temporarily to work with me in Porto, for giving me a different perspective on life and showing me that life is full of opportunities. Thank you for all of your attention and concern during my stay in Israel.

To Dr. Isidoro Caraballo, for having me in his laboratory in Seville, for all of the effort and scientific discussion of the project, and for all of your affection. To his students, particularly Vicente Linares, for the collaboration and friendship that we have formed, and for demonstrating to me that everything can be accomplished with commitment and dedication.

To Dr. Nazende Günday-Türeli, for welcoming me so warmly into her company, for helping me in improving my critical thinking, finding alternatives when something goes wrong, and understand how to plan everything ahead of time. Your enthusiasm and optimism are contagious. To her sister, Cemre Günday, for the German classes, the friendship we've formed, and her unwavering assistance both inside and outside the company.

To Dr. Vítor Seabra and Dr. Hassan Bousbaa, for their availability and for providing all of the necessary conditions for me to carry out a part of my PhD project at IINFACTS, CESPU. Also, thanks to Virgínia Gonçalves for the assistance and friendship over the years.

To Marco Araújo, for his unending assistance with chemical synthesis, for the friendship we built, for cheering me up after each failed attempt, and for making me laugh in the worst moments.

To Ramón Novoa-Carballal, for his support with chemical synthesis and for carrying out the gel permeation chromatography tests, as well as for his overall availability and commitment to this project.

To Sofia Lamas, for all the help with the animal studies and for always being willing to help with all the kindness. Also, to Carlos Resende, for the availability to help and scientific discussions during the *in vivo* studies.

To Francisca Rodrigues, thank you for all of your support and friendship throughout my PhD.

To everyone who has passed through and is still a part of the Nanomedicines and Translational Drug Delivery group, thank you for your help, the company, and the good times. However, I must express my heartfelt gratitude to the following individuals who

were/are members of a group: Flávia Sousa, Helena Macedo, Cláudia Azevedo, Elisabete Fernandes, Flávia Castro, Rute Nunes, Ana Costa, Cassilda Reis, Daniella Souza, and Fabíola Prezotti, you made my way easier and happier.

I have no words to express my gratitude to Flávia Sousa. Thank you for calming me down, for listening to me (practically) every day and at any time, for all of the scientific debate, for the exchange of professional opinions, and for demonstrating that, in reality, everything is very simple and that, in the end, everything goes well. Thank you for all of your strength and for always believing in me. Thank you for the wonderful quartet we formed.

To Helena Macedo, thank you for your complicity, for all the conversations and laughs. For always paying attention to me and sharing common ideals. Thank you for all our professional collaborations, as well as the exchange of ideas and scientific criticism. Thank you for forcing me to try foods I had never tried before, and with that, I realized that in life, we have to try and live, and we have to enjoy every moment because it could be our last. Thank you for sharing the laboratory desk with me and for sharing our life together. Thank you for the wonderful quartet we formed.

To Cláudia Azevedo, for always being by my side and for the friendship that has lasted since the beginning. Thank you for all of the projects (and prizes) in common, for your entrepreneurial spirit, and for encouraging us to participate and overcome our own challenges. Thank you for the positive conversations, encouragement and belief in a better tomorrow. Your positive attitude and energy are contagious, and I am glad to have you around. Thank you for the wonderful quartet we formed.

To Elisabete Fernandes, for our friendship, the most recent mother who inspires me to be one day, for being able to reconcile work and home in a perfectly harmonious manner.

To Flávia Castro, for your tireless help with *in vitro* and *in vivo* studies, as well as the beautiful friendship created during this journey. Thank you for your professionalism and guidance, for your critical spirit, and for all of your support during the difficult times. Thank you for all our conversations! It is good that life brought us together.

To Rute Nunes, Ana Costa, Cassilda Reis, Daniella Souza, and Fabiola Prezotti for all of their support and availability since the start of my PhD. Thank you for pointing me in

the right direction and for all of your personal and professional lessons. I will cherish these memories for the rest of my life.

To Sofia Marques, dear friend, thank you for all the times we have spent together, for all the walks we have taken to forget about work, for all the conversations, and for all your help over the years. Thank you for your loyal friendship.

To Marlene Silva, my heart's goddaughter, for our endless conversations, and for all of your care and support during the tough times; I know I can always count on you. Thank you for your spontaneity, sincerity and friendship.

I have no words to express my gratitude to Andreia Barbosa, a childhood friend and neighbor in Barcelona. Thank you for showing me around the city, including me in your circle of friends, for the evenings at your house, and, in general, for making me feel at home. And it was truly my home!

To Inês Pereira, former laboratory colleague and Barcelona neighbor, for our adventures and travels, and for your contagious joy and good mood. Thank you for, even you did not hold me on those stairs, have me taken to the hospital and take care of me. Your simplicity and sincerity are admirable.

Anabela Seabra and Inês Oliveira, thank you for your friendship and for coming into my life. Our sessions always leave me with a warm feeling in my heart. I enjoy talking to you, sharing my life with you, and being your friend. Thank you very much.

To all of my family and friends who have supported and encouraged me to be more and better in some way. Especially to the people who mean the most to me:

Aos meus pais, Francisco e Rosa, pessoas a quem devo tudo o que sou e tudo o que consegui. Obrigada por sempre, mas sempre me apoiarem, acreditarem e lutarem por mim. Acredito que não há palavras para descrever o vosso amor incondicional. Obrigada por serem sempre o meu porto de abrigo, por ampararem as minhas quedas e por me fazerem levantar mais forte no dia seguinte. Não há pais como vocês, garanto.

Ao meu irmão e cunhada, Mário e Anabela, por serem um pilar para mim, por me ouvirem sempre, pela vossa disponibilidade, sensatez e carinho. Nunca esquecerei

todas as nossas conversas e todos os vossos conselhos. A família não se escolhe, mas se eu pudesse, escolher-vos-ia igualmente.

À Joana, afilhada e sobrinha, um amor que não cabe no coração. Tu não sabes nem percebes, mas o teu sorriso e abraço fizeram em mim maravilhas, principalmente nos dias mais tristes em que chegava a casa depois de um dia mau de trabalho, lá estavas tu, de sorriso de orelha a orelha à minha espera e a gritar 'madrinha' para me dar um abraço muito apertado. Esses momentos são impagáveis e inesquecíveis. Um dia mau passa logo a ser um dia bom!

Por fim, ao Javier, o meu melhor amigo, namorado e amante. Entrou na minha vida a meio do doutoramento, mas trouxe consigo as coisas mais belas do mundo: amor, felicidade e paz. Obrigada por todo o carinho, amor e compreensão, por me fazeres rir a todo o momento, por ao teu lado não existirem problemas e tudo parecer tão fácil e linear. Obrigada por todo o apoio durante a reta final, por acreditares em mim, por me dares na cabeça quando precisei, mas sobretudo, pelas lufadas de ar fresco que, sem saberes, me davas e que eu tanto precisava. Obrigada por toda a paz que me fazes sentir a teu lado. Que seja sempre assim!

Só é lutador quem sabe lutar consigo mesmo.

Carlos Drummond de Andrade

TABLE OF CONTENTS

ABSTRACT ..... **i**

RESUMO ..... **v**

LIST OF FIGURES ..... **ix**

LIST OF TABLES ..... **xx**

LIST OF ACRONYMS AND ABBREVIATIONS ..... **xxiii**

CHAPTER 1 ..... **1**

Overview and Aims **1**

1.1. Overview **3**

1.2. Aim and specific objectives **4**

1.3. Structure **5**

CHAPTER 2 ..... **7**

Literature Review **7**

2.1. Cancer **11**

2.1.1. Colorectal cancer development 11

2.1.2. Colorectal cancer treatment 13

2.1.3. Camptothecin in colorectal cancer treatment 14

2.2. Gastrointestinal tract **14**

2.2.1. Cellular constitution of the gastrointestinal tract 15

2.2.2. Differences between normal and diseased tissues 16

2.2.3. Oral administration 19

2.2.3.1. Limitations to the oral administration of drugs 19

2.2.3.2. Drug delivery at the colon 20

2.2.3.3. Intestinal absorption mechanisms 21

2.3. Polymeric micelles **23**

2.3.1. Polymeric micelles constitution 25

2.3.2. Micelle-based anticancer drug delivery systems 26

2.4. Chitosan **30**

2.4.1. Alkylation 31
2.4.2. Acylation 32
2.4.3. Hydroxylation and carboxylation 32
2.4.4. Chitosan-based polymeric micelles as drug delivery systems 32
2.4.4.1. Paclitaxel delivery 33
2.4.4.2. Other hydrophobic anticancer drugs 36
References 39
CHAPTER 3 55
A biophysical insight of camptothecin biodistribution: towards a molecular understanding of its pharmacokinetic issues 55
3.1. Abstract 58
3.2. Introduction 58
3.3. Materials and Methods 60
3.3.1. Materials 60
3.3.2. In silico predictors of drug-profiling 61
3.3.3. Preparation of membrane models 61
3.3.4. Drug distribution coefficient in membrane/aqueous systems studied by derivative spectroscopy 61
3.3.5. Drug location in membrane/aqueous systems studied by steady-state fluorescence quenching 63
3.3.6. Plasma protein binding evaluation using steady-state fluorescence quenching 64
3.3.7. Small- and wide-angle X-ray scattering studies at the Synchrotron 64
3.3.8. Studies on dynamic and electrophoretic light scattering 65
3.3.9. Modelling biodistribution using in vitro parameters 65
3.3.10. Statistical analysis 67
3.4. Results and Discussion 67
3.4.1. In silico analysis of camptothecin physicochemical properties 67
3.4.2. Distribution and location of camptothecin in a membrane/aqueous system 69
3.4.3. The CPT effect on membrane biophysical properties 76
3.4.4. Plasma protein binding of camptothecin and prediction of biodistribution parameters 81
3.5. Conclusion 83
References 84

CHAPTER 4 ..... **91**

Novel amphiphilic chitosan micelles as carriers for hydrophobic anticancer drugs **91**

4.1. Abstract **94**

4.2. Introduction **94**

4.3. Material and Methods **95**

4.3.1. Materials 95

4.3.2. Synthesis of mPEG-chitosan-oleic acid 96

4.3.2.1. Chitosan modification with mPEG-COOH 96

4.3.2.2. Pegylated chitosan modification with oleic acid 96

4.3.3. Characterization of mPEG-chitosan and mPEG-chitosan-oleic acid 97

4.3.3.1. FTIR and ^{1}H NMR spectroscopy 97

4.3.3.2. Gel permeation chromatography 97

4.3.3.3. Trinitrobenzene sulfonic acid assay 97

4.3.3.4. Contact angle 98

4.3.3.5. Differential scanning calorimetry / thermogravimetric analysis 98

4.3.3.6. X-Ray diffraction analysis 98

4.3.3.7. Critical micellar concentration determination 99

4.3.4. Preparation of camptothecin-loaded mPEG-chitosan-oleic acid polymeric micelles 99

4.3.5. Characterization of polymeric micelles 99

4.3.5.1. Particle size distribution, zeta potential and morphological analysis 99

4.3.5.2. Association efficiency and drug loading 100

4.3.5.3. Micelles stability at 4 ºC and effect of different cryoprotectants on micelles size 100

4.3.6. *In vitro* camptothecin release in simulated gastrointestinal fluids 100

4.3.7. Camptothecin lactone ring protection from hydrolysis 101

4.3.8. Statistical analysis 101

4.4. Results and Discussion **101**

4.4.1. Synthesis and characterization of mPEG-chitosan 101

4.4.2. Synthesis and characterization of mPEG-chitosan-oleic acid 104

4.4.4. Critical micelle concentration 113

4.4.5. Preparation and characterization of mPEG-chitosan-oleic acid polymeric micelles 114

4.4.6. Camptothecin release from mPEG-chitosan-oleic acid micelles in simulated gastrointestinal fluids 116
4.4.7. Micelles protective effect on lactone ring form of camptothecin 118
4.5. Conclusion 119
CHAPTER 5 127
A scale-up strategy for the synthesis of chitosan derivatives used in micellar nanomedicines 127
5.1. Abstract 130
5.2. Introduction 130
5.3. Materials and Methods 131
5.3.1. Materials 131
5.3.2. Polymer synthesis at bench scale 132
5.3.2.1. Synthesis of methoxypolyethylene glycol-chitosan 132
5.3.2.2. Synthesis of methoxypolyethylene glycol-chitosan-oleic acid 132
5.3.3. Polymer synthesis by scale-up continuous manufacturing 133
5.3.3.1. Synthesis of methoxypolyethylene glycol-chitosan 133
5.3.3.2. Synthesis of methoxypolyethylene glycol-chitosan-oleic acid 133
5.3.4. Physicochemical characterization of the copolymers 133
5.3.5. Cell culture 134
5.3.6. Cell viability assessment of the produced polymers 134
5.3.7. Production and characterization of chitosan-based polymeric micelles 135
5.3.8. Long-term storage study 135
5.3.9. Statistical analysis 135
5.4. Results and Discussion 135
5.4.1. Characterization of the polymers 135
5.4.3. *In vitro* safety of the produced polymers 139
5.4.5. Long-term stability study 141
5.5. Conclusion 143
References 144
CHAPTER 6 147
3D printed systems for specific colonic delivery of camptothecin-loaded chitosan micelles 147
6.1. Abstract 150

6.2. Introduction **150**

6.3. Materials and Methods **152**

6.3.1. Materials 152

6.3.2. Production of camptothecin-loaded polymeric micelles 152

6.3.3. Characterization of camptothecin-loaded micelles 152

6.3.4. 3D printed systems production 153

6.3.4.1. Preparation of drug printable ink 153

6.3.4.2. 3D printing process 153

6.3.5. Characterization of the 3D printed systems 154

6.3.5.1. Physical characteristics of 3D printed systems 154

6.3.5.2. Scanning electron microscopy 154

6.3.6. Camptothecin release from the printfills 154

6.3.7. Cell culture 155

6.3.8. Metabolic assay using drug and micelle released medium 156

6.3.9. Intestinal permeability models 156

6.3.10. Camptothecin intestinal permeability 157

6.3.11. Cellular integrity by hematoxylin and eosin staining 158

6.3.12. Statistical analysis 158

6.4. Results and Discussion **158**

6.4.1. Characterization of camptothecin-loaded micelles 158

6.4.2. Characterization of the 3D printed systems 159

6.4.2.1. Physical characteristics of 3D printed systems 159

6.4.2.2. Scanning electron microscopy 160

6.4.3. *In vitro* release profile of camptothecin from the printfills loaded with polymeric micelles 161

6.4.4. *In vitro* cytocompatibility of polymeric micelles 162

6.4.5. Permeability of camptothecin after simulated gastrointestinal passage 163

6.4.6. Cellular integrity of the intestinal models 165

6.5. Conclusion **166**

References **167**

CHAPTER 7 ..... **171**

Oral delivery of camptothecin-loaded in chitosan-based micelles is effective in reducing colorectal cancer **171**

7.1. Abstract **174**

7.2. Introduction **174**

7.3. Materials and Methods **176**

7.3.1. Ethics statement 176

7.3.2. Materials 176

7.3.3. Production of camptothecin-loaded polymeric micelles 176

7.3.4. Characterization of camptothecin-loaded polymeric micelles 177

7.3.5. Cell culture conditions 177

7.3.6. Polymeric micelles cytocompatibility in human peripheral blood mononuclear cells 178

7.3.7. *In vitro* antitumor efficacy studies in 2D colorectal cancer cell lines 179

7.3.8. *In vitro* antitumor efficacy studies using multicellular tumor spheroids 179

7.3.8.1. Multicellular tumor spheroids formation 179

7.3.8.2. Multicellular tumor spheroids size measurement 179

7.3.8.3. Multicellular tumor spheroids metabolic activity 180

7.3.9. *In vitro* permeability studies 180

7.3.10. *In vivo* studies 181

7.3.10.1. Pharmacodynamic study in a xenograft model 181

7.3.10.2. Colorectal cancer disease model 182

7.3.10.3. *In vivo* pharmacokinetic study 182

7.3.10.4. *In vivo* biodistribution of polymeric micelles 182

7.3.10.5. *In vivo* pharmacodynamic study 183

7.3.11. Statistical analysis 183

7.4. Results and Discussion **183**

7.4.1. Characterization of chitosan-based micelles 183

7.4.2. Polymeric micelles cytocompatibility 184

7.4.3. *In vitro* antitumor efficacy of camptothecin-loaded micelles 186

7.4.4. *In vitro* intestinal permeability of CPT from chitosan micelles 189

7.4.5. *In vivo* antitumor activity in HCT116 xenograft mouse model 190

7.4.6. Pharmacokinetic and biodistribution studies in a chemically-induced colorectal cancer model 191

7.4.7. Antitumor efficacy of camptothecin-loaded micelles in chemically induced colorectal cancer model 193

7.5. Conclusion **196**

References **198**

CHAPTER 8 ..... **203**

Conclusions and Future Perspectives **203**

8.1. Conclusions **205**

8.2. Future perspectives **207**

Appendix 1 ..... **209**

The effect of hypergravity in intestinal permeability of nanoformulations and molecules **209**

Supplementary Material for Supporting the Appendix 1 ..... **234**

Appendix 2 ..... **241**

Supplementary information for supporting the Chapter 4 ..... **241**

Appendix 3 ..... **249**

Supplementary information for supporting the Chapter 6 ..... **249**

Appendix 4 ..... **255**

Supplementary information for supporting the Chapter 7 ..... **255**

BIBLIOGRAPHIC NOTE **263**

ABSTRACT

Cancer is a leading cause of death worldwide, characterized by the uncontrollable division and survival of abnormal cells. In particular, colorectal cancer (CRC) shows high incidence and mortality patterns in both males and females. Nevertheless, CRC treatment has rapidly progressed over the last decades with advances in imaging, surgical techniques, and chemo/immunotherapy. Surgery is usually the first-line treatment, with adjuvant chemo/immunotherapy commonly applied to suppress the disease. Despite the intrinsic therapeutic effect, chemotherapeutic drugs, due to its side-toxicity, are not well tolerable by the majority of patients. Thus, there is growing need to find alternatives to reduce the treatment side-effects.

Oral chemotherapy has attractive advantages over conventional intravenous chemotherapy regarding patient's convenience and administration flexibility. Still, most anticancer drugs, as camptothecin (CPT), have low solubility in biological fluids, undergoing low intestinal dissolution and bioavailability, and can be degraded during the passage through the gastrointestinal tract (GIT). Therefore, the use of nanotechnology has been extensively explored to encapsulate anticancer drugs for oral chemotherapy, overcoming their unfavorable pharmacokinetic properties.

Taking all the above-mentioned considerations, the main goal of this thesis was to develop chitosan-based micelles of new self-assembling chitosan derivatives and encapsulate CPT for the CRC treatment upon oral administration.

Firstly, CPT was extensively studied regarding its biophysical interaction with biointerface models to predict the pharmacokinetic profile after oral administration. The *LogD* values obtained indicate that the drug can be well distributed across biological membranes. In addition, similar *LogD* values obtained in membrane models that simulate cancerous or normal cells indicate that CPT has a strong binding to serum albumin, predicting only 8% of the drug available to be distributed to tissues. The interaction with plasma proteins, allied to the large biodistribution obtained (VD_{SS}=5.75 ± 0.932 $L \cdot Kg^{-1}$) and tendency to bioaccumulate in off-target tissues, were projected to be pharmacokinetic issues of CPT, implying the need to develop drug delivery systems to improve its therapeutic potential.

Thus, chitosan (112 kDa, 15% degree of acetylation) was grafted with *O*-methyl-*O*′-succinyl polyethylene glycol (mPEG) and oleic acid (OA) in a two-step carbodiimide coupling, where mPEG-CS and mPEG-CS-OA copolymers were consequently obtained. The structural and physicochemical characterization of the copolymers confirmed the successful conjugation of the hydrophilic and hydrophobic moieties to the chitosan

backbone. The amphiphilic chitosan derivative was able to spontaneously form polymeric micelles with an average size of 180 nm, low polydispersity index (PdI) <0.28, and positive superficial charge around 43 mV. CPT was successfully associated into chitosan micelles with 8% loading (w/w). The *in vitro* release profile of CPT was evaluated under simulated gastrointestinal fluids, exhibiting <10% release of CPT in gastric media in 2 h and a controlled release in intestinal fluids for 72 h, reaching close to 45%. Furthermore, it was demonstrated that chitosan micelles were able to stabilize CPT, protecting up to 75% of the drug released from hydrolysis.

The synthesis and production of mPEG-CS and mPEG-CS-OA copolymers were scaled-up under industrial environment using cross flow filtration (CFF) as purification method. Both copolymers were able to maintain the physicochemical properties when produced in a higher batch size, with reduced time of production and increased yield. Also, both chitosan derivatives presented no *in vitro* cytotoxicity, confirming the success of the purification by the continuous manufacturing method, i.e., through CFF. Additionally, polymeric micelles produced from the scaled-up mPEG-CS-OA copolymer were stable at – 20 ºC for at least 6 months regarding its size, PdI, surface charge and morphologic appearance. The production of the copolymers and polymeric micelles at an industrial pilot batch confirmed their suitability for good manufacturing practices (GMP) production.

Micelles were associated to 3D printing technology aiming to protect them from the harsh environment of the GIT. The 3D printing systems (*printfills*), sealed with Eudragit FS30D as an enteric coating, were filled with CPT-loaded micelles and characterized regarding the CPT release and intestinal permeability. Thus, a simulated digestion of the *printfills* upon an oral administration was performed in gastrointestinal fluids, where *printfills* were maintained intact at the simulated gastric pH of the stomach and, only at the colonic pH, around 40% of CPT was released from the chitosan micelles. The dissolution media containing CPT and CPT-loaded micelles was used to recreate the intestinal absorption, where CPT-loaded into chitosan micelles showed an increase of the CPT permeability compared to the free drug. The combination of 3D printing with nanotechnology revealed great potential for the colon-specific release of polymeric micelles, thereby increasing the amount of the drug at the colon and consequent intestinal absorption, while protecting the system/drug from degradation throughout the GIT.

The anticancer activity of CPT-loaded micelles was tested *in vitro*. Empty micelles demonstrated a safe profile when incubated with human blood cells and CRC cell lines, while CPT-loaded micelles demonstrated *in vitro* anticancer activity against HCT116, Caco-2 and HT29 CRC cell lines by the decrease of their cellular viability. When tested in a more complex model, 3D multicellular CRC spheroids, data showed a significant

effect on the spheroid's metabolic activity and size reduction, demonstrating the *in vitro* antitumor efficacy of CPT-loaded micelles.

The *in vivo* therapeutic potential of CPT-loaded micelles was assessed in both HCT116 xenograft and orthotopic CRC models. The first *in vivo* model, used as proof of concept, showed a significant reduction on the tumor growth during and after treatment with CPT-loaded micelles subcutaneously administered. This was also translated in the tumor volume, where a 50% reduction was verified, compared to the non-treated animals. The biodistribution of chitosan micelles loaded with cyanine 7.5 was studied in a more realistic CRC *in vivo* model developed through chemical induction. Chitosan micelles were primarily accumulated in the colon, with no evidence of distribution in other tissues. Taking this into account, the anticancer activity of the drug-loaded system was evaluated using this later animal model. Orally administered CPT-loaded micelles demonstrated a significative reduction on tumor burden after the treatment. Moreover, the size of the tumors found in the animals treated with CPT-loaded micelles was smaller compared to placebo and untreated animals, corroborated by qualitative colonoscopy. Furthermore, animals treated with CPT-loaded micelles presented lower spleen index, indicating that these micelles may be beneficial in reducing CRC-related inflammation.

Overall, the developed CPT-loaded micelles demonstrated to be a promising drug delivery system capable of effectively inhibiting the development and progression of CRC upon oral administration, making it a potential therapeutic approach for CRC oral chemotherapy.

RESUMO

O cancro é uma das principais causas de morte em todo o mundo, caracterizado pela divisão incontrolável e sobrevivência de células anormais. Em particular, o cancro colorretal (CRC) apresenta altos padrões de incidência e de mortalidade tanto em homens como em mulheres. No entanto, o tratamento do CRC tem progredido rapidamente nas últimas décadas com avanços na imagiologia, técnicas cirúrgicas e químio/imunoterapia. A cirurgia é, geralmente, a primeira linha de tratamento com a ajuda da químio/imunoterapia adjuvante para levar à supressão da doença. Apesar do efeito terapêutico intrínseco, os fármacos usados em quimioterapia, devido à sua toxicidade, não são bem tolerados pela maioria dos pacientes. Assim, é crescente a necessidade de limitar seu uso e encontrar alternativas para reduzir os efeitos colaterais do tratamento.

A quimioterapia oral tem vantagens atraentes sobre a quimioterapia intravenosa convencional relativamente à conveniência do paciente e flexibilidade de administração. Ainda assim, a maioria dos fármacos anticancerígenos, como a camptotecina (CPT), apresentam baixa solubilidade em fluidos biológicos, sofrendo baixa dissolução e biodisponibilidade intestinal, e podem degradar-se durante a passagem pelo trato gastrointestinal (GIT). Portanto, o uso da nanotecnologia através de micelas poliméricas tem sido amplamente explorado para encapsular fármacos anticancerígenos para quimioterapia oral, superando suas propriedades farmacocinéticas desfavoráveis.

Tendo em conta todas as considerações acima mencionadas, o objetivo principal desta tese foi desenvolver novos derivados de quitosano com capacidade de formar micelas e encapsular CPT para o tratamento do CRC por via oral.

Em primeiro lugar, a CPT foi extensivamente estudada em relação à sua interação biofísica com modelos de biointerface para prever o perfil farmacocinético após administração oral. Os valores *LogD* obtidos indicam que o fármaco pode ser bem distribuído nas membranas biológicas. Além disso, valores semelhantes *de LogD* obtidos em modelos de membrana que simulam células cancerígenas ou células normais, indicam que a CPT tem uma forte ligação à albumina sérica, prevendo apenas 8,05% do fármaco disponível para ser distribuído pelos tecidos. A interação com as proteínas plasmáticas, aliada à grande biodistribuição obtida (VD_{SS}=5,75 ± 0,932 $L \cdot Kg^{-1}$) e a tendência a bioacumular em tecidos não desejados, foram projetados como problemas farmacocinéticos da CPT, implicando a necessidade de desenvolver um sistema de administração da CPT para melhorar o seu potencial terapêutico.

Assim, o quitosano (112 kDa, grau de acetilação de 15%) foi enxertado com *O*-metil-*O'*-succinil polietilenoglicol (mPEG) e ácido oleico (OA) após uma reação carbodiimida realizada em duas etapas, onde os copolímeros mPEG-CS e mPEG-CS-OA foram obtidos. A caracterização estrutural e físico-química dos copolímeros confirmou o sucesso da conjugação das frações hidrofílicas e hidrofóbicas à estrutura do quitosano. O derivado anfifílico de quitosano permitiu a formação espontânea de micelas poliméricas com tamanho médio de 180 nm, baixo índice de polidispersividade (PdI) <0,28 e carga superficial positiva em torno dos 43 mV. A CPT foi associada com sucesso às micelas de quitosano com uma quantidade de fármaco de 8% (p/p). O perfil de libertação da CPT foi avaliado *in vitro* em fluidos gastrointestinais simulados, exibindo uma libertação de CPT <10% em meio gástrico durante 2 h e uma libertação controlada em fluidos intestinais por 72 h, chegando perto dos 45% de libertação. Além disso, foi demonstrado que as micelas de quitosano foram capazes de estabilizar a CPT, protegendo da hidrólise até 75% do fármaco libertado.

A síntese e produção dos copolímeros mPEG-CS e mPEG-CS-OA foram produzidos numa escala aumentada em ambiente industrial usando a filtração de fluxo cruzado (CFF) como método de purificação. Ambos copolímeros foram capazes de manter as propriedades físico-químicas quando produzidos em lotes maiores, com redução do tempo de produção e aumento do rendimento. Além disso, ambos os derivados de quitosano não apresentaram citotoxicidade *in vitro*, confirmando o sucesso da purificação pelo método de fabricação contínua, ou seja, por meio de CFF. Além disso, as micelas poliméricas produzidas a partir do copolímero mPEG-CS-OA, após aumento de escala de produção, demonstraram estabilidade a -20 ºC por pelo menos 6 meses em relação ao seu tamanho, PdI, carga superficial e aparência morfológica. A produção dos copolímeros e das micelas poliméricas num lote industrial piloto confirmou que se adequam para a produção de boas práticas de fabricação (GMP).

As micelas foram associadas à tecnologia de impressão 3D com o objetivo de proteger o sistema do ambiente hostil do GIT. Os sistemas de impressão 3D (*printfills*) foram selados com Eudragit FS30D como revestimento entérico, e preenchidos com micelas carregadas de CPT e caracterizados quanto à libertação de CPT e a sua permeabilidade intestinal. Assim, uma digestão simulada após administração oral dos *printfills* foi realizada em fluidos gastrointestinais, onde os *printfills* se mantiveram intactos no pH gástrico simulado do estômago e, apenas no pH do cólon, cerca de 40% da CPT foi libertada das micelas de quitosano. O meio de dissolução contendo CPT e micelas carregadas de CPT foi usado para recriar a absorção intestinal, onde a CPT associada às micelas de quitosano demonstrou uma permeabilidade aumentada, em comparação com o fármaco livre. A combinação da impressão 3D com a nanotecnologia revelou

grande potencial para a libertação específica de micelas poliméricas no cólon, aumentando a quantidade do fármaco no local e a consequente absorção intestinal, protegendo o sistema/fármaco da degradação através do GIT.

A atividade anticancerígena das micelas carregadas com CPT foi testada *in vitro*. As micelas vazias demonstraram um perfil seguro quando incubadas com células sanguíneas humanas e linhas celulares de CRC, enquanto as micelas carregadas com CPT demonstraram uma atividade anticancerígena *in vitro* contra as linhas celulares de CRC, HCT116, Caco-2 e HT29, pela diminuição de sua viabilidade celular. Quando testado num modelo mais complexo, esferoides multicelulares 3D de CRC, as micelas com fármaco associado mostraram um efeito significativo na redução da atividade metabólica e do tamanho do esferoide, demonstrando a eficácia antitumoral *in vitro* dessas micelas carregadas com fármaco.

O potencial terapêutico *in vivo* de micelas carregadas com CPT foi avaliado num modelo de xenoenxerto através da inoculação das células HCT116 e, também num modelo de CRC ortotópico. O primeiro modelo *in vivo*, usado como prova de conceito, mostrou uma redução significativa no crescimento do tumor durante e após o tratamento para as micelas carregadas com CPT administradas subcutaneamente. Isso também se traduziu no volume do tumor, onde se verificou uma redução de 50% em relação aos animais não tratados. A biodistrubuição de micelas de quitosano carregadas com cianina 7,5 foi estudada num modelo *in vivo* mais realista de CRC desenvolvido por indução química. Os resultados obtidos revelaram que as micelas de quitosano se acumulam principalmente no cólon, sem evidência de distribuição em outros tecidos. Tendo isso em consideração, este último modelo animal foi usado para avaliar a atividade anticancerígena do sistema carregado com fármaco. Micelas carregadas com CPT administradas oralmente demonstraram uma redução significativa na carga tumoral após o fim do tratamento. Além disso, o tamanho dos tumores encontrados nos animais tratados com micelas carregadas com CPT foi menor em comparação com o placebo e os animais não tratados, resultados qualitativamente corroborados por colonoscopia. Além disso, os animais tratados com micelas carregadas com fármaco apresentaram menor *spleen index*, o que pode indicar um efeito benéfico dessas micelas na redução da inflamação associada ao CRC.

No geral, as micelas desenvolvidas carregadas com CPT demonstraram ser um sistema de entrega de fármacos promissor, capaz de inibir efetivamente o desenvolvimento e a progressão do CRC após a administração oral, tornando-se uma potencial abordagem terapêutica para a quimioterapia oral do CRC.

LIST OF FIGURES

Figure 2.1. Stages of colorectal cancer according to the American Joint Committee on Cancer. Stage 0: tumor confined to mucosa (carcinoma in situ); Stage I: tumor invades submucosa and muscularis propria; Stage II: tumor invades through the muscularis propria into pericolorectal tissues (IIA), then penetrates to the surface of the visceral peritoneum (IIB), then directly invades or is adherent to other organs or structures (IIC); Stage III: tumor invades muscularis propria with metastases in 1–3 regional lymph nodes or nearby tissue, or invades submucosa with metastases in 4–6 regional lymph nodes (IIIA). Then tumor penetrates to the surface of the visceral peritoneum with metastases in 1–3 regional lymph nodes or nearby tissue, or invades through the muscularis propria into pericolorectal tissues with metastases in 4–6 regional lymph nodes, or invades muscularis propria with metastases in 7 or more regional lymph nodes (IIIB). Then tumor penetrates to the surface of the visceral peritoneum with metastases in 4–6 regional lymph nodes, or invades through the muscularis propria into pericolorectal tissues with metastases in 7 or more regional lymph nodes, or directly invades or is adherent to other organs or structures with metastases in one or more regional lymph nodes (IIIC); Stage IV: metastasis confined to one organ or site (e.g., liver, lung, ovary, nonregional node). Reprinted with permission from [15].

Figure 2.2. Tumor targeting. The right-hand part of the figure depicts the increased accumulation of nanoparticles in tumor owing to leaky tumor vasculature, leading to the enhanced permeability and retention effect. The left-hand part of the figure shows active targeting mediated by targeted nanoparticles. Reproduced with permission from [2].

Figure 2.3. Schematic illustration of the passage of orally delivered targeted nanotherapeutics for CRC treatment. After oral administration, drug formulations pass through the mouth, esophagus, stomach, small intestine, and colon, successively. Subsequently, the matrix of delivery system surrounding targeted nanotherapeutics collapses in colon. These nanotherapeutics are released in colonic lumen and enable the loaded drugs to be specifically internalized by colon cancer cells. Reprinted with permission from [89].

Figure 2.4. Different mechanisms involved in the small intestine absorption. (A) passive diffusion; (B) active transport; (C) paracellular transport; (D) receptor-mediated endocytosis; (E) endocytosis via M cells; (F) pinocytosis.

Figure 2.5. Examples of nanosized-systems obtained using amphiphilic compounds.

Figure 2.6. Schematic representation of a micelle and its formation through self-assembling of polymer monomers above CMC and CMT**.**

Figure 2.7. Schematic representation of a multifunctional micelle for drug delivery.

Figure 2.8. Chitosan structure, where n is the average degree of polymerization.

Figure 2.9. Antitumor efficacy of PTX, TMC-PTX and FA-TMC-PTX on H22 tumor-bearing mice. Five administrations were conducted every alternate day. (a) Tumor growth curves following i.v. or p.o. administration of saline and distinct PTX formulations. Indicated values were mean ± SD (n = 6). *P < 0.05 versus PTX (i.v.); #P < 0.05 versus TMC-PTX via the same administration route; $ P < 0.05 versus p.o. administration. (b) Survival curves of H22 tumor-bearing mice receiving i.v. or p.o. administration of saline and distinct PTX formulations (n = 6). Reprinted with permission from [198].

Figure 3.1. 3D chemical structure of CPT generated with 'Chemicalize' tool from Chemaxon® software.

Figure 3.2. (A) First derivative of CPT ($2x10^{-5}$) absorption spectra with increasing concentrations of cancer membrane models (0 to 1.0 $x10^{-3}$ M) in Acetate buffer pH = 5.8. In red is represented the absorption spectra of CPT in the absence of the cancer membrane models. With the addition of increasing concentrations of membrane model (samples represented in black) there is a shift in λ values. In grey are represented the derivative spectra of the references containing only membrane models. (B) Nonlinear fitting of derivative absorbance values at λ = 234 nm as a function of membrane model concentration.

Figure 3.3. (A) Fluorescence emission spectra of CPT ($2x10^{-5}$) with increasing concentrations of cancer membrane models (0 to 3.0 $x10^{-3}$ M) in Acetate buffer pH = 5.8. In red is represented the absorption spectra of CPT in the absence of the cancer membrane models. With the addition of increasing concentrations of membrane model (samples represented in black) there is a shift in λ values. (B) Correspondent nonlinear fitting (Equation 3.1) of fluorescence emission values at λ_{max} = 440 nm as a function of membrane model concentration.

Figure 3.4. (A) Fluorescence excitation spectra of CPT ($[CPT]_T$ of 0 to $4x10^{-5}$ M) added to cancer membrane models (3.0×10^{-2} M) labelled with NBD-PE probe and correspondent emission spectra of the probe (λ exc=360 nm). (B) Stern-volmer plot of fluorescence quenching as a function of membrane concentrations of CPT calculated according to Equation 3.6.

Figure 3.5. Normalized MCR of DMPC membrane models in absence (●) and in the presence of CPT (●) as a function of temperature. Each point corresponds to the mean value ± standard deviation of three experiments. Continuous lines are the best fits according to Equation 3.8.

Figure 3.6. Small angle X-ray diffraction (SAXS) patterns of DMPC (black) or DMPC containing CPT (red) measured in the Lβ′ (14.0 °C), Pβ (20.6 °C) and Lα (40.8 °C) phases of DMPC. Solid lines give the best fit of the Lorentzian' s analysis model (dashed lines) to the scattered intensities. A model of drug–membrane interaction is proposed for each diffractogram together with the resultant d_L values.

Figure 3.7. Wide angle X-ray diffraction (WAXS) patterns of DMPC (black) or DMPC containing CPT (red) measured in the Lβ′ (14.0 °C) and Pβ (20.6 °C) phases of DMPC. Solid lines give the best fit of the Lorentzian' s analysis model (dashed lines) to the scattered intensities. A model of drug–membrane interaction is proposed for each diffractogram together with the resultant ds values.

Figure 3.8. (A) Fluorescence spectra of HSA (2.0×10^{-6} M) in the presence of increasing CPT concentrations (0 to 3.0×10^{-4} M) at 37 °C. (B) Binding isotherm plot of CPT-HSA. The non-linear fit to the experimental data was made using Equation 3.7 and allowed to determine the dissociation constant (K_{diss}) and the number of binding sites (n).

Figure 4.1. (A) ATR-FTIR spectra of mPEG-COOH, physical mixture of mPEG-COOH and CS, mPEG-CS copolymer and chitosan (CS) and (B) ^{1}H NMR spectra of chitosan, mPEG-COOH and mPEG-CS in 2% DCl (1 mg/mL, 400 MHz).

Figure 4.2. (A) ATR-FTIR spectra of OA, physical mixture of mPEG-CS+OA, mPEG-CS-OA copolymer and CS and (B) ^{1}H NMR spectra of chitosan in 2% DCl, oleic acid in DMSO-d_6 and mPEG-CS-OA (1 mg/mL, 400 MHz).

Figure 4.3. Thermogravimetric curves of (A) blend of mPEG and chitosan (mPEG+CS) and grafted polymer of mPEG and chitosan (mPEG-CS) and (B) grafted polymer of mPEG and chitosan without oleic acid (mPEG-CS) or conjugated with 2.5% (mPEG-CS-OA2.5) or 5% (mPEG-CS-OA5) of oleic acid.

Figure 4.4. Calorimetric curves of grafted polymer of mPEG and chitosan (mPEG-CS); blend of mPEG and chitosan (mPEG+CS); grafted polymer of mPEG and chitosan conjugated with 2.5% (mPEG-CS-OA2.5) or 5% (mPEG-CS-OA5) of oleic acid.

Figure 4.5. XRD patterns of: (A) mPEG; chitosan (CS); blend of mPEG and chitosan (mPEG+CS) and grafted polymer of mPEG and chitosan (mPEG-CS); and (B) grafted polymer of mPEG and chitosan conjugated with 2.5% (mPEG-CS-OA2.5) or 5% (mPEG-CS-OA5) of oleic acid. Red arrows indicate reflections that may arise from mPEG, black arrows indicate reflections that may arise from CS.

Figure 4.6. Effect of the cryoprotectants on micelles size and PdI and its stability at 4 ºC: (A) trehalose, (B) glucose and (C) mannitol. Micelles size and PdI during one week in water at 4 ºC (D).

Figure 4.7. Cumulative CPT release in simulated gastrointestinal fluids during 72 h at 37 ºC.

Figure 4.8. The effect of chitosan micelles on the CPT protection from hydrolysis over time in simulated gastrointestinal fluids.

Figure 5.1. (A) 1H NMR spectra of chitosan, mPEG-COOH and mPEG-CS bench scale and mPEG-CS scaled-up in 2% DCl (1 mg/mL, 400 MHz) and (B) ATR-FTIR spectra of mPEG-COOH, physical mixture of mPEG-COOH and CS, mPEG-CS bench scale, mPEG-CS scaled-up and chitosan (CS).

Figure 5.2. (A) 1H NMR spectra of chitosan, oleic acid and mPEG-CS-OA bench scale and mPEG-CS-OA scaled-up in 2% DCl (1 mg/mL, 400 MHz) and (B) ATR-FTIR spectra of oleic acid, physical mixture of mPEG-CS and oleic acid, mPEG-CS-OA bench scale, mPEG-CS-OA scaled-up and chitosan (CS).

Figure 5.3. Cellular viability of (A) mPEG-CS from the bench synthesis (B) mPEG-CS from the continuous manufacturing method (C) mPEG-CS-OA from the bench synthesis

(D) from the continuous manufacturing method tested in Caco-2 and HT29-MTX colorectal cancer cell lines for 4 and 24 h of incubation. Error bars represent mean ± SD (n = 3). *p<0.05 denotes a significant difference between 4 and 24 h of incubation by two-way analysis of variance (ANOVA) Sidak's multiple comparison test.

Figure 5.4. Characterization and stability of the chitosan micelles after long-term storage: (**A**) Average of micelle size, (**B**) polydispersity index, and (**C**) zeta potential for empty micelles placed at -20 ºC, 4 ºC, 25 ºC/60% HR and 40 ºC/75% HR after 0, 1, 3 and 6 months of storage. Error bars represent mean ± SD (n = 3). ***p< 0.001 and ****p<0.0001 denotes a significant difference denotes a significant difference compared with the formulation at time 0 by two-way analysis of variance (ANOVA) Dunnett's multiple comparison test.

Figure 5.5. TEM microphotographs of chitosan micelles after freeze-drying and after 1, 3 and 6 months of storage at -20 ºC, 4 ºC, 25 ºC/60% HR and 40 ºC/75% HR. Scale bar corresponding to 200 nm.

Figure 5.6. Macroscopic differences of chitosan micelles when subjected at different storage temperatures after 6 months.

Figure 6.1 – Scanning electron microscopy images of (A) Eudragit top layer of the printfill; (B) CPT crystals inside of the printfill; (C) CPT-loaded micelles inside of the printfill; (D) amplification of the printfill with polymeric micelles inside. Scale bar corresponding to 400, 30, 50 and 10 µm, respectively.

Figure 6.2. Cumulative CPT release from the printfills in simulated gastrointestinal fluids. *Squares* represent the release of CPT-loaded micelles and *circles* represent the release of free CPT. Error bars represent mean ± SD (n = 6).

Figure 6.3. Cellular viability of the dissolution medium from the printfills containing CPT-loaded micelles (blue columns) and free CPT (pink columns) after 4, 6 and 24 h of incubation with Caco-2 cells. Error bars represent mean ± SD (n = 6).

Figure 6.4. Intestinal permeability and respective TEER values of the CPT-loaded micelles and free CPT after being released in the simulated GIT fluid. (A) CPT permeability across Caco-2 standard model; (B) CPT permeability across a 3D intestinal model; (C) apparent permeability coefficients (P_{app}) of CPT-loaded micelles and free CPT

across Caco-2 monoculture model and across the 3D model. All experiments were conducted from the apical to basolateral side in HBSS at 37 °C. Error bars represent mean ± SD (n = 3). *p<0.05, ***p<0.001 and ****p<0.0001 denotes a significant difference by two-way analysis of variance (ANOVA) Sidak's multiple comparison test.

Figure 6.5. H&E staining to address the cellular integrity when cells were exposed to the dissolution medium containing CPT-loaded micelles and free CPT for the permeability assay. Cytoplasm stained with pink and nucleus with purple. The Transwell® membrane is transparent and is right below the cellular monolayer. Scale bar = 100 µm.

Figure 7.1. Cytocompatibility of empty chitosan-based polymeric micelles during 24, 48 and 72 h of incubation. (A) metabolic activity of PBMC's; (B) metabolic activity of HCT116 cell line. Concentration is represented in function to the micelle mass. Error bars represent mean ± SD (n = 3). *p<0.05, **p<0.01 and ***p<0.001 denotes a significant difference between incubation times by two-way analysis of variance (ANOVA) Tukey's multiple comparison test.

Figure 7.2 Cytotoxicity of free CPT and CPT-loaded micelles tested in PBMC's during (A) 24 h; (B) 48 h and (C) 72 h of incubation. Concentrations are represented in function of CPT. Error bars represent mean ± SD (n = 3). **p<0.01, ***p<0.001 and ****p<0.0001 denotes a significant difference between free CPT and CPT-loaded micelles by two-way analysis of variance (ANOVA) Sidak's multiple comparison test.

Figure 7.3 *In vitro* therapeutic efficacy of free CPT and CPT-loaded micelles against HCT116 cell line during (A) 24 h; (B) 48 h and (C) 72 h of incubation. Concentrations are represented in function of CPT. Error bars represent mean ± SD (n = 3). *p<0.05, ***p<0.001 and ****p<0.0001 denotes a significant difference between free CPT and CPT-loaded micelles by two-way analysis of variance (ANOVA) Sidak's multiple comparison test.

Figure 7.4. Metabolic activity and diameter measurement of 3D multicellular CRC spheroids after incubation with free CPT, empty micelles and CPT-loaded micelles. (A) 3D multicellular CRC spheroid; (B) schematic representation of the 3D multicellular CRC spheroid; spheroids metabolic activity after (A) 24 h, (B) 48 h and (C) 72 h of incubation with free CPT, empty micelles and CPT-loaded micelles; spheroids diameter after (A) 24 h, (B) 48 h and (C) 72 h of incubation with free CPT, empty micelles and CPT-loaded micelles. Concentrations are represented in function of CPT. Error bars represent mean

± SD (n = 3). *p<0.05, **p<0.01, ***p<0.001 and ****p<0.0001 denotes a significant difference when compared with the control (non-treated spheroids) by two-way analysis of variance (ANOVA) Tukey's (C, D and E) and Dunnet's (F, G and H) multiple comparison test.

Figure 7.5. Intestinal permeability and respective TEER values of free CPT and CPT-loaded mPEG-CS-OA micelles. (A) CPT permeability across Caco-2 standard model; (B) CPT permeability across a 3D intestinal model; (C) Apparent permeability coefficients (P_{app}) of free CPT and CPT-loaded mPEG-CS-OA micelles across Caco-2 monoculture model and the 3D intestinal model. All experiments were conducted from the apical to basolateral side in HBSS at 37 °C. Error bars represent mean ± SD (n = 3). *p<0.05, **p<0.01, ***p<0.001 and ****p<0.0001 denotes a significant difference by two-way analysis of variance (ANOVA) Sidak's multiple comparison test.

Figure 7.6. (A) Experimental timeline. N:NIH(S)II-*nu/nu* mice were injected with colorectal cancer HCT116 cells into the right flank of the mice. After 7 days of tumor inoculation, animals were subcutaneously (saline, CPT s.c., empty micelles, CPT-loaded micelles) and intravenously (CPT i.v.) treated three times per week, during two weeks. Saline-treated animals were used as experimental control (no treatment). After 21 days, animals were maintained for survival curve. (B) Change in the animal body weight was evaluated until day 40 after tumor cells inoculation. (C) Tumor growth (%) was measured using a caliper and normalized to the initial tumor volume for each animal, before any treatment. (D) Tumor volume (mm^3) in a HCT116 xenograft model after the end of the treatment. (E) Survival curves of tumor bearing mice. Error bars represent mean ± SD (n = 5-6). **p<0.01, ***p<0.001 and ****p<0.0001 denotes a significant difference when compared with the control (no treatment) by one-way (D) or two-way (C) analysis of variance (ANOVA) Dunnet's or Tukey's multiple comparison test, respectively.

Figure 7.7. Assessment of the distribution and retention of fluorescent chitosan micelles following oral administration by NIR imaging. (A) Representative fluorescence signal obtained from full body, live animals in supine position after 3 h of administration Cy7.5-loaded micelles (B) total efflux (photons/second) of Cy7.5-loaded chitosan micelles overtime after oral administration. (C) Representative fluorescence signal of animal *ex vivo* organs and colon after 12 h of administration. (D) total efflux (photons/second) of Cy7.5-loaded chitosan micelles distributed by the organs and colon after 12 of the oral administration. Error bars represent mean ± SD (n = 3). **p<0.01 denotes a significant difference t-test.

Figure 7.8. (A) Experimental timeline. C57BL/6 mice were chemically induced to develop colorectal cancer through the intraperitoneal injection of AOM, and DSS in the drinking water. After confirmation of the tumor formation by colonoscopy, animals were orally (saline, CPT suspension, empty micelles, CPT-loaded micelles) and intravenously (CPT i.v.) treated three times per week, during two weeks. Saline-treated animals were used as experimental control (no treatment). After the end of the treatment, animals were euthanized and the tumors counted. (B) Change in the animal body weight during treatment. (C) tumor score and (D) sum of the tumor area, (E) Intestine length (cm), (F) colon length (cm) and (G) spleen index were calculated after the euthanasia of animals. Error bars represent mean ± SD (n = 7). *p<0.05 and **p<0.01 denotes a significant difference when compared with the control (no treatment) by one-way analysis of variance (ANOVA) Dunnet's multiple comparison test.

Figure A1.1. Experimental procedure of the intestinal permeability under different gravity levels (g-levels). (A) Schematic illustration of cell culture and HG exposure process: Caco-2 cells were cultured for 21 days, to allow their differentiation into enterocyte-like cells. After this, FITC-dextran and CPT-micelles were incubated for 4 h, at different g-levels; (B) Schematic diagram for an example of HG exposure, which entailed 10 min rest period at different time points (0.5, 1, 2, 3 and 4 h). During this rest period at 1.0 g, TEER was measured and samples were removed from the basolateral side, for further quantification. This set up was performed for 2.5 g, 5.0 g and 7.5 g using the LDC and for the reference using an orbital-shaker, as control.

Figure A1.2. Evaluation of metabolic activity of Caco-2 cells after HG exposure. (A) Evaluation of cellular viability through resazurin assay; (B) Evaluation of cellular toxicity through LDH assay. Shown are the arithmetic means ± SD. *P<0.05 comparing with the reference, by one-way analysis of variance (ANOVA) Dunnett's multiple comparison test (*n*=6).

Figure A1.3. Assessment and comparison of different proteins at different g-levels. (A) Schematic illustration of the studied cellular components involved in different transport vias. Visualization of nuclei and (B) occludin and MRP2; (C) claudin-1 and MUC2; (D) claudin-2 and P-gp; (E) ZO-1 and PEPT1. Occludin, claudin-1, claudin-2 and ZO-1 are presented in green. MRP2, MUC2, P-gp and PEPT1 are presented in red. Nuclei are presented in blue.

Figure A1.4. H&E staining to address the cellular integrity when cells were exposed to different compounds and g-levels. Dextran and CPT-micelles were exposed to different g-levels (2.5 g, 5.0 g and 7.5 g) for 4 h. Cells without samples and the reference (shaking at 1.0 g) were included as controls. Cytoplasm stained with pink and nucleus with purple. The Transwell® membrane is transparent and is right below the cellular monolayer. Scale bar = 100 µm.

Figure A1.5. Intestinal permeability and respective TEER values of compounds with different pathways of internalization. (A) Schematic representation of the paracellular via used by FITC-Dextran; (B) Permeability percentage of FITC-Dextran quantified by fluorescence and respective TEER values; (C) Schematic representation of the CPT transport; (D) Permeability percentage of CPT from the micelles, quantified by HPLC, and respective TEER values during 4 h of incubation at different g-levels. Shown are the arithmetic means ± SD. $*P < 0.05$, $**P < 0.001$, and $\#P < 0.0001$ comparing with the reference, by two-way analysis of variance (ANOVA) Dunnett's multiple comparison test, *n=6*).

Figure S1. Visualization of occludin and MRP2 at different g-levels. Occludin is presented in **green**, MRP2 in **red** and nuclei in **blue.**

Figure S2. Visualization of claudin-1 and MUC2 at different g-levels. Claudin-1 is presented in **green**, MUC2 in **red** and nuclei in **blue**.

Figure S3. Visualization of claudin-2 and P-gp at different g-levels. Claudin-2 is presented in **green**, P-gp in **red** and nuclei in **blue**.

Figure S4. Visualization of ZO-1 and PEPT1 at different g-levels. ZO-1 is presented in **green**, PEPT1 in **red** and nuclei in **blue**.

Figure S5. ORTO visualization of cellular components at different g-levels. Occludin, claudin-1, claudin-2 and ZO-1 are presented in **green**. MRP2, MUC2, P-gp and PEPT1 are presented in **red**. Nuclei are **blue**.

Figure S6. Evaluation of the safety of nanosystems. (A) Cellular viability, assessed by the MTT assay and (B) cellular cytotoxicity assessed by the LDH assay, of micelles loaded with CPT or not. Free CPT was included as control. Shown are the arithmetic

means ± SD. ∗P < 0.05, comparing with the control, by two-way analysis of variance (ANOVA) Tukey's multiple comparison test, *n*=4).

Figure A2.1. Schematic representation of the mPEG-CS synthesis by a carbodiimide amidation.

Figure A2.2. Schematic representation of the mPEG-CS-OA synthesis by a carbodiimide amidation.

Figure A2.3. GPC chromatograms of (A) chitosan, (B) mPEG-COOH, (C) mPEG-CS and (D) mPEG-CS-OA2.5%.

Figure A2.4. From the left to the right, chitosan, mPEG-chitosan, mPEG-chitosan-oleic acid 2.5% and mPEG-chitosan-oleic acid 5% contact angle.

Figure A2.5. Thermogravimetric curves of the raw material: chitosan (CS), mPEG and oleic acid (OA).

Figure A2.6. DSC thermograms for raw materials: chitosan (CS) and oleic acid (OA). In the case of CS first and second run curves are different.

Figure A2.7. Critical micelle concentration determined by (A) Rayleigh scattering measured by DLS and by (B) surface tension method. Graphs are plotted in function of polymer concentration.

Figure A2.8. TEM images of empty (A) and CPT-loaded micelles (B).

Figure A2.9. XRD diffraction patterns of CS-OA 2.5%, mPEG-CS-OA 2.5%, mPEG-CS-OA 5.0%, mPEG-CS-OA 7.5% and mPEG-CS-OA 10.0%.

Figure A3.1. Digital design of printfills: (A) injection points for micelles; (B) injection points for free drug; (C) injection points of Eudragit FS30D for both batches; and (D) general design of the printfill.

Figure A3.2. Printfill before (A) and after drying step (B).

Figure A3.3. SEM images of top film of Eudragit FS30D (A) and sealed PLA perimeter (B).

Figure A3.4. TEER values of Caco-2 and 3D models during 21 days of culture. Error bars represent mean ± SD (*n* = 6).

Figure A4.1. Transmission electron microscopy images of (A) unloaded chitosan micelles and (B) CPT-loaded chitosan micelles. Scale bar corresponding to 0.5 µm.

Figure A4.2. Anticancer activity of free CPT and CPT-loaded micelles against Caco-2 (A, C and E) and HT29 (B, D and F) colorectal cancer cell lines during 24 h (A and B), 48 h (C and D) and 72 h (E and F) of incubation. Concentration is represented in function of CPT. Error bars represent mean ± SD (n = 3). *p<0.05, **p<0.01, ***p<0.001 and ****p<0.0001 denotes a significant difference by two-way analysis of variance (ANOVA) Sidak's multiple comparison test.

Figure A4.3. Wound healing assay performed in HCT116 cells incubated with complete DMEM (control) or with different CPT concentrations of free CPT or CPT-loaded micelles and empty micelles after (A) 24 h and (B) 48 h of incubation. Concentration is represented in function of CPT. Error bars represent mean ± SD (n = 3). *p<0.05, **p<0.01 and ***p<0.001 denotes a significant difference when compared with the control (no treatment) by two-way analysis of variance (ANOVA) Dunnett's multiple comparison test.

Figure A4.4. Visualization of CPT, EpCAM and nuclei of the 2D and 3D intestinal monolayers after permeability tested with free CPT, CPT-loaded mPEG-CS-OA micelles and CPT-loaded CS-OA micelles. EpCAM is present in **green**, nuclei in **red** and CPT in **blue**. Scale bar represents 50 µm.

Figure A4.5. Animal body weight change during chemical CRC induction.

Figure A4.6. Images acquired by colonoscopy before and after the treatment started. Saline (non-treated), CPT suspension, empty micelles and CPT-loaded micelles were administered orally, while CPT i.v. was administered intravenously.

Figure A4.7. Percentage of tumor size distribution expressed in millimeters (mm).

LIST OF TABLES

Table 2.1. Main biological differences between normal and inflamed and tumor tissues.

Table 2.2. Examples of self-assembled particles under clinical trials evaluation for cancer treatment.

Table 2.3. Summary of the chitosan derivatives used to encapsulate and deliver paclitaxel.

Table 2.4. Summary of the chitosan derivatives used to encapsulate and deliver camptothecin, doxorubicin and docetaxel.

Table 3.1. *In silico* prediction of several physicochemical descriptors using the CPT chemical structure on Chemaxon® software.

Table 3.2. Distribution coefficients of CPT obtained in a biphasic membrane/aqueous system.

Table 4.1. Thermodynamic parameters obtained from DSC of grafted polymer of mPEG and chitosan (mPEG-CS); blend of mPEG and chitosan (mPEG+CS); grafted polymer of mPEG and chitosan conjugated with 2.5% (mPEG-CS-OA2.5) or 5% (mPEG-CS-OA5) of oleic acid.

Table 4.2. Substitution degree (SD) and critical micelle concentration (CMC) of the new chitosan derivatives.

Table 4.3. The particle size, PdI, micelles surface charge, EE and DL of CPT-loaded mPEG-CS-OA micelles and unloaded micelles. Values are represented as mean ± SD (n = 3).

Table 4.4. Constant rates (k) and correlation coefficients (R^2) obtained through the modeling of CPT release from mPEG-CS-OA micelles following: zero-order, first-order kinetic, Weibull, and Korsmeyer–Peppas models.

Table 5.1. Relationship between bench synthesis and continuous manufacturing method methods regarding the manufacturing time, substitution degree calculated by ^{1}H NMR and the yield.

Table 6.1. The theoretical drug loading (DL_T), association efficiency (AE), the drug loading (DL), particle size, PdI and micelles surface charge empty and CPT-loaded mPEG-CS-OA micelles. Values are represented as mean ± SD (*n* = 3).

Table 6.2. Physical characteristics of printfills with free CPT and CPT-loaded micelles.

Table 7.1. The particle size, polydispersity index (PdI), micelles surface charge, association efficiency (AE) and drug loading (DL) of empty chitosan micelles and CPT-loaded micelles. Values are represented as mean ± SD (n = 3).

Table 6.3. Mathematical modelling and drug release kinetics from enteric printfills.

Table 7.2. Pharmacokinetic parameters of CPT-loaded micelles, CPT suspension and CPT i.v. in C57BL/6 CRC induced mice.

Table A1.1. Apparent permeability coefficients calculated after 4 h of incubation in Caco-2 cells.

Table A2.1. XRD peak positions of mPEG, CS, mPEG+CS, mPEG-CS, mPEG-CS-OA2.5 and mPEG-CS-OA5.

Table A3.1. FDM settings for batches with free CTP and CPT-loaded micelles.

Table A3.2. IVF settings for every printable ink injected (free drug, delaying polymer, micelles) corresponding to both batches.

Table A3.3. Details of the four phases of the intestinal transit for drug release test.

Table A3.4. Switch solution compositions used in the dissolution assay.

LIST OF ACRONYMS AND ABBREVIATIONS

^{1}H NMR	Proton nuclear magnetic resonance
3DP	Three-dimensional printing
5-FU	5-fluorouracil
ADMET	Absorption, distribution, metabolism, excretion and toxicity
AE	Association efficiency
ANOVA	Analysis of variance
AOM	Azoxymethane
ASI	Adipose store index
ATCC	American type culture collection
AUC	Area under the curve
BBB	Blood brain barrier
BCS	Biopharmaceutical classification system
BPL	Brain polar lipids
BSA	Bovine serum albumin
CFF	Cross flow filtration
CHUSJ	Centro Hospitalar Universitário São João
CHOL	Cholesterol
CL	Cardiolipin
C_{max}	Maximum concentration
CMC	Critical micelle concentration
CMT	Critical micellization temperature
CPT	Camptothecin
CRC	Colorectal cancer
CS	Chitosan
CYP3A4	Cytochrome P450 3A4
CYP450	Cytochrome P450
DA	Degree of acetylation
DAPI	4', 6-diamidino-2-phenylindole, dihydrochloride
DDS	Drug delivery systems
DL	Drug loading
DLS	Dynamic light scattering
DMEM	Dulbecco's Modified Eagle's Medium
DMPC	Dipalmitoylphosphatidylcholine
DMPG	1,2-dimyristoyl-*sn*-glycero-3-phosphoglycerol

DMSO	Dimethyl sulfoxide
DOPE	1,2-di-oleoyl-*sn*-glycero-3-phosphoethanolamine
DOPG	1,2-dioleoyl-*sn*-glycero-3-[phospho-rac-(1-glycerol)]
DOPS	1,2-dioleoyl-*sn*-glycero-3-phospho-*L*-serine
DOX	Doxorubicin
DSC	Differential scanning calorimetry
DSS	Dextran sodium sulfate
DTX	Docetaxel
ECGS	Endothelial Cell Growth Supplement
EDC	1-ethyl-3-(3-dimethylaminopropyl) carbodiimide
eEPR	Epithelial enhanced permeability and retention
EGFR	Epidermal growth factor receptor
ELS	Electrophoretic light scattering
EPC	Egg phosphatidylcholine
EpCAM	Epithelial cell adhesion molecule
EPR	Enhanced permeability and retention
ESA	European Space Agency
ESTEC	European Space Research and Technology Centre
FA	Folic acid
FBS	Fetal bovine serum
FDA	Food and Drug Administration
FDM	Fused deposition modelling
FGS	Fibroblast Growth Supplement
FITC	Fluorescein isothiocyanate
Fr	Relative bioavailability
FRET	Fluorescence resonance energy transfer
FTIR	Fourier Transform Infrared Spectroscopy
GlcN	2-amino-2-deoxy-*D*-glucopyranose
GlcNAc	2-acetamido-2-deoxy-D-glucopyranose
H&E	Hematoxylin and eosin
HG	Hypergravity
HSA	Human serum albumin
i3S	Institute for Research and Innovation in Health
IBD	Inflammatory bowel disease
ICH	International Conference on Harmonization

IINFACTS	Institute of Research and Advanced Training in Health Sciences and Technology
ISO	International organization for standardization
i.v.	Intravenous
IVF	Injection volume filling
GIT	Gastrointestinal tract
GMP	Good manufacturing practice
GPC	Gel permeation chromatography
HBSS	Hank's balanced salt solution
HIF	Human intestinal fibroblast
HOBt	1-hydroxybenzotriazole hydrate
HPLC	High performance liquid chromatography
LDC	Large diameter centrifuge
LDH	Lactate dehydrogenase
LogD	Distribution coefficient
LogP	Partition coefficient
mAb	Monoclonal antibodies
MCR	Mean count rate
MCTSs	Multicellular tumor spheroids
mPEG	Methoxy poly(ethylene glycol)
mPEG-CS	Methoxy poly(ethylene glycol)-grafted-chitosan
mPEG-CS-OA	Methoxy poly(ethylene glycol)-grafted-chitosan-grafted-oleic acid
MPS	Mononuclear phagocyte system
MRP2	Multidrug resistance-associated protein 2
MTT	3-(4,5-Dimethylthiazol-2-yl)-2,5-diphenyltetrazolium bromide
MUC2	Mucin 2
Mw	Molecular weight
NanoDDS	Nano drug delivery systems
NBD-PE	1,2-dipalmitoyl-*sn*-glycero-3-phosphoethanolamine-N-(7-nitro-2-1,3-benzoxadiazol-4-yl)
NHS	*N*-hydroxysuccinimide
NIR	Near-infrared imaging
NOSC	*N*-octyl-*O*-sulfate chitosan
NPs	Nanoparticles
OA	Oleic acid

P_{app}	Apparent permeability coefficient
PBMCs	Peripheral blood mononuclear cells
PBS	Phosphate-buffered saline
PBST	PBS 1X with 0.05% Tween® 20
PC	Phosphocholine
PdI	Polydispersity index
PE	Phosphatidyl ethanolamine
PEG	Poly(ethylene glycol)
PEPT1	Peptide transporter 1
PFA	Paraformaldehyde
P-gp	P-glycoprotein
PK	Pharmacokinetic
PLA	Poly(*D,L*-lactide acid)
PLGA	Poly(*D,L*-lactide-*co*-glycolic acid)
PPO	Polypropylene oxide
PS	Phosphatidyl serine
PSA	Polar surface area
PTX	Paclitaxel
PVP	Poly(*N*-vinylpyrrolidone)
RES	Reticuloendothelial system
RFUs	Relative fluorescence units
RH	Relative humidity
RPMI-1640	Roswell Park Memorial Institute medium
RT	Room temperature
SAXS	Small angle X-ray diffraction
s.c.	Subcutaneous
SD	Substitution degree
SEM	Scanning electron microscopy
SGF	Simulated gastric fluid
SIF	Simulated intestinal fluid
SM	Sphingomyelin
TEER	Transepithelial electrical resistance
TEM	Transmission electron microscopy
TGA	Thermogravimetric analysis
TJs	Tight junctions
t_{max}	Maximum time

TMC	Trimethyl chitosan
TNBS	2,4,6-trinitrobenzenesulfonic acid solution
TOP1	Topoisomerase I
VD_{ss}	Steady-state volume distribution
VEGF	Vascular-endothelial growth factor
VWSA	Van der Waals surface area
WAXS	Wide angle X-ray diffraction
WT	Wild type
XRD	X-ray diffraction
ZO-1	Zona occludens 1

CHAPTER 1

Overview and Aims

1.1. Overview

Colorectal cancer (CRC) is among the cancers with highest prevalence and mortality worldwide. Currently, conventional CRC chemotherapy has limited efficacy, and the side effects of the treatment are not well tolerated by patients. Thus, other approaches must be considered in order to achieve a better therapeutic outcome. Camptothecin (CPT) is a powerful anticancer drug, but due to its hydrophobicity and toxicity, it is not feasible be administered intravenously. The use of nanotechnology can be a great tool to enhance the therapeutic efficacy of this drug, while decreasing the unwanted systemic toxicity. Accordingly, in this thesis, nanotechnology was used to develop oral CPT-loaded mucoadhesive polymeric micelles for CRC treatment. Polymeric micelles are able to encapsulate hydrophobic drugs with high efficiency, increasing its solubility and stability. Thus, these nanosystems are able to protect the drug from the enzymatic degradation and the harsh environment of the GIT after an oral administration, increasing the amount of drug at the intestine in order to exert its therapeutic function.

In the framework of this thesis, a collaborative work between the Institute for Research and Innovation in Health (i3S) at the University of Porto (Portugal), Centro de Física das Universidades do Minho e Porto (Portugal), Vall d'Hebron Research Institute (Spain), University of Seville (Spain), MyBiotech GmbH (Germany), Institute of Research and Advanced Training in Health Sciences and Technology (IINFACTS) (Portugal) and European Space Agency (ESA) (The Netherlands) was established.

The Bruno Sarmento's group at i3S is focused on drug delivery systems with great emphasis on nanotechnology and its applications in the pharmaceutical and biomedical fields. In particular, the group is interested in engineering new oral drug formulations for the delivery of hydrophobic anticancer drugs for cancer treatment, aiming to improve drug solubility and, consequently, the therapeutic efficacy of anticancer drugs. Additionally, the group has a specific interest in mucosal engineering models for nanomedicines validation as well as in *vitro/in vivo* correlation. Marlene Lúcio's group from Centro de Física das Universidades do Minho e Porto is specialized on biophysical studies at the molecular level to clarify the mechanism of action and toxicity of drugs, offering valuable insights to improve the therapeutical value and effectiveness of drugs. The Simo Schwartz's group at Vall d'Hebron Research Institute is focused on the development of novel scientific applied therapies and nanotechnology-based therapeutic applications. Advanced cell therapies, novel biomaterials and drug delivery technologies, image-based diagnostic systems, and preclinical evaluation of therapeutic conjugates, primarily in oncology and rare diseases, are of particular interest. The Isidoro Caraballo's group at University of Seville is expert in the development of pharmaceutical formulations and have been using 3D printers to design

colon-specific drug delivery systems. Nazende Günday-Türeli from MyBiotech GmbH works on quality-by-design of pharmaceutical nanotechnology products, aiming to bring them into the market in a fast and efficient way. IINFACTS's mission is to conduct high-quality basic and translational research to better understand and address complex health problems. Lastly, the TEC-MMG LIS Lab at ESA is interested on life and physical sciences related research and projects for microgravity and hypergravity testing.
The above stablished collaborations between groups enabled the fulfilment of this thesis and the improvement of my scientific knowledge, while developing new oral delivery systems based on chitosan for CRC treatment.

1.2. Aim and specific objectives

The main aim of this thesis was engineer chitosan-based polymeric micelles to deliver CPT to CRC through oral administration. This biocompatible delivery system would be expected to effectively overcome the poor solubility drawbacks of CPT, while allowing a superior intestinal mucosa retention of the drug and consequent enhanced anticancer activity. The ultimate goal was to use these engineered polymeric micelles to treat CRC.

The specific objectives of this thesis were to:

a) Investigate the *in silico* and *in vitro* pharmacokinetic and physicochemical properties of CPT in order to predict its *in vitro* and *in vivo* behavior (Chapter 3);

b) Design, synthetize and characterize new amphiphilic graft copolymers of unsaturated fatty acids, methoxy poly(ethylene glycol) and chitosan with self-assembling properties in aqueous environment (Chapter 4);

c) Produce polymeric micelles based on chitosan derivatives to encapsulate and enhance the solubility of CPT, and characterize their physico-chemical properties and drug release kinetics in simulated biological media (Chapter 4);

d) Produce and characterize the new chitosan derivatives in a continuous manufacturing method with capacity of scaling-up and study the long-term storage stability of the polymeric micelles obtained from the scaled-up copolymer (Chapter 5);

e) Explore 3D printing as a strategy to provide a handling oral macroplatform for a colon-specific release of CPT (Chapter 6);

f) Evaluate polymeric micelles behavior regarding cytotoxicity, *in vitro* anticancer efficacy and *in vitro* intestinal permeability of CPT (Chapter 7);

g) Validate the *in vivo* therapeutic capabilities of the CPT-loaded polymeric micelles using nude mice bearing a subcutaneous xenograft tumor derived from CRC cells as a local therapy and, CRC C57BL/6 mice to study the micelles biodistribution, CPT pharmacokinetic and therapeutic efficacy of CPT-loaded micelles after oral administration (Chapter 7);

1.3. Structure

This thesis is organized in eight chapters. In Chapter 1, a general overview of the work is given as well as the specific objectives of the study and the description of the collaborative entities that supported the development of this thesis. In Chapter 2, a review of the literature is provided taking in consideration the main problem to address, the CRC, as well as the use of polymeric micelles based on chitosan derivatives to improve the solubility of anticancer drugs. Chapter 3 details the *in silico* pharmacokinetic profile and the biophysical characteristics of CPT in order to predict *in vitro*/*in vivo* biodistribution and bioaccumulation, supporting the exploitation of this drug molecule. Chapter 4 describes the synthesis of new chitosan derivatives with ability to form micelles by self-assembly. Also, the encapsulation of CPT was evaluated as well as the ability of micelles to protect the drug from hydrolysis. Chapter 5 contains the description of copolymer synthesis by a continuous manufacturing method proving the industrialization process potential of these copolymers. Moreover, the long-term stability of chitosan-based micelles was studied at four different temperatures in order to find the most appropriated store conditions maintaining its physicochemical properties. In Chapter 6, polymeric micelles were printed in a 3D system with an enteric coating, which allows a colon-specific delivery of the micelles, protecting the drug from the harsh environment of the gastrointestinal tract. Chapter 7 describes the *in vitro* therapeutic efficacy of CPT-loaded micelles in 2D cells and 3D spheroids and, the *in vivo* therapeutic efficacy in a CRC xenograft and orthotopic animal models demonstrating its potential as oral delivery platform. Chapter 8 includes the overall conclusions of the work, as well as discusses several possibilities regarding future studies. At the end, it is possible to find the appendix section that contains the support of several chapters of this thesis.

CHAPTER 2

Literature Review

This chapter was based on the following published papers and book chapters:

- Silva, D., **Almeida, A**., Azevedo, C., Campana-Filho, S. P., & Sarmento, B. (2018). Synthesis and Applications of Amphiphilic Chitosan Derivatives for Drug Delivery Applications. In *Nanoparticles in Life Sciences and Biomedicine* (45-73), Pan Stanford.

In this book chapter, I was responsible for the conception and execution of part of the contained information. The remained part was written by Daniella Silva and Cláudia Azevedo, which also included reorganizing the topics and improve the discussion and images. The supervisors were responsible for reviewing and submit the manuscript. This book chapter was not previously included in other thesis, and it is partially reproduced in this section.

- Andrade, F., **Almeida, A**., Rafael, D., Schwartz, S., & Sarmento, B. (2018). Micellar-Based Nanoparticles for Cancer Therapy and Bioimaging. In *Nanooncology*, (211-238), Springer, Cham.

In this book chapter, I was responsible for the conception and execution of part of the contained information. The remained part was written by Fernanda Andrade and Diana Rafael revised the manuscript. The supervisors were responsible for reviewing and submit the manuscript. This book chapter was not previously included in other thesis, and it is partially reproduced in this section.

- **Almeida, A**., Macedo, M. H., das Neves, J., & Sarmento, B. (2018). Thermo-responsive Nanomedicines for Drug Delivery in the Gastrointestinal Tract. In *Stimuli-responsive Drug Delivery Systems* (83-108).

In this book chapter, I was responsible for the conception, execution of most of the manuscript. Maria Macedo helped writing the thermosensitive liposomes section, José das Neves was responsible for reviewing the manuscript and the supervisor was responsible for reviewing and submit the manuscript. This book chapter was not previously included in other thesis, and it is partially reproduced in this section.

- **Almeida, A**. & Sarmento, B., (2021). Chitosan polymeric micelles as oral delivery platform of hydrophobic anticancer drugs. In *Chitosan for Biomaterials IV: Biomedical Applications*, Advances in Polymer Science, Springer.

In this book chapter, I was responsible for the conception, execution and revision of the manuscript. The supervisor was responsible for reviewing and submit the manuscript. This book chapter was not previously included in other thesis, and it is partially reproduced in this section.

2.1. Cancer

Cancer comprises a multitude of heterogeneous pathological conditions and has been one of the most studied fields in biomedical sciences. Despite all efforts being made over the last decades, many aspects of this group of diseases are complex and remain misunderstood. Cancer is generally characterized by the deregulation of the normal cell cycle, leading to abnormal cell growth and spreading beyond its natural limits [1]. When self-regulation of cellular division fails, the resulting cells can invade other parts of the body and spread to other tissues and organs through a mechanism called metastasis, which is a major cause of death by cancer [2, 3].

The number of new cancer cases has been increasing over the years. In 2020, cancer was the second group of diseases with the highest mortality rate worldwide and the numbers are expected to increase about 70% over the next decades [4, 5]. The probability to develop cancer increases with aging in association with other external factors such as tobacco use, infectious diseases, unhealthy diet or exposure to ultraviolet and ionizing radiation, or by internal factors such as genetic mutations, hormones or immune conditions [3, 6]. In addition, it has been established that most cancers are the result of chronic inflammatory diseases related to infection. Particularly, inflammatory bowel disease (IBD), which is a condition characterized by the intestinal inflammation, can increase twice the risk of developing colorectal cancer (CRC) [4].

2.1.1. Colorectal cancer development

In 2020, CRC was considered the fourth leading cause of death worldwide and the third most common cancer in both male and female [4]. The incidence of this type of cancer as well as the number of deaths is higher for males than for females and, the probability to develop cancer increases with age in association with other factors. In fact, only about 10% of CRC cases are due to heredity and around 90% are occasional, i.e., with no family history or genetic predisposition [7, 8].

It has been described the risk factors to develop CRC and, some of them are absence of physical activity, unhealthy diet, smoking and excessive alcohol consumption [9]. Additionally, patients with IBD have been tightly related to the risk of developing CRC when compared with the general population [10, 11]. The change in bowel habits (diarrhea or constipation), blood in the stool, abdominal pain, loss of appetite, or weight loss are some of the most common symptoms that lead to diagnosis.

CRC develops, usually, as a non-cancerous polyp on the inner layer of the colon or rectum. Adenomatous polyps, also known as adenomas, are the most common type of polyp, which are formed from glandular cells that secrete mucus to the colon and rectum [12]. This

happens due to the clonal expansion of colonic crypt cells with APC loss-of-function mutations or CTNNB1 gain-of-function mutations. These mutations promote the sustained activation of the Wnt pathway, which controls the stem cell compartment and cell fate along the crypt-villus axis [12]. This causes β-catenin to translocate to the nucleus and interact with the transcription factors TCF/LEF and YAP/TEAD, encouraging cell proliferation and stemness. Following these initial events, subsequent mutations in oncogenes as KRAS and BRAF, and/or tumor suppressors as SMAD4 and TP53, contribute to the transformation of adenomatous polyps [13]. If the adenoma grows in size, there is a greater chance that it may develop into adenocarcinomas and the initiation of metastatic disease is possible to occur.

CRC has a high cellular heterogeneity due to many genetic and biological changes. This heterogeneity is responsible for the high variability between tumors, which means CRC can progress from other genetic mutations as the alteration of TTN, PIK3CA, FBXW7, CVR2A, TGFBR2, MSH3 or MSH6 genes [14].

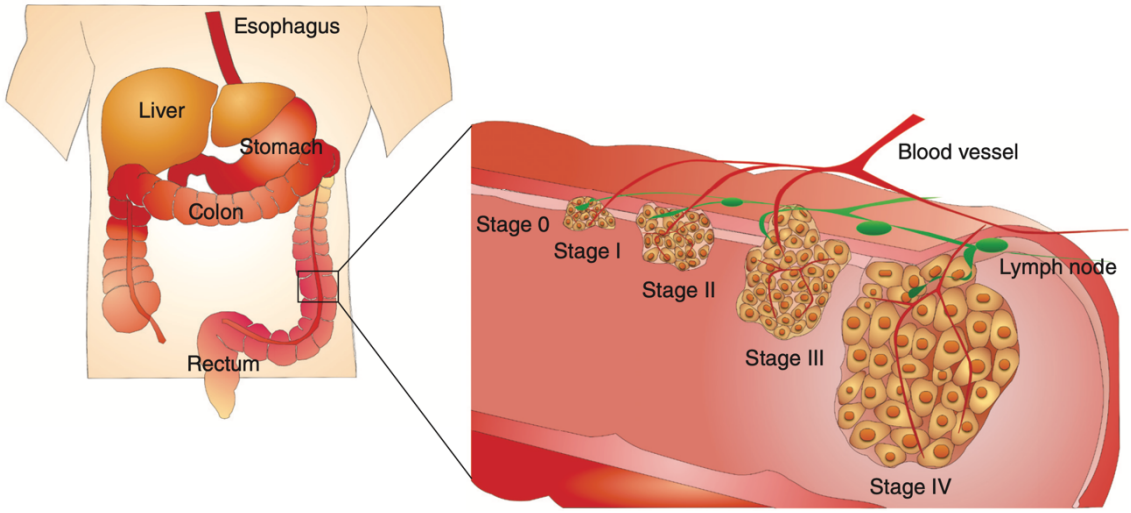

Figure 2.1. Stages of colorectal cancer according to the American Joint Committee on Cancer. Stage 0: tumor confined to mucosa (carcinoma in situ); Stage I: tumor invades submucosa and muscularis propria; Stage II: tumor invades through the muscularis propria into pericolorectal tissues (IIA), then penetrates to the surface of the visceral peritoneum (IIB), then directly invades or is adherent to other organs or structures (IIC); Stage III: tumor invades muscularis propria with metastases in 1–3 regional lymph nodes or nearby tissue, or invades submucosa with metastases in 4–6 regional lymph nodes (IIIA). Then tumor penetrates to the surface of the visceral peritoneum with metastases in 1–3 regional lymph nodes or nearby tissue, or invades through the muscularis propria into pericolorectal tissues with metastases in 4–6 regional lymph nodes, or invades muscularis propria with metastases in 7 or more regional lymph nodes (IIIB). Then tumor penetrates to the surface of the visceral peritoneum with metastases in 4–6 regional lymph nodes, or invades through the muscularis propria into pericolorectal tissues with metastases in 7 or more regional lymph nodes, or directly invades or

is adherent to other organs or structures with metastases in one or more regional lymph nodes (IIIC); Stage IV: metastasis confined to one organ or site (e.g., liver, lung, ovary, nonregional node). Reprinted with permission from [15].

2.1.2. Colorectal cancer treatment

CRC therapy faces significant challenges, such as: (i) nonspecific systemic distribution of drugs, in which active molecules reach both normal and abnormal cells/tissues; (ii) unsuitable drug concentrations at affected sites; (iii) adverse drug effects; and (iv) development of drug resistance [16]. CRC treatment depends also on the location, size, and extent of cancer spread, as well as the patient's health [17].

Although patients in the early stages of non-metastatic CRC (stages I-III) often benefit from surgery followed by chemotherapy as a successful treatment, patients with metastatic CRC have a five-year survival rate after surgery and adjuvant chemo/immunotherapy and/or radiotherapy [18]. Nowadays, the chemotherapeutic treatment usually adopted is the combination of 5-fluorouracil (5-FU) with leucovorin and oxiplatin (FOLFOX) or the combination of 5-FU with leucovorin and irinotecan (FOLFIRI) [19]. The use of 5-FU started in the 1980s and, in the mid-1990s, the combination of 5-FU with leucovorin and later with oxiplatin and irinotecan was adopted as routine adjuvant therapy for patients with stage III colon cancer. Nonetheless, the Food and Drug Administration (FDA) approved multiple monoclonal antibodies (mAb) for targeted therapy in 2004, including vascular-endothelial growth factor (VEGF) inhibitors such as bevacizumab, epidermal growth factor receptor (EGFR) inhibitors such as cetuximab and panitumumab, and BRAF inhibitors as encorafenib [20]. Immune checkpoint inhibitors such as pembrolizumab, nivolumab (anti-PD1 mAb), and ipilimumab (anti-CTLA-4 mAb) were approved in 2017 for advanced CRC patients with malignant lesions with increased levels of microsatellite instability and DNA mismatch repair deficiency, who had not responded to first-line chemotherapy [21, 22]. Also, recently, the FDA approved pembrolizumab as first-line immunotherapy for patients with metastatic CRC [23].

Despite all attempts to improve screening methods and clinical techniques, CRC diagnosis remains neglected, and therapies for patients with advanced disease are scarce and unsuccessful. Thus, researchers and doctors have been looking for other therapeutic approaches as the use of doxorubicin (DOX) [24, 25], paclitaxel (PTX) [26, 27] or camptothecin (CPT) [28, 29] for CRC treatment. The adjuvant or neoadjuvant therapy is given according to the cancer stage. However, if highly aggressive chemotherapy resistance, tumor heterogeneity, and metastases develop, these methods of treatment become ineffective [30]. As a result, new approaches to improving existing

chemotherapeutic treatments are urgently needed.

2.1.3. Camptothecin in colorectal cancer treatment

CPT is a potent anticancer drug that is being tested in clinical trials for a variety of cancers, including CRC. It is an alkaloid isolated from the Chinese tree *Camptotheca acuminata* with a pH-dependent behavior. This molecule may exist in two forms: the lactone form, which is stable at pH 5.5 and biologically active, or the carboxylate form, which is stable at pH > 9 and do not exert a therapeutic function [31].

Its mechanism of action is based on binding to DNA topoisomerase I, an enzyme that is essential for removing supercoils during DNA transcription, replication, and chromosome condensation [31-33]. However, CPT shows some drawbacks as the poor water-solubility and lack of specific, leading to major side-effects, reason why has been failing on clinical trials and never reached clinic until now.

Due to CPT high hydrophobicity, several CPT analogues have been synthesized aiming to improve its aqueous solubility, as the case of irinotecan (Camptosar®), topotecan (Hycamtin®) and Belotecan (Camtobell®), the only three analogues approved for clinical administration [34, 35]. In fact, irinotecan has been used as adjuvant therapy in CRC together with 5-FU and leucovorin and, topotecan is also approved for cancer treatment. Still, its effectiveness falls short of expectations in patients with tumors in more advanced stages. The use of CPT associated with nanosystems may be a new approach to the treatment of CRC. In this sense, the water solubility can be increased, as well as, a decrease in the toxic side-effects on healthy tissues can be also observed. Thus, there are some CPT-loaded nanosystems in clinical trials for CRC treatment at the moment [36-38].

2.2. Gastrointestinal tract

Being CRC a gastrointestinal disease, it is important to know the composition of the gastrointestinal tract (GIT) and understand where the tumor is developed. Thus, the main function of the GIT is the digestion of food and absorption of nutrients and vitamins. It is designed to facilitate absorption of relatively low molecular weight compounds, but also to prevent the entry of macromolecules, toxins or antigens [39]. The GIT begins in the oral cavity and continues through the esophagus to the stomach, small intestine (duodenum, jejunum and ileum) and large intestine (colon), ending up at the rectum. Each part of the GIT presents distinct anatomical, biochemical and physiological properties, which determine digestion and absorption.

The intestine wall is composed of several layers that are not fully separated from each

other, but are joined together by connective tissue and vascular and neuronal elements [40]. There are four main layers: mucosa, submucosa, muscularis propria and serosa. The mucosa is structurally and functionally more complex and contacts directly with the intestinal lumen. Absorption phenomena occur mainly at the mucosa, which can be further subdivided into epithelium, lamina propria and muscularis mucosae. The intestinal epithelium comprises epithelial cells that are directly in contact with nutrients, microbiota and mucus, being connected to the basal membrane covering the second layer, known as lamina propria. This last layer consists in subepithelial connective tissue featuring blood capillaries and lymph nodes. The next underlying layer is called muscularis mucosae and is constituted by a thin layer of smooth muscle [40, 41]. The submucosa is a thin layer of connective tissue that supports mucosa and connects it to the muscularis propria, which is constituted by longitudinal and circular muscle cells that facilitate peristalsis [42]. Finally, the innermost layer, the serosa, is formed essentially by fat and, also by a layer of epithelial cells called mesothelium [43].

Two main barriers can be implied in drug absorption and in the entry of undesirable materials. The first is a physical barrier constituted by a mucus layer and epithelial cells and, the second is a biochemical barrier composed by catabolic enzymes and efflux systems, such as P-glycoprotein (P-gp) and multidrug resistance-associated protein 2 (MRP2), which act against drug absorption [44]. However, it has been described that mucus can also influence nanocarriers adhesion, thus favoring drug absorption [45]. This is the case of nanoparticles densely coated with polyethylene glycol (PEG) that are able to cross mucus with a higher diffusion rate than non-modified nanoparticles [46]. It is also widely described that if their surface is modified by the incorporation of lipid-grafted PEG chains, the GIT will slow the clearance by the mononuclear phagocyte system (MPS), thereby prolonging the circulation time [47, 48].

2.2.1. Cellular constitution of the gastrointestinal tract

The epithelium of the small intestine consists of different cell types that are located in the villi (enterocytes, goblet and enteroendocrine cells) and differentiated cells residing at the bottom of the crypts, such as Paneth cells and microfold or membranous cells (M-cells) [40, 49]. Crypts are tubular invaginations of the intestinal epithelium being characterized by presenting basal Paneth cells and stem cells, which continuously divide and are the source of all intestinal epithelial cells [49]. Villi are tiny finger-like projections, which increase the surface area by approximately 30-fold [50].

The large intestine or colon begins in the right iliac region of the small intestine and is very similar to the small intestine in terms of cellular organization and morphology. Unlike the

latter, the mucosa of the large intestine is not covered with villous projections but contains deep tubular pits, which increase in depth as they approach the rectum, as well as the muscularis propria and further increase the surface area for digestion and absorption by approximately 600-fold [40, 50].

The colon is covered by a highly viscoelastic mucus layer, which avoids bacteria and virus from crossing the epithelium due to constant turnover [51]. Mucins, lipids and mucopolysaccharides are the main constituents of mucus and, changes in mucus composition and thickness have been reported in cancer, which can even be useful in detecting early cases of cancer [52].

Understanding where CRC arises and from which cells, as well as how a local tumor is staged, requires a review of these layers and their associated structures. The penetration into or across specific layers, as well as regional lymph node activity, influence the staging, prognosis, and suggested therapies of CRC that have not metastasized. As an example, a CRC that spreads through but not beyond the outer layer, adventitia or serosa, but has not spread to regional lymph nodes or distant organs is thus classified as stage IIA.

2.2.2. Differences between normal and diseased tissues

It is well-known that anticancer drugs have to overcome diverse biological barriers until attaining the bloodstream in therapeutically relevant concentrations. Drugs should, ideally, reach damaged cells and increase the intracellular concentrations, leaving normal cells unaffected, thus reducing toxicity. There are several differences between normal and inflammatory and/or tumor tissues that can be useful when considering differential drug delivery using nanomedicines. The main differences between normal and pathological tissues are listed in Table 2.1.

In tumor tissues, the formation of new blood vessels occurs through a process called angiogenesis. Nevertheless, these new vessels display several abnormalities such as vessel tortuosity, deficient pericytes and large gaps between adjacent endothelial cells [53]. These gaps can reach 100-800 nm, whereas in healthy vasculature the endothelial cells are tightly bound with fenestrations around 1-10 nm [54, 55]. In this sense, nanomedicines can preferentially bypass tumor vasculature allowing the extravasation of drugs into affected tissues. It has been described that the fenestrations of tumor vasculature are due to abnormal levels of vascular mediators such as bradykinins, nitric oxide, vascular endothelial growth factor, fibroblast growth factor, prostaglandins, among others [2, 56]. This unique feature of tumor vessels combined with reduced lymphatic drainage leads to the enhanced permeability and retention (EPR) effect [57, 58]. This phenomenon allows macromolecules and small particulates, such as the case of

nanomedicines, to leave the systemic circulation and enter in the extravascular space to be concentrated within the tumor tissue by a mechanism called passive targeting (Figure 2.2).

Additionally, inflammatory colon tissue is characterized by enterocyte disruption, which can lead to an increase on intestinal permeability due to enterocyte barrier damage [59]. Thus, nanomedicines can accumulate at intercellular gaps by means of the epithelial enhanced permeability and retention (eEPR) effect, allowing an increase of drug concentration at the desired site. The rupture of the barrier formed by the enterocytes provides access to the entrance of luminal and mucosa bacteria, which leads to the increase of immune cells levels [60]. In this sense, the resulting immune response induces overexpression of inflammatory cytokines that disrupt intestinal homeostasis, leading to the development of IBD [60, 61].

In the case of cancer cells, nanocarriers can find membrane receptor molecules that are overexpressed as compared to normal tissues. Nanomedicines functionalized with targeting ligands can bind specifically to these receptors, thus leading to increased interaction and uptake into the cancer cells via receptor-mediated endocytosis (Figure 2.2) [62, 63]. In cancer, there are specific receptors overexpressed only at the inflamed tissue, which can lead to a more specific and effective targeting. Most of these receptor-specific ligands are very used in oral colon-specific strategies such as lectin, which is a sugar binding protein with great capacity to bind specific carbohydrate residues [64], transferrin, which receptor is expressed at low levels in normal cells, but overexpressed in inflamed colon cells [65], bacterial adhesins [66] or ligands for CD98, a type II membrane glycoprotein overexpressed during intestinal inflammation [67].

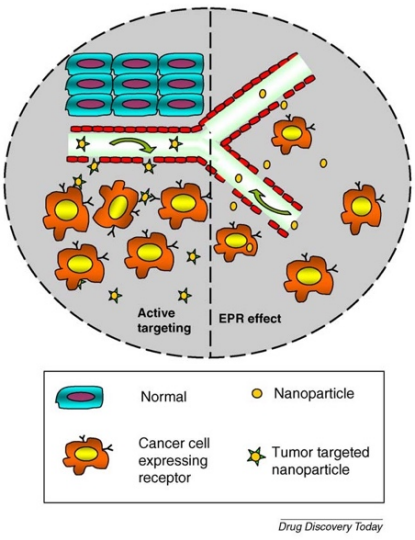

Figure 2.2. Tumor targeting. The right-hand part of the figure depicts the increased accumulation of nanoparticles in tumor owing to leaky tumor vasculature, leading to the enhanced permeability and

retention effect. The left-hand part of the figure shows active targeting mediated by targeted nanoparticles. Reproduced with permission from [2].

Another distinction between normal and tumor tissue is the pH. As it is known, cancer cells have very rapid growth and hence a high metabolic rate. Even though there are low levels of oxygen and nutrients for tumor cells to continue proliferating, these can use glycolysis to obtain extra energy, which results in an acidic environment [56]. Thus, the extracellular environment of solid tumors presents a pH around ~6.5, while healthy tissues present a pH of ~7.4 [68-70]. Also, colon has the most extensive and distinct microbial population, which is responsible for the weakly acidic pH and, together with the numerous enzymes, are responsible for drug breakdown in the colon [51].

Finally, temperature differences between pathologic and healthy tissue are present in various diseases. In particular, inflammation and cancer tissues are characterized for having temperature values above the physiological temperature, typically between 39-41 °C [71, 72]. Since cancer cells cannot dissipate heat as efficiently as normal cells, the tumor is heated and the temperature continues to increase due to the lack of vasodilatation. This may, in turn, lead to apoptosis or disruption of cell metabolism, which can make the tumor more susceptible to another type of treatment such as chemotherapy or radiation [73, 74]. On the other hand, nanomedicines may be engineered to take advantage of this characteristic as a therapeutic strategy in the treatment of inflammation and cancer. Such systems should be sensitive to small temperature changes in order to distinguish healthy from diseased areas. However, in most of the cases this does not happen. Thus, hyperthermia or thermotherapy, is used as a complementary strategy after the administration of thermo-responsive systems administration in order to improve the effect of anti-cancer drugs [47, 48, 75, 76].

Table 2.1. Main biological differences between normal and inflamed and tumor tissues.

Biological features	Normal tissues	Inflammatory and tumor tissues	References
Blood vessels	Tight fenestrations between endothelial cells around 1-10 nm	Vessel tortuosity, pericytes deficiency, large gaps between endothelial cells around 100-800 nm	[53-55]
Lymphatic system	Regular lymphatic network	Lack of lymphatic drainage	[57, 58, 77]

Colon	Continuous enterocyte layer; intact mucus layer	Enterocyte disruption (eEPR effect); differences in mucus thickness layer and constitution	[52, 60, 78]
pH	~7.4	~ 6.5 in tumor extracellular sites and inflammatory tissues	[68-70]
Temperature	~37 ºC	~40-42 ºC	[71, 72]
Enzymes and other proteins	Expressed at normal values	Overexpression of enzymes such as matrix metalloproteinases; overexpression of P-gp and cytochrome P405 3A	[68, 79]

2.2.3. Oral administration

Oral chemotherapy is a cost-effective treatment preferable for patients and doctors. Differently from intravenous administration, that exposes a high dose of a cytotoxic agent to the systemic circulation but still at a low concentration for cancer treatment, oral chemotherapy can prolong the time that a drug is in contact with the cancer cells at a relatively low dose and, in a safer concentration for normal cells. However, the oral route has some limitations due to the biological and/or physicochemical interactions of the drug with the GIT, which includes pH variations, presence of various enzymes as well as the bacterial flora in the intestine. Next, we will discuss in more detail why it is not that easy to develop new orally administrable drugs.

2.2.3.1. Limitations to the oral administration of drugs

The pH differences along the GIT, especially in the stomach, together with the enzymatic production can lead to modifications on drug solubility and stability due to oxidation and hydrolysis processes [80], making it critical to protect drugs from this harsh environment of the GIT by carrying them in nanosystems, such as polymeric micelles.

When a drug is administered orally, it is subjected to mechanisms called efflux of drugs. One of the most common efflux pumps present in the intestinal tract is the P-gp, which is highly expressed in the apical side of the intestinal epithelial cells, particularly, in the jejunum [81]. It is an ATP-dependent membrane transporter protein, that has been identified as the main responsible for the development of multidrug resistance. Thus, drugs that are substrates for this protein are pumped out to the lumen of the intestine and do not reach the epithelial cells, reducing the bioavailability of many molecules. Additionally, the GIT is

covered by a mucus layer, from the gastric mucosa to the colon, that is thicker at the ileum and colon regions. At the colon, the mucus layer can reach up to 800 μm, which can be a physical barrier for the intestinal absorption of molecules [82]. Nowadays, this limitation can be overcome by the use of nanoformulations, which protect the drug until it reaches the intestine and, have the surface modified to enhance its mucodiffusion for a better drug absorption. Also, the use of mucoadhesive polymers, as chitosan, or the use of mucopenetrating polymers, as PEG, can improve the bioadhesion and penetration thus, enhancing the drug intake to the systemic circulation [83].

If the main aim is to cross the epithelial barrier and reach the systemic circulation, drugs can undergo first-pass intestinal metabolism [84]. It is a drug metabolism, that occurs before the drug reaches the blood circulation, through the enzymes present in the brush border or inside the enterocytes, the main cellular population of the intestine, which also leads to a decrease on the intestinal absorption.

After passing the first-pass intestinal metabolism and reaching the blood capillaries, drugs are subjected to the first-pass hepatic metabolism. This consists in the metabolization of the drug by the liver, where every drug that is absorbed is transported through the portal circulation [84]. In the liver, due to the metabolization by several hepatic enzymes, the amount of drug available to proceed to the systemic circulation is decreased, since the main function of the liver is to clean the body from endogenous compounds. This is the main reason why many drugs have little oral bioavailability [85]. These processes, both intestinal and hepatic metabolisms, involve the presence of the cytochrome P450 3A4 (CYP3A4), a member of cytochrome P450 (CYP450), a super family of enzymes [81].

2.2.3.2. Drug delivery at the colon

Direct administration at the rectum or the oral route may be used to target drugs to the colon. The rectal administration offers several disadvantages as restricted distribution, high variation of distribution also leads to an ineffective treatment and, thus, it is not a recommended approach for delivering targeted drugs in the treatment and prevention of CRC. The oral route, in turn, is preferred if the drug transport across the GIT can be managed to reach the colon, using nanodelivery systems for instance. High concentrations of a drug can be achieved locally in the colorectal region by using a delivery system directed to the colon. At the same time, it is possible to achieve a prolonged drug release, which can be beneficial to reduce the drug frequency of administration. Mucoadhesive and diffusive systems, as those based on chitosan, are a potential approach for local CRC therapy [86-88]. As a result, a significantly lower dosage is employed, decreasing the undesired side effects.

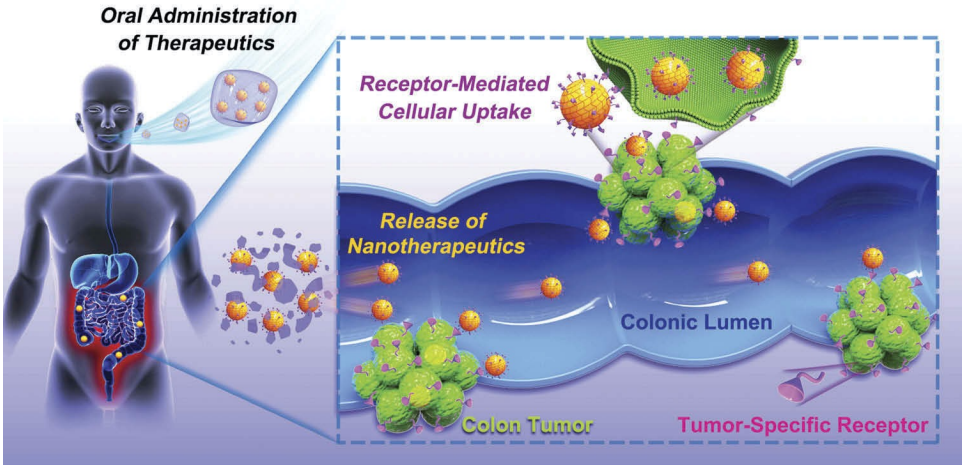

Figure 2.3. Schematic illustration of the passage of orally delivered targeted nanotherapeutics for CRC treatment. After oral administration, drug formulations pass through the mouth, esophagus, stomach, small intestine, and colon, successively. Subsequently, the matrix of delivery system surrounding targeted nanotherapeutics collapses in colon. These nanotherapeutics are released in colonic lumen and enable the loaded drugs to be specifically internalized by colon cancer cells. Reprinted with permission from [89].

The addition of targeting ligands to the nanosystems surface through the use of peptides, antibodies, antibody fragments or aptamers will increase the binding affinities to cancer cells, giving them successful tumor-targeting properties. In the particular case of CRC, CD98 glycoprotein [90, 91], folate receptor [92] or CD44 glycoprotein [93] are the most common receptors used for CRC-targeted drug delivery.

2.2.3.3. Intestinal absorption mechanisms

Other approach for CRC is the passive targeting and, thus, drugs must be absorbed and transported through the intestinal wall to reach the blood circulation. It can occur by several mechanisms depending on the molecule/system used (Figure 2.4).

The paracellular transport involves the diffusion of molecules through the spaces between the cells by the opening of the tight junctions (TJs) until they reach the blood stream (Figure 2.4C). Usually, this type of transport involves smaller molecules and, it is known that chitosan has the ability to temporarily open the TJs of the epithelium [94, 95].

Transcellular transport is a process where substances can cross the epithelial cell from the apical side of the membrane to the basolateral side, and it includes passive or active transport as well as endocytosis [96]. The passive diffusion is the simple diffusion of substances through the cell, a process that is more frequent for lipophilic molecules (Figure 2.4A). On the other hand, the active transport is energy-dependent because it uses ATP to selectively transfer substances across the cellular membrane (Figure 2.4B). Endocytosis is

defined as the transport of substances from the cellular membrane to the cytoplasm and is the most frequent mechanism of transport of nanosystems. There are three types of endocytosis: 1) receptor-mediated endocytosis, which involves the combination of a ligand with a receptor at the apical side of the cell, which crosses the cell to the basolateral side and delivers the molecule to the blood capillaries (Figure 2.4D). It is based on a targeted delivery, and in the case of nanosystems, they are decorated with a ligand for a specific type of cells that has the receptor for this specific ligand; 2) phagocytosis via M-cells, where macromolecules and nanosystems are thought to be transported, although this cells are very rare present in the intestine (Figure 2.4E); 3) the pinocytosis, which involves the invagination of the cellular membrane forming a vesicle, which will transport the molecules until the basolateral side of the cell and, consequently, reach the blood circulation (Figure 2.4F). This latter type can even be divided in four main mechanisms: macropinocytosis, clathrin-mediated endocytosis, caveolae-mediated endocytosis, clathrin-independent endocytosis and caveolae-independent endocytosis [97].

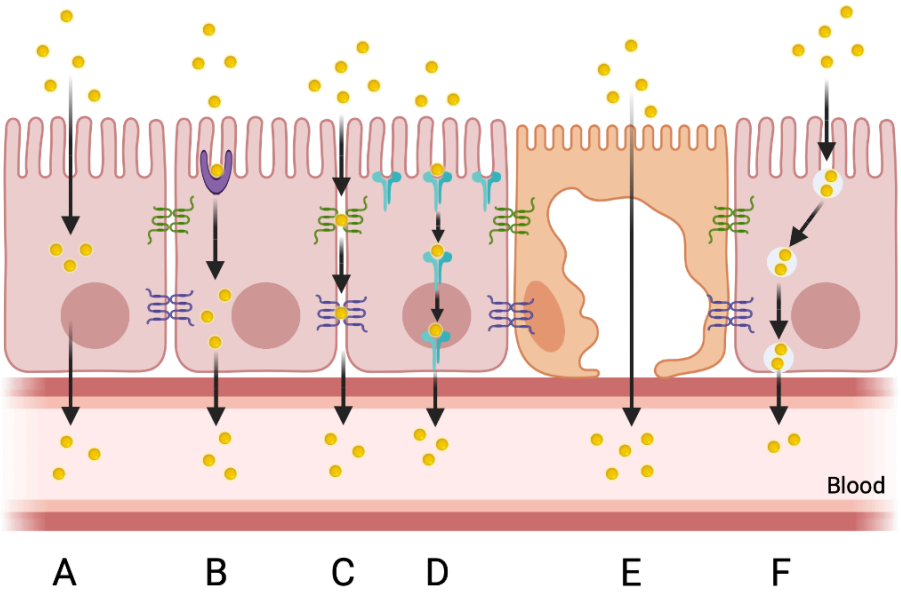

Figure 2.4. Different mechanisms involved in the small intestine absorption. (A) passive diffusion; (B) active transport; (C) paracellular transport; (D) receptor-mediated endocytosis; (E) endocytosis via M cells; (F) pinocytosis.

When developing new oral delivery dosage forms, the use of nanotechnology as polymeric micelles can be advantageous. Chitosan is a biocompatible and biodegradable polymer with a chemical structure that facilitates the formation of derivatives. Because of their amphiphilic nature, these chitosan derivatives have been widely used to form polymeric

micelles for oral administration. Later on, the main chemical modifications of chitosan to produce amphiphilic polymers and, as a result, polymeric micelles will be explained.

2.3. Polymeric micelles

Amphiphilic compounds bear both hydrophilic and hydrophobic units, that could be of lipidic (amphiphilic phospholipids or fatty acids) or polymeric (amphiphilic polymers) nature. Changing characteristics like unit composition, chain length and conformation it is possible to modulate polymer properties and consequently, their suitability for a given pharmaceutical application [98, 99]. Amphiphilic compounds have been widely used as excipients such as emulsifiers, wetting, thickening and stabilizing agents of suspensions, colloidal dispersions and gel forming agents. In the last decades, however, they had risen an increased interest as new drug delivery systems (DDS) sustained by the progresses seen in pharmaceutical sciences and nanomedicine [99, 100]. Phospholipids are successfully used in the clinical practice as main components of liposomes, emulsions, and some lipidic/surfactant micelles [101]. On the other hand, amphiphilic polymers, precursors of polymeric micelles, have been highlighted with some products already on the market, due to their ability to form nanoscopic structures of different morphologies and, higher stability upon administration and in shelf-life, compared to phospholipids (Figure 2.5) [100, 102, 103].

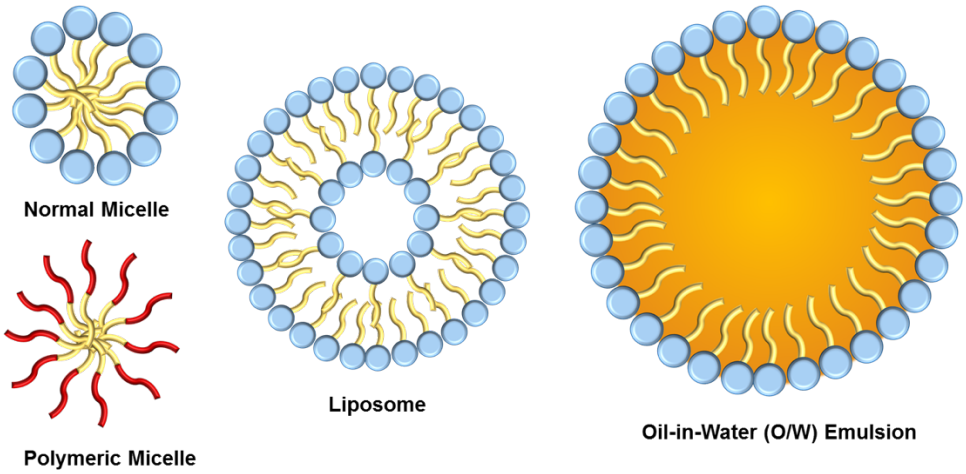

Figure 2.5. Examples of nanosized-systems obtained using amphiphilic compounds.

Micelles are spherical nanosized colloidal dispersions having a hydrophobic core coated by a hydrophilic shell arising from the self-assembly of amphiphilic molecules above the critical micelle concentration (CMC) and critical micellization temperature (CMT) (Figure 2.6) [104, 105]. This process is driven by an increase in entropy of the solvent molecules in contact to

the hydrophobic units of the phospholipid/polymer and a consequent decrease of free energy ($\Delta°G_m$) of the system as the hydrophobic components are withdrawn from the aqueous media originating the micelle core [106]. $\Delta°G_m$ is given by the Equation 2.1 where, R is the gas constant and T is the temperature of the system.

$$\Delta°G_m = RT \ln CMC \quad (2.1)$$

Different parameters have influence on the self-assembly, namely chemical composition, molecular weight, and architecture (linear versus branched, double bounds, etc.), concentration, temperature, solvent-polymer interactions, or salt concentration. By increasing the temperature of the system, the solvation of hydrophilic unit as well as the CMC value will decrease, promoting micelle formation. In the same way, this phenomenon is favored when the attractive hydrophobic interactions increase as result of a gain in molecular weight of the hydrophobic domain [107-109].

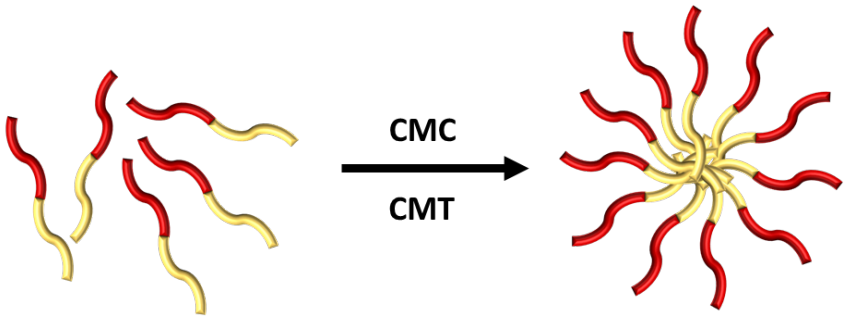

Figure 2.6. Schematic representation of a micelle and its formation through self-assembling of polymer monomers above CMC and CMT.

Micelles have been developed to modify several major intrinsic characteristics of drugs, including drug aqueous solubility, release pattern, pharmacokinetics, biodistribution, and *in vivo* stability [104, 110]. They allow the formulation and administration of highly hydrophobic drugs, which are otherwise often withdraw from drug development at early stages [111], as well as the elimination of excipients such as Cremophor EL® which causes severe side effects [112]. Despite being mainly proposed to formulate hydrophobic drugs, micelles, especially polymeric micelles, permit the encapsulation of drugs with different polarities. Hydrophobic drugs are incorporated into the micelle core being the solubilization capacity of drugs proportional to its hydrophobicity. Further, water-soluble drugs are preferentially located on the micelle shell and/or its surface. Drugs with intermediate polarity are distributed along the amphiphilic molecules [113, 114].

Polymeric micelles have higher core hydrophobicity and viscosity than surfactant micelles, conferring them higher thermodynamic and kinetic stability, thus presenting slower and

delayed disintegration and drug release in circulation, even upon dilution below CMC value [99]. Due to their small size, generally lower than 200 nm, and hydrophilic surface, micelles are poorly recognized by the reticuloendothelial system (RES), present long-term blood circulation and EPR effect in neovascularized tumors [115-117]. Additionally, polymeric micelles present high association efficiency, which together with the possibility of being sterilized by filtration, make these systems an interesting alternative for drug delivery of anticancer agents [104, 113, 118].

2.3.1. Polymeric micelles constitution

Among the different amphiphilic polymers available, the most extensively investigated to produce DDS are composed by PEG or poly(*N*-vinylpyrrolidone) (PVP) as hydrophilic block and a variety of hydrophobic blocks, namely: (i) polypropylene oxide (PPO); (ii) poly(ester)s like poly(*D,L*-lactide-*co*-glycolic acid) (PLGA), poly(*D,L*-lactide acid) (PLA), or poly(*ε*-caprolactone) (PCL); (iii) poly(amino acid)s such as poly(*L*-lysine) poly(*L*-aspartic acid) or poly(*L*-glutamic acid); and (iv) lipids [104, 105, 119]. Also, chitosan is a natural polymer with very interesting properties, as the ease of modification, and thus, it is widely used to be modified with hydrophilic and hydrophobic moieties to obtain an amphiphilic copolymer with ability to form polymeric micelles.

The main characteristics of the majority of amphiphilic compounds that make them suitable for clinical application are water-solubility, biodegradability, biocompatibility, low immunogenicity, surface hydrophilicity, stimuli-responsiveness, among others [99, 100]. Apart from the encapsulation and protection of drugs, the hydrophobic core of micelles provides appropriate mechanical properties for the desired application whereas the hydrophilic shell conceals the particle from the biological environment enhancing its stability [120, 121]. The presence of a hydrophilic layer on the surface of particles provides them with stealth properties by reducing or delaying opsonization via steric repulsion forces and macrophage recognition. The latter aspect increases the plasma circulation time of particles and the half-life of drugs [122, 123]. PEG and poloxamers are commonly used as hydrophilic polymers to decorate the surface of many nanoDDS creating the so-called stealth systems [124]. Moreover, the resultant functionalization potential by either chemical modification or bioconjugation could be used to bind specific targeting moieties to particles surface, allowing a better control of their biodistribution and increasing the therapeutic index of drugs [125]. A variety of ligands such as peptides, antibodies, folate, transferrin, or polysaccharides, can be used, accordingly to the required application.

2.3.2. Micelle-based anticancer drug delivery systems

The use of nanomedicines in the treatment of solid tumors, particularly, micelles to delivery anticancer drugs, has been widely investigated in recent years. The main advantages of these carriers over conventional therapies are the possibility to (i) deliver poorly water-soluble drugs; (ii) to use ligands in their surface with high affinity and specificity for target cells; (iii) to induce an efficient cellular endosomal escape and transport of the drugs to specific organelles; and, (iv) to circumvent drug resistance mechanisms [2, 126]. Overall, these systems may provide similar or better therapeutic profiles at lower drug concentrations when compared with classical drug formulations, while reducing side-effects at the same time.

As referred above, micelles are self-assembled structures of amphiphilic molecules with the ability to incorporate both hydrophobic and hydrophilic drugs that can be administered by several routes, such as oral, intravenous or rectal. The inner core is where hydrophobic drugs are encapsulated, improving the stability of the system, providing drug protection from degradation, and defining drug release kinetics. The outer shell on the other hand, is responsible for the *in vivo* pharmacokinetic behavior of the system and can be specifically functionalized with targeting moieties (peptides, ligands of receptors or antibodies) that are recognized by overexpressed molecules (receptors/antigens) of target cells. Such moieties allow specific binding to tumor cells achieving active targeting. However, for a successful delivery, molecules targeted at the tumor cells surface must be homogeneously overexpressed [2]. Some systems' specific composition or surface functionalization also aids the carried drug in crossing biological and mucosal barriers (Figure 2.7) [2, 127].

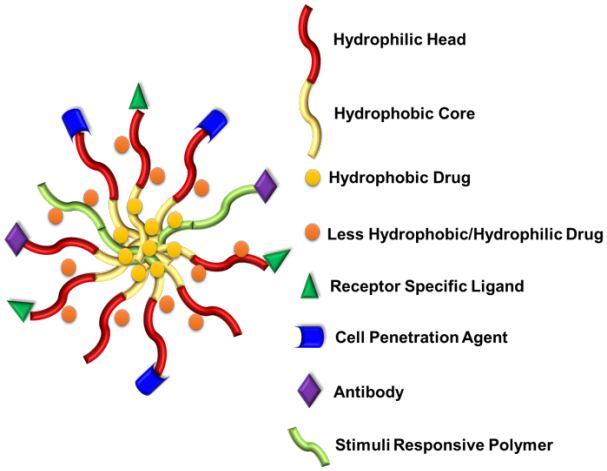

Figure 2.7. Schematic representation of a multifunctional micelle for drug delivery.

Most anticancer drugs show poor water solubility and short blood circulation time. Certainly, the use of micellar carriers can contribute to overcome these drawbacks. PEG is the most

used polymer to produce polymeric micelles due to their hydrophilic character, which can improve water solubility, and reduce protein adsorption and RES recognition, which increases the blood circulation time of the system [128].

Lv S. *et al.* [129], designed micelles based on methoxy poly(ethylene glycol)-*b*-poly(L-glutamic acid)-*b*-poly(L-lysine) decorated with deoxycholate (mPEG-*b*-PLG-*b*-PLL/DOCA) for the co-delivery of DOX and PTX, which are the most common chemotherapeutic drugs and present different mechanisms of action as well as different water solubility. The micellar system with both anticancer drugs was produced by self-assembly in aqueous solution, where DOX and PTX were encapsulated through electrostatic and hydrophobic interactions, respectively [130]. *In vivo* antitumor efficacy was tested on A549 human lung tumor-bearing nude mice. The results showed that the combination of both drugs (free or encapsulated) was more effective in tumor growth suppression than the single drugs [129]. However, the stronger tumor growth suppression was seen when DOX and PTX were encapsulated in mPEG-*b*-PLG-*b*-PLL/DOCA micelles. In addition, co-delivery of DOX and PTX demonstrated reduced systemic toxicity and higher tumor accumulation, which may indicate that the use of micelles for the co-delivery of anticancer drugs are less toxic and more effective against cancer cells [129].

Polymeric micelles-based on polysaccharides have also attracted attention due to their low toxicity and biodegradable nature. It is known that i.v. administration of PTX presents serious drawbacks such as low drug stability and high toxicity caused by non-specific delivery. Also, oral administration is the choice preferred by most patients. Thus, oral delivery has been investigated to replace the i.v. administration of drugs, however, the most used anticancer drugs present low oral bioavailability [131]. Mo R., *et al.* synthesized *N*-octyl-*O*-sulfate chitosan (NOSC) micelles to improve the oral absorption of PTX [132]. It was demonstrated significant enhancement of PTX oral bioavailability compared to Taxol® based on pharmacokinetic studies performed *in vivo* [132]. Also, uptake studies in Caco-2 cells revealed a significantly higher uptake of NOSC micelles compared to Taxol®, being almost 10-fold higher than Taxol®. Moreover, the potential permeability of PTX across the intestinal barrier indicated an improvement on PTX transport by NOSC micelles compared to commercially available product, in Caco-2 monolayers [128].

Due to their promising therapeutic potentiality demonstrated both *in vitro* and *in vivo*, some polymeric micelles-based formulations have advanced from pre-clinical assessment to enrolled clinical trials (Table 2.2). In this context, NK911 (Nippon Kayaku, Co.) was the first micellar system to proceed into clinical evaluation in 2001 [133]. Preclinical data showed longer blood circulation of the micelles with a 29-fold higher AUC in plasma than free DOX, and 3.4-fold higher accumulation in tumors compared to free DOX in mice models of sarcoma, lung, breast, and colon cancer [134]. Based on the results obtained in Phase I,

NK911 micelles had proceed into Phase II clinical trials against metastatic pancreatic cancer.

Furthermore, Genexol-PM® (Samyang Co.), firstly approved in 2007 in Korea is now being evaluated/marketed by the European Union and America under the name of Cynviloq® for the treatment of breast, ovary and non-small cell lung cancers [135-137]. Genexol®-PM is a polymeric micellar system loaded with PTX based on monomethoxy poly(ethylene glycol)-block-poly(*D,L*-lactide) (mPEG-PDLLA). This system presents advantages compared to Taxol® such as higher drug accumulation in the tumor, low toxicity levels, and effective P-gp inhibition effect [138]. Also, a Pluronic-based micellar system to delivery DOX, SP1049C (Surpatek Pharma, Inc.) has been granted orphan drug designation by FDA for the treatment of gastric cancer. Even though this system presents similar biodistribution compared to DOX, SP1049C showed to be more efficient in tumor suppression [139].

NK105 is a PTX-loaded polymeric micellar system based on poly(ethylene glycol)-poly(aspartic acid) (PEG-P(Asp)) modified with 4-phenyl-1-butanol in order to increase its hydrophobicity [140]. Preclinical results of NK105 showed a plasma AUC of micellar-PTX 50-fold higher than free PTX. Further, tumoral AUC of NK105 in subcutaneous human adenocarcinoma tumor models (HT-29) was 25-fold higher than free PTX [140]. Currently, NK105 has advanced to Phase III clinical trials in order to compare NK105 with free PTX in patients with metastatic as well as recurrent breast cancer, and to determine the survival and therapeutic benefits of NK105.

In the future, micelle-based medicines may change the way that anticancer drugs are used in cancer therapy. By considering fundamental parameters such as the choice of the polymer, drug encapsulation or micelle coating decoration, it is possible to optimize the solubility, biocompatibility, release profile and pharmacokinetic behavior of each system. In this way, polymeric micelles may provide efficient solutions for the treatment of different cancers.

Table 2.2. Examples of self-assembled particles under clinical trials evaluation for cancer treatment.

Formulation	Copolymer	Drug	Indication	Clinical phase	Reference
SP1049C	Pluronic® L61 and F127	DOX	Advanced adenocarcinoma of the esophagus, gastroesophage	III	[141]

			al junction and stomach		
Genexol-PM®/ Cynviloq®	PEG-PLA	PTX	Breast cancer, non-small cell lung cancer, advanced pancreatic cancer and ovarian cancer	II/III/IV	[142-146]
NK012	PEG-poly(L-glutamic acid)-SN-38 conjugated	SN-38	Advanced breast cancer and small cell lung cancer	II	[147, 148]
NK105	PEG-poly(L-aspartic acid)	PTX	Advanced or recurrent breast cancer	III	[149]
NK-911	PEG–poly(aspartic acid)-doxorubicin conjugated	DOX	Solid tumors	I	[150]
NC-4016	PEG-DACH-platin	Oxaliplatin	Advanced solid tumors or lymphoma	I	[151]
NC-6300	PEG-b-poly(aspartate-hydrazone)	Epirubicin	Advanced solid tumors or soft tissue sarcoma	I/II	[152]
NC-6004 (Nanoplatin®)	PEG-poly(L-glutamic acid)-cisplatin conjugated	Cisplatin	Solid tumors, non-small cell lung, biliary and bladder cancer, pancreatic cancer	II/III	[153, 154]
IT-101	Polymer-cyclodextrin-	CPT	Advanced solid tumors, ovarian cancer	I/II	[155, 156]

	camptothecin conjugated				
BIND-014	PEG-PLA	Docetaxel	Non-small cell lung cancer, prostate cancer, advanced solid tumors	I/II	[157-160]

DACH-platin: diaminocyclohexane platinum; DOX: doxorubicin; PEG: polyethylene glycol; PLA: poly(*D,L*-lactide); PTX: paclitaxel

2.4. Chitosan

Chitosan, a linear polysaccharide which occurs in the cell wall of some fungi, is generally prepared from chitin, one of the most abundant natural polymers in the world [161]. Chitin is composed mainly by 2-acetamido-2-deoxy-D-glucopyranose (GlcNAc) units linked by β-(1,4) glycosidic bonds while chitosan is a copolymer in which 2-amino-2-deoxy-*D*-glucopyranose (GlcN) units predominate (Figure 2.4). Thus, these polymers possess different contents of GlcNAc and GlcN units, such a structural difference resulting in distinct physicochemical properties. Chitosan exhibits excellent properties, such as non-toxicity [162-164], antimicrobial activity [165, 166], biocompatibility [167-169], biodegradability [170, 171], mucoadhesiveness and ability to open, temporarily, the TJs of the epithelium, thereby facilitating the permeation of drugs [171-174]. These properties may double the therapeutic effects making chitosan a polymer with pronounced potential for biomedical and biopharmaceutical applications, especially for drug delivery.

The structural distinction between chitin and chitosan is expressed by the content of GlcNAc units, which is quantitatively given by the average degree of acetylation (DA), higher in chitin (DA > 80 %) as compared to chitosan (DA < 60 %). Thus, the conversion of chitin into chitosan is referred to as an *N*-deacetylation reaction since acetamido groups of GlcNAc units are converted to amino groups, increasing the content of GlcN units in the polymeric chains. The *N*-deacetylation of chitin can be achieved by enzymatic hydrolysis, but it is most frequently carried out by treating the polymer with concentrated aqueous alkaline solutions [175]. As a consequence of their different composing units and, although sharing some polymeric structural similarity as both polymers, chitin and chitosan, possess primary (C3) and secondary (C6) hydroxyl groups, but only chitosan possesses primary amino groups (C2). Thus, due the presence of primary amino groups pertaining to GlcN units, chitosan offers additional possibilities for carrying out chemical modifications as compared to chitin and other polysaccharides.

Although chitosan presents interesting properties, its solubility is limited to moderately acidic aqueous media (pH 4 – 5), which restricts some applications. However, the control of the structural characteristics of chitosan, mainly its average DA and the distribution of GlcNAc and GlcN units, which is expressed by pattern of acetylation, but also of its average molecular weight and dispersity, can generate chitosans with excellent properties, including solubility in physiological media [176-178]. Moreover, chemical modifications are carried out to prepare derivatives of chitosan with improved properties, including solubility, aiming to expand its application possibilities. As result, various derivatives of chitosan have been proposed. The strategy of carrying out chemical modifications in chitosan aiming to change or improve given physicochemical properties and biological activities is advantageous as it is possible to modify selectively the chitosan functional groups without any effects on its main structural backbone. Moreover, a wide range of derivatives can be prepared with modified properties, which can be tailored according to the needs of specific applications. Indeed, the chitosan derivatives can exhibit improved or novel properties and functionalities depending on the locus of as well as on the nature of the chemical modification to be explored.

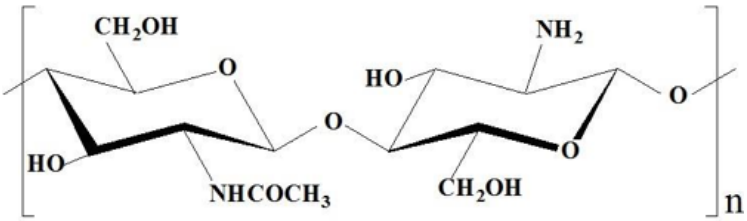

Figure 2.8. Chitosan structure, where n is the average degree of polymerization.

The presence of C2-amine, C3-hydroxyl and C6-hydroxyl make possible several chemical reactions as alkylation, acylation, hydroxyalkylation or carboxyalkylation. Here, we briefly describe the main properties of these modifications.

2.4.1. Alkylation

Alkylation can occur with both functional groups of chitosan (-NH_2 or -OH), however, the reactions using the amino groups are more frequent. This is one of the most frequent modifications of chitosan and is characterized by the grafting of alkyl chains in the chitosan backbone. Since alkylation occurs mainly in the amino groups by the reductive amination of chitosan, *N*-alkylated chitosan derivatives are generated [179]. As in other substitutions, the hydrophobic character of chitosan will depend on the length of the alkyl chain and the substitution degree (SD). As higher the alkyl chain and/or the SD, a more hydrophobic

chitosan derivative will be obtained. Several works have been developed based on this reaction and, typically, new chitosan derivatives are obtained to improve chitosan properties. Chen *et al*. [180], demonstrated better hemostatic activity in the *N*-alkylated chitosan as compared with unmodified chitosan. Better properties, make chitosan more attractive for biomedical applications.

2.4.2. Acylation

In this type of derivatives, both -NH_2 and -OH groups are used in the reaction. Thus, we can have *N*-acylation or *O*-acylation, depending on the site of the grafting. This modification is characterized by the incorporation of acyl groups, which is typically a carbodiimide reaction mediated by 1-ethyl-3-(3-dimethylaminopropyl) carbodiimide (EDC) and *N*-hydroxysuccinimide (NHS) [179]. From these derivatives, it is mostly obtained nanoparticles or micelles with ability to self-assembly. Also, the chitosan solubility in aqueous or organic solvents is improved, depending on the molecular weight, acyl chain length and SD. Piegat *et al*. [181], demonstrated that chitosan grafted with linoleic acid had better antibacterial activity, compared to unmodified chitosan. Several other studies used acylation to make chitosan an amphiphilic derivative to produce polymeric micelles [182-186].

2.4.3. Hydroxylation and carboxylation

Both reactions are also common when modifying chitosan mainly because they improve the solubility of chitosan in water. Hydroxyalkylated and carboxyalkylated chitosan respectively, obtained by the reaction of chitosan with epoxides or acidic groups. The reaction may occur in both reactive groups of chitosan and, besides improving its water solubility, other biological properties are improved, as the antibacterial and antioxidant activity [187, 188].

An ideal carrier should be biocompatible and biodegradable, present no cytotoxicity and form stable complexes able to cross the GIT and deliver the drug for an improved intestinal permeability. Chitosan is able to form those complexes through its chemical modification into an amphiphilic polymer and, consequently produce polymeric micelles. In the next section, it will be discussed in detail the main advantages of using chitosan-based polymeric micelles and its main properties.

2.4.4. Chitosan-based polymeric micelles as drug delivery systems

Chemical modifications of chitosan are the most efficient and well-known method to create self-assembled systems. These changes lead to the formation of amphiphilic chitosan

derivatives by addition of hydrophobic groups, such as alkyl and acyl groups, to the chitosan backbone. Owing to the introduction of hydrophobic substituents on the chitosan chain, the resulting amphiphilic chitosan derivative is capable of forming micelles or nanoparticles by self-assembly in an aqueous medium. These DDS are developed to prevent drug degradation, as well as their loss, to avoid the harmful side effects and to increase the bioavailability of the drug in the required site of interest.

Chitosan-based micelles have been frequently used for oral delivery of anticancer drugs due to its capability to protect the drug through the GIT, enhancing the solubility and absorption of poor water-soluble drugs. Sometimes, there is a need to coat these systems by gastro-resistant polymers in order to protect them from the harsh environment of the stomach. [189, 190]. At the same time, polymeric micelles based on chitosan have been described as mucoadhesive nanocarriers due to the presence of amine groups on the chitosan backbone, which interact with sialic acid moieties of the mucin, improving the drug oral bioavailability [191, 192].

Chemotherapy is, in most of the cases, crucial for cancer treatment. There are several drugs effective against cancer, however, they have low solubility and low intestinal permeability, which turns the treatment ineffective. Moreover, these drugs are cytotoxic for normal cells, despite being efficient in stopping the cell division process. Thus, the scientific community started to think about adjuvants or other forms of delivery that could overcome these drawbacks. Actually, the improvements of oral dosage forms are still the major concerns of oral chemotherapy [193].

According to the biopharmaceutical classification system (BCS), most of the hydrophobic anticancer drugs are classified as BCS IV, which means low solubility and low permeability. Thus, if administered orally, these drugs will present low bioavailability. In that regard, polymeric micelles appeared as a promising strategy to efficiently delivery anticancer drugs, particularly, hydrophobic drugs. In this section, will be presented several hydrophobic anticancer drugs encapsulated or associated to polymeric micelles based on chitosan for oral cancer treatment.

2.4.4.1. Paclitaxel delivery

PTX is a well-known anticancer drug commonly used in chitosan-derived systems. Its mechanism of action influences the cell cycle through the hyperstabilization of the microtubules, which ceases the mitosis until cell death [194]. PTX is approved by U.S. Food and Drug Administration (FDA) for the treatment of several types of cancer such as breast, ovarian and lung cancer, and it is classified by the BCS as class IV drug, i.e., poorly soluble and poorly permeable. Thus, PTX is commercially formulated as Taxol® for intravenous

administration, however, its excipients lead to serious side effects as neurotoxicity, nephrotoxicity and hypersensitivity [195].

Other alternatives using nanomedicine are being applied to overcome these drawbacks. This is the case of Abraxane®, an FDA approved albumin nanoparticle-based system, Lipusu®, a liposome system approved by the State Food and Drug Administration of China, Paclical®, a micellar system in clinical phase III, or even Genexol-PM®, already in the market. However, all these nanosystems are being tested for intravenous administration, which is not the ideal route of administration due to the drug instability in the bloodstream and lack of specificity, the high probability of infections or thrombosis, and also, the high cost of these formulations for the patients [196]. Thus, there is an urgent need in developing new oral DDS with high efficacy and low toxicity and cost for the patients.

Almeida *et al*., developed a new chitosan-based system through the introduction of PCL into the chitosan backbone [182]. It is still a preliminary work, but the authors found a 2-fold increase in the *in vitro* intestinal permeability of PTX compared with the free drug. In a similar work, chitosan was modified with myristoyl chloride as hydrophobic segment to produce micelles. PTX was efficiently encapsulated into the system and showed no cytotoxicity against colorectal cancer cells, just as the PTX permeability that was doubly increased compared to the free drug [183].

In other study, Xu *et al*., used Pluronic F127-chitosan copolymer modified with cysteine and sodium cholate to prepare polyion complex micelles. The *in vivo* pharmacokinetic study in rats revealed an increase of the oral bioavailability of PTX from around 9% to 42%, when the drug is freely administered or encapsulated in the micelles, respectively. Moreover, it was observed an AUC 5-fold higher and a maximal plasma concentration (C_{max}) 3-fold higher when the drug was administered encapsulated into the micelles compared to the free drug [195]. The authors attributed these results to the cysteine modified micelles, which can improve the mucoadhesiveness and so, increase the contact of the micelles with the intestinal mucosa and, consequently, provide a higher drug concentration. Recently, chitosan was modified into a multifunctional amphiphilic polymer using polylysine and cysteine. The *in vitro* antitumor efficacy studies performed in Caco-2 cells showed higher cytotoxicity after 48 h of incubation for the micelles, compared with Taxol®, and higher cellular uptake compared with non-conjugated micelles. Furthermore, the *in vivo* data revealed a 6-fold higher AUC and oral absorption of PTX by the micelles, 9-fold increase of PTX in the tumor, and 2-fold tumor reduction, when comparing with the free drug [197].

In another study, trimethyl chitosan (TMC) was conjugated with PTX (TMC-PTX) and with FA (FA-TMC-PTX) containing around 11% of PTX were tested for its oral and intravenous administration. An increase in the oral absorption of PTX was firstly observed *in vitro*, where both systems presented a 2-fold increase on the intestinal mucoadhesion, and a 16 and 19-

fold increase of PTX intestinal permeability for TMC-PTX and FA-TMC-PTX micelles, respectively, compared to PTX solution [198]. The *in vivo* studies demonstrated that both micellar systems had an impact in the tumor suppression, where FA-TMC-PTX was the most efficient in both routes of administration (Figure 2.9). The animals body weight was maintained during the study, and survival experiment showed a significantly increase in the life span for the animals treated with both micellar systems, compared with saline or PTX. Thus, both systems showed promising results for cancer treatment by oral or intravenous administration.

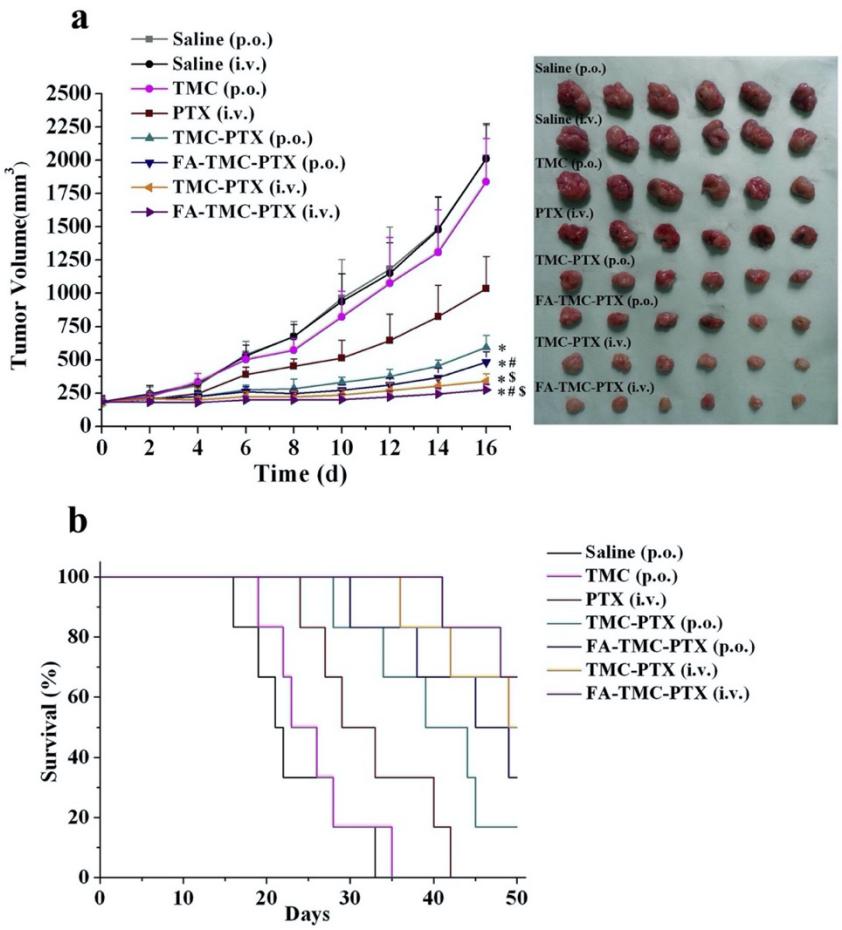

Figure 2.9. Antitumor efficacy of PTX, TMC-PTX and FA-TMC-PTX on H22 tumor-bearing mice. Five administrations were conducted every alternate day. (a) Tumor growth curves following i.v. or p.o. administration of saline and distinct PTX formulations. Indicated values were mean ± SD (n = 6). $^{*}P < 0.05$ versus PTX (i.v.); $^{\#}P < 0.05$ versus TMC-PTX via the same administration route; $ P < 0.05 versus p.o. administration. (b) Survival curves of H22 tumor-bearing mice receiving i.v. or p.o. administration of saline and distinct PTX formulations (n = 6). Reprinted with permission from [198].

Later, Wang *et al.*, used the same tumor model to assess the efficacy of the carboxymethyl chitosan derivative micelles (200 nm), highly encapsulated with PTX with a drug loading of 35%. These micelles were able to increase the AUC and the C_{max} of 16 and 26-fold,

respectively, compared with Taxol®, and also, the animals treated with micelles, showed an antitumor inhibition effect around 46%, 2-fold higher compared with the free drug [199].

Table 2.3. Summary of the chitosan derivatives used to encapsulate and deliver paclitaxel.

System	Average size (nm)	CMC	Loading efficiency	Evaluation	Reference
Chitosan-*g*-polycaprolactone	~ 400	9.55 × 10^{-4} mg/mL	82 %	*In vitro*	[182]
3,6-*o*,*o*'-dimyristoyl chitosan	~ 480	8.90 × 10^{-3} mg/mL	100 %	*In vitro*	[183]
F127-chitosan modified with cysteine and bile salt	~ 60	2.50 × 10^{-3} mol/L	85 %	*In vitro* and *in vivo*	[195]
Polylysine and cysteine functionalized chitosan	~ 165	-	91 %	*In vitro* and *in vivo*	[197]
Trimethyl chitosan and folic acid	~ 175	0.08 mg/mL	(drug loading of 11%)	*In vitro* and *in vivo*	[198]
Carboxymethyl chitosan-rhein	~ 217	31.25 µg/mL	87 %	*In vitro* and *in vivo*	[199]

2.4.4.2. Other hydrophobic anticancer drugs

DOX has been used against several types of cancer as chemotherapy. However, DOX can be easily pumped out of the cells due to the P-gp efflux pump. Thus, being encapsulated into polymeric micelles, can avoid the efflux transport and improve its absorption by oral route.

Stearic acid-*g*-chitosan was used to encapsulate and improve the oral availability of DOX through the formation of polymeric micelles by self-assembly [186]. This system revealed good permeability as compared with free DOX, increasing the transport in the Caco-2 monoculture model from 20-40-fold, depending on the SD. More interesting, *in vivo* studies

performed in rats demonstrated a 3-fold improvement in the oral availability of DOX encapsulated into micelles compared with free DOX and an AUC 4-times superior. Also, these micelles had an elimination half-life of 11h, much more prolonged than the control, which may favor the cancer treatment [186]. In another study, Mu *et al*. [200], used quercetin-chitosan conjugates (QT-CS) to produce polymeric micelles and improve the oral bioavailability and solubility of DOX. Results showed a safe profile for the polymeric micelles against Caco-2 cells and, a 2-fold higher DOX uptake from the loaded micelles, as compared with free DOX. The P_{app} performed in Caco-2 monolayers was 10-fold higher for the DOX-loaded chitosan micelles than for free DOX, demonstrating the effect of chitosan opening the TJs of the epithelium and, thus, increasing the intestinal permeability.

Docetaxel (DTX) is an antimicrotubular agent approved for the treatment of several types of cancer. However, this drug is administered i.v. and no oral form is available until now. Kumar *et al.* [201], recently developed a new chitosan amphiphilic derivative through the grafting of oleic acid on carboxymethyl chitosan backbone for the delivery of DTX. Caco-2 model was used to investigate the P_{app}, which revealed to be up to 6-fold higher for the DTX-loaded micelles than for the free DTX. The authors believe this increase on the intestinal permeability was achieved by paracellular transport, mainly due to the use of chitosan to open the TJs of the epithelium. These micelles also demonstrated to be stable in gastrointestinal fluids, where their size and PdI was nearly maintained. Moreover, the *in vivo* pharmacokinetic study after oral administration revealed an almost 2-fold and 3-fold increase on the C_{max} and AUC, respectively, for the DTX polymeric micelles as compared with the free DTX, leading to an increase of DTX oral absorption.

CPT is an anticancer drug with strong activity against several types of tumors. Its mechanism of action is based on the inhibition of the nuclear enzyme topoisomerase I, ending cell division, leading to apoptosis [202]. Despite being very powerful on stopping cell division, its therapeutic efficacy is hampered by the low solubility and bioavailability and due to the high toxicity. Also, CPT is pH-dependent, which can suffer hydrolysis in aqueous media easily. Thus, when encapsulated into polymeric micelles, CPT can be protected from the biological fluids and reach the target site in higher doses for a better treatment.

Silva *et al*. [203], developed a new chitosan amphiphilic derivative based on 3,6-*O*,*O*'-dimyristoyl to encapsulate and efficiently deliver CPT. Empty micelles presented a safe profile against colorectal cancer cell lines and CPT-loaded micelles exhibited a low release rate, showing no cytotoxic effect against the same cell lines. However, when the CPT permeability was tested, polymeric micelles showed to improve 7-fold the CPT transport across Caco-2/HT29-MTX co-culture model, which can be explained by the ability of chitosan in opening the TJs of the epithelium [203]. Also, in a preliminary study, Almeida *et al*. modified chitosan with *O*-methyl-*O*'-succinyl polyethylene glycol and oleic acid to

produce polymeric micelles to encapsulate CPT aiming to improve its solubility and bioavailability as potential candidate for oral chemotherapy [185].

Table 2.4. Summary of the chitosan derivatives used to encapsulate and deliver camptothecin, doxorubicin and docetaxel.

Drug	System	Average size (nm)	CMC	Loading efficiency	Evaluation	Reference
DOX	Stearic acid-*g*-chitosan	33.4-130.9	0.16 to 0.25 mg/mL	67 – 76 %	*In vitro* and *in vivo*	[186]
	Quercetin-chitosan conjugated	~ 137	0.03 mg/mL	88 %	*In vitro*	[200]
DTX	Oleic acid-*g*-carboxymethyl chitosan	~213	1.00 µg/mL	57 %	*In vitro* and *in vivo*	[201]
CPT	3,6-*o*,*o*'-dimyristoyl chitosan	~ 290	-	70 %	*In vitro*	[203]
	O-methyl-o'-succinyl polyethylene glycol and oleic acid-*g*-chitosan	~ 146	0.08 mg/mL	78 %	*In vitro*	[185]

References

1. Reichert, J.M. and J.B. Wenger, *Development trends for new cancer therapeutics and vaccines.* Drug Discovery Today, 2008. **13**(1): p. 30-37.
2. Misra, R., S. Acharya, and S.K. Sahoo, *Cancer Nanotechnology: application of nanotechnology in cancer therapy.* Drug Discovery Today, 2010. **15**(19): p. 842-850.
3. Organization, W.H. *Media Centre: Cancer*. [cited 2021 March]; Available from: https://www.who.int/health-topics/cancer#tab=tab_1.
4. Society, A.C. *Cancer Facts & Figures 2020*. 2020 [cited 2021 March]; Available from: https://www.cancer.org/research/cancer-facts-statistics/all-cancer-facts-figures/cancer-facts-figures-2020.html.
5. Sung, H., et al., *Global Cancer Statistics 2020: GLOBOCAN Estimates of Incidence and Mortality Worldwide for 36 Cancers in 185 Countries.* CA: A Cancer Journal for Clinicians, 2021. **71**(3): p. 209-249.
6. Kuper, H., H.O. Adami, and D. Trichopoulos, *Infections as a major preventable cause of human cancer.* Journal of Internal Medicine, 2000. **248**(3): p. 171-183.
7. Lucas, C., N. Barnich, and H.T.T. Nguyen, *Microbiota, Inflammation and Colorectal Cancer.* International Journal of Molecular Sciences, 2017. **18**(6): p. 1310-1337.
8. Taylor, D.P., et al., *Population-based family history–specific risks for colorectal cancer: a constellation approach.* Gastroenterology, 2010. **138**(3): p. 877-885.
9. Hermann Brenner, M.K., Christian Peter Pox, *Colorectal Cancer.* Lancet, 2014. **383**(9927): p. 1490-1502.
10. Farraye, F.A., et al., *AGA medical position statement on the diagnosis and management of colorectal neoplasia in inflammatory bowel disease.* Gastroenterology, 2010. **138**(2): p. 738-745.
11. Jess, T., C. Rungoe, and L. Peyrin–Biroulet, *Risk of colorectal cancer in patients with ulcerative colitis: a meta-analysis of population-based cohort studies.* Clinical Gastroenterology and Hepatology, 2012. **10**(6): p. 639-645.
12. Colangelo, T., et al., *Friend or foe?: The tumour microenvironment dilemma in colorectal cancer.* Biochimica et Biophysica Acta (BBA)-Reviews on Cancer, 2017. **1867**(1): p. 1-18.
13. Cunningham, D., et al., *Colorectal cancer.* The Lancet, 2010. **375**(9719): p. 1030-1047.
14. Network, C.G.A., *Comprehensive molecular characterization of human colon and rectal cancer.* Nature, 2012. **487**(7407): p. 330.

15. Cisterna, B.A., et al., *Targeted nanoparticles for colorectal cancer.* Nanomedicine, 2016. **11**(18): p. 2443-2456.
16. Kapse-Mistry, S., et al., *Nanodrug delivery in reversing multidrug resistance in cancer cells.* Frontiers in Pharmacology, 2014. **5**(159): p1-22.
17. Fernandes, E., et al., *New trends in guided nanotherapies for digestive cancers: A systematic review.* Journal of Controlled Release, 2015. **209**: p. 288-307.
18. Miller, K.D., et al., *Cancer treatment and survivorship statistics, 2019.* CA: A Cancer Journal for Clinicians, 2019. **69**(5): p. 363-385.
19. Gustavsson, B., et al., *A review of the evolution of systemic chemotherapy in the management of colorectal cancer.* Clinical Colorectal Cancer, 2015. **14**(1): p. 1-10.
20. Xie, Y.-H., Y.-X. Chen, and J.-Y. Fang, *Comprehensive review of targeted therapy for colorectal cancer.* Signal Transduction and Targeted Therapy, 2020. **5**(1): p. 1-30.
21. Overman, M.J., et al., *Durable clinical benefit with nivolumab plus ipilimumab in DNA mismatch repair-deficient/microsatellite instability-high metastatic colorectal cancer.* Journal of Clinical Oncology, 2018. **36**(8): p. 773-779.
22. Ganesh, K., et al., *Immunotherapy in colorectal cancer: rationale, challenges and potential.* Nature Reviews Gastroenterology & Hepatology, 2019. **16**(6): p. 361-375.
23. André, T., et al., *Pembrolizumab in microsatellite-instability–high advanced colorectal cancer.* New England Journal of Medicine, 2020. **383**(23): p. 2207-2218.
24. Emami, F., et al., *Doxorubicin and anti-PD-L1 antibody conjugated gold nanoparticles for colorectal cancer photochemotherapy.* Molecular Pharmaceutics, 2019. **16**(3): p. 1184-1199.
25. Gu, X., et al., *cRGD-decorated biodegradable polytyrosine nanoparticles for robust encapsulation and targeted delivery of doxorubicin to colorectal cancer in vivo.* Journal of Controlled Release, 2019. **301**: p. 110-118.
26. Tsai, H.-L., et al., *Impact of BMI1 expression on the apoptotic effect of paclitaxel in colorectal cancer.* American Journal of Cancer Research, 2019. **9**(11): p. 2544-2553.
27. Dai Phung, C., et al., *PEGylated-Paclitaxel and Dihydroartemisinin Nanoparticles for Simultaneously Delivering Paclitaxel and Dihydroartemisinin to Colorectal Cancer.* Pharmaceutical Research, 2020. **37**(7): p. 1-11.
28. Du, H., et al., *Two novel camptothecin derivatives inhibit colorectal cancer proliferation via induction of cell cycle arrest and apoptosis in vitro and in vivo.* European Journal of Pharmaceutical Sciences, 2018. **123**: p. 546-559.

29. Shimada, Y., et al., *Phase II study of CPT-11, a new camptothecin derivative, in metastatic colorectal cancer. CPT-11 Gastrointestinal Cancer Study Group.* Journal of Clinical Oncology, 1993. **11**(5): p. 909-913.
30. Ramos, P. and M. Bentires-Alj, *Mechanism-based cancer therapy: resistance to therapy, therapy for resistance.* Oncogene, 2015. **34**(28): p. 3617-3626.
31. Wall, M.E., *Camptothecin and taxol: discovery to clinic.* Medicinal Research Reviews, 1998. **18**(5): p. 299-314.
32. Wang, J.C., *Cellular roles of DNA topoisomerases: a molecular perspective.* Nature Reviews Molecular Cell Biology, 2002. **3**(6): p. 430-440.
33. Pommier, Y., *Topoisomerase I inhibitors: camptothecins and beyond.* Nature Reviews Cancer, 2006. **6**(10): p. 789-802.
34. Venditto, V.J. and E.E. Simanek, *Cancer therapies utilizing the camptothecins: a review of the in vivo literature.* Molecular Pharmaceutics, 2010. **7**(2): p. 307-349.
35. Botella, P. and E. Rivero-Buceta, *Safe approaches for camptothecin delivery: structural analogues and nanomedicines.* Journal of Controlled Release, 2017. **247**: p. 28-54.
36. Batist, G., et al., *Safety, pharmacokinetics, and efficacy of CPX-1 liposome injection in patients with advanced solid tumors.* Clinical Cancer Research, 2009. **15**(2): p. 692-700.
37. Pal, A., et al., *Preclinical safety, pharmacokinetics and antitumor efficacy profile of liposome-entrapped SN-38 formulation.* Anticancer Research, 2005. **25**(1A): p. 331-341.
38. Ghamande, S., et al., *A phase 1 open-label, sequential dose-escalation study investigating the safety, tolerability, and pharmacokinetics of intravenous TLC388 administered to patients with advanced solid tumors.* Investigational New Drugs, 2014. **32**(3): p. 445-451.
39. Shen, L., *Functional morphology of the gastrointestinal tract*, in *Molecular Mechanisms of Bacterial Infection via the Gut*. 2009, Springer. p. 1-35.
40. Jaladanki, R.N. and J.-Y. Wang. *Regulation of gastrointestinal mucosal growth*. in *Colloquium Series on Integrated Systems Physiology: From Molecule to Function*. 2011. Morgan & Claypool Life Sciences.
41. Pereira, C., et al., *Dissecting stromal-epithelial interactions in a 3D in vitro cellularized intestinal model for permeability studies.* Biomaterials, 2015. **56**: p. 36-45.
42. Montgomery, R.K., A.E. Mulberg, and R.J. Grand, *Development of the human gastrointestinal tract: twenty years of progress.* Gastroenterology, 1999. **116**(3): p. 702-731.

43. Gannon, B., *The vasculature and lymphatic drainage.* Gastrointestinal and oesophageal pathology. Edinburgh: Churchill Livingstone, 1995. p. 129-199.
44. Weiss, J., et al., *Interaction of angiotensin receptor type 1 blockers with ATP-binding cassette transporters.* Biopharmaceutics & Drug Disposition, 2010. **31**(2-3): p. 150-161.
45. Larhed, A.W., P. Artursson, and E. Björk, *The influence of intestinal mucus components on the diffusion of drugs.* Pharmaceutical Research, 1998. **15**(1): p. 66-71.
46. Wang, Y.Y., et al., *Addressing the PEG mucoadhesivity paradox to engineer nanoparticles that "slip" through the human mucus barrier.* Angewandte Chemie International Edition, 2008. **47**(50): p. 9726-9729.
47. Kono, K., et al., *Multi-functional liposomes having temperature-triggered release and magnetic resonance imaging for tumor-specific chemotherapy.* Biomaterials, 2011. **32**(5): p. 1387-1395.
48. Kono, K., et al., *Highly temperature-sensitive liposomes based on a thermosensitive block copolymer for tumor-specific chemotherapy.* Biomaterials, 2010. **31**(27): p. 7096-7105.
49. Abreu, M.T., *Toll-like receptor signalling in the intestinal epithelium: how bacterial recognition shapes intestinal function.* Nature Reviews Immunology, 2010. **10**(2): p. 131-144.
50. Daugherty, A.L. and R.J. Mrsny, *Transcellular uptake mechanisms of the intestinal epithelial barrier Part one.* Pharmaceutical Science & Technology Today, 1999. **2**(4): p. 144-151.
51. Xiao, B. and D. Merlin, *Oral colon-specific therapeutic approaches toward treatment of inflammatory bowel disease.* Expert Opinion on Drug Delivery, 2012. **9**(11): p. 1393-1407.
52. Filipe, M.I. and A. Branfoot, *Abnormal patterns of mucus secretion in apparently normal mucosa of large intestine with carcinoma.* Cancer, 1974. **34**(2): p. 282-290.
53. Jain, R.K., *Delivery of molecular and cellular medicine to solid tumors.* Advanced Drug Delivery Reviews, 2001. **46**(1): p. 149-168.
54. Allen, T.M. and P.R. Cullis, *Drug delivery systems: entering the mainstream.* Science, 2004. **303**(5665): p. 1818-1822.
55. Sapra, P. and T. Allen, *Ligand-targeted liposomal anticancer drugs.* Progress in Lipid Research, 2003. **42**(5): p. 439-462.
56. Thakor, A.S. and S.S. Gambhir, *Nanooncology: the future of cancer diagnosis and therapy.* CA: A Cancer Journal for Clinicians, 2013. **63**(6): p. 395-418.

57. Maeda, H. and Y. Matsumura, *Tumoritropic and lymphotropic principles of macromolecular drugs.* Critical Reviews in Therapeutic Drug Carrier Systems, 1988. **6**(3): p. 193-210.
58. Maeda, H., et al., *Tumor vascular permeability and the EPR effect in macromolecular therapeutics: a review.* Journal of Controlled Release, 2000. **65**(1): p. 271-284.
59. Ingersoll, S.A., et al., *The role and pathophysiological relevance of membrane transporter PepT1 in intestinal inflammation and inflammatory bowel disease.* American Journal of Physiology-Gastrointestinal and Liver Physiology, 2012. **302**(5): p. 484-492.
60. Lamprecht, A., *Nanomedicines in gastroenterology and hepatology.* Nature Reviews Gastroenterology & Hepatology, 2015. **12**(4): p. 195.
61. Ali, H., et al., *Nanomedicines for the treatment of inflammatory bowel diseases.* European Journal of Nanomedicine, 2013. **5**(1): p. 23-38.
62. Du, Y.-Z., et al., *Tumor cells-specific targeting delivery achieved by A54 peptide functionalized polymeric micelles.* Biomaterials, 2012. **33**(34): p. 8858-8867.
63. Seow, W.Y., J.M. Xue, and Y.-Y. Yang, *Targeted and intracellular delivery of paclitaxel using multi-functional polymeric micelles.* Biomaterials, 2007. **28**(9): p. 1730-1740.
64. Andrews, G.P., T.P. Laverty, and D.S. Jones, *Mucoadhesive polymeric platforms for controlled drug delivery.* European Journal of Pharmaceutics and Biopharmaceutics, 2009. **71**(3): p. 505-518.
65. Tirosh, B., et al., *Transferrin as a luminal target for negatively charged liposomes in the inflamed colonic mucosa.* Molecular Pharmaceutics, 2009. **6**(4): p. 1083-1091.
66. Devriendt, B., et al., *Crossing the barrier: Targeting epithelial receptors for enhanced oral vaccine delivery.* Journal of Controlled Release, 2012. **160**(3): p. 431-439.
67. Charania, M.A., et al., *Intestinal epithelial CD98 directly modulates the innate host response to enteric bacterial pathogens.* Infection and Immunity, 2013. **81**(3): p. 923-934.
68. Cook, M.T., et al., *Microencapsulation of probiotics for gastrointestinal delivery.* Journal of Controlled Release, 2012. **162**(1): p. 56-67.
69. Ojugo, A.S., et al., *Measurement of the extracellular pH of solid tumours in mice by magnetic resonance spectroscopy: a comparison of exogenous 19F and 31P probes.* NMR in Biomedicine, 1999. **12**(8): p. 495-504.
70. Tannock, I.F. and D. Rotin, *Acid pH in tumors and its potential for therapeutic exploitation.* Cancer Research, 1989. **49**(16): p. 4373-4384.

71. Danhier, F., O. Feron, and V. Préat, *To exploit the tumor microenvironment: passive and active tumor targeting of nanocarriers for anti-cancer drug delivery.* Journal of Controlled Release, 2010. **148**(2): p. 135-146.
72. Yahara, T., et al., *Relationship between microvessel density and thermographic hot areas in breast cancer.* Surgery Today, 2003. **33**(4): p. 243-248.
73. Hildebrandt, B., et al., *The cellular and molecular basis of hyperthermia.* Critical Reviews in Oncology/Hematology, 2002. **43**(1): p. 33-56.
74. Dewhirst, M.W., et al., *Re-setting the biologic rationale for thermal therapy.* International Journal of Hyperthermia, 2005. **21**(8): p. 779-790.
75. Wells, J., A. Sen, and S.W. Hui, *Localized delivery to CT-26 tumors in mice using thermosensitive liposomes.* International Journal of Pharmaceutics, 2003. **261**(1): p. 105-114.
76. Peng, C.-L., et al., *Dual chemotherapy and photodynamic therapy in an HT-29 human colon cancer xenograft model using SN-38-loaded chlorin-core star block copolymer micelles.* Biomaterials, 2009. **30**(21): p. 3614-3625.
77. Maeda, H., *The enhanced permeability and retention (EPR) effect in tumor vasculature: the key role of tumor-selective macromolecular drug targeting.* Advances in Enzyme Regulation, 2001. **41**(1): p. 189-207.
78. Lai, S.K., Y.-Y. Wang, and J. Hanes, *Mucus-penetrating nanoparticles for drug and gene delivery to mucosal tissues.* Advanced Drug Delivery Reviews, 2009. **61**(2): p. 158-171.
79. Lamprecht, A., et al., *Nanoparticles enhance therapeutic efficiency by selectively increased local drug dose in experimental colitis in rats.* Journal of Pharmacology and Experimental Therapeutics, 2005. **315**(1): p. 196-202.
80. Sood, A. and R. Panchagnula, *Peroral route: an opportunity for protein and peptide drug delivery.* Chemical Reviews, 2001. **101**(11): p. 3275-3304.
81. Dahmani, F.Z., et al., *Enhanced oral bioavailability of paclitaxel in pluronic/LHR mixed polymeric micelles: preparation, in vitro and in vivo evaluation.* European Journal of Pharmaceutical Sciences, 2012. **47**(1): p. 179-189.
82. Ensign, L.M., R. Cone, and J. Hanes, *Oral drug delivery with polymeric nanoparticles: the gastrointestinal mucus barriers.* Advanced Drug Delivery Reviews, 2012. **64**(6): p. 557-570.
83. Palazzo, C., et al., *Mucoadhesive properties of low molecular weight chitosan-or glycol chitosan-and corresponding thiomer-coated poly (isobutylcyanoacrylate) core-shell nanoparticles.* European Journal of Pharmaceutics and Biopharmaceutics, 2017. **117**: p. 315-323.

84. Pond, S.M. and T.N. Tozer, *First-pass elimination basic concepts and clinical consequences.* Clinical Pharmacokinetics, 1984. **9**(1): p. 1-25.
85. Thanki, K., et al., *Oral delivery of anticancer drugs: challenges and opportunities.* Journal of Controlled Release, 2013. **170**(1): p. 15-40.
86. Borghi-Pangoni, F.B., et al., *Screening and in vitro evaluation of mucoadhesive thermoresponsive system containing methylene blue for local photodynamic therapy of colorectal cancer.* Pharmaceutical Research, 2016. **33**(3): p. 776-791.
87. Al Sabbagh, C., et al., *Thermosensitive hydrogels for local delivery of 5-fluorouracil as neoadjuvant or adjuvant therapy in colorectal cancer.* European Journal of Pharmaceutics and Biopharmaceutics, 2020. **157**: p. 154-164.
88. Narayan, R., et al., *Chitosan-glucuronic acid conjugate coated mesoporous silica nanoparticles: A smart pH-responsive and receptor-targeted system for colorectal cancer therapy.* Carbohydrate Polymers, 2021. **261**: p. 117893.
89. Zhang, X., et al., *Orally delivered targeted nanotherapeutics for the treatment of colorectal cancer.* Expert Opinion on Drug Delivery, 2020. **17**(6): p. 781-790.
90. Xiao, B., et al., *Glycoprotein CD98 as a receptor for colitis-targeted delivery of nanoparticles.* Journal of Materials Chemistry B, 2014. **2**(11): p. 1499-1508.
91. Kucharzik, T., et al., *Activation of epithelial CD98 glycoprotein perpetuates colonic inflammation.* Laboratory Investigation, 2005. **85**(7): p. 932-941.
92. Fernández, M., F. Javaid, and V. Chudasama, *Advances in targeting the folate receptor in the treatment/imaging of cancers.* Chemical Science, 2018. **9**(4): p. 790-810.
93. Bendardaf, R., et al., *Comparison of CD44 expression in primary tumours and metastases of colorectal cancer.* Oncology Reports, 2006. **16**(4): p. 741-746.
94. Su, F.-Y., et al., *Protease inhibition and absorption enhancement by functional nanoparticles for effective oral insulin delivery.* Biomaterials, 2012. **33**(9): p. 2801-2811.
95. Wang, J., et al., *Mechanism of surface charge triggered intestinal epithelial tight junction opening upon chitosan nanoparticles for insulin oral delivery.* Carbohydrate Polymers, 2017. **157**: p. 596-602.
96. Shakweh, M., G. Ponchel, and E. Fattal, *Particle uptake by Peyer's patches: a pathway for drug and vaccine delivery.* Expert Opinion on Drug Delivery, 2004. **1**(1): p. 141-163.
97. Conner, S.D. and S.L. Schmid, *Regulated portals of entry into the cell.* Nature, 2003. **422**(6927): p. 37-44.

98. Kataoka, K., A. Harada, and Y. Nagasaki, *Block copolymer micelles for drug delivery: design, characterization and biological significance.* Advanced Drug Delivery Reviews, 2001. **47**(1): p. 113-131.
99. Adams, M.L., A. Lavasanifar, and G.S. Kwon, *Amphiphilic block copolymers for drug delivery.* Journal of Pharmaceutical Sciences, 2003. **92**(7): p. 1343-55.
100. Xiong, X.B., et al., *Amphiphilic block co-polymers: Preparation and application in nanodrug and gene delivery.* Acta Biomaterialia, 2012. **8**(6): p. 2017-33.
101. Li, J., et al., *A review on phospholipids and their main applications in drug delivery systems.* Asian Journal of Pharmaceutical Sciences, 2015. **10**(2): p. 81-98.
102. Urbani, C.N., et al., *Self-Assembly of amphiphilic polymeric dendrimers synthesized with selective degradable linkages.* Macromolecules, 2008. **41**: p. 76-86.
103. Letchford, K. and H. Burt, *A review of the formation and classification of amphiphilic block copolymer nanoparticulate structures: micelles, nanospheres, nanocapsules and polymersomes.* European Journal of Pharmaceutics and Biopharmaceutics, 2007. **65**(3): p. 259-269.
104. Torchilin, V., *Micellar nanocarriers: pharmaceutical perspectives.* Pharmaceutical Research, 2007. **24**(1): p. 1-16.
105. Andrade, F., et al., *Micelle-based systems for pulmonary drug delivery and targeting.* Drug Delivery Letters, 2011. **1**(2): p. 171-185.
106. Myers, D., *Surfactant science and technology*. 3 ed. 2006, USA: Wiley-Interscience. 380.
107. Malmsten, M., *Surfactants and Polymers in Drug Delivery* 2002: Marcel Dekker, Inc. 335.
108. Chen, L., et al., *Effects of Molecular Weight Distribution of Amphiphilic Block Copolymers on Their Solubility, Micellization, and Temperature-Induced Sol–Gel Transition in Water.* Macromolecules, 2014. **47**(17): p. 5895–5903.
109. Abdelhamid, D., et al., *Role of branching of hydrophilic domain on physicochemical properties of amphiphilic macromolecules.* Polymer Chemistry, 2014. **5**(4): p. 1457–1462.
110. Lu, Y. and K. Park, *Polymeric micelles and alternative nanonized delivery vehicles for poorly soluble drugs.* International Journal of Pharmaceutics, 2013. **453**(1): p. 198-214.
111. Letchford, K., R. Liggins, and H. Burt, *Solubilization of hydrophobic drugs by methoxy poly(ethylene glycol)-block-polycaprolactone diblock copolymer micelles: theoretical and experimental data and correlations.* Journal of Pharmaceutical Sciences, 2008. **97**(3): p. 1179-90.

112. Gelderblom, H., et al., *Cremophor EL: the drawbacks and advantages of vehicle selection for drug formulation.* European Journal of Cancer, 2001. **37**(13): p. 1590-8.
113. Kwon, G. and T. Okano, *Polymeric micelles as new drug carriers.* Advanced Drug Delivery Reviews, 1996. **21**: p. 107-116.
114. Zhang, Y., Y. Huang, and S. Li, *Polymeric micelles: nanocarriers for cancer-targeted drug delivery.* AAPS PharmSciTech, 2014. **15**(4): p. 862-71.
115. Opanasopit, P., et al., *Block copolymer design for camptothecin incorporation into polymeric micelles for passive tumor targeting.* Pharmaceutical Research, 2004. **21**(11): p. 2001-8.
116. Kedar, U., et al., *Advances in polymeric micelles for drug delivery and tumor targeting.* Nanomedicine, 2010. **6**(6): p. 714-29.
117. Le Garrec, D., M. Ranger, and J.-C. Leroux, *Micelles in Anticancer Drug Delivery.* American Journal of Drug Delivery, 2004. **2**(1): p. 15-42.
118. Ohuchi, M., et al., *Physiologically Active Polypeptide- or Protein-Encapsulating Polymer Micelles, and Method for Production of the Same*, U.S. Patent 8,147,868, issued April 3, 2012.
119. Movassaghian, S., O.M. Merkel, and V.P. Torchilin, *Applications of polymer micelles for imaging and drug delivery.* Wiley Interdisciplinary Reviews: Nanomedicine and Nanobiotechnology, 2017. **7**(5): p. 691-707.
120. Ho, K., et al., *Amphiphilic polymeric particles with core-shell nanostructures: emulsion-based syntheses and potential applications.* Colloid and Polymer Science, 2010. **288**(16-17): p. 1503-1523.
121. Kwon, G.S., *Amphiphilic block copolymer micelles for nanoscale drug delivery.* Drug Development Research, 2006. **67**: p. 15-22.
122. Owens, D.E. and N.A. Peppas, *Opsonization, biodistribution, and pharmacokinetics of polymeric nanoparticles.* International Journal of Pharmaceutics, 2006. **307**(1): p. 93-102.
123. Moghimi, S.M. and J. Szebeni, *Stealth liposomes and long circulating nanoparticles: critical issues in pharmacokinetics, opsonization and protein-binding properties.* Progress in Lipid Research, 2003. **42**(6): p. 463-78.
124. Chaudhari, K.R., et al., *Opsonization, biodistribution, cellular uptake and apoptosis study of PEGylated PBCA nanoparticle as potential drug delivery carrier.* Pharmaceutical Research, 2012. **29**(1): p. 53-68.
125. Rösler, A., G.W. Vandermeulen, and H.A. Klok, *Advanced drug delivery devices via self-assembly of amphiphilic block copolymers.* Advanced Drug Delivery Reviews, 2001. **53**(1): p. 95-108.

126. Plapied, L., et al., *Fate of polymeric nanocarriers for oral drug delivery.* Current Opinion in Colloid & Interface Science, 2011. **16**(3): p. 228-237.
127. Csaba, N., M. Garcia-Fuentes, and M.J. Alonso, *The performance of nanocarriers for transmucosal drug delivery.* Expert Opinion on Drug Delivery, 2006. **3**(4): p. 463-478.
128. Deshmukh, A.S., et al., *Polymeric micelles: Basic research to clinical practice.* International Journal of Pharmaceutics, 2017. **532**(1), 249-268.
129. Lv, S., et al., *Co-delivery of doxorubicin and paclitaxel by PEG-polypeptide nanovehicle for the treatment of non-small cell lung cancer.* Biomaterials, 2014. **35**(23): p. 6118-6129.
130. Zhang, W., et al., *Multifunctional Pluronic P123/F127 mixed polymeric micelles loaded with paclitaxel for the treatment of multidrug resistant tumors.* Biomaterials, 2011. **32**(11): p. 2894-2906.
131. Bromberg, L., *Polymeric micelles in oral chemotherapy.* Journal of Controlled Release, 2008. **128**(2): p. 99-112.
132. Mo, R., et al., *The mechanism of enhancement on oral absorption of paclitaxel by N-octyl-O-sulfate chitosan micelles.* Biomaterials, 2011. **32**(20): p. 4609-4620.
133. Matsumura, Y., et al., *Phase I clinical trial and pharmacokinetic evaluation of NK911, a micelle-encapsulated doxorubicin.* British Journal of Cancer, 2004. **91**(10): p. 1775-1781.
134. Nakanishi, T., et al., *Development of the polymer micelle carrier system for doxorubicin.* Journal of Controlled Release, 2001. **74**(1): p. 295-302.
135. Kim, D.W., et al., *Multicenter phase II trial of Genexol-PM, a novel Cremophor-free, polymeric micelle formulation of paclitaxel, with cisplatin in patients with advanced non-small-cell lung cancer.* Annals of Oncology, 2007. **18**(12): p. 2009-14.
136. Lee, K.S., et al., *Multicenter phase II trial of Genexol-PM, a Cremophor-free, polymeric micelle formulation of paclitaxel, in patients with metastatic breast cancer.* Breast Cancer Research and Treatment, 2008. **108**(2): p. 241-50.
137. Saif, M.W., et al., *Multicenter phase II trial of Genexol-PM (GPM), a novel Cremophor-free, polymeric micelle formulation of paclitaxel in patients with advanced pancreatic cancer (APC): Final results*, in *2008 Gastrointestinal Cancers Symposium*. 2008: Orlando.
138. Kim, S.C., et al., *In vivo evaluation of polymeric micellar paclitaxel formulation: toxicity and efficacy.* Journal of Controlled Release, 2001. **72**(1): p. 191-202.
139. Valle, J.W., et al., *A phase 2 study of SP1049C, doxorubicin in P-glycoprotein-targeting pluronics, in patients with advanced adenocarcinoma of the esophagus*

and gastroesophageal junction. Investigational New Drugs, 2011. **29**(5): p. 1029-1037.

140. Hamaguchi, T., et al., *NK105, a paclitaxel-incorporating micellar nanoparticle formulation, can extend in vivo antitumour activity and reduce the neurotoxicity of paclitaxel.* British Journal of Cancer, 2005. **92**(7): p. 1240-1246.
141. Sawant, R. and A. Jhaveri, *Micellar nanopreparations for medicine*, in *Handbook of Nanobiomedical Research: Fundamentals, Applications and Recent Developments*, V. Torchilin, Editor. 2014, World Scientific.
142. Hammad, A., et al., *Interleukin-17A rs2275913, Interleukin-17F rs763780 and rs2397084 gene polymorphisms as possible risk factors in Juvenile lupus and lupus related nephritis.* Autoimmunity, 2016. **49**(1): p. 31-40.
143. *Evaluate the Efficacy and Safety of Genexol®-PM Compared to Genexol® in Recurrent or Metastatic Breast Cancer*. 2016; Available from: https://clinicaltrials.gov/ct2/show/NCT00876486.
144. Lu, H.Q., et al., *Photodynamic therapy and anti-vascular endothelial growth factor for acute central serous chorioretinopathy: a systematic review and meta-analysis.* Eye, 2016. **30**(1): p. 15-22.
145. *A Phase II Trial of Genexol-PM and Gemcitabine in Patients With Advanced Non-small-cell Lung Cancer*. 2016; Available from: https://clinicaltrials.gov/ct2/show/NCT01770795.
146. Ronnekleiv-Kelly, S.M., et al., *Aryl hydrocarbon receptor-dependent apoptotic cell death induced by the flavonoid chrysin in human colorectal cancer cells.* Cancer Letters, 2016. **370**(1): p. 91-9.
147. Spigel, D.R. *A Study of NK012 in Patients With Relapsed Small Cell Lung Cancer*. 2016; Available from: https://clinicaltrials.gov/ct2/show/NCT00951613.
148. Schneider, M., et al., *A paired comparison between glioblastoma "stem cells" and differentiated cells.* International Journal of Cancer, 2016. **138**(7): p. 1709-18.
149. *A Phase III Study of NK105 in Patients With Breast Cancer*. 2016; Available from: https://clinicaltrials.gov/ct2/show/NCT01644890.
150. Matsumura, Y., et al., *Phase I clinical trial and pharmacokinetic evaluation of NK911, a micelle-encapsulated doxorubicin.* British Journal of Cancer, 2004. **91**(10): p. 1775-81.
151. *A Phase 1 Dose-Escalation and Pharmacokinetic Study of NC-4016 in Patients With Advanced Solid Tumors or Lymphoma*. 2016; Available from: https://clinicaltrials.gov/ct2/show/NCT01999491.

152. *Dose-Escalation and Expansion Trial of NC-6300 in Patients With Advanced Solid Tumors or Soft Tissue Sarcoma*. 2017; Available from: https://clinicaltrials.gov/ct2/show/record/NCT03168061.
153. *Combination Therapy With NC-6004 and Gemcitabine Versus Gemcitabine Alone in Pancreatic Cancer*. 2016; Available from: https://clinicaltrials.gov/ct2/show/NCT02043288.
154. *Combination Therapy With NC-6004 and Gemcitabine in Advanced Solid Tumors or Non-Small Cell Lung, Biliary and Bladder Cancer*. 2016; Available from: https://clinicaltrials.gov/ct2/show/NCT02240238.
155. *Efficacy Study of Maintenance IT-101 Therapy for Ovarian Cancer Patients*. 2016; Available from: https://clinicaltrials.gov/ct2/show/NCT00753740.
156. *Study of CRLX101 (Formerly Named IT-101) in the Treatment of Advanced Solid Tumors*. 2016; Available from: https://clinicaltrials.gov/ct2/show/NCT00333502.
157. *BIND Therapeutics. An open label, multicenter, Phase 2 study to determine the safety and efficacy of BIND-014 (docetaxel nanoparticles for injectable suspension) as a second-line therapy for patients with KRAS mutation positive or squamous cell non-small cell lung cancer.* Available from: https://clinicaltrials.gov/ct2/show/NCT02283320.
158. *BIND Therapeutics. A phase 1 open label, safety, pharmacokinetic and pharmacodynamic dose escalation study of BIND-014 (docetaxel nanoparticles for injectable suspension), given by intravenous infusion to patients with advanced or metastatic cancer.* Available from: https://clinicaltrials.gov/ct2/show/NCT01300533.
159. *BIND Therapeutics. An open label, multicenter, phase 2 study to determine the safety and efficacy of BIND-014 (docetaxel nanoparticles for injectable suspension), administered to patients with metastatic castration-resistant prostate cancer.* Available from: https://clinicaltrials.gov/ct2/show/*NCT01812746*.
160. Von Hoff, D.D., et al., *Phase I Study of PSMA-Targeted Docetaxel-Containing Nanoparticle BIND-014 in Patients with Advanced Solid Tumors.* Clinical Cancer Research, 2016. **22**(13): p. 3157-3163.
161. Honarkar, H. and M. Barikani, *Applications of biopolymers I: chitosan.* Monatshefte für Chemie-Chemical Monthly, 2009. **140**(12): p. 1403-1420.
162. Hernández-Valdepeña, M.A., et al., *Suppression of the tert-butylhydroquinone toxicity by its grafting onto chitosan and further cross-linking to agavin toward a novel antioxidant and prebiotic material.* Food Chemistry, 2016. **199**: p. 485-491.
163. Berezin, A.S. and Y.A. Skorik, *Chitosan-isoniazid conjugates: Synthesis, evaluation of tuberculostatic activity, biodegradability and toxicity.* Carbohydrate Polymers, 2015. **127**: p. 309-315.

164. Shukla, S., et al., *In vitro toxicity assessment of chitosan oligosaccharide coated iron oxide nanoparticles.* Toxicology Reports, 2015. **2**: p. 27-39.
165. Madureira, A.R., et al., *Production of antimicrobial chitosan nanoparticles against food pathogens.* Journal of Food Engineering, 2015. **167**: p. 210-216.
166. Kaya, M., et al., *Porous and nanofiber α-chitosan obtained from blue crab (Callinectes sapidus) tested for antimicrobial and antioxidant activities.* LWT-Food Science and Technology, 2016. **65**: p. 1109-1117.
167. De Souza, R., et al., *Biocompatibility of injectable chitosan–phospholipid implant systems.* Biomaterials, 2009. **30**(23-24): p. 3818-3824.
168. Roy, P. and R. Sailaja, *Chitosan–nanohydroxyapatite composites: Mechanical, thermal and bio-compatibility studies.* International Journal of Biological Macromolecules, 2015. **73**: p. 170-181.
169. Sarhan, W.A. and H.M. Azzazy, *High concentration honey chitosan electrospun nanofibers: biocompatibility and antibacterial effects.* Carbohydrate Polymers, 2015. **122**: p. 135-143.
170. Bagheri-Khoulenjani, S., S. Taghizadeh, and H. Mirzadeh, *An investigation on the short-term biodegradability of chitosan with various molecular weights and degrees of deacetylation.* Carbohydrate Polymers, 2009. **78**(4): p. 773-778.
171. Chang, S.-H. and C.-H. Chian, *Plasma surface modification effects on biodegradability and protein adsorption properties of chitosan films.* Applied Surface Science, 2013. **282**: p. 735-740.
172. Liu, M., et al., *Efficient mucus permeation and tight junction opening by dissociable "mucus-inert" agent coated trimethyl chitosan nanoparticles for oral insulin delivery.* Journal of Controlled Release, 2016. **222**: p. 67-77.
173. Hsu, L.-W., et al., *Effects of pH on molecular mechanisms of chitosan–integrin interactions and resulting tight-junction disruptions.* Biomaterials, 2013. **34**(3): p. 784-793.
174. Sonaje, K., et al., *Effects of chitosan-nanoparticle-mediated tight junction opening on the oral absorption of endotoxins.* Biomaterials, 2011. **32**(33): p. 8712-8721.
175. Tsigos, I., et al., *Chitin deacetylases: new, versatile tools in biotechnology.* Trends in Biotechnology, 2000. **18**(7): p. 305-312.
176. Younes, I., et al., *Cytotoxicity of chitosans with different acetylation degrees and molecular weights on bladder carcinoma cells.* International Journal of Biological Macromolecules, 2016. **84**: p. 200-207.
177. Zając, A., et al., *Determination of N-acetylation degree in chitosan using Raman spectroscopy.* Biomolecular Spectroscopy, 2015. **134**: p. 114-120.

178. Novoa-Carballal, R., R. Riguera, and E. Fernandez-Megia, *Chitosan hydrophobic domains are favoured at low degree of acetylation and molecular weight.* Polymer, 2013. **54**(8): p. 2081-2087.
179. Silva, D.S., et al., *Synthesis and applications of amphiphilic chitosan derivatives for drug delivery applications.* Nanoparticles in Life Sciences and Biomedicine, 2018: p. 45.
180. Chen, Z., et al., *Blood coagulation evaluation of N-alkylated chitosan.* Carbohydrate Polymers, 2017. **173**: p. 259-268.
181. Piegat, A., et al., *Antibacterial Activity of N, O-Acylated Chitosan Derivative.* Polymers, 2021. **13**(1): p. 107.
182. Almeida, A., et al., *Synthesis and characterization of chitosan-grafted-polycaprolactone micelles for modulate intestinal paclitaxel delivery.* Drug Delivery and Translational Research, 2018. **8**(2): p. 387-397.
183. Silva, D.S., et al., *Synthesis and characterization of 3, 6-O, O'-dimyristoyl chitosan micelles for oral delivery of paclitaxel.* Colloids and Surfaces B: Biointerfaces, 2017. **152**: p. 220-228.
184. Silva, D.S., et al., *N-(2-hydroxy)-propyl-3-trimethylammonium, o-mysristoyl chitosan enhances the solubility and intestinal permeability of anticancer curcumin.* Pharmaceutics, 2018. **10**(4): p. 245.
185. Almeida, A., et al., *Novel amphiphilic chitosan micelles as carriers for hydrophobic anticancer drugs.* Materials Science and Engineering: C, 2020: p. 110920.
186. Yuan, H., et al., *Stearic acid-g-chitosan polymeric micelle for oral drug delivery: in vitro transport and in vivo absorption.* Molecular Pharmaceutics, 2011. **8**(1): p. 225-238.
187. Mi, Y., et al., *New synthetic chitosan derivatives bearing benzenoid/heterocyclic moieties with enhanced antioxidant and antifungal activities.* Carbohydrate Polymers, 2020. **249**: p. 116847.
188. Zhao, D., et al., *Biomedical applications of chitosan and its derivative nanoparticles.* Polymers, 2018. **10**(4): p. 462.
189. Caddeo, C., et al., *Chitosan–xanthan gum microparticle-based oral tablet for colon-targeted and sustained delivery of quercetin.* Journal of Microencapsulation, 2014. **31**(7): p. 694-699.
190. Alhakamy, N.A., et al., *Chitosan-based microparticles enhance ellagic acid's colon targeting and proapoptotic activity.* Pharmaceutics, 2020. **12**(7): p. 652.
191. Yuan, X., et al., *Mucoadhesive guargum hydrogel inter-connected chitosan-g-polycaprolactone micelles for rifampicin delivery.* Carbohydrate Polymers, 2019. **206**: p. 1-10.

192. Dubashynskaya, N.V., et al., *Mucoadhesive cholesterol-chitosan self-assembled particles for topical ocular delivery of dexamethasone.* International Journal of Biological Macromolecules, 2020. **158**: p. 811-818.
193. Feng, S.S. and S. Chien, *Chemotherapeutic engineering: application and further development of chemical engineering principles for chemotherapy of cancer and other diseases.* Chemical Engineering Science, 2003. **58**(18): p. 4087-4114.
194. Spencer, C.M. and D. Faulds, *Paclitaxel.* Drugs, 1994. **48**(5): p. 794-847.
195. Xu, W., et al., *Cysteine modified and bile salt based micelles: Preparation and application as an oral delivery system for paclitaxel.* Colloids and Surfaces B: Biointerfaces, 2015. **128**: p. 165-171.
196. Fonte, P., et al., *Polymer-based nanoparticles for oral insulin delivery: Revisited approaches.* Biotechnology Advances, 2015. **33**(6): p. 1342-1354.
197. Du, X., et al., *Polylysine and cysteine functionalized chitosan nanoparticle as an efficient platform for oral delivery of paclitaxel.* Carbohydrate Polymers, 2020. **229**: p. 115484.
198. He, R. and C. Yin, *Trimethyl chitosan based conjugates for oral and intravenous delivery of paclitaxel.* Acta Biomaterialia, 2017. **53**: p. 355-366.
199. Wang, X., et al., *Preparation and evaluation of carboxymethyl chitosan-rhein polymeric micelles with synergistic antitumor effect for oral delivery of paclitaxel.* Carbohydrate Polymers, 2019. **206**: p. 121-131.
200. Mu, Y., et al., *Multifunctional quercetin conjugated chitosan nano-micelles with P-gp inhibition and permeation enhancement of anticancer drug.* Carbohydrate Polymers, 2019. **203**: p. 10-18.
201. Kumar, R., et al., *Polymeric micelles based on amphiphilic oleic acid modified carboxymethyl chitosan for oral drug delivery of bcs class iv compound: Intestinal permeability and pharmacokinetic evaluation.* European Journal of Pharmaceutical Sciences, 2020. **153**: p. 105466.
202. Liu, L.F., et al., *Mechanism of action of camptothecin.* Annals of the New York Academy of Sciences, 2000. **922**(1): p. 1-10.
203. Silva, D.S., et al., *Self-aggregates of 3, 6-O, O'-dimyristoylchitosan derivative are effective in enhancing the solubility and intestinal permeability of camptothecin.* Carbohydrate Polymers, 2017. **177**: p. 178-186.

CHAPTER 3

A biophysical insight of camptothecin biodistribution: towards a molecular understanding of its pharmacokinetic issues

The information provided in this chapter was based in the following publication:

Almeida, A.*, Fernandes, E.*, Sarmento, B. & Lúcio, M., 2021. A biophysical insight of camptothecin biodistribution: towards a molecular understanding of its pharmacokinetic issues, *Pharmaceutics, 13*(6), 869. (*equal contribution)

In this paper, I was responsible for the conception, execution and revision of the manuscript. Eduarda Fernandes was also responsible for the conception, execution and revision of the manuscript. The supervisors were responsible for reviewing and submit the manuscript. This paper was not previously included in other thesis, and it is partially reproduced in this section.

3.1. Abstract

Camptothecin (CPT) is a potent anticancer drug, and its putative oral administration is envisioned although difficult due to physiological barriers that must be overcome. A comprehensive biophysical analysis of CPT interaction with biointerface models can be used to predict some pharmacokinetic issues after oral administration of this or other drugs. To that end, different models were used to mimic the phospholipid composition of normal, cancer, and blood-brain barrier endothelial cell membranes. The distribution coefficient (*LogD*) values obtained indicate that the drug is well distributed across membranes. CPT-membrane interaction studies also confirm the drug's location at the membrane cooperative and interfacial regions. The drug can also permeate membranes at more ordered phases by altering phospholipid packing. The similar *LogD* values obtained in membrane models mimicking cancer or normal cells imply that CPT has limited selectivity to its target. Furthermore, CPT binds strongly to serum albumin, leaving only 8.05% of free drug available to be distributed to the tissues. The strong interaction with plasma proteins, allied to the large distribution (VD_{SS}=5.75 ± 0.932 L·Kg^{-1}) and tendency to bioaccumulate in off-target tissues, were predicted to be pharmacokinetic issues of CPT, implying the need to develop drug delivery systems to improve its biodistribution.

3.2. Introduction

Camptothecin (CPT) is an alkaloid isolated from the Chinese tree *Camptotheca acuminata* and it is a promising agent against cancer [1]. CPT is a pH dependent molecule that can exist in two different forms: the lactone form, which is stable at pH < 5.5 and biologically active or the carboxylate form, which is stable at pH > 9 and inactive. CPT inhibits the topoisomerase I, which is a nuclear enzyme implied in the DNA replication, by binding the topoisomerase I-DNA complex, avoiding the replication process and, consequently, leading to the cell death [2, 3]. Its mechanism of action only occurs in the S-phase of the cell cycle. Interestingly, cancer cells spend more time in the S-phase compared to healthy cells, which means that CPT is more likely to bind to cancer cells and therefore, exert its mechanism of action. This selectivity is one of the characteristics that makes CPT a potential drug for cancer treatment.

However, CPT has some disadvantages that make its effectiveness less than expected, as the case of the pH-dependency and the poor water solubility.

CPT at physiologic pH is hydrolyzed and the molecule is partially converted into the carboxylate form, where the ring is opened and, thus biologically inactive. The lactone active form is present in the biological fluids at a very low concentration. It is described that after 2 h in contact with human blood, only 5% of the CPT lactone form remains [3], which makes

its effectiveness against cancer impossible. In addition, in the human plasma, the carboxylate form is the most abundant microspecie, which has great affinity to the human serum albumin (HSA). Once CPT and HSA are bound, it is no longer possible to convert the molecule into its lactone form [4]. However, the stability of CPT can be improved once the molecule bounds to membranes, which avoids its hydrolysis [5]. Thus, it is very important to understand the interaction of CPT when in contact with cellular membranes, proteins or biological fluids to predict its behavior for further *in vitro* and *in vivo* studies.

The pharmacokinetic (PK) parameters of a drug are dependent on its freely or bound form present in the biological fluids, as well as, the therapeutic efficacy is tightly related to the affinity to plasma proteins [6]. However, drug design goes beyond drug-protein interactions. The membrane location and orientation, and the membrane affinity and distribution dictated by the partition coefficient (*LogP*) and *LogD* of a drug are parameters used to predict the transport, distribution, accumulation and the therapeutic effects of compounds *in vivo* [7]. Thus, the determination of the drug ADMET profile (absorption, distribution, metabolism, elimination and toxicity) through the study of molecular interactions play a key role on the drug PK [8, 9]. 1,2-dioleoyl-*sn*-glycero-3-phosphatidyl-choline (DOPC), 1,2-dioleoyl-*sn*-glycero-3-phospho-L-serine (DOPS), 1,2-di-oleoyl-*sn*-glycero-3-phosphoethanolamine (DOPE), sphingomyelin (SM) or cholesterol (CHOL) are widely used to mimic the performance of biological membranes *in vitro* since they represent some of the main lipid components of the biological membranes [10]. Additionally, while using computational *in silico* models, it is possible to determine these PK key factors and evaluate if a molecule is worth to progress for *in vitro* and/or *in vivo* studies [11, 12].

The interaction of CPT with membrane models and with plasma proteins has already been addressed in previously reported studies [13-15]. However, the reports in literature are sparse, use few techniques and do not provide a comprehensive overview of the molecular interactions established between the drug and biological interfaces throughout its physiological path. In the literature it is possible to find a few studies of binding of CPT to membranes of dipalmitoylphosphatidylcholine (DMPC), 1,2-dimyristoyl-*sn*-glycero-3-phosphoglycerol (DMPG), DOPC or 1,2-dioleoyl-*sn*-glycero-3-[phospho-rac-(1-glycerol)] (DOPG) and CPT binding to HSA or bovine serum albumin (BSA) [16-18]. The purpose of this research is to give a more complete overview of the interactions between CPT and biointerfaces after a putative oral administration of this drug and simultaneously provide researchers with an example of *in vitro* profiling of a known drug, used as model, that can be applied to predict/explain some aspects of the biological behavior of other drugs *in vivo*. Therefore, the current study is intended to go further than the reported CPT/membrane interaction studies by evaluating the distribution of CPT in more complex membrane models mimicking cancer or normal cells and endothelial membranes of the blood brain barrier

(BBB). These different membrane models will permit using more accurate *in vitro* membrane distribution values to be used together with theoretical models and predict drug distribution at therapeutic targets as well as at off-target sites. Moreover, this study also focuses on the biophysical aspects of the interaction of CPT with membrane models, which to our knowledge have not been addressed, such as the location/orientation of CPT within the membrane, CPT effect on the membrane fluidity and the effect of the drug on the membrane structure and phospholipid packing at different lipid phases. To achieve the aims proposed a detailed study of the CPT physicochemical properties was conducted and several biophysical techniques were employed, such as dynamic light scattering (DLS), derivative UV-Vis spectroscopy, fluorescence spectroscopy, intrinsic and extrinsic fluorescence quenching or synchrotron small and wide-angle X-ray scattering (SAXS and WAXS).

Since CPT is used as a model drug, the results obtained can help to understand what the drug's possible responses will be when after administration it is exposed to different biointerfaces. This approach allowed to accurately predict some challenges of CPT biodistribution and to purpose drug delivery strategies to overcome these challenges. Therefore, the results here presented can be used by researchers as an example of an *in vitro* profile to predict the behavior of drugs *in vivo*, at early stages of formulation developing avoiding the unnecessary use of cells and/or animals in agreement with the EU principles (Directive 2010/63/EU).

3.3. Materials and Methods

3.3.1. Materials

Camptothecin (CPT) was acquired from Hangzhou ROYAL Import & Export Co., Ltd. The lipids DOPC, DOPS, DOPE, Cardiolipin (CL), the lipid labelled probe 1,2-dipalmitoyl-*sn*-glycero-3-phosphoethanolamine-N-(7-nitro-2-1,3-benzoxadiazol-4-yl) (NBD-PE) and the brain polar lipids (BPL) were obtained from Avanti Polar Lipids, Inc. (Instruchemie, Delfzijl, The Netherlands). Egg Phosphatidylcholine (EPC), SM and CHOL were purchased to Sigma-Aldrich Química, S.L. (Portugal). All reagents were the highest purity available and were used without further purification. Membrane models of cancer cells were prepared in acetate buffer (pH 5.8) and membrane models of normal cells were prepared in HEPES buffer (pH 7.4). All other solutions were prepared with water from a Milli-Q plus system with specific conductivity less than 0.1 μS cm^{-1}.

3.3.2. *In silico* predictors of drug-profiling

Relevant drug physical-chemical properties (e.g., number of hydrogen bonds, polar surface area (PSA) and van der Waals surface area (VWSA), solubility, *LogD* and *LogP*, and ionization) were calculated using in the module MarvinSketch® from Chemaxon® software. From these physicochemical properties and based on reported molecular descriptors, a drug-profiling was established to give insights about formulation design challenges for CPT delivery [19].

3.3.3. Preparation of membrane models

Single-lipid liposomal membrane models composed of DMPC, or lipid mixture liposomal membrane models mimetic of breast cancer cell membrane - DOPC (25%), CHOL (15%), EPC (31.8%), DOPS (17%), DOPE (8%), CL (2.5%) and SM (0.7%) – mimetic of cell membrane – DOPC (45%), DOPE (20%), DOPS (20%), CHOL (10%) and SM (10%) – and, BBB membrane constituted by the BPL – phosphocholine (PC) (12.6%), phosphatidyl ethanolamine (PE) (33.1%), PI (4.1%), phosphatidyl serine (PS) (18.5%) and PA (0.8%) were prepared by the classical thin film hydration method [20]. Briefly, lipids were co-dissolved in chloroform:methanol (8:2, v/v) and the solvents were evaporated under a stream of nitrogen in a rotary evaporator (Buchi R-200; Sigma-Aldrich Corp., Buchs, Switzerland). The resultant dried lipid film was hydrated with buffer at temperature of 40 ± 0.1 °C and lipid colloidal dispersions were formed by alternating vortex and thermostatic bath (40 ± 0.1 °C). Subsequently, unilamellar lipid model systems were obtained from extruding (Lipex® extruder, Tranferra Nanosciences, Burnaby, Canada) colloidal dispersions through polycarbonate filters with a pore diameter of 100 nm (Millipore SAS, France).

For the location studies, NBD-PE labelled lipid model systems were used, prepared by the lipid film hydration method above described followed by extrusion. In the lipid film preparation process, the probe was co-dried with the lipid in a ratio of 300:1 (lipid:probe) to prevent changes in the structure of the membrane [21].

3.3.4. Drug distribution coefficient in membrane/aqueous systems studied by derivative spectroscopy

The *LogD* of CPT between membrane and aqueous buffered solution (pH 5.8 for breast cancer cell membrane model and pH 7.4 for cell membrane model and BBB membrane model) was determined by fluorescence spectroscopy and derivative UV/Vis spectroscopy. For each model, two groups of suspensions were prepared: the samples and references.

The samples contained a fixed concentration of CPT (2×10^{-5}M) and increasing concentrations of lipid suspension (0 to 1×10^{-3} M for absorbance or 3×10^{-3} M for fluorescence). The references were identically prepared in absence of CPT. Then, all the suspensions were incubated during 30 minutes at 37.0 ± 0.1 °C. After incubation, the absorption spectra of samples and references were plotted in the 230-500 nm range, on a Perkin-Elmer Lambda 45 UV-Vis, accordingly to a well-established protocol [22] at 37.0 ± 0.1 °C. The fluorescence spectra were also measured on a Perkin-Elmer LS-50B spectrofluorimeter. The emission spectra were obtained in 380-480 nm range with $\lambda_{excitation}$=250 nm and the excitation spectra were recorded in 220-400 nm range with $\lambda_{emission}$=430 nm. The excitation and emission slits were adjusted to 6 nm. The second and third derivative spectra of the absorbance UV-Vis spectra was determined to improve the resolution of spectral bands and to eliminate the spectral interferences due to light scattered by the lipid suspensions and. Representing the λ_{max} or λ_{min} values of the 1st, 2nd or 3rd derivative spectra as a function of the concentration of lipid model systems ([Membrane]) a non-linear regression was obtained from which it was possible to determine the distribution coefficient (D):

$$\frac{d^n S_T}{d\lambda^n} = \frac{d^n S_a}{d\lambda^n} + \frac{\frac{d^n S_m}{d\lambda^n} - \frac{d^n S_a}{d\lambda^n} \cdot D \cdot [Membrane] \cdot V_m}{1 + D \cdot [Membrane] \cdot V} \quad (3.1)$$

where S_T, *Sa* and *Sm* stands respectively for total (*T*) absorbance of the drug in membrane (*m*) and aqueous media (*a*). The membrane model systems' concentration, *[Membrane]* expressed in mol·L^{-1}, is multiplied by the lipid molar volume in L·mol^{-1} (V_m) of each membrane model to obtain a dimensionless value of *D*, from which *logD* is calculated.

Because CPT is a fluorescent compound with spectral variations due to its distribution between the lipid/aqueous phases (e.g., λ shifts), *LogD* of CPT can also be calculated using fluorescence spectroscopy [23]. The fluorescence emission intensity, *I*, can be used to calculate the distribution D, and the correspondent *LogD*, through Equation 3.2:

$$I_T = I_a + \frac{(I_l - I_a) D [Membrane] V_l}{1 + D [Membrane] V_l} \quad (3.2)$$

where the fluorescence emission intensity (I_T) of CPT distributed in lipid accounts for the fluorescence emission intensity contributions of the drug distributed in the membrane (I_m) and aqueous (I_a) phases which can be related to *D* and then *LogD* values [23].

3.3.5. Drug location in membrane/aqueous systems studied by steady-state fluorescence quenching

Cancer cell membrane model was labelled with NBD-PE probe. The fluorescence of the fluorophore was monitored by steady-state fluorescence studies to predict CPT location at membrane level. Increasing concentrations of CPT (0 – 4.0×10^{-5} M) and a fixed concentration of the labelled cancer membrane model system (3.0×10^{-2} M) were used. Steady-State fluorescence emission (Perkin-Elmer LS-50B spectrofluorimeter) was obtained using $\lambda_{excitation}$= 360 nm (maximum excitation of CPT). Fluorescence excitation (300-400 nm) and emission spectra (500-600 nm) were recorded using slits of 9 and an integration time of 10 s was used. The extent of fluorescence quenching induced by CPT in NBD-PE probe was evaluated by Stern-Volmer constant (K_{SV}) obtained by fitting data to the Stern-Volmer linear plots:

$$\frac{I_0}{I} = 1 + K_{SV} \cdot [CPT]_m \tag{3.3}$$

where I and I_0 are the steady-state fluorescence, respectively, in the presence or in the absence of CPT. $[CPT]_m$ is the membrane concentration of CPT calculated as described elsewhere [24]:

$$[CPT]_m = \frac{K_d \cdot [CPT]_T}{K_d \cdot V_m + (1 - V_m)} \tag{3.4}$$

where K_d is the distribution coefficient of CPT in the membrane model system (calculated as described in Equation 3.1), $[CPT]_T$ is the total concentration of CPT and α_m is the membrane volume fraction.

The efficacy of CPT to quench the fluorescence of the probe was evaluated by the bimolecular constant (K_q) [25]:

$$K_q = \frac{K_{SV}}{\tau_0} \tag{3.5}$$

where τ_0 is the unquenched lifetime. All fluorescence intensity data were corrected from absorption and inner filter effect [25].

3.3.6. Plasma protein binding evaluation using steady-state fluorescence quenching

The fluorescence excitation and emission spectra of increasing CPT concentrations (0 to 3×10^{-4} M) with a constant HSA concentration (2.0×10^{-6} M) were acquired at 37.0 ± 0.1 °C (Perkin-Elmer LS-50B), with excitation at 280 nm and emission at 342 nm, each with 5 nm slits. The following binding isotherm equation can be used to explain the quenching of HSA fluorescence caused by increasing CPT concentrations [25]:

$$\%\ Quenching = \frac{y_{max} \cdot n}{1 + \frac{K_{diss}}{[CPT]}} \tag{3.6}$$

where y_{max} is the maximum fluorescence quenching measured, n is the number of binding sites of HSA to CPT and K_{diss} is the dissociation constant (i.e., the inverse of binding constant, K_{bind}). In addition, the following equation expresses the relationship between the K_{diss} value and the Gibbs free energy (ΔG) of complex binding:

$$\Delta G_{bind} = R \cdot T \cdot \ln K_{bind} \tag{3.7}$$

where R is the ideal gas constant and T is the temperature in Kelvin (K).

3.3.7. Small- and wide-angle X-ray scattering studies at the Synchrotron

Membrane model systems (DMPC) in the presence or absence of CPT were put into 1.5 mm diameter X-ray clear glass capillaries for X-ray scattering studies (Germany). Capillaries were sealed with a flame and kept at 4 °C. SAXS and WAXS experiments were carried out at the Austrian SAXS/WAXS beamline at the synchrotron light source ELETTRA (Italy), using monochromatic synchrotron radiation with a wavelength of 1.54 nm and an X-ray energy of 8 keV. SAXS and WAXS patterns were captured at locations that covered the normal diffraction spacing spectrum ($s = 2 \sin \boldsymbol{\theta}/\boldsymbol{\lambda}$, where $\boldsymbol{\lambda}$ is the wavelength and $2\boldsymbol{\theta}$ is the scattering angle) of interest using a 2D Pilatus3 1M and a 2D Pilatus 100K detector device, respectively, with a pixel size of 172 µm. The lamellar peaks of silver behenate (SAXS) and *p*-bromo benzoic acid (WAXS) were used as criteria to calibrate the diffraction spacings. Static exposures were taken below and above the main transition temperature as controlled by a thermostated water bath (stability ± 0.1 °C; Unistat CC, Germany) to obtain the diffraction patterns of normal lipid phases ($L_{\beta'}$, ripple phase P_{β} and L_{α}) and the effect of CPT in those phases. The data was analyzed in the same way as it had been in previous studies [26].

3.3.8. Studies on dynamic and electrophoretic light scattering

DLS was used to assess the influence of CPT addition in the main phase transition temperature and cooperativity (B) of the DMPC membrane model system [28, 29]. As a result, the light scattered (Mean Count Rate, MCR) by membrane system (5.0×10^{-2} M) in the absence and presence of CPT (2.0×10^{-2} M) was measured as a function of temperature (T) between 30 and 55 °C (with 1°C intervals and 2 min of equilibration time). A sigmoidal function based on a modified Boltzmann equation was used to fit the results [26, 27]:

$$MCR = b_1 + m_1 \cdot T + \frac{b_2 - b_1 + m_2 \cdot T - m_1 \cdot T}{1+10^{B \cdot \left(1/T - 1/Tm\right)}} \quad (3.8)$$

where m_1 and m_2 are the slopes obtained by fitting the data linearly before and after *Tm*, respectively, and b_1 and b_2 are the corresponding y-intercepts. All DLS and electrophoretic light scattering (ELS) experiments were carried out in a Zetasizer Nano ZS with disposable polystyrene cells and a dipcell (ZEN1002) for the ELS studies.

3.3.9. Modelling biodistribution using *in vitro* parameters

The *LogD* value obtained can be used with *in silico* descriptors to predict many biodistribution parameters using mathematical methods. As a result, the value of *LogD* was used to predict CPT bioaccumulation (as expressed by the bioaccumulation constant, $K_{bioaccumulation}$), which is associated to tissue blood flow (Q) and its volume (V) [28]:

$$K_{bioaccumulation} = \frac{Q}{V \cdot logD} \quad (3.9)$$

To determine if the drug is stored in adipose tissue, the adipose store index (ASI) of CPT was calculated using the following equation [29]:

$$ASI = 1.81 \cdot LogD - LogD + 0.40 \quad (3.10)$$

Furthermore, the obtained distribution coefficient in the BPL model system – $logD_{(BBB)}$ – can be compared to *logBB*, according to Waterbeem and Kansy [30]. The logarithm of the ratio of drug concentrations in brain and blood is known as *logBB*, and it represents the drug's relative affinity variations between plasma proteins and brain tissue [31]:

$$LogBB = 0.388 \cdot LogD_{BBB} - 0.00618 \cdot V_m + 1.359 \quad (3.11)$$

where V_m is the membrane model system's molar volume, determined from the individual lipid volumes [25].

The Steady-State Volume Distribution (VD_{SS}) is one of the most useful pharmacokinetic criteria for describing a drug's biodistribution [32]. The effect of the PPB, permeability, partitioning, and active transport on the drug's physiological distribution is translated by this predictor. Based on human clinical pharmacokinetic evidence of a wide set of drugs (670 drugs), the first physiological statistical model of VD_{SS} for predicting the biodistribution of neutral and basic drugs was proposed [33]:

$$\boldsymbol{VD_{SS} = V_P\left(1 + R_{E/L}\right) + f_u \cdot V_P\left(\frac{V_E}{V_P} - R_{E/L}\right) + \frac{V_R \cdot f_u}{f_{ut}}} \quad (3.12)$$

where V_P and V_E are the plasma and extracellular fluid volumes with corresponding value in human of 0.0436 and 0.0151 $L \cdot Kg^{-1}$; $R_{E/I}$ represents the ratio of extravascular and intravascular proteins, and is strictly referred to the distribution of albumin, assuming an approximate value of 1.4; V_R is defined as the physical volume into which the drug distributes minus the extracellular space (0.380 $L \cdot Kg^{-1}$); f_u and f_{ut} are, respectively, the unbound drug fraction in plasma and the unbound fraction in tissues [33].
The f_u values can be obtained by the following equation [34]:

$$f_u = 1 - \frac{PPB}{100} \quad (3.13)$$

where PPB is the percentage of PPB and can be obtained from the *in vitro* values of K_{bind} [34]:

$$\boldsymbol{PPB = \frac{100}{1 + \frac{1}{C_p \cdot K_{bind}}}} \quad (3.14)$$

where C_P is the physiological plasma protein concentration (750 μM) [34].
Lastly, f_{ut} can be obtained by the following equation [33]:

$$Logf_{ut} = -0.0289 - 0.1739 \cdot LogD - 0.8324 \cdot f_{i(7.4)} + 1.0400 \cdot Logf_u \quad (3.15)$$

where $f_{i(7.4)}$ is the fraction of ionized drug at pH 7.4 which has been calculated considering the pH hydrolysis and conversion of CPT from lactone neutral form to the anionic form carboxylate reported [35].

3.3.10. Statistical analysis

All data were expressed as mean ± standard deviation of 3 independent experiments. Multiple comparisons were performed using a two-way variance analysis (ANOVA) with a Sidak's multiple comparisons test or one-way ANOVA with the Student–Newman–Keuls as a post-test. Values of * P<0.05; ** P<0.01; *** P<0.001 have been considered statistically significant.

3.4. Results and Discussion

3.4.1. *In silico* analysis of camptothecin physicochemical properties

CPT is expected to communicate with a variety of biological interfaces immediately after oral administration, raising obstacles to its biodistribution [9, 36]. *In silico* methods are widely used to perform systematic analysis of the physicochemical and biopharmaceutical properties of potential drugs. Understanding the challenges that a drug may present is critical and can lead to new methods in the formulation manufacturing in order to overcome these challenges. Some pertinent physicochemical properties of CPT (Figure 3.1) were predicted *in silico* (Table 3.1). Following that, conclusions regarding its ionization, lipophilicity, permeability, and solubility were drawn, as well as its classification according to the Biopharmaceutical Classification System (BCS).

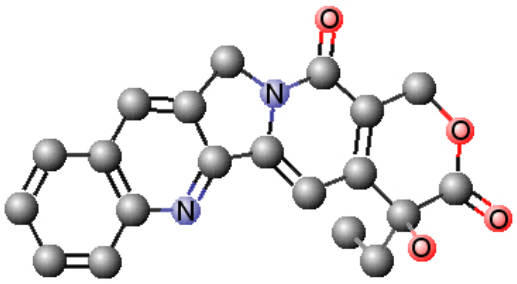

Figure 3.1. 3D chemical structure of CPT generated with 'Chemicalize' tool from Chemaxon® software.

Table 3.1 – *In silico* prediction of several physicochemical descriptors using the CPT chemical structure on Chemaxon® software.

MW (g/mol)	PSA ($Å^2$)	VWSA ($Å^2$)	logP	S (mg/mL)	pKa	H donors	H acceptors
348.36	79.73	441.88	1.52	0.0559	3.07 11.71	1	4

Abbreviations: MW – molecular weight; PSA – polar surface area; VWSA – Van der Waals surface area; logP – $\log_{10}$ of the octanol/water partition coefficient; S – intrinsic aqueous solubility; pKa – negative $\log_{10}$ of the ionization constant.

Taking into consideration the Lipinski 'rule of five', a compound is more likely to have poor permeability if at least two of the following parameters are observed: *LogP* > 5, MW > 500 Da, H donors > 5, and H acceptors > 10 [37]. Since CPT does not follow any parameters of the Lipinski rule, it is thus expected to have good permeability. Moreover, CPT demonstrated to have low polarizability (PSA = 79.73 $Å^2$), which is correlated with a good permeability profile at the cell membranes [40]. However, when its lipophilicity is observed, we can conclude that CPT is moderate lipophilic (0 < *LogP* < 3) [39] and presents poor aqueous solubility (0.0559 $mg \cdot mL^{-1}$). These factors, despite not being contemplated by the Lipinski rule, do not facilitate the permeability of the compound, which agrees with other published work [40]. Also, the permeability of a compound can be related with the concentration used. Indeed, CPT permeability is dependent of the concentration, being more permeable at lower concentrations (5 μM) and, even so, its P_{app} is relatively low (3×10^{-5} $cm \cdot s^{-1}$) [40]. Moreover, from the *in silico* evaluation of the physicochemical properties of a molecule it is not possible to predict if the molecule will suffer hydrolysis, as in the case of CPT. Since CPT is pH-dependent and not stable at neutral pH, it can easily suffer hydrolysis and, at physiologic pH, be converted in the carboxylate form, which is more aqueous soluble, less permeable and it is not biological active to bind the topoisomerase I. None of these aspects could be predicted only from the *in silico* evaluation of CPT. Indeed, if we would only rely on *in silico* calculations CPT would be classified by the BCS as Class II. However, as previously described, this prediction does not take into consideration the stability of the molecule and the pH-dependency, thus, the BCS classification of CPT should be the one officially adopted, that is, a class IV compound [41]. Additionally, along the GIT the drug will experience a pH gradient that will cause its hydrolysis originating an anionic carboxylate form. It is well described in the literature that non-ionized drugs are more readily absorbed along the GIT [28, 42], thus the anionic form of the drug will reduce its membrane permeability consequently reducing its absorption. The contradictory results in the absorption potential of CPT highlight the fallibility of using solely *in silico* molecular

calculations as tools to predict ADMET profile of drugs. Regarding the CPT ionization character, the obtained *in silico* pKa values (Table 3.1) are similar to the pKa values found for CPT analogues (pKa = 2.32 and 9.15) [41, 42].

From the analysis made for CPT it is possible to conclude that using only *in silico* approaches is not always a straightforward or reliable method to predict biodistribution. Recent developments in biodistribution prediction and PK profiling recommend the use of *in vitro* approaches, complemented by *in silico* analysis and models, to predict tissue distribution using physicochemical properties [33, 43-45]. Therefore, it is important to evaluate other parameters, like the interaction with biological membranes, in order to predict the molecule behavior in the biological fluids. These predictions can be further improved by considering *in vitro* data and binding of drugs to plasma proteins [33, 45-47]. Therefore, in the following sections *in vitro* studies of the interactions of CPT with models of biointerfaces will be conjugated with *in silico* properties and theoretical models to evaluate CPT biodistribution. This approach may be very helpful when formulating new oral delivery dosage forms of CPT, aiming to understand how to maintain drug's stability and biological function, at the same time improving its aqueous solubility and mucus diffusion.

3.4.2. Distribution and location of camptothecin in a membrane/aqueous system

The *LogD* between lipid and aqueous phases, which allows estimation of drug lipophilicity and distribution in hydrophobic and hydrophilic microenvironments, is the first physicochemical property that provides strong evidence to support drug distribution in body tissues [48].

Accordingly, the *LogD* of CPT was determined in cancer cell membrane models, cell membrane models, and BBB membrane models in order to simulate the various membrane barriers encountered by this drug during its biological distribution. The study in cancer cell membrane models was carried out at a pH of 5.8 to mimic the acidic microenvironment of tumors (pH 5.6 to 6.8), which is a hallmark of malignant cancer cells and is caused by glycolysis in cancer cells, hypoxia, and insufficient blood perfusion [49]. The studies in cell membrane models were carried out at pH 7.4 representative of blood and healthy tissues. Figure 3.2 shows an example of absorbance spectra and the subsequent derivative method for data analysis.

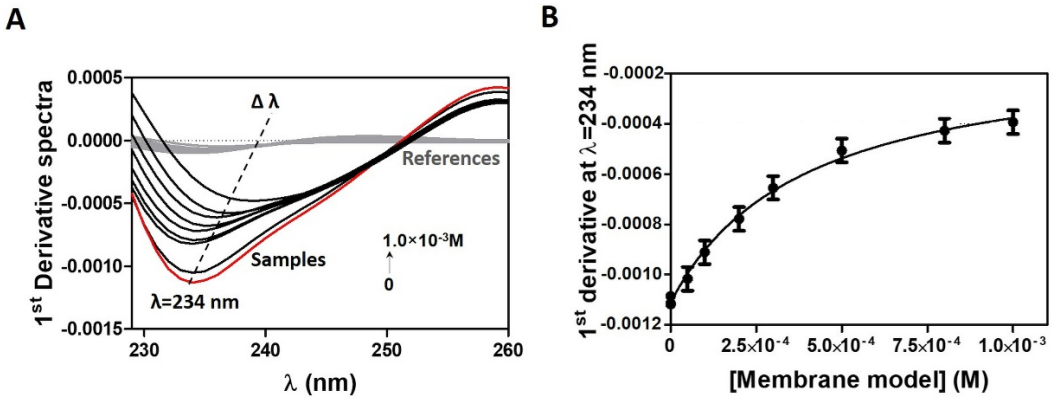

Figure 3.2. (A) First derivative of CPT ($2x10^{-5}$) absorption spectra with increasing concentrations of cancer membrane models (0 to 1.0 $x10^{-3}$ M) in Acetate buffer pH = 5.8. In red is represented the absorption spectra of CPT in the absence of the cancer membrane models. With the addition of increasing concentrations of membrane model (samples represented in black) there is a shift in λ values. In grey are represented the derivative spectra of the references containing only membrane models. (B) Nonlinear fitting of derivative absorbance values at λ = 234 nm as a function of membrane model concentration.

The first derivative spectra were calculated from the CPT absorbance spectra experimentally obtained for increasing concentrations of the membrane model (Figure 3.2A), as this eliminates the effect of Rayleigh dispersion, which is higher for shorter wavelengths [23]. The use of first derivative spectra eliminates light scattering interference and improves spectral resolution, revealing more details about the CPT–lipid interaction. Indeed, at the derivative minimum, a shift of λ (of about 25 nm) is visible, indicating CPT distribution into lower polarity environments (distribution of CPT into the lipid phase) [23], with a decrease in the intensity of the bands as the lipid concentration increases. There is also an isosbestic point observed, indicating the presence of a balance between two CPT forms (interacting with the lipid medium and free in aqueous buffered medium) and the elimination of light-scattering interference [23]. Data were plotted against the respective membrane model concentration (Figure 3.2B) using maximum or minimum values from derivative spectra (e.g., 234 nm), and the resulting data points were fitted to Equation 3.1 (Figure 3.2B).

The determination of *LogD* in membrane/aqueous phase by fluorescence methods is more advantageous over UV-Vis spectrophotometric methods, since the light scattering caused by the lipid media is negligible and was subtracted from each sample spectrum to cancel out any contribution (Figure 3.3A). With exception of the BBB membrane model, where the higher membrane scattering invalidated the use of fluorescence method, it was possible to plot the maximum emission values against the respective membrane model concentration

(Figure 3.3B) without having to derive the spectra, and the resulting data points were fitted to Equation 3.2.

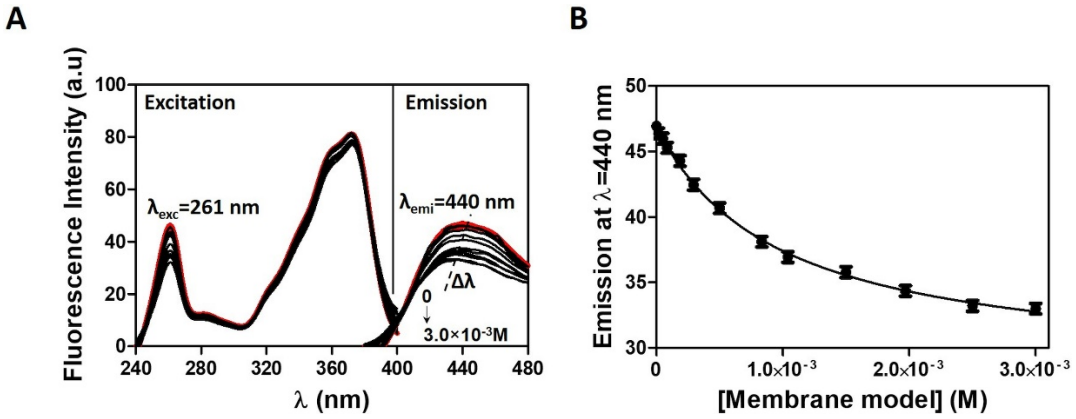

Figure 3.3. (A) Fluorescence emission spectra of CPT ($2x10^{-5}$) with increasing concentrations of cancer membrane models (0 to 3.0 $x10^{-3}$ M) in Acetate buffer pH = 5.8. In red is represented the absorption spectra of CPT in the absence of the cancer membrane models. With the addition of increasing concentrations of membrane model (samples represented in black) there is a shift in λ values. (B) Correspondent nonlinear fitting (Equation 3.1) of fluorescence emission values at λ_{max} = 440 nm as a function of membrane model concentration.

D values were calculated based on both absorbance or fluorescence nonlinear fittings and used to express membrane distribution of CPT as *Log D* values (Table 3.2).

LogD results also indicate that CPT is well distributed within lipid membranes and can thus have large body distribution. The moderate lipophilic CPT profile can also lead to non-specific binding to mucin hydrophobic domains, potentially reducing its diffusion in GIT mucus [55]. Thus, its encapsulation into drug delivery systems (DDS) can be a good approach to improve CPT aqueous solubility, maintain the stability of the molecule across the GIT and, protect the drug from mucin interaction and improve the drug delivery after crossing the mucous layer. *LogD* values are also important deciding the more adequate type of DDS has it has been found strong relations between drug lipophilicity and DDS hydrolipidic balance [56]. Based on the *LogD* determined CPT is more compatible with micelles and albumin nanoparticles.

When the *LogD* values for the membrane models and pH values mimetic of normal and cancer cells are compared, regardless of the method used (derivative UV-Vis spectroscopy or fluorescence spectroscopy), it can be concluded that CPT can distribute between the membrane and aqueous phases with no significant differences, with an average *LogD* value of 2.89 ± 0.23, which is typical of intermediate to lipophilic molecules (0< *LogD* < 3) [28]. A drug's ability to distribute between membrane/aqueous media indicates that it can penetrate cell membranes through the phospholipid polar head region, diffuse through lipophilic

hydrocarbon chains, and emerge into the inner region of phospholipid polar headgroups, which determines its body distribution [53, 54]. Therefore, these logD results also indicate that CPT is well distributed within lipid membranes and can thus have large body distribution.

Table 3.2. Distribution coefficients of CPT obtained in a biphasic membrane/aqueous system.

Membrane Model	pH	Composition	Method	Log D
Cancer cells membranes	5.8	DOPC (25%), CHOL (15%), EPC (31.8%), DOPS (17%), DOPE (8%), CL (2.5%), SM (0.7%)	Derivative UV–Vis spectroscopy	3.14 ± 0.13^{ns}
			Fluorescence spectroscopy	3.01 ± 0.31^{ns}
Normal cells membranes	7.4	DOPC (45%), DOPE (20%), DOPS (20%), CHOL (10%), SM (10%)	Derivative UV–Vis spectroscopy	2.78 ± 0.28^{ns}
			Fluorescence spectroscopy	2.63 ± 0.15^{ns}
		DMPC or DMPG[16, 50]	Fluorescence anisotropy	$2.00 \pm 0.16^{***}$
		DOPC[51]		$1.55 \pm 0.05^{***}$
		DOPG[51]		$1.97 \pm 0.05^{***}$
		Octanol: water[18, 51, 52]	Fluorescence spectroscopy	$1.73 \pm 0.08^{***}$
BBB endothelial membrane	7.4	PC (12.6%), PE (33.1%), PI (4.1%), PS (18.5%) and PA (0.8%)	Derivative spectroscopy	$3.64 \pm 0.15^{***}$

ns: Comparisons between derivative UV-Vis spectroscopy and fluorescence spectroscopy or between cancer cell and normal cells model used in this work were performed using two-way ANOVA with the Sidak's multiple comparisons test and indicate no statistical significance.

***: Comparisons between BBB and normal cells model used in this work or between normal cells model used in this work and normal cells model reported in the literature were performed using one-way ANOVA and indicate statistical significance ($p<0.05$).

When free CPT leaves systemic circulation, mutual associations with various biological interfaces continue to occur until CPT reaches the therapeutic target. The *LogD* obtained in membrane model of normal cells, suggests capacity to permeate cell membranes and low metabolic tendency [28, 57]. The lipophilicity properties of CPT can also influence its biodistribution and bioaccumulation in different tissues. Regarding this, the *LogD* value was

also used to estimate the CPT bioaccumulation. As shown in Equation 3.9, the factors that determine the distribution coefficient of a drug into an organ are related to the blood flow to the organ, the organ's volume, and the drug's distribution into the tissues. Based on the experimental results of CPT distribution in normal membrane cells (Table 3.2) and the described values of blood flow and volume of different organs, it is possible to predict CPT off-target distribution using reported drug profiling models [28] by the following tissues: adrenal glands (61.44 %), thyroid (30.72%), kidneys (3.07%) and heart (3.07%).

Aside from estimating drug distribution in the off-target organs mentioned above, the CPT adipose storage index (Equation 3.10) was calculated to be 2.53 ± 0.12, which accounts for drug distribution in adipose tissue indicating a high distribution in these tissues comparable to other neutral drugs such as clobazam [29]. Furthermore, the brain accumulation index (Equation 3.11), that accounts for the distribution of the CPT in the brain tissues, was calculated, using the *LogD* values in BBB endothelial membrane, to be *LogBB*=2.76 ± 0.06, which suggests potential BBB permeability [58].

The lipophilicity of drugs is typically expressed as a partition of the drug in the octanol/water system, and the reported *LogP* value (value of drug distribution at a pH value where the drug is in its neutral form) of CPT in the octanol/water system was 1.73 ± 0.08 [18, 51, 52] (Table 3.2), whereas the *in silico* calculated *LogD* (at pH 7.4 or 5.8) and *LogP* values in the octanol/water system using Chemaxon® software was 1.52 (Table 3.1), i.e. significantly lower than the distribution *LogD* values determined *in vitro* in the membrane/aqueous system (Table 3.2).

The fact that octanol does not mimic the amphiphilic nature of membranes is a significant disadvantage of theoretical models based on octanol/water biphasic systems. [48, 59, 60]. Contrastingly, because they mimic the hydrophobic core and polar surface of biomembranes, lipid/water systems have been developed as improved cell membrane models and are used to represent drug distribution in biological media [61]. Hydrophobic, H-bonding, dipole-dipole, and electrostatic interactions between drug and membrane are considered using biomimetic membrane models, whereas the octanol/water system can only model nonpolar interactions [62, 63]. Since interactions between the drug and the polar headgroups of membrane lipids are not considered when octanol is used, it is understandable that CPT partitioning in octanol/water systems yielded lower values than partitioning in membrane/water systems. The use of membrane/water systems rather than octanol/water systems is especially important for amphoteric compounds or highly ionized drugs that are charged at physiological pH, and it has been observed that, aside from non-ionic drugs, partitioning values in octanol/water systems do not correlate well with experimental values [64, 65].

When the results for the different mimetic systems of normal membrane cells are compared, the CPT distribution between the membrane and the aqueous medium varies significantly depending on the lipid composition and biophysical properties (Table 3.2). Changes in average area per lipid affect lipid packing density, which is determined by the competition between lipid headgroup repulsion and hydrophobic attraction [10]. Because they have headgroups and tails with similar cross-sectional area, major membrane lipids containing PC and PS have a cylindrical shape. Due to its large headgroup, SM has an inverted-cone shape; thus, SM lipids preferentially adopt the non-lamellar arrangement [10]. Due to their small headgroups, PE, CL, and CHOL have a cone shape and prefer inverted nonlamellar arrangements. Membrane lipids typically self-assemble and form thermodynamically stable aggregates. As a result, any changes in this balance are expected to have an impact on the optimal area per lipid (i.e., their packing) and membrane shape [10]. Changes in lipid composition can affect the curvature and due to differences in molecular shapes and volumes of lipids can ultimately affect permeability of the membrane and alter the distribution of drug in membrane/aqueous systems [10]. Therefore, it is acceptable that CPT presents higher distributions in membrane models containing non-lamellar assemblies of lipids (e.g., DOPE, CL) that can confer more permeable non-lamellar regions [66] than less complex models of lamellar packing like DOPC or DMPC.

Following the quantification of CPT distribution between the lipid and aqueous phases of the membrane model system, it is important to determine where the drug is most likely to be located within the lipid phase of the membrane. Since drug distribution was not significantly different in normal or cancer mimetic membrane models, we chose cancer mimetic membrane models to investigate drug location and assess if the drug is more superficially embedded in the phospholipid headgroups or more profoundly buried in the hydrophobic microenvironment of the phospholipid acyl chains. The CPT location in membrane was evaluated by measuring the steady-state fluorescence of the probe NBD-PE incorporated into cancer cell membrane models in the absence and presence of increasing concentrations of CPT. NBD-PE was used as a molecular ruler as previous reports have shown that contrary to other NBD based probes the fluorescent probe group does not project into the external aqueous phase [67] and it is well-known that NBD-PE locate at the membrane interface approximately between 19 and 20 Å from the center of the bilayer [68]. CPT is a fluorescent compound that emits between 400 and 550 nm (λmax of 431 nm) when excited at 360 nm, whereas NBD-PE is a fluorescent probe that emits between 500 and 600 nm (λmax of 530 nm) when excited at 465 nm. Fluorescence resonance energy transfer (FRET) was used to infer CPT location because it occurs when donor molecules (CPT) emit at shorter wavelengths that overlap with the acceptor's absorption spectrum (NBD-PE) [69]. FRET is only sensitive for very short distances (1.5 to

6 nm) between each donor/acceptor pair [69]. As a result of the occurrence of FRET, it was possible to conclude that the donor CPT was located close to the acceptor NBD chromophores, which ultimately suggests that CPT was inserted at the membrane and close to the membrane interface, similar to NBD-PE. Figure 3.4A demonstrates the presence of FRET between CPT and NBD-PE.

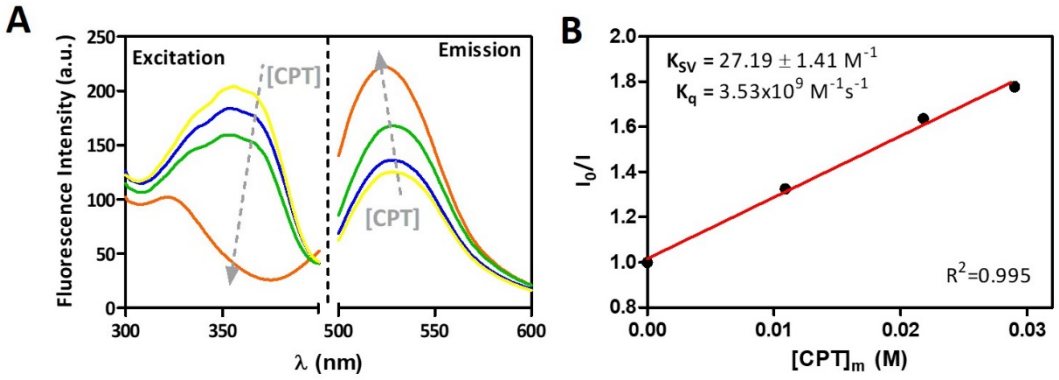

Figure 3.4. (A) Fluorescence excitation spectra of CPT ($[CPT]_T$ of 0 to 4x10^{-5} M) added to cancer membrane models (3.0×10^{-2} M) labelled with NBD-PE probe and correspondent emission spectra of the probe (λ exc=360 nm). (B) Stern-volmer plot of fluorescence quenching as a function of membrane concentrations of CPT calculated according to Equation 3.6.

The excitation wavelength was set to 360 nm, which is the maximum excitation wavelength for CPT. The fluorescence excitation of the donor (CPT) is decreasing in the spectra presented, and the emission intensity of the acceptor (NBD-PE) is increasing, indicating that an energy transfer is occurring from CPT to NBD-PE (Figure 3.4A). This means that when CPT is excited, the fluorescence emitted by CPT can excite the NBD-PE probe, which acts as the acceptor emitting fluorescence. The transfer efficiency can be determined by steady-state measurements of the extent of donor quenching due to the acceptor [25]. The extent of donor fluorescence quenching can in turn be calculated using a Stern-Volmer plot (Figure 3.4B) according to Equation 3.3. After determining the *LogD* values of CPT in the membrane model, the effective concentrations of the drug in the membrane model system – $[CPT]_m$ – were calculated using Equation 3.4. The Stern-Volmer linear plot (Figure 3.4B) can be used to calculate the Stern-Volmer constant (K_{SV} = 27.19 ± 1.41 M^{-1}) as well as the bimolecular quenching constant (Kq = 3.53x10^9 $M^{-1}s^{-1}$) which reflects quenching efficiency or fluorophore accessibility to the quencher (Equation 3.5). The obtained Kq value, is close to the reported diffusion-controlled quenching in lipid membranes, which typically results in values of Kq near 1.1 x 10^9 $M^{-1}s^{-1}$ [25]. This also confirms that CPT is inserted at the membrane and close to the membrane interface.

3.4.3. The CPT effect on membrane biophysical properties

Aside from investigating how CPT distributes inside a membrane model, it is also critical to investigate how this drug may influence the biophysical integrity of such models. Changes in parameters like membrane fluidity and phospholipid order and/or packing play a key role in the conservation of membrane dynamics, which serves the most essential cellular functions, and changes in these parameters caused by drugs may provide useful details on their therapeutic abilities and potential toxic effects at the membrane level [9, 26]. Previous *LogD* studies have focused on model systems comprising relevant lipid mixtures to mimic drug distribution in different cell membranes (Table 3.2). However, we chose a pure DMPC model for studying membrane biophysical properties since it adopts the fluid lamellar phase across a broad range of hydrations and temperatures and allows simulating both organized and disordered phases found in membrane domains. Model membranes like this, which are made up of a specific class of purified lipids, are often used *in vitro* to mimic the behavior of biological membranes [70]. These simple membrane models are a robust and repeatable platform with physical properties close to those of most cells, allowing for clear and quantitative study of phenomena in a membrane setting [70]. While these models are simplified in comparison to the mimetic models used in distribution experiments, they are a viable alternative for *in vitro* characterization of CPT effects in both more ordered (gel phase, Lβ) and disordered (fluid phase, Lα) membrane phases.

There are distinct ordered phases that can disperse light of varying intensities during the lipid phase transition [71]. As a result, within a temperature range and utilizing DLS, the average number of photons dispersed (MCR) by the lipid membrane system can be monitored [71]. This method of calculation yields a sigmoidal profile, as seen in Figure 3.5, which presents the results of MCR obtained with DMPC membrane model in the presence and absence of CPT fitted by Equation 3.8. This equation can be used to calculate the parameters *B* and *Tm*, which describe the transition of lipid bilayers from the Lβ to the Lα phase.

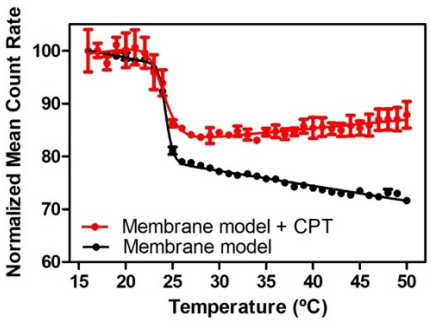

Figure 3.5. Normalized MCR of DMPC membrane models in absence (●) and in the presence of CPT (●) as a function of temperature. Each point corresponds to the mean value ± standard deviation of three experiments. Continuous lines are the best fits according to Equation 3.8.

Tm of DMPC membrane models was determined to be 24.29 ± 0.05 °C in agreement with the transition temperature reported for this phospholipid membrane [72]. The transition between the gel and the fluid phase of DMPC presented a *B* of 670.4 ± 62.21 indicating a cooperative transition, as expected for the pure lipid system. The addition of CPT to the membrane mimetic system has little effect on *Tm* (24.06 ± 0.16 °C) meaning that does not provoke a membrane fluidization but does induce a significant decrease of *B* to 303.9 ± 42.78 ($P<0.001$). Since the cooperative unit that undergoes the transition is primarily dominated by certain carbons, these findings point to a distribution of CPT at the polar headgroup area and at the C1-C8 level of the acyl chains of membrane phospholipids [73]. The interaction at this level explains why the main transition's cooperativity is reduced and shows that the drug is not homogeneously dispersed inside the membrane, otherwise the phase transition will occur with high cooperativity. Nonetheless, the limited influence of CPT on membrane fluidization observed is most likely attributable to the drug's planar nature (Figure 3.1), which enables it to intercalate between the phospholipids of the bilayer without disrupting its integrity significantly.

As previously stated, drug-biomembrane interactions may affect membrane biophysical properties such as fluidity and phospholipid order and/or packing. After determining that CPT has little effect on membrane fluidity, SAXS and WAXS were used to investigate the long-range bilayer order (d_L from SAXS) and the short-range bilayer order that determines hydrocarbon chain packing (d_S from WAXS) after CPT was added to DMPC bilayers. In Figure 3.6 are presented the SAXS diffraction patterns of DMPC in the presence and in the absence of CPT at each characteristic lipid phase: DMPC is in the gel phase (Lβ' phase) at 14 °C; the ripple gel phase (Pβ phase) can be found at 20.6 °C; and the DMPC bilayer is in the fluid phase (Lα phase) at 44.8 °C. Through viewing the graphical illustrations in conjunction with the diffraction patterns, it is possible to envision the effect of CPT in the long-range bilayer order, i.e., its effect on the thickness of the bilayer plus the water layer.

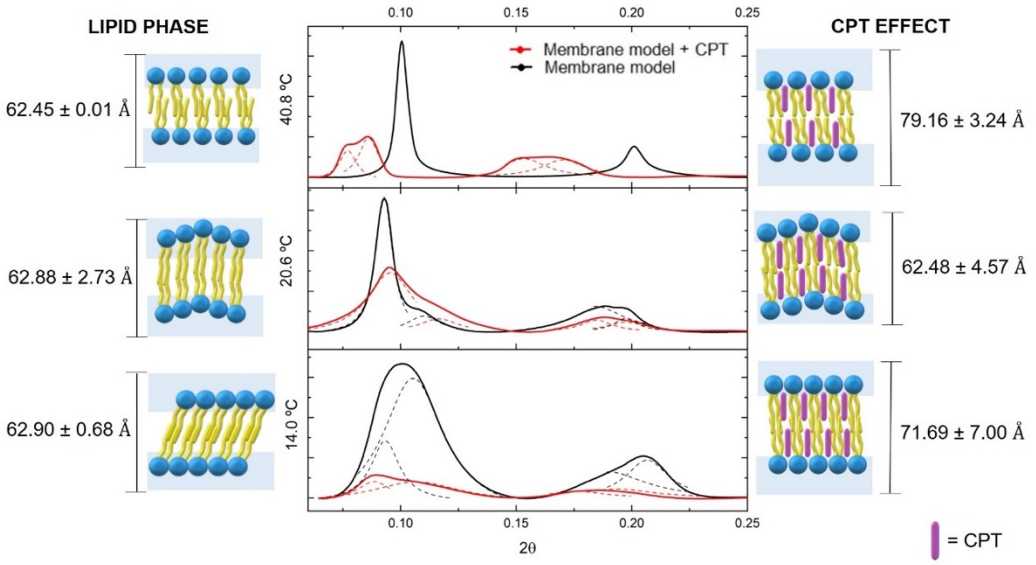

Figure 3.6. Small angle X-ray diffraction (SAXS) patterns of DMPC (black) or DMPC containing CPT (red) measured in the Lβ′ (14.0 °C), Pβ (20.6 °C) and Lα (40.8 °C) phases of DMPC. Solid lines give the best fit of the Lorentzian' s analysis model (dashed lines) to the scattered intensities. A model of drug–membrane interaction is proposed for each diffractogram together with the resultant d_L values.

Fully hydrated DMPC bilayer alone is characterized at the Lβ' phase by presenting a tilted bilayer with a ratio distance between Bragg peaks characteristic of lamellar packing (1:2:3). The Bragg peaks spacing was used to calculate a d_L of 62.90 ± 0.68 Å and a correlation length of 547.00 ± 89.35 Å.

When the drug was inserted into the bilayer, there was a significant decrease in correlation length (258.00 ± 42.02 Å, $p<0.05$) and an increase in d_L (71.69 ± 7.00 Å). The membrane insertion of CPT into the bilayer at C1-C8 level was determined using location and transition temperature studies. Thus, the increase in bilayer thickness could be attributed to the proposed CPT location causing a change in the area requirement of the headgroups, allowing the chains to lose their tilt and be oriented upright. This stretched position of the acyl chains may account for some of the increase in d_L values. Indeed, when the hydrocarbon chains of the fatty acids that comprise the phospholipids are rigidly packed, C-C bonds are in an *all-trans* conformation, allowing the hydrocarbon chains to be accommodated in a minimum volume. The hydrocarbon chains are organized in CH_2 groups with distances of 1.26 Å, while the distance between the C-C bonds in the terminal CH_3 group is 1.46 Å, giving a chain length of 19.1 Å considering the 14 C atoms of myristic acid of DMPC. This length corresponds to hydrocarbon stretched chain, however at the Lβ' phase fully hydrated DMPC have hydrocarbon chains that are tilted by approximately 32.3° relative to the bilayer plane [74]. Given that the chains are tilted, the thickness of the bilayer will be 19.1 Å × cos (32.3°) = 16.1 Å, and the difference in thickness between the stretched

and tilted hydrocarbon chains is given by 19.1 Å – 16.1 Å = 3.0 Å /monolayer, i.e., 6.0 Å /bilayer. This means that the loss of tilt caused by CPT insertion within the lipid membrane would result in a d_L increase of 6.0 Å. However, the addition of CPT resulted in an 8.8 Å d_L increase, indicating that, in addition to changing the lipid packing from pseudohexagonal (tilted) to hexagonal packing by loss of tilt angle, CPT may also induce an increase in the water layer, which will be confirmed later by WAXS measurements.

At the Pβ phase, phospholipids in DMPC system in the absence of CPT also lost their tilt, however with the undulated ripple effect, two *dL* values are observed with an average value of 62.88 ± 2.73 Å and a correlation length of 855 ± 134.68 Å. The rippled undulated phase is maintained after CPT insertion, with an average *dL* value of 62.48 ± 4.57, which is similar to that found in the lipid membrane without the drug. The lack of changes in the *dL* values of this phase can be explained by the fact that the phospholipids in the ripple lipid phase are less tightly packed than in the gel phase, giving a planar drug like CPT a better chance of penetrating the bilayer without disrupting the hydrocarbon chains' characteristic packing. Nonetheless, despite maintaining the *dL* and lipid packing, the presence of CPT in the lipid bilayer can be identified by a significant decrease in the correlation length to 431.00 ± 36.72 Å ($p<0.05$), indicating a noticeable breakdown of the multilamellar correlation and indicating a disruption effect of this drug on the membrane structure.

The phospholipids are less ordered in the Lα phase, and the relaxation of hydrocarbon chains promotes phospholipid separation. As a result, the incorporation of CPT is facilitated, and the *dL* (from 62.45 ± 0.01 Å to 79.16 ± 3.24 Å) and the correlation length (from 1549.00 ± 275.08 Å to 664.00 ± 263.68 Å, $p<0.01$) change significantly. At the fluid phase, the increase in the *dL* values cannot be justified by the packing change causing elongation of the hydrocarbon chain; thus, drug insertion is expected to cause an increase in the hydration layer rather than an increase in the bilayer thickness. Furthermore, the drug causes a significant decrease in correlation length during this phase as well. The overall effect of the drug decreasing correlation length observed in all lipid phases indicates a disrupting effect in the global molecular organization of the multilayer stack of lipid bilayer.

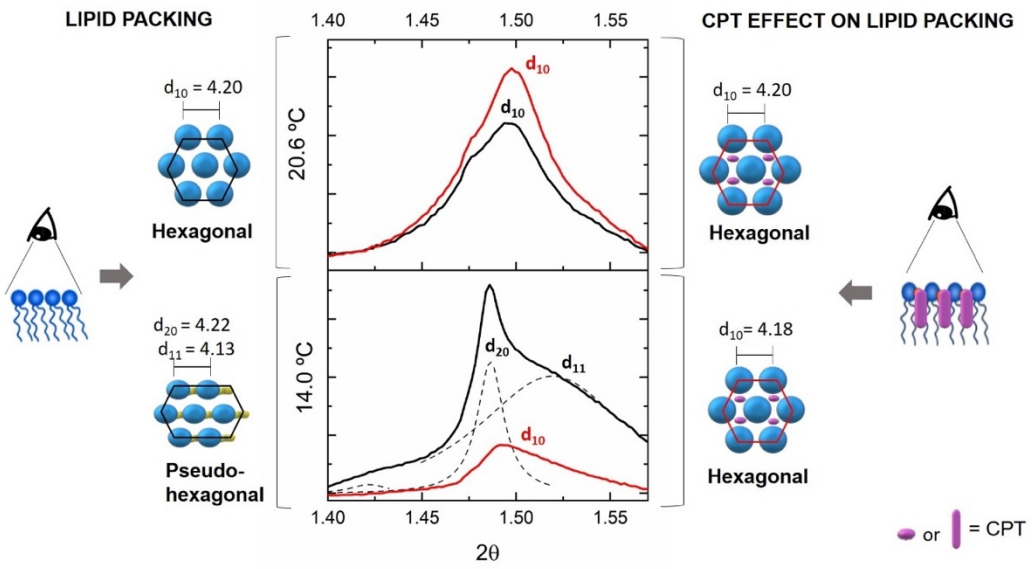

Figure 3.7. Wide angle X-ray diffraction (WAXS) patterns of DMPC (black) or DMPC containing CPT (red) measured in the Lβ′ (14.0 °C) and Pβ (20.6 °C) phases of DMPC. Solid lines give the best fit of the Lorentzian' s analysis model (dashed lines) to the scattered intensities. A model of drug–membrane interaction is proposed for each diffractogram together with the resultant ds values.

The WAXS pattern is shown in Figure 3.7 only for the Lβ' and Pβ phases, because the freedom degree of the headgroups is so high at the Lα phase that WAXS produces overly broad diffractograms and there are no defined *ds* for this phase. The WAXS pattern of DMPC without drug in the Lβ', exhibits the characteristic double Bragg peak correspond to two *ds* values (d20 = 4.22 Å and d11 = 4.13 Å) caused by tilted phospholipids packed in a pseudohexagonal chain lattice. The addition of CPT results in a single Bragg peak, which confirms the loss of tilt effect observed by SAXS studies resulting in a change in the lipid packing to a hexagonal chain lattice, as well as a non-significant decrease of *ds* (d10 = 4.18 Å).

As observed in SAXS, the incorporation of CPT in the DMPC Pβ phase is facilitated and did not change the lattice parameters of the DMPC headgroups, yielding a *ds* value of 4.20 Å in both the presence and absence of CPT.

Overall, these findings suggest that CPT influences the biophysical properties of lipid membranes, particularly in the more ordered domains mimicked by the Lβ' phase. Drug incorporation within the membrane phospholipids of these ordered phases causes loss of tilt angle, changes in lipid packing from pseudohexagonal to hexagonal lattice, and increased hydration of the headgroup region. Given that cell membrane ordered domains and lipid packing are critical for the functioning of several integrated proteins and receptors, these biophysical effects of CPT may imply membrane impairment and cell toxicity [9]. This fact justifies the need to encapsulate CPT in nanocarrier systems to avoid membrane

impairment caused by free drug distribution. Indeed, our previous research showed that incorporating CPT into a nanocarrier system like SLN could preserve the membrane's chain packing parameters [75].

3.4.4. Plasma protein binding of camptothecin and prediction of biodistribution parameters

After considering GIT absorption it is important to consider other physiological barriers like plasma proteins. As the drug enters the systemic circulation, it may be exposed to plasma proteins, where their primary purpose is to transport exogenous molecules across the body. If the drug-plasma protein interaction is not balanced and reversible, biodistribution problems may be triggered due to the either too low or too high affinity of a drug to plasma proteins like HSA [76]. Thus, CPT biodistribution is highly dependent not only on its interaction with cell membranes, but also on its freely and bound forms present in systemic circulation. In this regard, serum proteins such as HSA function as vehicles for transporting endogenous compounds, thereby limiting the unbound fraction available for subsequent tissue distribution. As a result, studying drug affinity to HSA is also important for understanding its biodistribution and overall pharmacokinetic behavior.

The fluorescence of HSA is mainly due to the presence of two intrinsic fluorophores, tryptophan and tyrosine residues, and changes in HSA fluorescence are associated with its interaction or binding to a variety of quenchers. Monitoring HSA fluorescence in the absence and in the presence of a drug is a common method for determining the drug's affinity for this plasmatic protein.

The fluorescence emission spectra of HSA solutions in the presence of increased amounts of CPT are shown in Figure 3.8.

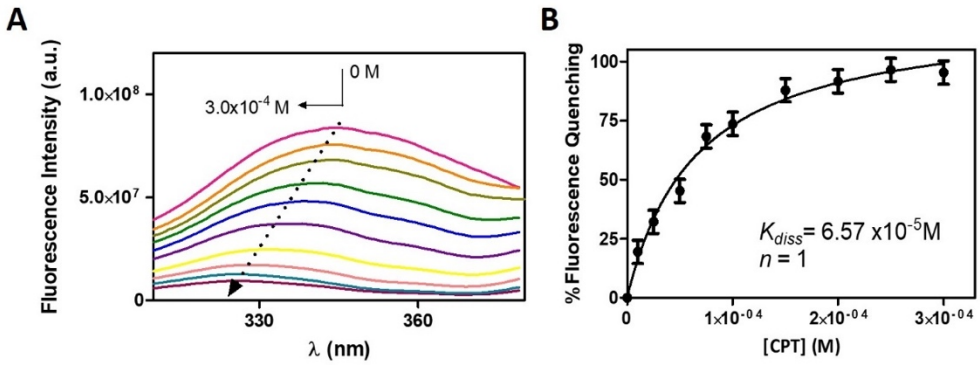

Figure 3.8. (A) Fluorescence spectra of HSA (2.0×10^{-6} M) in the presence of increasing CPT concentrations (0 to 3.0×10^{-4} M) at 37 °C. (B) Binding isotherm plot of CPT-HSA. The non-linear fit

to the experimental data was made using Equation 3.6 and allowed to determine the dissociation constant (K_{diss}) and the number of binding sites (n).

As the CPT concentration increased, there was a clear decrease in the intensity of the HSA fluorescence emission (fluorescence quenching). A shift in the maximum emission band to shorter wavelengths is also visible as a result of the fluorescence quenching. Both observations point to a strong interaction between CPT and HSA, with the possibility of a complex formation. Emission spectral shifts can be interpreted as a change in the surrounding hydrophobicity of the chromophore because fluorescence emission is highly dependent on the local microenvironment. Typically, hypsochromic shifts (or blue shifts) are associated with decreased polarity, indicating that HSA complexation with CPT has resulted in the formation of a hydrophobic environment around the tryptophan and tyrosine residues. Similar observations were noticed by Yang *et al*. when they studied the binding of CPT to BSA. In the same study the authors collected information provided by several methodologies about the drug-membrane binding and concluded that the formation of the CPT-BSA complex occurs mainly through electrostatic interactions and hydrogen bonds. To the fluorescence quenching data, a non-linear fitting was applied (Equation 3.6) from which it was possible to determine that CPT binds to a single HSA site (n=1) with a binding constant (K_{bind}=1.52 ± 0.26 × 10^4 M^{-1}) and a negative value of Gibbs free energy (ΔG_{bind}=-5.93 ± 0.10 kcal·mol^{-1}) suggesting that drug and serum protein associate spontaneously (Equation 3.7). The HSA–CPT binding constant falls within the range of previously published binding constants of CPT in carboxylate or lactone form for the interaction of HSA with CPT (5.5 × 10^3 to 1.2 × 10^6 M^{-1}) [13] and is also close to the binding constant reported by Li *et al.* for the interaction of CPT with BSA (K_{bind}=3.72 × 10^4 M^{-1}) [17]. Based on K_{bind} values, a PPB of 91.95% (Equation 3.14) was calculated indicating that the majority of CPT is bound to HSA, leaving only 8.05% of the free drug available for distribution to the tissues. The magnitude of these values indicates that CPT and HSA have a strong interaction [25]. Additional biodistribution parameters of CPT were also determined using the values of PPB to HSA and *LogD* values (Table 3.2 normal cells) obtained. The unbound CPT fraction in plasma and tissues were respectively determined as f_u=0.081 (Equation 3.13) and f_{ut}=0.0054 (Equation 3.15). These parameters were used to obtain VD_{SS}=5.75 ± 0.93 L·Kg^{-1} (Equation 3.12), which can be translated in a high volume of distribution [78]. The high *VDss* value obtained agrees with the high *ASI* value obtained. Indeed, drugs with VD_{SS} values between 1 and 5 L·Kg^{-1} are characterized as having large volumes of distribution due to affinity for adipose tissues which hampers their elimination from the body. Moreover, the VD_{SS} value calculated from *in vitro LogD* and PPB values agrees with the *in vivo* VD_{SS}

value of 5.16 ± 1.25 $L \cdot Kg^{-1}$, obtained from the reported value of 190 ± 46 $L \cdot m^{-2}$ [78], considering the average values of body surface (1.9 m^2) and body weight (70 kg).
Considering the high volume of distribution as well as the bioaccumulated sites, including the *ASI* value, it is possible to conclude that CPT will face potential clearance problems. Because of the compound's tendency to accumulate in fat tissue and the high value of *VDss*, the CPT half-life can be enhanced, reducing its elimination rate and, its excretion from the body is hindered [77, 79].

3.5. Conclusion

Gathering all the obtained information, it is possible to identify potential issues in the oral administration of CPT at absorption level and, even when it is absorbed, its large biodistribution can result in potential lack of selectivity. This lack of selectivity for the therapeutic target is also demonstrated by the lack of significant differences in *LogD* of CPT in cancer cell and normal cell membrane models. Therefore, and as previously referred, encapsulation of CPT in DDS could present a promising alternative to overcome the here reported pharmacokinetic issues. Suggested DDS systems could be albumin nanoparticles or micelles containing lipid moieties where CPT can be distributed and polymeric coatings to promote a balance of GIT mucoadhesion and mucopenetration and for stealth purposes. Additionally, CPT encapsulation into nanosystems could be also an alternative to reach the tumor site in a more selective way by the EPR effect.

References

1. Wall, M.E., et al., *Plant antitumor agents. I. The isolation and structure of camptothecin, a novel alkaloidal leukemia and tumor inhibitor from camptotheca acuminata.* Journal of the American Chemical Society, 1966. **88**(16): p. 3888-3890.
2. Kohn, K.W. and Y. Pommier, *Molecular and biological determinants of the cytotoxic actions of camptothecins: perspective for the development of new topoisomerase I inhibitors.* Annals of the New York Academy of Sciences, 2000. **922**(1): p. 11-26.
3. Moukharskaya, J. and C. Verschraegen, *Topoisomerase 1 inhibitors and cancer therapy.* Hematology/Oncology Clinics of North America, 2012. **26**(3): p. 507-525.
4. Kruszewski, S. and D. Kruszewska, *Fluorescence spectroscopy in camptothecins studies.* Acta Physica Polonica B, 2010. **118**: p. 99-102.
5. Bom, D., et al., *The highly lipophilic DNA topoisomerase I inhibitor DB-67 displays elevated lactone levels in human blood and potent anticancer activity.* Journal of Controlled Release, 2001. **74**(1-3): p. 325-333.
6. Hu, Y.-J., et al., *Binding of anti-inflammatory drug cromolyn sodium to bovine serum albumin.* International Journal of Biological Macromolecules, 2006. **39**(4-5): p. 280-285.
7. Rösler, A., G.W. Vandermeulen, and H.-A. Klok, *Advanced drug delivery devices via self-assembly of amphiphilic block copolymers.* Advanced Drug Delivery Reviews, 2012. **64**: p. 270-279.
8. Lúcio, M., et al., *Interactions between oxicams and membrane bilayers: an explanation for their different COX selectivity.* Medicinal Chemistry, 2006. **2**(5): p. 447-456.
9. Lucio, M., J. Lima, and S. Reis, *Drug-membrane interactions: significance for medicinal chemistry.* Current Medicinal Chemistry, 2010. **17**(17): p. 1795-1809.
10. Peetla, C., S. Vijayaraghavalu, and V. Labhasetwar, *Biophysics of cell membrane lipids in cancer drug resistance: Implications for drug transport and drug delivery with nanoparticles.* Advanced Drug Delivery Reviews, 2013. **65**(13-14): p. 1686-1698.
11. Tian, S., et al., *The application of in silico drug-likeness predictions in pharmaceutical research.* Advanced Drug Delivery Reviews, 2015. **86**: p. 2-10.
12. Cheng, F., et al., *In silico ADMET prediction: recent advances, current challenges and future trends.* Current Topics in Medicinal Chemistry, 2013. **13**(11): p. 1273-1289.

13. Mi, Z. and T.G. Burke, *Marked interspecies variations concerning the interactions of camptothecin with serum albumins: a frequency-domain fluorescence spectroscopic study.* Biochemistry, 1994. **33**(42): p. 12540-12545.
14. Fleury, F., et al., *Camptothecin-binding site in human serum albumin and protein transformations induced by drug binding.* FEBS letters, 1997. **411**(2-3): p. 215-220.
15. Burke, T.G. and Z. Mi, *The structural basis of camptothecin interactions with human serum albumin: impact on drug stability.* Journal of Medicinal Chemistry, 1994. **37**(1): p. 40-46.
16. Stefan, K., *Camptothecins affinity to HSA and membranes determined by fluorescence anisotropy measurements.* Optica Applicata, 2002. **32**(4).
17. Li, Q., et al., *Binding interactions of water-soluble camptothecin derivatives with bovine serum albumin.* Spectrochimica Acta Part A: Molecular and Biomolecular Spectroscopy, 2012. **86**: p. 124-130.
18. Tang, P.K., et al., *Interaction of camptothecin with model cellular membranes.* Journal of Chemical Theory and Computation, 2020. **16**(5): p. 3373-3384.
19. Lawrence, X.Y., *Pharmaceutical quality by design: product and process development, understanding, and control.* Pharmaceutical Research, 2008. **25**(4): p. 781-791.
20. Zhang, H., *Thin-film hydration followed by extrusion method for liposome preparation*, in *Liposomes*. 2017, Springer. p. 17-22.
21. Lúcio, M., et al., *Influence of some anti-inflammatory drugs in membrane fluidity studied by fluorescence anisotropy measurements.* Physical Chemistry Chemical Physics, 2004. **6**(7): p. 1493-1498.
22. Magalhães, L.M., et al., *High-throughput microplate assay for the determination of drug partition coefficients.* Nature Protocols, 2010. **5**(11): p. 1823-1830.
23. Fernandes, E., et al., *Spectroscopic studies as a toolbox for biophysical and chemical characterization of lipid-based nanotherapeutics.* Frontiers in Chemistry, 2018. **6**: p. 323.
24. Fernandes, E., et al., *A molecular biophysical approach to diclofenac topical gastrointestinal damage.* International Journal of Molecular Sciences, 2018. **19**(11).
25. Lakowicz, J.R., *Principles of Fluorescence Spectroscopy*. 3 ed. 2006: Springer US. 954.
26. Fernandes, E., et al., *A molecular biophysical approach to diclofenac topical gastrointestinal damage.* International Journal of Molecular Sciences, 2018. **19**(11): p. 3411.

27. Carvalho, A.M., et al., *Prediction of paclitaxel pharmacokinetic based on in vitro studies: Interaction with membrane models and human serum albumin.* International Journal of Pharmaceutics, 2020. **580**: p. 119222.
28. Di, L. and E.H. Kerns, *Drug-like properties: concepts, structure design and methods from ADME to toxicity optimization*. 2015: Academic press.
29. Seydel, J.K. and M. Wiese, *Drug-membrane interactions: analysis, drug distribution, modeling*. Vol. 15. 2009: John Wiley & Sons.
30. van de Waterbeemd, H. and M. Kansy, *Hydrogen-bonding capacity and brain penetration.* CHIMIA International Journal for Chemistry, 1992. **46**(7-8): p. 299-303.
31. Liu, X., et al., *Development of a computational approach to predict blood-brain barrier permeability.* Drug Metabolism and Disposition, 2004. **32**(1): p. 132-139.
32. Korzekwa, K. and S. Nagar, *Drug distribution part 2. Predicting volume of distribution from plasma protein binding and membrane partitioning.* Pharmaceutical Research, 2017. **34**(3): p. 544-551.
33. Lombardo, F., et al., *Prediction of volume of distribution values in humans for neutral and basic drugs using physicochemical measurements and plasma protein binding data.* Journal of Medicinal Chemistry, 2002. **45**(13): p. 2867-2876.
34. Musteata, F.M., *Clinical utility of free drug monitoring.* Therapeutic Drug Monitoring: Newer Drugs and Biomarkers, 2012: p. 75-101.
35. Waters, N.J., et al., *Validation of a rapid equilibrium dialysis approach for the measurement of plasma protein binding.* Journal of Pharmaceutical Sciences, 2008. **97**(10): p. 4586-4595.
36. Pignatello, R., et al., *Biomembrane models and drug-biomembrane interaction studies: Involvement in drug design and development.* Journal of Pharmacy and Bioallied Sciences, 2011. **3**(1): p. 4.
37. Lipinski, C.A., et al., *Experimental and computational approaches to estimate solubility and permeability in drug discovery and development settings.* Advanced Drug Delivery Reviews, 1997. **23**(1-3): p. 3-25.
38. Clark, D.E., *Rapid calculation of polar molecular surface area and its application to the prediction of transport phenomena. 1. Prediction of intestinal absorption.* Journal of Pharmaceutical Sciences, 1999. **88**(8): p. 807-814.
39. Mandic, Z., *Physico Chemical Methods in Drug Discovery and Development*. 2012: IAPC Publishing.
40. Martínez-Martínez, M., et al., *Covalently crosslinked organophosphorous derivatives-chitosan hydrogel as a drug delivery system for oral administration of camptothecin.* European Journal of Pharmaceutics and Biopharmaceutics, 2019. **136**: p. 174-183.

41. Benet, L.Z., F. Broccatelli, and T.I. Oprea, *BDDCS applied to over 900 drugs.* AAPS PharmSciTech, 2011. **13**(4): p. 519-547.
42. Schanker, L., *Absorption of drugs from the gastrointestinal tract*, in *Concepts in Biochemical Pharmacology*. 1971, Springer. p. 9-24.
43. Kim, J.-H., et al., *Preformulation studies of a novel camptothecin anticancer agent, CKD-602: physicochemical characterization and hydrolytic equilibrium kinetics.* International Journal of Pharmaceutics, 2002. **239**(1-2): p. 207-211.
44. Rahman, S., D. Patel, and M. Savva, *Physicochemical characterization of 9-aminocamptothecin in aqueous solutions.* AAPS PharmSciTech, 2014. **15**(1): p. 223-229.
45. Dickins, M. and H. van de Waterbeemd, *Simulation models for drug disposition and drug interactions.* Drug Discovery Today: Biosilico, 2004. **2**(1): p. 38-45.
46. Choi, G.-W., Y.-B. Lee, and H.-Y. Cho, *Interpretation of non-clinical data for prediction of human pharmacokinetic parameters: in vitro-in vivo extrapolation and allometric scaling.* Pharmaceutics, 2019. **11**(4): p. 168.
47. Poulin, P. and F.P. Theil, *Prediction of pharmacokinetics prior to in vivo studies. 1. Mechanism-based prediction of volume of distribution.* Journal of Pharmaceutical Sciences, 2002. **91**(1): p. 129-156.
48. Fernandes, E., et al., *Spectroscopic studies as a toolbox for biophysical and chemical characterization of lipid-based nanotherapeutics.* Frontiers in Chemistry, 2018. **6**: p. 323.
49. Lin, B., et al., *Acidic pH and high-H2O2 dual tumor microenvironment-responsive nanocatalytic graphene oxide for cancer selective therapy and recognition.* ACS Applied Materials & Interfaces, 2019. **11**(12): p. 11157-11166.
50. Sørbotten, N. and S. Kruszewski, *Fluorescence spectroscopy in a study of anticancer drugs: 7-tert-butyldimethylsilyl-camptothecin and 7-tert-butyldimethylsilyl-10-[4-(1-piperidino)-1-piperidino] carbonyloxycamptothecin.* Medical Research Journal, 2013. **1**(1): p. 23-30.
51. Selvi, B., S. Patel, and M. Savva, *Physicochemical characterization and membrane binding properties of camptothecin.* Journal of Pharmaceutical Sciences, 2008. **97**(10): p. 4379-4390.
52. Leo, A., C. Hansch, and D. Elkins, *Partition coefficients and their uses.* Chemical Reviews, 1971. **71**(6): p. 525-616.
53. Pignatello, R., et al., *Biomembrane models and drug-biomembrane interaction studies: Involvement in drug design and development.* Journal of Pharmacy and Bioallied Sciences, 2011. **3**(1): p. 4-14.

54. Bemporad, D., J.W. Essex, and C. Luttmann, *Permeation of small molecules through a lipid bilayer: a computer simulation study.* Journal of Physical Chemistry B, 2004. **108**(15): p. 4875-4884.
55. Sigurdsson, H.H., J. Kirch, and C.-M. Lehr, *Mucus as a barrier to lipophilic drugs.* International Journal of Pharmaceutics, 2013. **453**(1): p. 56-64.
56. Norvaisas, P. and A. Ziemys, *The role of payload hydrophobicity in nanotherapeutic pharmacokinetics.* Journal of Pharmaceutical Sciences, 2014. **103**(7): p. 2147-2156.
57. Di, L. and E. Kerns, *Pharmaceutical profiling in discovery research.* Current Opinion in Chemical Biology, 2003. **7**: p. 402-408.
58. Oliveira, C., et al., *Benzoic acid-derived nitrones: A new class of potential acetylcholinesterase inhibitors and neuroprotective agents.* European Journal of Medicinal Chemistry, 2019. **174**: p. 116-129.
59. Chapeaux, A., et al., *Liquid phase behavior of ionic liquids with water and 1-octanol and modeling of 1-octanol/water partition coefficients.* Journal of Chemical & Engineering Data, 2007. **52**(6): p. 2462-2467.
60. Lucio, M., J.L. Lima, and S. Reis, *Drug-membrane interactions: significance for medicinal chemistry.* Current Medicinal Chemistry, 2010. **17**(17): p. 1795-809.
61. Giaginis, C. and A. Tsantili-Kakoulidou, *Alternative measures of lipophilicity: from octanol–water partitioning to IAM retention.* Journal of Pharmaceutical Sciences, 2008. **97**(8): p. 2984-3004.
62. Azevedo, A.M.O., et al., *Imidazolium ionic liquids as solvents of pharmaceuticals: Influence on HSA binding and partition coefficient of nimesulide.* International Journal of Pharmaceutics, 2013. **443**(1–2): p. 273-278.
63. Brittes, J., et al., *Effects of resveratrol on membrane biophysical properties: relevance for its pharmacological effects.* Chemistry and Physics of Lipids, 2010. **163**(8): p. 747-754.
64. Hodges, G., et al., *A comparison of log Kow (n-octanol–water partition coefficient) values for non-ionic, anionic, cationic and amphoteric surfactants determined using predictions and experimental methods.* Environmental Sciences Europe, 2019. **31**(1): p. 1.
65. Magalhaes, L.M., et al., *High-throughput microplate assay for the determination of drug partition coefficients.* Nature Protocols, 2010. **5**(11): p. 1823-1830.
66. Pennington, E.R., et al., *Distinct membrane properties are differentially influenced by cardiolipin content and acyl chain composition in biomimetic membranes.* Biochimica et Biophysica Acta-Biomembranes, 2017. **1859**(2): p. 257-267.

67. Raghuraman, H., S. Shrivastava, and A. Chattopadhyay, *Monitoring the looping up of acyl chain labeled NBD lipids in membranes as a function of membrane phase state.* Biochimica et Biophysica Acta-Biomembranes, 2007. **1768**(5): p. 1258-1267.
68. Mukherjee, S., et al., *Organization and dynamics of N-(7-nitrobenz-2-oxa-1, 3-diazol-4-yl)-labeled lipids: a fluorescence approach.* Chemistry and Physics of Lipids, 2004. **127**(1): p. 91-101.
69. Loura, L. and M.J. Prieto, *FRET in membrane biophysics: An overview.* Frontiers in Physiology, 2011. **2**: p. 82.
70. Casey, D., et al., *Amphiphilic drug interactions with model cellular membranes are influenced by lipid chain-melting temperature.* Journal of The Royal Society Interface, 2014. **11**(94): p. 20131062.
71. Michel, N., et al., *Determination of phase transition temperatures of lipids by light scattering.* Chemistry and Physics of Lipids, 2006. **139**(1): p. 11-19.
72. Lúcio, M., et al., *Effect of anti-inflammatory drugs in phosphatidylcholine membranes: a fluorescence and calorimetric study.* Chemical Physics Letters, 2009. **471**(4-6): p. 300-309.
73. Jain, M.K. and N.M. Wu, *Effect of small molecules on the dipalmitoyl lecithin liposomal bilayer: III. Phase transition in lipid bilayer.* The Journal of Membrane Biology, 1977. **34**(1): p. 157-201.
74. Tristram-Nagle, S. and J.F. Nagle, *Lipid bilayers: thermodynamics, structure, fluctuations, and interactions.* Chemistry and Physics of Lipids, 2004. **127**(1): p. 3-14.
75. Martins, S.M., et al., *Brain targeting effect of camptothecin-loaded solid lipid nanoparticles in rat after intravenous administration.* European Journal of Pharmaceutics and Biopharmaceutics, 2013. **85**(3): p. 488-502.
76. Lambrinidis, G., T. Vallianatou, and A. Tsantili-Kakoulidou, *In vitro, in silico and integrated strategies for the estimation of plasma protein binding. A review.* Advanced Drug Delivery Reviews, 2015. **86**: p. 27-45.
77. Ballard, P., et al., *Metabolism and pharmacokinetic optimization strategies in drug discovery.* Drug Discovery and Development-E-Book: Technology in Transition, 2012: p. 135.
78. Gerrits, C., et al., *Phase I and pharmacological study of the new topoisomerase I inhibitor GI147211, using a daily x 5 intravenous administration.* British Journal of Cancer, 1996. **73**(6): p. 744-750.
79. Greenblatt, D.J., D.R. Abernethy, and M. Divoll, *Is volume of distribution at steady state a meaningful kinetic variable?* The Journal of Clinical Pharmacology, 1983. **23**(8-9): p. 391-400.

CHAPTER 4

Novel amphiphilic chitosan micelles as carriers for hydrophobic anticancer drugs

The information provided in this chapter was based in the following publication:

Almeida, A., Araújo, M., Novoa-Carballal, R., Andrade, F., Gonçalves, H., Reis, L. R., Lúcio, M., Schwartz Jr, S. & Sarmento, B, 2020. Novel amphiphilic chitosan micelles as carriers for hydrophobic anticancer drugs. *Materials Science and Engineering: C:* 110920.

In this paper, I was responsible for the conception, execution and revision of the manuscript. Marco Araújo, Ramon Novoa-Carballal, Fernanda Andrade, Hugo Gonçalves and Rui Reis were responsible for part of the methodology. The supervisor and co-supervisors were responsible for reviewing and submit the manuscript. This paper was not previously included in other thesis and it is partially reproduced in this section.

4.1. Abstract

Chitosan was grafted with *O*-methyl-*O'*-succinyl polyethylene glycol and oleic acid after a two-step carbodiimide coupling. The structural and physicochemical characterization of the compounds confirmed the successful conjugation of the hydrophilic and hydrophobic moieties to the chitosan backbone. The amphiphilic chitosan derivative obtained allowed the formation of polymeric micelles with an average size of 140 nm, a polydispersity index <0.234, and a positive superficial charge. Camptothecin (CPT), used as a model hydrophobic drug, was successfully carried into the polymeric micelles with an association efficiency of 78%. The *in vitro* drug release was evaluated in simulated gastrointestinal fluids, exhibiting a low release of CPT in gastric media and a controlled release in intestinal fluids. Furthermore, it was demonstrated that chitosan micelles were able to stabilize CPT, protecting up to 75% of the drug from hydrolysis, preserving its active lactone form. This new chitosan amphiphilic system exhibits great potential to load hydrophobic drugs, acting as a promising delivery system.

4.2. Introduction

Chitosan (CS) is a natural polysaccharide that appears in several species of the mucorales fungi order. Although CS can be isolated from those fungi, it is commercially derived from chitin in a cost-effective process. It is composed of *D*-glucosamine and *N*-acetyl-*D*-glucosamine units linked by β-(1-4) glycosidic linkages, which are randomly assigned. The presence of free amine groups confers to CS a polycationic character that is unique within the polysaccharide family. The positive charge allows a simple encapsulation of negatively charged proteins and peptides, and DNA while, simultaneously, confers mucoadhesivity and possibility to transiently open the epithelial tight junctions [1]. These properties, together with the well-reported biocompatibility and biodegradability [1-4], have turned CS as one of the most used biomaterials for drug delivery.

However, besides its versatility, CS presents some drawbacks: it is insoluble at physiological pH (only soluble at pH below approximately 6, depending on the CS degree of acetylation (DA) [5]; it is not able to encapsulate hydrophobic drugs, increasing the difficulty of developing systems with controlled release profiles [6, 7]. Nonetheless, these drawbacks can be overcome due to the presence of -NH_2 and –OH groups, which are more prone to be functionalized. Several modifications have been described to improve its water solubility, including the most prominent carboxymethylation [8, 9] and modification with polyethylene glycol (PEG, i.e., PEGylation) [10-12]. PEGylation not only improves CS water solubility but also creates a stabilizing and protective shell around CS self-assembled systems. The PEG shell increases the colloidal stability and protects encapsulated

molecules from the aggressive enzymes in the gastric environment while retaining its mucoadhesiveness and improving its penetration ability [10, 13, 14]. Moreover, PEGylation is known to increase blood circulation times and reduce the immune response of many different systems (micelles, nanoparticles, liposomes), becoming an essential tool in the design of DDS (drug delivery systems) state of the art. Importantly, PEGylation provides lower toxicity and higher stability of CS-based DDS carrying peptides and DNA, as demonstrated in several *in vivo* studies [10, 15-17].

To improve the carrying capacity and control the drug release rate of CS-based DDS, acylation [18-20] or alkylation [21, 22] are the most commonly used reactions, since they also allow the encapsulation of hydrophobic drugs. The use of fatty acids such as palmitic, linoleic or oleic acid (OA) as hydrophobic moieties turns CS into an amphiphilic molecule [19, 23-25]. These CS amphiphiles can spontaneously form micelles in aqueous solution above a critical micelle concentration (CMC) [26]. Polymeric micelles based on CS have been explored as solubility enhancers and DD systems of many anticancer drugs such as paclitaxel [18, 27], doxorubicin [28, 29], or CPT [19, 30]. Such polymeric micelles can reduce the side effects of the encapsulated drugs protecting them from the harsh environment and potentially enabling adequate release at the target site. However, to obtain the desired CMC and an efficient drug encapsulation/release, parameters such as hydrophobic chain length and also the substitution degree (SD), have to be carefully thought out.

In the present study, we have combined the benefits of PEGylation with those of acylation to develop novel CS polymeric micelles, which could efficiently encapsulate and protect hydrophobic drugs. The simultaneous modification of CS with PEG and a hydrophobic molecule by acylation was described before for hexyl and octyl groups [31-33]. In some of these articles, the self-assembly of polymers has been studied and the resulting systems are proposed for drug delivery, but no encapsulation/release or *in vitro* studies have been performed. In other studies, CS-PEG-C6 was applied as a surface modifying agent [34, 35]. To the best of our knowledge, this work describes for the first time a CS amphiphilic derivative developed through the conjugation of both mPEG and OA to the CS backbone (mPEG-CS-OA), providing a detailed investigation of its delivery ability.

4.3. Material and Methods

4.3.1. Materials

CS, with 15% DA and weight-average molecular weight value (Mw) of 112 kDa (determined by ^{1}H NMR spectroscopy and gel permeation chromatography (GPC), respectively); *N*-(3-dimethylaminopropyl)-*N*′-ethylcarbodiimide hydrochloride (EDC·HCl), 1-

hydroxybenzotriazole hydrate (HOBt), OA, 2,4,6-trinitrobenzenesulfonic acid solution (TNBS), *O*-methyl-*O*′-succinyl polyethylene glycol 5′000 (mPEG-COOH), pancreatin from porcine pancreas and pepsin from porcine gastric mucosa were all purchased from Sigma-Aldrich. Ultracel® 30 kDa ultrafiltration discs (PLTK04310, 44.5 mm diameter, Merck Millipore) were used to purify the mPEG-CS polymer, while a 3.5 kDa cutoff dialysis membrane (regenerated cellulose, Spectra/Por® 3 Dialysis Tubing, Fisher Scientific) was used to purify the amphiphilic polymer and to produce the polymeric micelles. CPT was purchased from Hangzhou ROYAL Import & Export Co., Ltd.

4.3.2. Synthesis of mPEG-chitosan-oleic acid

4.3.2.1. Chitosan modification with mPEG-COOH

Briefly, 0.5% (w/v) CS solution was prepared in HCl 0.1 M and left overnight until complete dissolution. The pH was then adjusted to 5.5 with 1M NaOH, before the addition of mPEG-COOH at a stoichiometric ratio (mPEG-COOH/NH_2 CS molar ratio expressed as mol% (COOH/NH_2)) of 5%, corresponding to 76.7 mg of mPEG-COOH and HOBt (10.1 mg, 0.0747 mmol, 5 equiv). The mixture was allowed to stir for 15 min at RT, and the pH readjusted to 5.5, before the addition of the EDC·HCl (71.6 mg, 0.3736 mmol, 25 equiv), distributed in four portions in intervals of 30 min each [36]. After overnight stirring at RT, the final product was submitted to ultrafiltration with a 30 kDa ultrafiltration discs through 5 washing steps with HCl 10^{-3} M and 3 washing steps with MilliQ water to eliminate the unreacted mPEG-COOH, HOBt and EDC·HCl and the secondary products of the reaction. The copolymer mPEG-CS was then freeze-dried and kept at - 20 ºC until further use.

4.3.2.2. Pegylated chitosan modification with oleic acid

mPEG-CS-OA was synthesized by reacting the primary amino groups of CS with the OA carboxyl groups, in the presence of the coupling pair EDC·HCl/HOBt. Briefly, 100 mg of mPEG-CS was dissolved in 20 mL of HCl 0.1 M until its complete dissolution and pH adjusted to 5.5 through the addition of 1M NaOH. To the mixture, 20 mL ethanol were added followed by the addition of OA, previously dissolved in 0.5 mL of ethanol, at a stoichiometric ratio (OA/NH_2 CS molar ratio expressed as mol % (COOH/NH_2)) of 2.5 or 5.0%, corresponding to a 4.8 and 9.5 µL of OA, respectively, and HOBt (9.6 or 19.2 mg, 0.0711 or 0.1421 mmol, 5 equiv, for 2.5 or 5%, respectively, previously dissolved in 0.5 mL of ethanol). The pH of the solution was readjusted to 5.5, as previously mentioned, before the addition of EDC·HCl (13.6 or 27.2 mg, 0.0710 or 0.1419 mmol, 5 equiv, for 2.5 or 5%, respectively, also dissolved in 0.5 mL of ethanol). After overnight stirring at RT, the solution

was dialyzed in a 3.5 kDa cutoff membrane against water, with three cycles of water exchange, to remove the unreacted OA, HOBt, EDC·HCl and the secondary products of the reaction. The copolymer mPEG-CS-OA was freeze-dried and kept at - 20 ºC until further use.

4.3.3. Characterization of mPEG-chitosan and mPEG-chitosan-oleic acid

4.3.3.1. FTIR and ^{1}H NMR spectroscopy

The FTIR analysis was performed in an ABB MB3000 FTIR spectrometer from ASEA Brown Boveri (ABB Zurich, Switzerland) and all the spectra collected with 256 scans and a 4 cm^{-1} resolution in the region of 4000– 600 cm^{-1} as previously described [18]. For ^{1}H NMR, samples were prepared at 1 mg/mL and solubilized in 2% DCl for CS and mPEG-CS, and in 2% DCl:DMSO-d_6 (7:3) for mPEG-CS-OA, and heated at 70 ºC during 8 h [36]. ^{1}H NMR spectra were obtained in a Bruker AVANCE III 400 spectrometer at 25 ºC with 10 sec between pulses and 32 scans. Mnova software (Mestrelab Research) was used for analysis processing. The DA [37] was also determined by this technique through the relative integration of acetyl peak (I_{CH_3} at δ=1.75 ppm) combined with H2-H6 CS protons in the region of 3.2–3.8 ppm. The mPEG SD was determined from the ratio between integrals corresponding to the mPEG methylene group peaks and the number of mPEG protons by the H1 of the CS glucosamine residue in the ^{1}H NMR spectra [12]. The OA SD was calculated similarly, using the ratio between the integrals from OA peaks and the total number of OA protons by the H1 of monosaccharide residue in the ^{1}H NMR spectra.

4.3.3.2. Gel permeation chromatography

Mw of CS and the purity of mPEG-CS and mPEG-CS-OA polymers were determined by GPC. Sample processing and equipment configuration were used as described [38]. 0.18 was used as a refractive index increment value (dn/dC) to calculate the absolute Mw of all samples [39].

4.3.3.3. Trinitrobenzene sulfonic acid assay

The SD of CS was also determined using TNBS assay [40]. Briefly, 200 µL of the samples, mPEG-CS and mPEG-CS-OA, at 4 mg/mL in HCl 0.05 M solution, 200 µL of 4 % $NaHCO_3$ and 200 µL 0.01 % TNBS solutions were mixed. Samples were kept for 2 h at 37 ºC and the reaction quenched through the addition of 2 N HCl (200 µL). The absorbance was measured at λ_{max}= 340 nm using UV–vis spectrophotometer (PerkinElmer, USA). SD of

each CS derivative was obtained using a calibration curve constituted by CS solutions with different concentrations. The assay was performed in triplicate.

4.3.3.4. Contact angle

To evaluate the hydrophilicity and hydrophobicity of CS and the new CS derivatives, the contact angle was measured using an optical contact angle measuring device (OCA15, Dataphysics Instruments Co. Ltd., Filderstadt, Germany), and the data was acquired as previously reported [18].

4.3.3.5. Differential scanning calorimetry / thermogravimetric analysis

Differential scanning calorimetry (DSC) experiments were performed using a DSC 214 Polyma (NETZSCH, Germany) calorimeter calibrated with pure indium (T_m=156.6 °C) as previously reported [41] with some modifications. Briefly, 5-10 mg of each sample were used under a nitrogen atmosphere in sealed and pierced aluminum crucibles and the temperature ranged from 25 to 200 °C with a scanning rate of 10 °C/min. The thermodynamic parameters (characteristic transition temperatures T_m and enthalpy changes ΔH) were calculated from the heating scans using NETZSCH Proteus – Thermal Analysis v7.1 software. Thermogravimetric analysis (TGA) was used to study the thermal stability. TGA was carried out using a STA 449 F3 (NETZSCH, Germany) instrument with aluminum crucibles as a sample holder in a nitrogen atmosphere. The temperature was programmed from RT to 600 °C with a heating rate of 10 °C/min. TGA data obtained (characteristic onset, mass loss, and residual mass) were analyzed using NETZSCH Proteus – Thermal Analysis v6.1 software.

4.3.3.6. X-Ray diffraction analysis

The samples analysis of X-ray diffraction (XRD) was carried out in a MiniFlex X-ray diffractometer (Rigaku, Japan) equipped with Cu Kα radiation (λ= 0.154 nm) using a generator voltage and current of 40 kV and 300 mA, respectively, equipped with a detector D/TeX Ultra 1D silicon strip. The measurements were obtained using a circular zero-background silicon holder and a scanning rate of 5 °C/min. The reflected intensities were recorded at 2θ scattering angle, and experimental data obtained were analyzed using the PDXL software of Rigaku, allowing the calculation of crystallite size according to Scherrer and Halder-Wagner method [42].

4.3.3.7. Critical micellar concentration determination

The CMC was determined by surface tension and by dynamic light scattering (DLS). Du Nouy ring method was applied to measure the surface tension through a tensiometer with a platinum ring at RT (DST 60 Surface Tension Analyzer, SEO, Korea), and the procedure was performed as described [43, 44] and repeated at least 3 times. To determine the CMC by DLS, a Zetasizer Nano ZS (Malvern Instruments) equipped with a 4 mW He–Ne laser operating at λ= 633 nm, with a controlled temperature of 25 °C in polystyrene cells was used. A series of solutions ranging from 0 to 1 mg/mL were prepared in MilliQ water from an aqueous stock solution of the grafted polymer at a concentration of 4 mg/mL. The data was processed using Malvern's Zetasizer software and represented as a derived count rate as a function of grafted polymer concentration.

4.3.4. Preparation of camptothecin-loaded mPEG-chitosan-oleic acid polymeric micelles

CPT-loaded polymeric micelle systems were obtained by dialysis method [30, 45]. Succinctly, 10 mg of mPEG-CS-OA were dissolved in 4 mL of DMSO:HCl 0.1 M (9:1) in a glass tube. The polymer was left stirring at RT until its complete dissolution. CPT, previously dissolved in DMSO, was added to the polymer solution and left under stirring for 6 h. The resultant mixture was dialyzed (3.5 kDa Mw cutoff) against water with three-cycle renewal to remove the DMSO and the free drug. The solution collected from the dialysis bag was centrifuged at 5,000 rpm for 20 min to isolate the precipitate formed during dialysis. Empty micelles were prepared following a similar procedure but without the addition of CPT to the solution.

4.3.5. Characterization of polymeric micelles

4.3.5.1. Particle size distribution, zeta potential and morphological analysis

Mean particle diameter determined by cumulants, polydispersity index (PdI), and surface charge were assessed by DLS and Laser Doppler Micro-electrophoresis (ZetaSizer Nano ZS, Malvern, UK), respectively, with an angle of 173 º at 25 ºC. CS micelles were analyzed after its production and after freeze-drying in MilliQ water at 1% (w/v) concentration. Morphological analysis of the obtained CS micelles was assessed by transmission electron microscopy (TEM). Samples were prepared on a grid treated with uranyl acetate by placing 10 µL of the micelles formulation and then examined using a JEM-1210 Transmission Electron Microscope (JEOL Ltd., Tokyo, Japan) operating at 120 kV.

4.3.5.2. Association efficiency and drug loading

The association efficiency (AE) was determined through the quantification of the precipitated drug during dialysis by high-performance liquid chromatography (HPLC) and calculated as defined in Equation 4.1. Drug loading (DL) was determined according to Equation 4.2. HPLC analysis was conducted in a Shimadzu UFLC Prominence System (USA) equipped with two Pumps LC-20AD, a column oven CTO-20AC, an autosampler SIL-20AC, a System Controller CBM-20A, a degasser DGU-20A5, a RF-10Axl fluorescence detector coupled to the LC System and a LC Solution, Version 1.24 SP1 (Shimadzu). The method used for CPT quantification was described by Martins et al. [46] and was carried out using an analytical reversed-phase MediterraneaTM Sea18 column (150 mm × 4.0 mm, 5 µm, Teknokroma, Spain).

$$AE\ \% = \frac{weight\ of\ CPT\ added - weight\ of\ CPT\ free}{weight\ of\ CPT\ added} \times 100 \quad (4.1)$$

$$DL\ \% = \frac{weight\ of\ CPT\ added - weight\ of\ CPT\ free}{total\ micelles\ weight} \times 100 \quad (4.2)$$

4.3.5.3. Micelles stability at 4 ºC and effect of different cryoprotectants on micelles size

The stability of micelles in water at 4 ºC was studied. After production, the micellar solution was stored in a glass tube at 4 ºC for one week, and at different days, their size and PdI analyzed as described before. Also, the study of the best cryoprotectant for mPEG-CS-OA micelles was performed. Briefly, mPEG-CS-OA formulations were produced, purified and freeze-dried using different concentrations of each cryoprotectant such as trehalose, mannitol and glucose. The freeze-dried micelles were then solubilized in MilliQ water at 1% (w/v) concentration, and their size and PdI analyzed as described before in section 4.3.5.1. The assay was performed in triplicate.

4.3.6. *In vitro* camptothecin release in simulated gastrointestinal fluids

The evaluation of CPT release overtime was performed under stirring (100 rpm) at 37 ºC using simulated gastric (SGF; pH 1.2; pepsin 0.32% w/v) and intestinal (SIF; pH 6.8; pancreatin 1% w/v) fluids. Tween 80 (1 % w/v) was added to the previous fluids to maintain the sink conditions. One milliliter of micelles formulation containing 0.3 mg of CPT or the same amount of free CPT was transferred to a dialysis membrane of 3.5 kDa against 40 mL of SGF for 2h and then changed to SIF until 72 h of experiment. At different time points (0.25, 0.5, 1, 2, 8, 12, 24, 48, and 72 h), 400 µL of the sample was withdrawn and replaced

by 400 µL of fresh medium. The amount of CPT released was quantified by HPLC, as described previously in section 2.5.2. Results are presented as a cumulative percentage of CPT released at each analyzed time, and the mathematical modeling for CPT release was evaluated using the zero-order, first-order, Weibull and Korsmeyer-Peppas fitting models. The assay was performed in triplicate.

4.3.7. Camptothecin lactone ring protection from hydrolysis

To assess the protective effect of mPEG-CS-OA micelles on CPT lactone ring against hydrolysis, CPT-loaded micelles were submitted to gastrointestinal conditions in SGF (pH 1.2, pepsin 0.32% w/v, 37 ºC) for 2 h and SIF (pH 6.8, pancreatin 1% w/v, 37 ºC) containing CPT at 8 µg/mL [47]. At predetermined time intervals, 200 µL aliquots were taken and analyzed by HPLC to assess the CPT lactone and carboxylate forms, which are detectable in the method used. At similar time periods, free CPT was also evaluated for comparison. The HPLC system and method was used as previously described [46]. Results are present as a normalized percentage from the initial lactone form of CPT ($t = 0$). The assay was performed in triplicate.

4.3.8. Statistical analysis

All data were presented as mean ± SD. A two-way ANOVA, with Bonferroni multiple/post hoc group comparisons ($P<0.001$), was applied to evaluate the CPT protection ring data in the GraphPadPrism® software Inc., USA.

4.4. Results and Discussion

4.4.1. Synthesis and characterization of mPEG-chitosan

Pegylated chitosan, mPEG-CS, was synthesized by a carbodiimide amidation through the reaction of -NH_2 groups from CS with the -COOH terminal groups of mPEG (Figure A2.1, supplementary information). This reaction was promoted through the addition of the pair EDC·HCl/HOBt, which reacts with mPEG carboxyl end groups to form active ester intermediates. These intermediates further react with primary amine groups of CS, leading to the formation of an amide bond. The success of the synthesis was confirmed by ATR-FTIR and ^{1}H NMR, as shown in Figure 4.1A and 4.1B, respectively.

The FTIR characteristic bands of CS and mPEG-COOH can be identified in Figure 4.1A. CS characteristic band at 3200-3600 cm^{-1} was assigned to O-H and N-H stretching vibration, where O-H stretching vibration was superimposed with N-H stretching vibration. The band at 890-1100 cm^{-1} was attributed to ether groups of the CS saccharine structures

(C–O–C stretching) [48]. The characteristic peaks of mPEG-COOH at 1100 cm^{-1} (C-O stretching), at 2880 cm^{-1} (C-H stretching) and at 1731 cm^{-1} (C=O stretching) were also identified [49].

After conjugation of mPEG to CS backbone, the abovementioned typical bands of CS and mPEG-COOH appeared in the mPEG-CS spectrum. It was observed a shift in the CS amide bands, from 1650 cm^{-1} (amide I) and 1589 cm^{-1} (amide II) to 1637 cm^{-1} and 1522 cm^{-1}, respectively. Moreover, the mPEG-COOH peak at 1731 cm^{-1}, assigned to C=O stretching vibrations in carboxylic acids, did not appear in the conjugate spectrum, confirming that the reaction between CS and mPEG-COOH occurred. It was also noticed the bands at 1100 cm^{-1} and 2870 cm^{-1}, attributed to the overlap of C-O and C-H stretching vibrations of CS and mPEG, respectively, became more pronounced compared to the ones in CS spectrum [50]. Furthermore, it was possible to compare the mPEG-CS with its physical mixture, where the carboxylic group of mPEG-COOH is well observed, further supporting the success of the synthesis.

^{1}H NMR also confirmed the grafting of mPEG-COOH to the CS backbone. From the analysis of Figure 4.1B, CS typical peaks were found at δ= 3.5-4.0 ppm (H-3, H-4, H-5, and H-6), assigned to the methylene CS protons. The peaks at δ= 2.05 (H-7) and δ= 3.18 (H-2) ppm were assigned to -$COCH_3$ and proton in $CHNH_2$ protons in the CS backbone, respectively. The peak at δ= 4.88 ppm (H-1) was assigned to the hydrogen-bonded of the anomeric carbon of *N*-glucosamine (GlcN) units in CS. On the mPEG-CS spectra, the peaks at δ= 3.70 ppm (H-b and H-c) and at δ= 3.52 ppm (H-d) were attributed to the methoxy group (-OCH_3) from mPEG and to its methylene protons from ethylene glycol repeating units. Moreover, the presence of the typical peaks of CS and mPEG-COOH in the mPEG-CS spectrum confirmed the success of functionalization [12]. Additionally, the DA of CS was calculated to be 15%, determined as explained in materials and methods section.

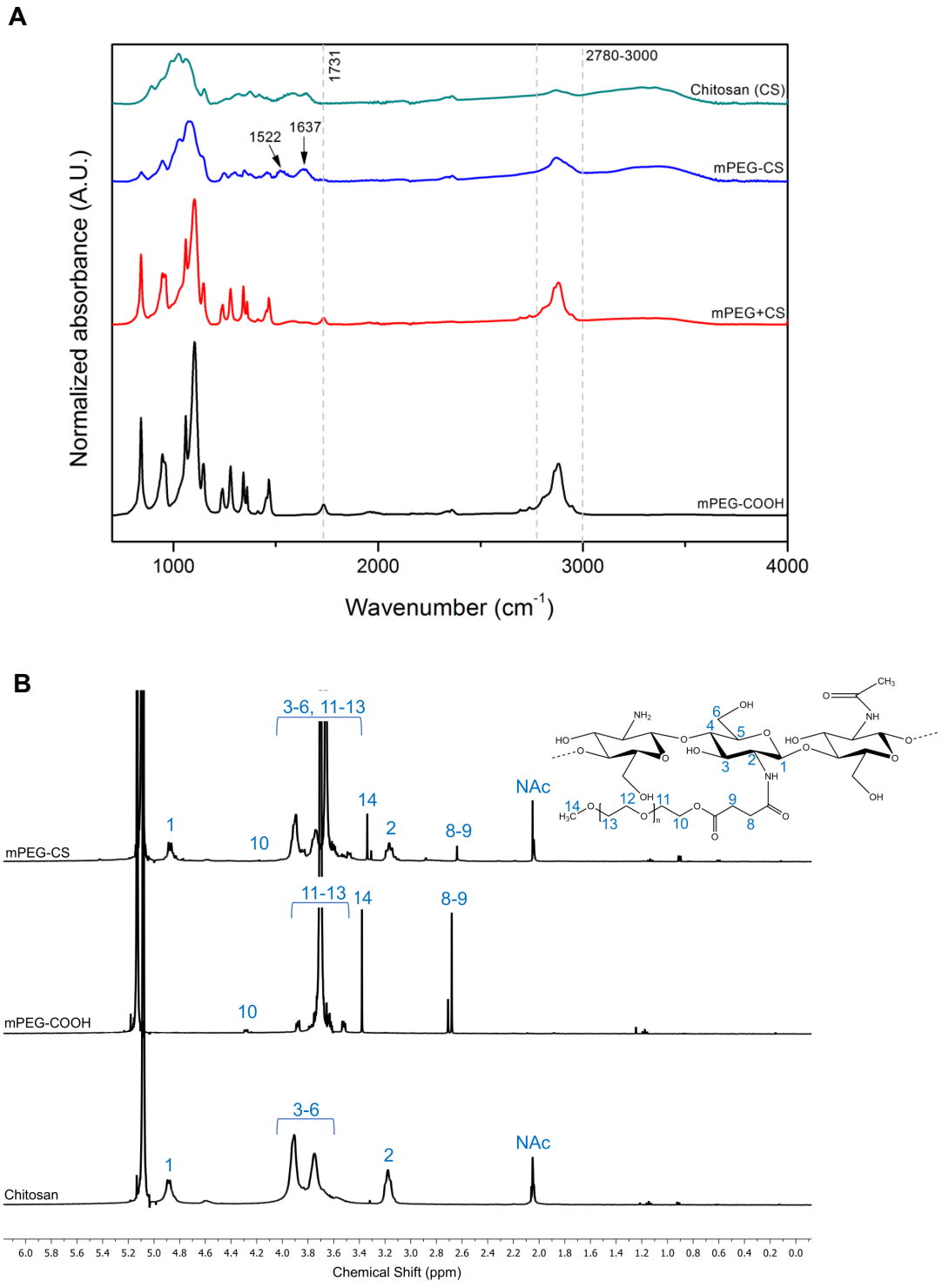

Figure 4.1. (A) ATR-FTIR spectra of mPEG-COOH, physical mixture of mPEG-COOH and CS, mPEG-CS copolymer and chitosan (CS) and (B) ^{1}H NMR spectra of chitosan, mPEG-COOH and mPEG-CS in 2% DCl (1 mg/mL, 400 MHz).

4.4.2. Synthesis and characterization of mPEG-chitosan-oleic acid

OA was grafted into CS backbone after its pegylation, i.e., taking mPEG-CS as starting material (Figure A2.2, supplementary information). The successful conjugation of OA to the polymer backbone was confirmed by ATR-FTIR (Figure 4.2A). In this second reaction, CS characteristic peaks were also present in the mPEG-CS-OA spectra. The characteristic bands around 2800-3000 cm^{-1}, attributed to the CH_2 stretching in the alkyl chain of OA, as well as and the characteristic OA band at 1700 cm^{-1} (C=O stretching) related to the carboxylic group, were well visible in mPEG-CS-OA spectra [51]. It was also observed the characteristic shift of the CS amide band at 1650 cm^{-1} and 1587 cm^{-1} to 1635 cm^{-1} and 1540 cm^{-1}, respectively, in the mPEG-CS-OA spectrum. Moreover, these bands increased its intensity as confirmation of the amide bond formation through the reaction of the amino groups of CS with the carboxyl groups of OA [52]. Additionally, the OA characteristic band at 1700 cm^{-1}, attributed to C=O stretching in carboxylic acids did not appear in the mPEG-CS-OA spectrum, indicating the success of the reaction. Clear differences were noticed on the spectrum from the physical mixture of mPEG-CS with OA. It was observed the presence of a band at 1700 cm^{-1} attributed to C=O stretching in carboxylic acids, and absence of characteristic amide bands, further confirms the success of the synthesis of mPEG-CS-OA. Indeed, the broad band around 3600-3000 cm^{-1} in the mPEG-CS-OA spectrum appears to be less pronounced than in the mPEG-CS spectrum, probably due to a decrease in CS amine groups after reaction with OA.

Figure 4.2B shows the ^1H NMR spectrum of mPEG-CS-OA, which exhibited the characteristic peaks of both CS and mPEG (H-1 to H-13). More importantly, it was observed the appearance of the characteristic peaks of OA in the mPEG-CS-OA spectrum at δ= 0.75 ppm (H-30) attributed to the methyl group of OA, at δ= 1.15 ppm (H-15 to H-19 and H-25 to H-28) assigned to the OA methylene groups, at δ= 1.87 ppm (H-14, H-20 and H-24) also attributed to the methylene group of the OA β-carbonyl and at δ= 5.20 ppm (H-21 and H-22) characteristic of the ethylene group of OA [52]. Thus, the chemical structure of mPEG-CS-OA was confirmed by ^1H NMR, revealing the success of the synthesis.

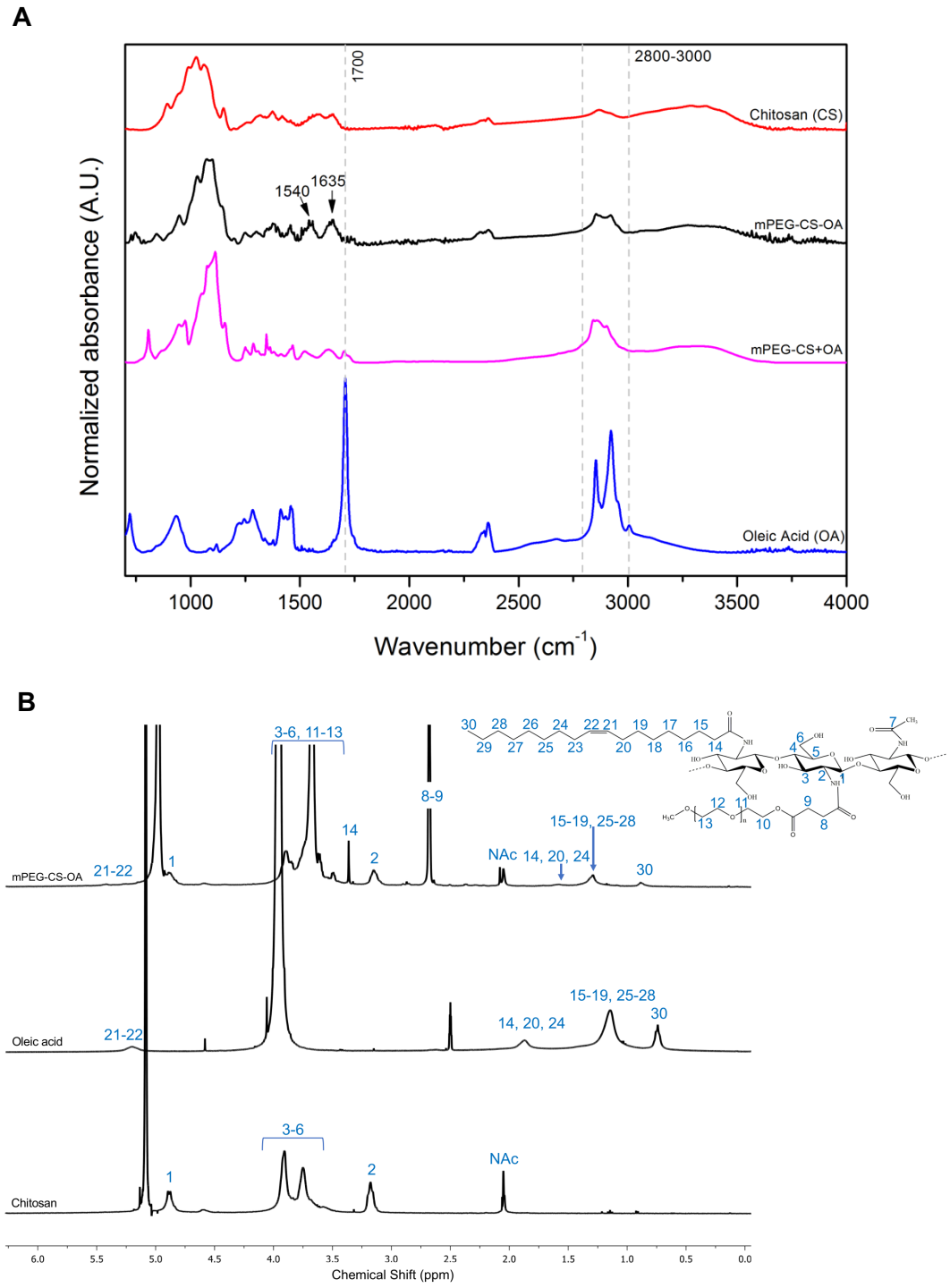

Figure 4.2. (A) ATR-FTIR spectra of OA, physical mixture of mPEG-CS+OA, mPEG-CS-OA copolymer and CS and (B) ^{1}H NMR spectra of chitosan in 2% DCl, oleic acid in DMSO-d_6 and mPEG-CS-OA (1 mg/mL, 400 MHz).

GPC analysis was conducted to assess the Mw and number-average molecular weight value (Mn) of CS (*M*n = 73,100 g/mol, *M*w = 112,000 g/mol, PdI 1.5), confirm the Mw and Mn of mPEG-COOH (*M*n = 4,700 g/mol, *M*w = 5,300 g/mol, PdI 1.1) and to assess the purity of the new polymers synthesized. From the analysis of Figure A2.3 (supplementary

information), it is possible to observe a mono-modal peak for CS and mPEG-COOH curves and the absence of free mPEG-COOH in the mPEG-CS and mPEG-CS-OA2.5% curves, revealing the purity of the material [53]. mPEG-CS, although apparently dissolved, formed aggregates in the GPC solvent that would lead to an overestimated Mw. This aggregation is evidenced by the bimodal distribution observed in the RI and LS detectors and the fact that the RI signal of the peak at lower retention time, that depends only on the concentration, is much weaker than the LS signal that depends on the Mw and concentration. The aggregation in aqueous solution was reported previously by DLS [54, 55]. Also, in a graft copolymer, the distribution of the polymers might change concerning the polymer's Mw. Therefore, an additional UV detector is necessary to accurately determine the dn/dc of the copolymer in each GPC fraction. However, it is not possible to be performed in mPEG-CS because the mPEG is not active in UV [56]. The estimation of the Mn (222 kDa) and Mw (376 kDa) applying a mean dn/dc (0.15) was made using the copolymer composition determined by NMR and the Mn and Mw determined by GPC. Comparing these values with theoretical values calculated from the composition determined by NMR (Mn 161 kDa and Mw 222 kDa), it is verified that some aggregation occurs, but also that the relatively small amount of aggregates does not affect the Mw determination strongly. The same occurred with mPEG-CS-OA2.5% and, in the case of mPEG-CS-OA5%, was not possible to analyze the Mw due to the difficulty of solubilization. Moreover, the fact that polymers form aggregates indicates CS suffered modification with mPEG-COOH and OA, when compared with the CS.

The optical contact angle was calculated to assess the hydrophilicity and hydrophobicity effect caused by the presence of mPEG and OA, respectively, in the CS chains when compared to unmodified CS. As demonstrated in Figure A2.4, the mPEG-CS contact angle decreased when compared to CS due to the grafting of mPEG-COOH into the CS backbone. On the other hand, the grafting of OA led to an increase in the contact angle, confirming the presence of OA on CS chains. Also, it was possible to verify the higher the SD of OA, the higher was the contact angle [18, 27].

Figure A2.5 (supplementary information) shows the thermogravimetric curves of the raw materials used in the conjugation: CS, mPEG and OA. In agreement with reported TGA [57], the thermogram of CS (black curve in Figure A2.5 of supplementary information) indicates two weight losses. The presence of water bound to CS by hydrogen bonds led to the first heat loss event (8.95%). The following thermal loss event (63.06%) occurring at 280 ºC was associated with the cleavage of the *O*-glucoside bonds and assigned to the CS chains degradation, leaving off oligomers. At 600 ºC CS was relatively stable and presented a residual mass of 24.34%. The mPEG thermogravimetric curve (red curve in Figure A2.5 of supplementary information) exhibited a one-step decomposition (92.84%), occurring at

388 ºC, which was also in agreement with reported results [58]. OA decomposition initiated at 240 ºC and occurred until a residual mass of 9% was reached in agreement with what has been reported [59].

Figure 4.3A shows the thermogravimetric curves of mPEG+chitosan (mPEG+CS) physical mixture sample, and mPEG-chitosan grafted sample (mPEG-CS). Both samples possess two stages of weight loss. The first stage (1) initiates at 220 ºC in the grafted sample and 280 ºC in the blend, related to CS thermal decomposition. The second stage (2) initiates at 388 ºC in both blend and grafted samples and can be assigned to the thermal decomposition of mPEG. The shift of CS degradation in the grafted sample (T_{onset} = 220 ºC), in comparison to the CS degradation in a blend or CS raw material (T_{onset} = 280 ºC), could be attributed to the grafting of mPEG to CS. Also, it was found that the extent of weight loss in the mPEG-CS grafted sample during the thermal degradation was higher than the mPEG+CS blend sample at the same temperature. Thus, this constitutes evidence that mPEG was conjugated to CS via grafting method and that the thermal stability of both mPEG and CS changed by the presence of the covalent bonding.

Figure 4.3B shows the thermogravimetric curves of mPEG-CS grafted samples without OA (mPEG-CS) or with 2.5 or 5% of OA (mPEG-CS-OA2.5 and mPEG-CS-OA5, respectively). The conjugation with OA keeps the onset temperatures found for each stage of degradation: stage (1) initiating at 220 ºC and attributed to CS degradation, and stage (2) initiating at 388 ºC and attributed to mPEG degradation. Also, the conjugation with OA improved the thermal stability of the copolymer since the residual mass increased from 5% in mPEG-CS to 48% in mPEG-CS-OA2.5 and mPEG-CS-OA5. As a general observation, it might be said that the thermal stability of a polymer, together with biocompatibility or biodegradability properties, might allow their use in several biomedical applications. In this sense, it is possible to avoid the problem of unexpected and unpredictable physical changes that can happen when they are processed during their production (such as thermal stability changes that might occur during freeze-drying), when applied to the human body, or when it is stored for later use [60, 61].

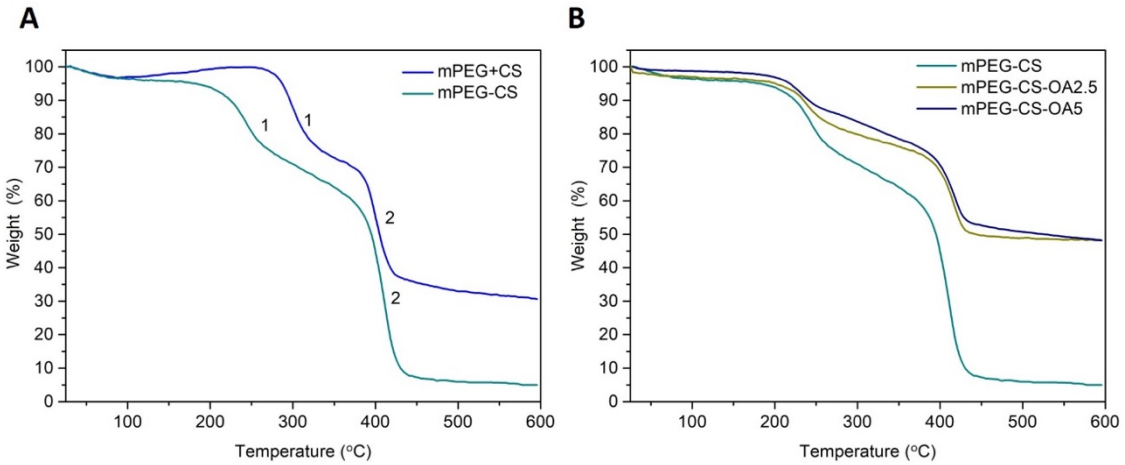

Figure 4.3. Thermogravimetric curves of (A) blend of mPEG and chitosan (mPEG+CS) and grafted polymer of mPEG and chitosan (mPEG-CS) and (B) grafted polymer of mPEG and chitosan without oleic acid (mPEG-CS) or conjugated with 2.5% (mPEG-CS-OA2.5) or 5% (mPEG-CS-OA5) of oleic acid.

Figure A2.6 (supplementary information) shows the thermograms of the raw materials CS and OA, respectively. DSC curves of CS presented some visible differences between the first and second heating runs. On the first run, a large asymmetric endothermic peak centered around 100 °C could be observed. This peak was attributed to some water bound, which was not removed [57], even when the samples were dried for some time in the desiccator before analysis, but then evaporated on heating during the second run. This water evaporation was also observed during the thermogravimetric analysis (Figure A2.5, black curve supplementary information), where it was evident that the first mass loss (8.95 %) was related to the existence of water bound to CS by hydrogen bonds. In the case of OA, there were no differences between the first and the second run and no thermal transitions were observed within the temperature range evaluated. As this fatty acid presents two negative transition temperatures (around -1 °C and -11 °C), associated with the crystallization of the meta-stable α form and the polymorphic conversion from α to γ forms, respectively [59]. As a result, in the second run of DSC curves, none of the raw materials CS or OA presented any transitions within the range of temperatures studied. Following the same methodology, we have chosen to present the second scan of each

sample (Figure 4.4) as this is a standard procedure in which the first heat scan in the DSC is mostly used to remove residual solvents and to erase the thermal history of the polymer.

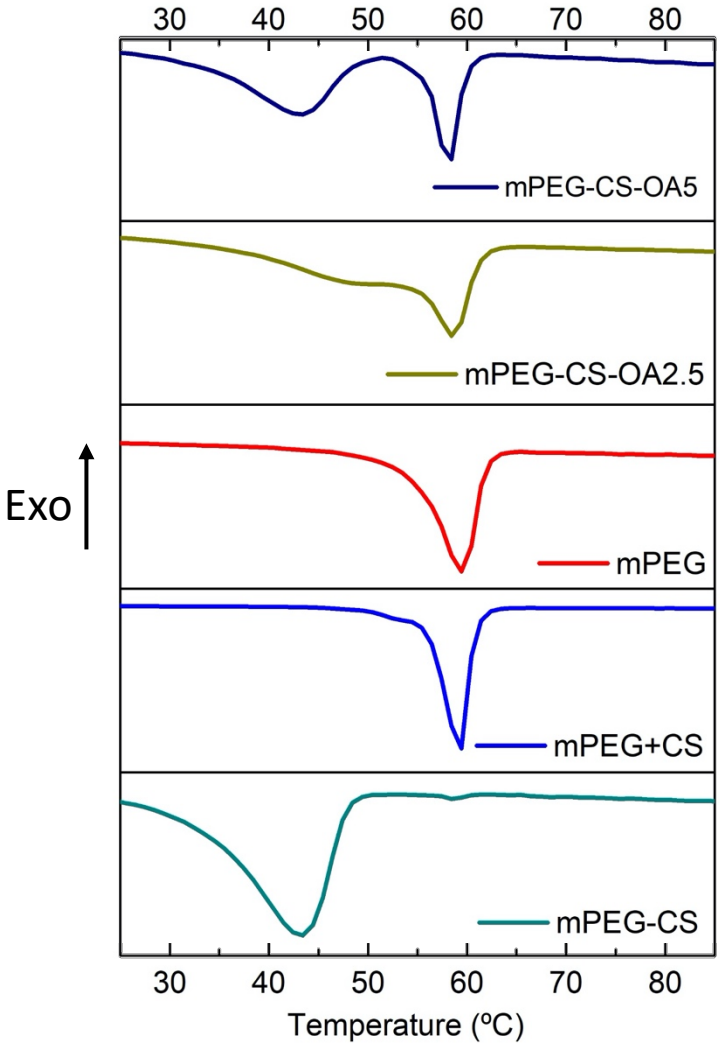

Figure 4.4. Calorimetric curves of grafted polymer of mPEG and chitosan (mPEG-CS); blend of mPEG and chitosan (mPEG+CS); grafted polymer of mPEG and chitosan conjugated with 2.5% (mPEG-CS-OA2.5) or 5% (mPEG-CS-OA5) of oleic acid.

Table 4.1 presents the thermodynamic parameters obtained from the second run DSC curves of: pure mPEG raw material (mPEG); grafted copolymer of mPEG and chitosan (mPEG-CS); physical mixture of mPEG and chitosan (mPEG+CS) and grafted copolymer of mPEG and chitosan with 2.5 or 5% of oleic acid (mPEG-CS-OA2.5 and mPEG-CS-OA5). In agreement with the literature [62, 63], the melting of mPEG occurred at a temperature of 59.20 °C and this transition was associated with high latent heat (ΔHm= 153.40 J/g, Table 4.1). The location of mPEG endothermic peak was practically the same in the physical mixture of mPEG and CS (mPEG+CS) (Tm = 58.89 °C, Table 4.1), however, the enthalpy has decreased due to the reduced mPEG content of this mixture. Moreover, and according

to the mPEG SD of 4.3 %, the theoretical area of the mPEG endothermic peak in the physical mixture of mPEG and CS should be 1.82 J/g, which was higher than the area of mPEG endothermic peak (0.25 J/g) in the grafted copolymer (mPEG-CS). This suggests that the degree of crystallinity of the mPEG-CS is smaller than the physical mixture, which is a likely explanation for the observed smaller thermal stability of mPEG-CS. In all grafted polymeric forms (mPEG-CS, mPEG-CS-OA2.5 and mPEG-CS-OA5), the endotherm corresponding to the mPEG melting peak (Endothermic peak 2, Table 4.1) practically disappeared (ΔH values =0.25 J/g mPEG-CS) or was very weak (ΔH values < 5 J/g for mPEG-CS-OA2.5 and mPEG-CS-OA5). In addition, another endothermic asymmetrical peak (Endothermic peak 1, Table 4.1), corresponding to the new polymeric entity, emerges suggesting a successful CS and mPEG conjugation. It is also relevant to note that the melting temperature of the mPEG-CS copolymers grafted with OA (Endothermic peak 1, Table 4.1) was always significantly higher than the body temperature, which is reassuring given that the polymeric micelles are meant to be stable while carrying the drug until the target tissues.

Table 4.1. Thermodynamic parameters obtained from DSC of grafted polymer of mPEG and chitosan (mPEG-CS); blend of mPEG and chitosan (mPEG+CS); grafted polymer of mPEG and chitosan conjugated with 2.5% (mPEG-CS-OA2.5) or 5% (mPEG-CS-OA5) of oleic acid.

Samples	Endothermic peak 1		Endothermic peak 2	
	T_m (ºC)	ΔH_m (J/g)	T_m (ºC)	ΔH_m (J/g)
mPEG-CS	43.10	32.05	58.60	0.25
mPEG+CS			58.80	42.45
mPEG			59.20	153.40
mPEG-CS-OA2.5	54.22	24.37	58.80	3.47
mPEG-CS-OA5	42.90	8.32	58.10	4.50

Figure 4.5A illustrates the XRD diffraction patterns of raw materials: mPEG or CS and their corresponding physical mixture (mPEG+CS) or conjugate (mPEG-CS). The results showed a CS diffraction pattern displaying three main crystalline reflections indexed as: (020) at 2θ of 10.75°; (110) at 2θ of 19.91° and (120) at 2θ of 23.70°, coherent with a possible hydrated polymorphic “tendon” [64]. mPEG also presented a diffraction pattern displaying several crystalline reflections, among which the most intense were at 2θ of 19.09º; 2θ of 23.33º and at 2θ of 26.11º in agreement with the literature [63]. The physical blend of CS and mPEG presented a combined diffraction pattern of mPEG and CS, showing crystalline reflections that can arise from both polymers (Figure 4.5A, black and red arrows). Conjugated copolymer showed a diffraction pattern that coincided with the most intense mPEG

reflection. The other smaller reflections present in both mPEG and mPEG+CS were not visible in the diffraction pattern of the mPEG-CS conjugated polymer. This is another proof of successful conjugation (the diffraction of the physical mixture was different from the diffraction of the conjugated polymer). Besides, this suggests that the crystalline structure of mPEG was maintained after conjugation, although the crystallinity was reduced, being consistent with the TG analysis, which also indicated reduced thermal stability for mPEG-CS conjugated polymers. Figure 4.5B demonstrates the XRD patterns of mPEG and CS copolymers grafted with OA. The position of the peaks in the mPEG-CS-OA (Figure 4.5B) was close to the peaks position in the mPEG raw material (Table A2.1 supplementary information). However, the intensity of these peaks has changed dramatically. The maximum intensity of the XRD diffraction peak indicates that the diffraction planes that produce this maximum intensity contain the highest number of atoms, i.e., indicates the preferred orientation of the crystallographic plane. Thus, while the small changes in the angular position of the diffraction peaks are related to changes in the interplanar distance between crystallographic planes in crystallites (Bragg equation), the observed intensity changes in the reflection are mainly affected by the preferred orientation as there are more/less crystallites with a particular orientation. Therefore, from the observation of the diffraction patterns in Figure 4.5B, it can be concluded that grafting with OA has changed the preferred orientation of the crystallographic planes of the crystallites in the polymer. This effect of OA, and other long fatty acids, have been used as structure-directing agents crucial to determine the structure of a crystal changing that inhibits the crystalline growth along with some directions, while promoting the growth rate along with other directions [65]. Furthermore, if we compare the crystallized size of mPEG raw material (5.90 nm) with the crystallized size of copolymers grafted with OA (69.5 nm for 2.5 % of OA and 63.10 nm for 5 % of OA), it can be inferred that the grafting process has led to the removal of an inter-crystalline boundary (grain boundary) aligning planes in several adjacent crystals. Table A2.1 of the supplementary information presents the crystalline reflections at the values found for the main peaks of Figure 4.5.

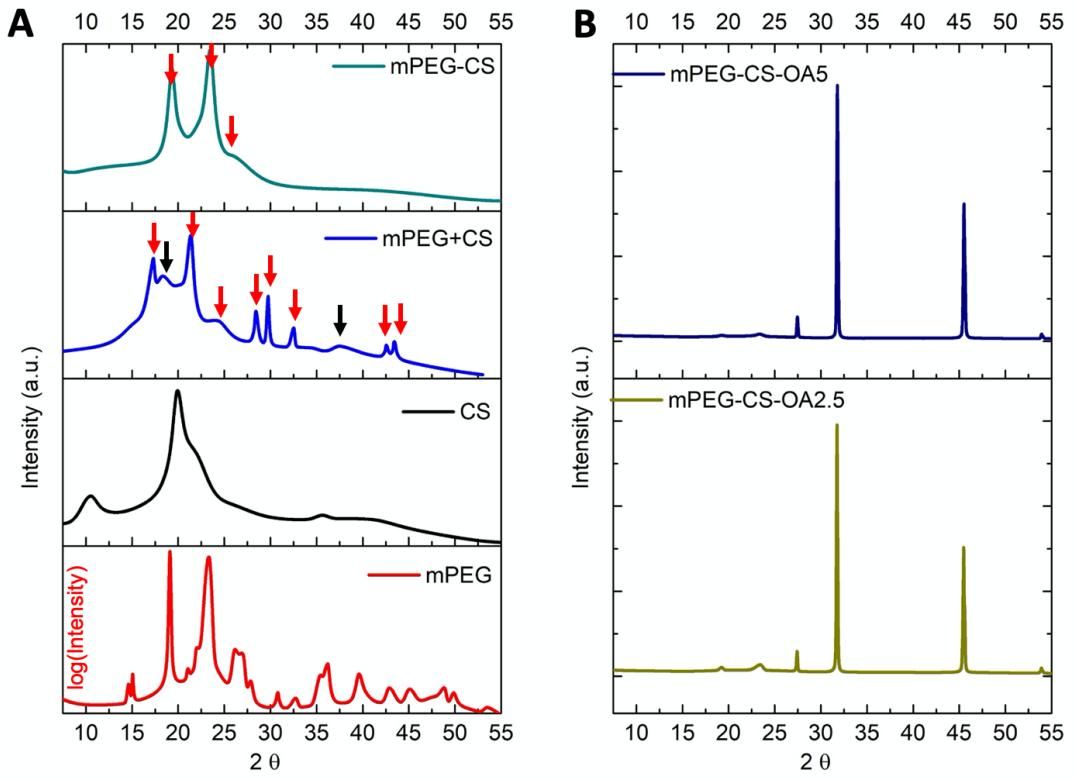

Figure 4.5. XRD patterns of: (A) mPEG; chitosan (CS); blend of mPEG and chitosan (mPEG+CS) and grafted polymer of mPEG and chitosan (mPEG-CS); and (B) grafted polymer of mPEG and chitosan conjugated with 2.5% (mPEG-CS-OA2.5) or 5% (mPEG-CS-OA5) of oleic acid. Red arrows indicate reflections that may arise from mPEG, black arrows indicate reflections that may arise from CS.

4.4.3. Chitosan substitution degree

The SD of CS was determined by ^{1}H NMR and TNBS assay, as explained in materials and methods section. For the mPEG-CS synthesis, an initial molar ratio COOH/NH_2 was set at 5%, which is described in the literature as it improves CS solubility in water and also increases its stability in diluted conditions [66, 67]. In the case of OA grafting, a molar ratio of 2.5 and 5.0 % was tested. From the theoretical molar ratio of 5% for mPEG-CS, a SD of 4.3 ± 0.2% was obtained by ^{1}H NMR and 5.9 ± 2.0% by TNBS. In the case of OA grafting, a SD of 2.9 ± 2.1% and 5.8 ± 2.9% was obtained for a theoretical molar ratio of 2.5% and 5.0%, respectively, by ^{1}H NMR and a SD of 2.9 ± 2.1% and 4.6 ± 2.6% by TNBS (Table 4.2). In the case of mPEG grafting, the theoretical value was similar to the practical value obtained by both techniques. On the other hand, the grafting of OA into CS was higher than the theoretical value, more evidently when determined by TNBS assay. This might occur due to the difficulty in solubilizing the mPEG-CS-OA without the addition of an organic solvent. In the case of NMR, the value obtained was closer to the theoretical value since

DMSO-d_6 was used to solubilize the copolymer. Also, the copolymer was used above the CMC, which means that micelles were formed, and this may interfere with SD determination, mostly in the TNBS assay. Despite the SD found, the nomenclature for the copolymers was based on the theoretical values (2.5 and 5%).

4.4.4. Critical micelle concentration

Due to the amphiphilic character imposed by its modification, mPEG-CS-OA can spontaneously form micelles in aqueous environment. Thermodynamically, there is a concentration where the monomers start to aggregate and form micelles by self-assembly, known as CMC. Thus, two different direct methods were used to determine it. The CMC found to mPEG-CS-OA 2.5% was 0.150 mg/mL and 0.147 mg/mL determined by DLS and surface tension, respectively. In the case of mPEG-CS-OA 5%, the CMC obtained was 0.076 mg/mL and 0.065 mg/mL for DLS and surface tension determination, respectively (Table 4.2 and Figure A2.7 in supplementary information), which were values lower than the low Mw surfactants as sodium dodecyl sulfate (CMC = 2.3 mg/mL) [68]. Both methods presented similar values for both polymers and, the CMC decreases with the OA increasing, which agreed with previously reported amphiphilic block copolymers [69, 70]. Moreover, CMC reveals the stability of the system after dilution by body fluids. A low CMC value is wanted to circumvent the disassociation of the polymeric micelles upon dilution, which turns them stable at very low polymer concentrations. Thus, the polymer mPEG-CS-OA 5% was chosen to proceed with further studies.

Table 4.2. Substitution degree (SD) and critical micelle concentration (CMC) of the new chitosan derivatives.

Sample	Feeding ratio (% mol)	SD[1]	SD[2]	CMC[3] (mg/mL)	CMC[4] (mg/mL)
mPEG-CS	5	4.3 ± 0.2	5.9 ± 2.0	-	-
mPEG-CS-OA2.5	2.5	2.9 ± 2.1	4.6 ± 2.6	0.150 ± 0.003	0.147 ± 0.009
mPEG-CS-OA5	5	5.8 ± 2.9	10.8 ± 3.1	0.076 ± 0.005	0.065 ± 0.002

[1] SD determined by ^{1}H NMR; [2] SD determined by TNBS assay; [3] CMC determined by DLS; [4] CMC determined by surface tension.

4.4.5. Preparation and characterization of mPEG-chitosan-oleic acid polymeric micelles

Micelles were obtained by self-assembly and purified by dialysis in order to eliminate the organic solvent. The size, PdI and surface charge of unloaded and loaded micelles were analyzed as well as the AE and, the results are presented in Table 4.3. Unloaded micelles presented an average hydrodynamic diameter of around 137 nm and, when CPT was encapsulated, the size increased to 146 nm. For a DL of 5%, CPT encapsulation did not affect the size of the micelles significantly. A narrow size distribution (bellow 200 nm) and good dispersity, taking into consideration the heterogenicity of CS (PdI < 0.240), was obtained for both empty and loaded micelles. However, the sizes obtained by DLS, which were performed in aqueous solution were bigger than those obtained by TEM, which was executed in a dry state (Figure A2.8 in the supplementary information). This occurred because polymeric micelles shrink during drying [19, 69] and because DLS determines the hydrodynamic diameter while microscopic techniques determine the nominal diameter. Moreover, it is possible to observe in Figure A2.8 (supplementary information) that micelles exhibited a spherical shape and a size distribution in agreement with the PdI obtained by DLS, as well as no aggregation. Micelle's surface presented large positive values of zeta potential (Table 4.3), which were due to the low substitution of CS and, consequently, the CS amine groups remain free to preserve the CS features. Moreover, highly charged micelles are more stable, favoring its interaction with the cell wall, which is negatively charged. Thus, enhanced absorption and uptake of CPT may be expected when in contact with the cells. Additionally, CPT was efficiently encapsulated into mPEG-CS-OA micelles, presenting an AE of 78% for a DL of 5%. It is known that AE increases with SD increasing. However, with a SD higher than 10%, hydrophobic moieties could appear in the micelle surface, leading to the drug entrapment in the surface, which affects the encapsulation and, at the same time, increases the cytotoxicity of the system [19]. Thus, 5% of CPT was chosen to be encapsulated by these micelles as they were able to increase 16-fold the CPT water solubility, compared with the free drug.

Table 4.3. The particle size, PdI, micelles surface charge, AE and DL of CPT-loaded mPEG-CS-OA micelles and unloaded micelles. Values are represented as mean ± SD (*n* = 3).

Sample	Size (nm)	PdI	Zeta potential (mV)	DL (%)	AE (%)
Unloaded mPEG-CS-OA5	137 ± 5	0.233 ± 0.025	+ 33.7 ± 1.8	0.0	-
CPT-loaded mPEG-CS-OA5	146 ± 3	0.229 ± 0.005	+ 41.8 ± 3.0	5.0	77.6 ± 7.7

The size and PdI of micelles were assessed for one week at 4 ºC to understand its stability in water. As can be seen in Figure 4.6D, mPEG-CS-OA micelles preserved its size (around 150 nm) during the seven days of the assay, and the PdI was maintained below 0.240. Further, these features were analyzed after freeze-drying. It is known that nanosystems tend to aggregate after freeze-drying, and, after its re-dispersion, the size and PdI are not maintained [71]. When no cryoprotectant was used, micelles increased its size up to 3000 nm, meaning that micelles were very aggregated (Figure 4.6A-C). Thus, cryoprotectants as sugars are used to avoid the aggregation and to increase micelles stability upon storage. In this study, several concentrations of trehalose, glucose and mannitol were tested to assess which one preserves better the micelles properties. Through the analysis of Figure 4.6C, mannitol was not efficient in preserving micelles size after freeze-drying at any concentration. The same occurred with glucose (Figure 4.6B), where micelles presented a size above 800 nm for all the tested concentrations, except for 1% w/v glucose, but presented a high PdI. Trehalose (Figure 4.6A) showed to be the best cryoprotectant for these micelles since several concentrations were found to preserve its features, size and PdI, after freeze-drying (1.0, 0.5 and 0.1% w/v concentrations). Thus, the 0.5% w/v concentration was chosen to proceed with the study and, it was always employed every time micelles were freeze-dried.

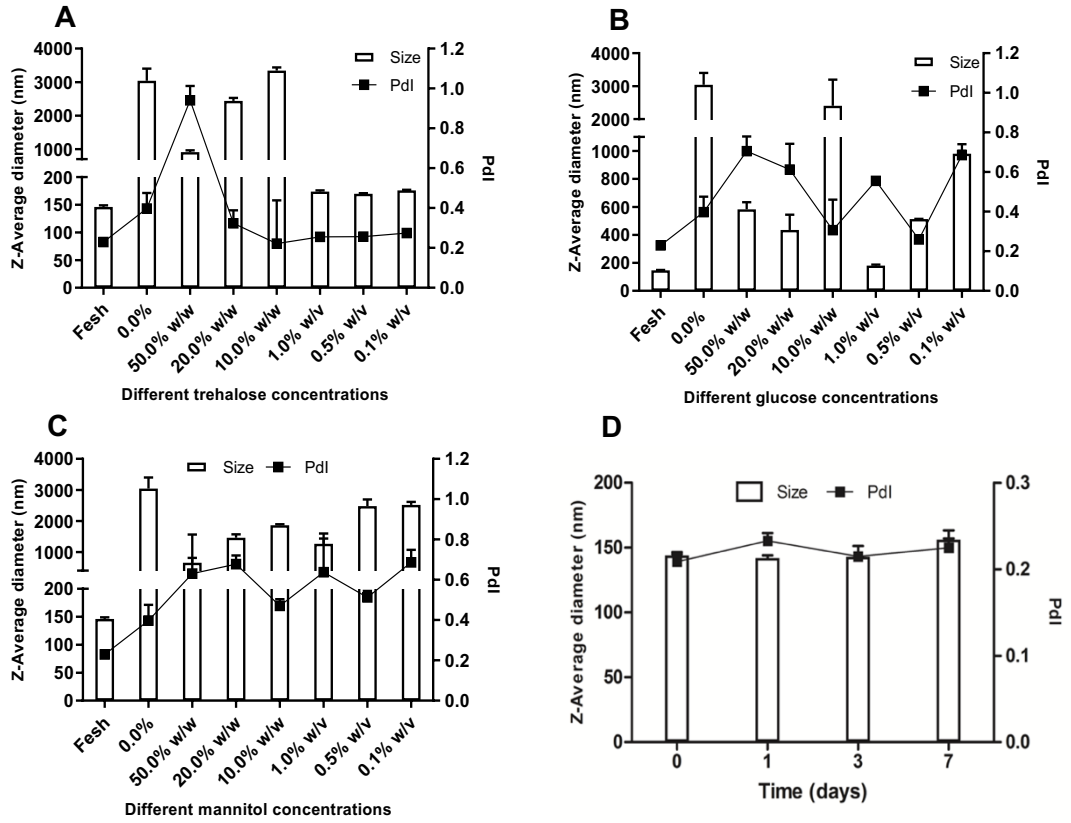

Figure 4.6. Effect of the cryoprotectants on micelles size and PdI and its stability at 4 ºC: (A) trehalose, (B) glucose and (C) mannitol. Micelles size and PdI during one week in water at 4 ºC (D).

4.4.6. Camptothecin release from mPEG-chitosan-oleic acid micelles in simulated gastrointestinal fluids

The CPT release from mPEG-CS-OA micelles was studied in simulated gastrointestinal fluids. Figure 4.7 shows the CPT release in the first 2h (SGF, pH 1.2, pepsin 0.32% w/v) and from 2 to 72 h (SIF, pH 6.8, pancreatin 1% w/v). Free CPT was used as control and presented a complete release after 24h, which agreed with other published works [6, 19]. Instead, polymeric micelles presented a low release of about 9% at gastric pH (SGF), but when transferred to the SIF, the CPT release started in a sustained and controlled manner up to 72 h. The transfer to the intestinal pH triggered the release of the drug, increasing from 9% to almost 45% in the final of the experiment, which may demonstrate a pH-dependent behavior of these micelles. This initial sustained release can be due to the drug entrapment in the micelles core and its difficulty in releasing itself from the micelle. Also, the pH-dependent profile can be explained since CS is extremely charged at acidic pH, which makes the CS chains very rigid, and this might difficult CPT release. At intestinal pH, CS is less charged, and the chains have more mobility, which may allow the CPT release.

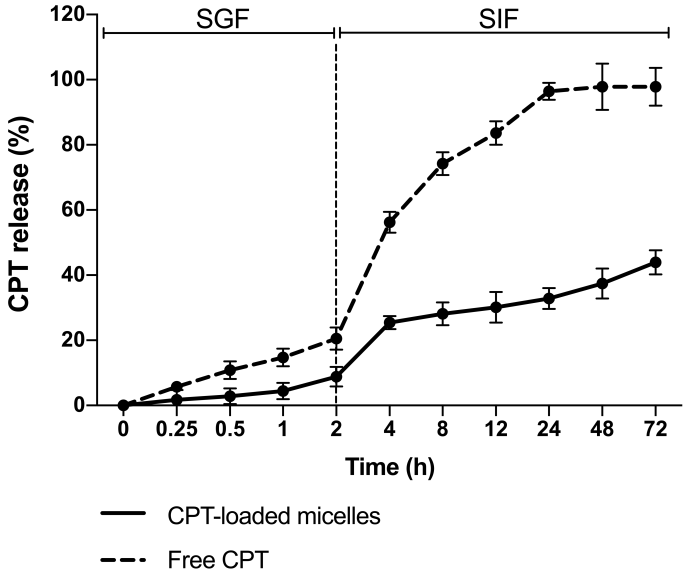

Figure 4.7. Cumulative CPT release in simulated gastrointestinal fluids during 72 h at 37 ºC.

In addition, and to understand the release mechanism of CPT from micelles, the release profile was adjusted to representative kinetic models as zero-order, first-order, Weibull and Korsmeyer-Peppas [72]. The assessed kinetic release parameters as constant rates and coefficient correlations are present in Table 4.4. The fitting was performed separately for SGF (pH 1.2) and SIF (pH 6.8). According to these data, and in the case of pH 1.2, all the models analyzed presented a high correlation with CPT release, revealing a diffusion of the drug from the polymeric micelles at the initial stage of release, which may be due to the CPT absorbed in the micelles surface. On the other hand, in the case of pH 6.8, the models that better fit to the experimental data were the Weibull and Korsmeyer-Peppas models, although the zero-order presented a good correlation as well. When analyzed according to the Weibull model, $b < 1$ (data not shown), revealing a Fickian diffusion combined with case II transport [73]. This agreed with the Korsmeyer-Peppas model, where $n < 0.5$ (data not shown), which also indicated a Fickian diffusion of CPT from mPEG-CS-OA micelles [74]. Indeed, the release behavior of a drug is strongly dependent on several factors such as the structure and properties of the polymeric micelles, type of drug, drug:polymer ratio, or drug-polymer-interactions. Other SD (mPEG and/or OA) could be tested and their AE and release profile evaluated to understand how AE may be improved as changes in the drug release.

Table 4.4. Constant rates (k) and correlation coefficients (R^2) obtained through the modeling of CPT release from mPEG-CS-OA micelles following: zero-order, first-order kinetic, Weibull, and Korsmeyer–Peppas models.

pH	Zero-order		First-order		Weibull		Korsmeyer–Peppas	
	k	R^2	k	R^2	k	R^2	k	R^2
1.2	4.2575	0.9920	0.2134	0.9907	0.8545	0.9944	0.8544	0.9947
6.8	0.2493	0.9792	0.2081	0.8459	0.1859	0.9614	0.1899	0.9614

4.4.7. Micelles protective effect on lactone ring form of camptothecin

Aiming to understand the CPT stability encapsulated into mPEG-CS-OA micelles, the protective effect of these micelles on preventing hydrolysis of CPT lactone ring under simulated gastrointestinal fluids was studied by HPLC. The CPT form (lactone or carboxylated) is fundamental to tumor treatment since the lactone form is much more efficient when compared to the carboxylated form and, the latter form has more potential cytotoxic effects [75]. As can be seen in Figure 4.8, free CPT and CPT released from the micelles maintained the lactone form in the first 2 h. However, when the pH changed to 6.8, free CPT lost almost 69% of its lactone form after 24 h of incubation, which indicates that once CPT was not protected, its lactone form was quickly converted into the inactive carboxylated form by hydrolysis. Compared with CPT encapsulated into the micelles, the lactone form was preserved up to 77% of its initial lactone form until the end of the experiment. Polymeric micelles significantly protected CPT from hydrolysis in simulated gastrointestinal fluids, improving CPT stability, revealing to be an advantageous carrier of CPT.

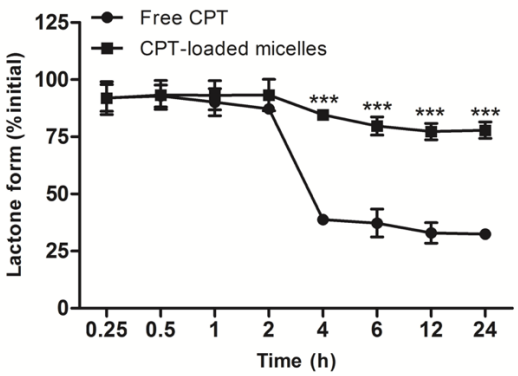

Figure 4.8. The effect of chitosan micelles on the CPT protection from hydrolysis over time in simulated gastrointestinal fluids.

4.5. Conclusion

Here we demonstrated a successful grafting of mPEG and OA into the CS backbone. With an improved polymer thermal stability and crystallinity after OA grafting, this modification allows the development of an amphiphilic polymer, which can form round shaped micelles with a diameter <150 nm. These mPEG-CS-OA micelles are able to encapsulate CPT efficiently and, the *in vitro* release exhibits a sustained and controlled release of CPT. Moreover, these micelles can protect CPT from hydrolysis up to 77% in simulated gastrointestinal fluids. Thus, we suggest this novel CS modification to produce polymeric micelles that could efficiently carry hydrophobic drugs, protecting and improving their stability after oral administration.

References

1. Bonferoni, M.C., et al., *Chitosan gels for the vaginal delivery of lactic acid: Relevance of formulation parameters to mucoadhesion and release mechanisms.* AAPS PharmSciTech, 2006. **7**(4): p. 141-147.
2. Rinaudo, M., *Main properties and current applications of some polysaccharides as biomaterials.* Polymer International, 2008. **57**(3): p. 397-430.
3. Choi, C., J.-P. Nam, and J.-W. Nah, *Application of chitosan and chitosan derivatives as biomaterials.* Journal of Industrial and Engineering Chemistry, 2016. **33**: p. 1-10.
4. Kean, T. and M. Thanou, *Biodegradation, biodistribution and toxicity of chitosan.* Advanced Drug Delivery Reviews, 2010. **62**(1): p. 3-11.
5. Sorlier, P., et al., *Relation between the degree of acetylation and the electrostatic properties of chitin and chitosan.* Biomacromolecules, 2001. **2**(3): p. 765-772.
6. Zhang, C., et al., *Polymeric micelle systems of hydroxycamptothecin based on amphiphilic N-alkyl-N-trimethyl chitosan derivatives.* Colloids and Surfaces B: Biointerfaces, 2007. **55**(2): p. 192-199.
7. Zhou, Y.-Y., et al., *Preparation and pharmacodynamics of stearic acid and poly (lactic-co-glycolic acid) grafted chitosan oligosaccharide micelles for 10-hydroxycamptothecin.* International Journal of Pharmaceutics, 2010. **393**(1-2): p. 144-152.
8. Mourya, V., N.N. Inamdar, and A. Tiwari, *Carboxymethyl chitosan and its applications.* Advanced Materials Letters, 2010. **1**(1): p. 11-33.
9. Wang, X., et al., *Preparation and evaluation of carboxymethyl chitosan-rhein polymeric micelles with synergistic antitumor effect for oral delivery of paclitaxel.* Carbohydrate Polymers, 2019. **206**: p. 121-131.
10. Prego, C., et al., *Chitosan–PEG nanocapsules as new carriers for oral peptide delivery: effect of chitosan pegylation degree.* Journal of Controlled Release, 2006. **111**(3): p. 299-308.
11. Leong, K., et al., *DNA-Polycation nanospheres as non-viral gene delivery vehicles.* Journal of Controlled Release, 1998. **53**(1-3): p. 183-193.
12. Sugimoto, M., et al., *Preparation and characterization of water-soluble chitin and chitosan derivatives.* Carbohydrate Polymers, 1998. **36**(1): p. 49-59.
13. Maisel, K., et al., *Nanoparticles coated with high molecular weight PEG penetrate mucus and provide uniform vaginal and colorectal distribution in vivo.* Nanomedicine, 2016. **11**(11): p. 1337-1343.

14. Huckaby, J.T. and S.K. Lai, *PEGylation for enhancing nanoparticle diffusion in mucus.* Advanced Drug Delivery Reviews, 2018. **124**: p. 125-139.
15. Aktaş, Y., et al., *Development and brain delivery of chitosan−PEG nanoparticles functionalized with the monoclonal antibody OX26.* Bioconjugate Chemistry, 2005. **16**(6): p. 1503-1511.
16. Csaba, N., et al., *Ionically crosslinked chitosan nanoparticles as gene delivery systems: effect of PEGylation degree on in vitro and in vivo gene transfer.* Journal of Biomedical Nanotechnology, 2009. **5**(2): p. 162-171.
17. Shi, Q., et al., *In vivo therapeutic efficacy of TNFα silencing by folate-PEG-chitosan-DEAE/siRNA nanoparticles in arthritic mice.* International Journal of Nanomedicine, 2018. **13**: p. 387.
18. Almeida, A., et al., *Synthesis and characterization of chitosan-grafted-polycaprolactone micelles for modulate intestinal paclitaxel delivery.* Drug Delivery and Translational Research, 2018. **8**(2): p. 387-397.
19. Silva, D.S., et al., *Self-aggregates of 3, 6-O, O'-dimyristoylchitosan derivative are effective in enhancing the solubility and intestinal permeability of camptothecin.* Carbohydrate Polymers, 2017. **177**: p. 178-186.
20. de Souza, R.H.F.V., et al., *Diethylaminoethyl-chitosan as an efficient carrier for siRNA delivery: Improving the condensation process and the nanoparticles properties.* International Journal of Biological Macromolecules, 2018. **119**: p. 186-197.
21. Chen, Z., et al., *A rapid hemostatic sponge based on large, mesoporous silica nanoparticles and N-alkylated chitosan.* Nanoscale, 2018. **10**(43): p. 20234-20245.
22. Larsson, M., et al., *Biomedical applications and colloidal properties of amphiphilically modified chitosan hybrids.* Progress in Polymer Science, 2013. **38**(9): p. 1307-1328.
23. Du, Y.-Z., et al., *Preparation and characteristics of linoleic acid-grafted chitosan oligosaccharide micelles as a carrier for doxorubicin.* Colloids and Surfaces B: Biointerfaces, 2009. **69**(2): p. 257-263.
24. Bonferoni, M., et al., *Ionic polymeric micelles based on chitosan and fatty acids and intended for wound healing. Comparison of linoleic and oleic acid.* European Journal of Pharmaceutics and Biopharmaceutics, 2014. **87**(1): p. 101-106.
25. Méndez, P.A., et al., *Chitosan/OA nanoparticle as delivery system for celecoxib: Parameters affecting the particle size, encapsulation, and release.* Journal of Applied Polymer Science, 2017. **134**(7).
26. Aranaz, I., R. Harris, and A. Heras, *Chitosan amphiphilic derivatives. Chemistry and applications.* Current Organic Chemistry, 2010. **14**(3): p. 308-330.

27. Silva, D.S., et al., *Synthesis and characterization of 3, 6-O, O'-dimyristoyl chitosan micelles for oral delivery of paclitaxel.* Colloids and Surfaces B: Biointerfaces, 2017. **152**: p. 220-228.
28. Guo, H., et al., *Self-assembled nanoparticles based on galactosylated O-carboxymethyl chitosan-graft-stearic acid conjugates for delivery of doxorubicin.* International Journal of Pharmaceutics, 2013. **458**(1): p. 31-38.
29. Balan, V., et al., *Doxorubicin-loaded magnetic nanocapsules based on N-palmitoyl chitosan and magnetite: synthesis and characterization.* Chemical Engineering Journal, 2015. **279**: p. 188-197.
30. Min, K.H., et al., *Hydrophobically modified glycol chitosan nanoparticles-encapsulated camptothecin enhance the drug stability and tumor targeting in cancer therapy.* Journal of Controlled Release, 2008. **127**(3): p. 208-218.
31. Cai, G. and H. Jiang, *pH-sensitive nanoparticles self-assembled from a novel class of biodegradable amphiphilic copolymers based on chitosan.* Journal of Materials Science: Materials in Medicine, 2009. **20**(6): p. 1315-1320.
32. Huang, Y., et al., *Structure and self-assembly properties of a new chitosan-based amphiphile.* The Journal of Physical Chemistry B, 2010. **114**(23): p. 7719-7726.
33. Liu, G., et al., *Synthesis and characterization of an amphiphilic chitosan bearing octyl and methoxy polyethylene glycol groups.* Natural Science, 2010. **2**(7): p. 707-712.
34. Mai-ngam, K., *Comblike poly (ethylene oxide)/hydrophobic C6 branched chitosan surfactant polymers as anti-infection surface modifying agents.* Colloids and Surfaces B: Biointerfaces, 2006. **49**(2): p. 117-125.
35. Sagnella, S. and K. Mai-Ngam, *Chitosan based surfactant polymers designed to improve blood compatibility on biomaterials.* Colloids and Surfaces B: Biointerfaces, 2005. **42**(2): p. 147-155.
36. Novoa-Carballal, R., R. Riguera, and E. Fernandez-Megia, *Disclosing an NMR-invisible fraction in chitosan and PEGylated copolymers and its role on the determination of degrees of substitution.* Molecular Pharmaceutics, 2013. **10**(8): p. 3225-3231.
37. Fernandez-Megia, E., et al., *Optimal routine conditions for the determination of the degree of acetylation of chitosan by 1H-NMR.* Carbohydrate Polymers, 2005. **61**(2): p. 155-161.
38. Vázquez, J.A., et al., *An integral and sustainable valorisation strategy of squid pen by-products.* Journal of Cleaner Production, 2018. **201**: p. 207-218.
39. Sorlier, P., et al., *Light scattering studies of the solution properties of chitosans of varying degrees of acetylation.* Biomacromolecules, 2003. **4**(4): p. 1034-1040.

40. Satake, K., et al., *The spectrophotometric determination of amine, amino acid and peptide with 2, 4, 6-trinitrobenzene 1-sulfonic acid.* The Journal of Biochemistry, 1960. **47**(5): p. 654-660.
41. Kyrili, A., et al., *Design and development of pH-sensitive liposomes by evaluating the thermotropic behavior of their chimeric bilayers.* Journal of Thermal Analysis and Calorimetry, 2017. **127**(2): p. 1381-1392.
42. Halder, N. and C. Wagner, *Analysis of the broadening of powder pattern peaks using variance, integral breadth, and Fourier coefficients of the line profile*, in *Advances in X-ray Analysis*. 1966, Springer. p. 91-102.
43. Fluksman, A. and O. Benny, *A robust method for critical micelle concentration determination using coumarin-6 as a fluorescent probe.* Analytical Methods, 2019. **11**(30): p. 3810-3818.
44. Ataci, N. and A. Sarac, *Determination of critical micel concentration of PEG-10 tallow propane amine: effects of salt and pH.* American Journal of Analytical Chemistry, 2014. **5**(1): p. 22.
45. Opanasopit, P., et al., *Incorporation of camptothecin into N-phthaloyl chitosan-g-mPEG self-assembly micellar system.* European Journal of Pharmaceutics and Biopharmaceutics, 2006. **64**(3): p. 269-276.
46. Martins, S.M., et al., *Development and validation of a simple reversed-phase HPLC method for the determination of camptothecin in animal organs following administration in solid lipid nanoparticles.* Journal of Chromatography B, 2012. **880**: p. 100-107.
47. Fassberg, J. and V.J. Stella, *A kinetic and mechanistic study of the hydrolysis of camptothecin and some analogues.* Journal of Pharmaceutical Sciences, 1992. **81**(7): p. 676-684.
48. Van de Velde, K. and P. Kiekens, *Structure analysis and degree of substitution of chitin, chitosan and dibutyrylchitin by FT-IR spectroscopy and solid state 13C NMR.* Carbohydrate Polymers, 2004. **58**(4): p. 409-416.
49. Kolhe, P. and R.M. Kannan, *Improvement in ductility of chitosan through blending and copolymerization with PEG: FTIR investigation of molecular interactions.* Biomacromolecules, 2003. **4**(1): p. 173-180.
50. Bhattarai, N., et al., *PEG-grafted chitosan as an injectable thermosensitive hydrogel for sustained protein release.* Journal of Controlled Release, 2005. **103**(3): p. 609-624.
51. Shukla, N., et al., *FTIR study of surfactant bonding to FePt nanoparticles.* Journal of Magnetism and Magnetic Materials, 2003. **266**(1-2): p. 178-184.

52. Li, Y.Y., et al., *Aggregation of hydrophobically modified chitosan in solution and at the air–water interface.* Journal of Applied Polymer Science, 2006. **102**(2): p. 1968-1973.
53. Novoa-Carballal, R. and A.H. Müller, *Synthesis of polysaccharide-b-PEG block copolymers by oxime click.* Chemical Communications, 2012. **48**(31): p. 3781-3783.
54. Ohya, Y., et al., *Preparation of PEG-grafted chitosan nanoparticles as peptide drug carriers.* STP Pharma Sciences, 2000. **10**(1): p. 77-82.
55. Kulkarni, A.R., et al., *A novel method for the preparation of nanoaggregates of methoxy polyethyleneglycol linked chitosan.* Journal of Nanoscience and Nanotechnology, 2006. **6**(9-10): p. 2867-2873.
56. Medrano, R., et al., *Analysis of copolymers of styrene and methyl methacrylate using size exclusion chromatography with multiple detection.* Physical Chemistry Chemical Physics, 2003. **5**(1): p. 151-157.
57. Neto, C.d.T., et al., *Thermal analysis of chitosan based networks.* Carbohydrate Polymers, 2005. **62**(2): p. 97-103.
58. Xia, Y., et al., *Facile synthesis and self-assembly of amphiphilic polydimethylsiloxane with poly (ethylene glycol) moieties via thiol-ene click reaction.* RSC Advances, 2015. **5**(63): p. 50955-50961.
59. García-Zapateiro, L., et al., *Viscous, thermal and tribological characterization of oleic and ricinoleic acids-derived estolides and their blends with vegetable oils.* Journal of Industrial and Engineering Chemistry, 2013. **19**(4): p. 1289-1298.
60. Giron, D., *Applications of thermal analysis and coupled techniques in pharmaceutical industry.* Journal of Thermal Analysis and Calorimetry, 2002. **68**(2): p. 335-357.
61. Chiu, M.H. and E.J. Prenner, *Differential scanning calorimetry: An invaluable tool for a detailed thermodynamic characterization of macromolecules and their interactions.* Journal of Pharmacy and Bioallied Sciences, 2011. **3**(1): p. 39.
62. Zhao, Y., et al., *Synthesis and characterization of graft copolymer of chitosan and polyethylene glycol.* Molecular Biology Reports, 2011. **38**(4): p. 2455-2462.
63. Li, Y., et al., *Cellulose-based solid–solid phase change materials synthesized in ionic liquid.* Solar Energy Materials and Solar Cells, 2009. **93**(8): p. 1321-1328.
64. Kawada, J., et al., *Crystalline transformation of chitosan from hydrated to anhydrous polymorph via chitosan monocarboxylic acid salts.* Journal of Carbohydrate Chemistry, 1999. **18**(5): p. 559-571.
65. Bu, W., et al., *Oleic acid/oleylamine cooperative-controlled crystallization mechanism for monodisperse tetragonal bipyramid NaLa (MoO4) 2 nanocrystals.* The Journal of Physical Chemistry C, 2009. **113**(28): p. 12176-12185.

66. Jeong, Y.-I., et al., *Preparation and spectroscopic characterization of methoxy poly (ethylene glycol)-grafted water-soluble chitosan.* Carbohydrate Research, 2008. **343**(2): p. 282-289.
67. Belabassi, Y., et al., *Synthesis and characterization of PEGylated and fluorinated chitosans: Application to the synthesis of targeted nanoparticles for drug delivery.* Biomacromolecules, 2017. **18**(9): p. 2756-2766.
68. Lee, K.Y., et al., *Physicochemical characteristics of self-aggregates of hydrophobically modified chitosans.* Langmuir, 1998. **14**(9): p. 2329-2332.
69. Duan, K., et al., *Fabrication of cationic nanomicelle from chitosan-graft-polycaprolactone as the carrier of 7-ethyl-10-hydroxy-camptothecin.* Colloids and Surfaces B: Biointerfaces, 2010. **76**(2): p. 475-482.
70. Feng, H. and C.-M. Dong, *Preparation, characterization, and self-assembled properties of biodegradable chitosan− poly (l-lactide) hybrid amphiphiles.* Biomacromolecules, 2006. **7**(11): p. 3069-3075.
71. Fonte, P., S. Reis, and B. Sarmento, *Facts and evidences on the lyophilization of polymeric nanoparticles for drug delivery.* Journal of Controlled Release, 2016. **225**: p. 75-86.
72. Costa, P. and J.M.S. Lobo, *Modeling and comparison of dissolution profiles.* European Journal of Pharmaceutical Sciences, 2001. **13**(2): p. 123-133.
73. Papadopoulou, V., et al., *On the use of the Weibull function for the discernment of drug release mechanisms.* International Journal of Pharmaceutics, 2006. **309**(1-2): p. 44-50.
74. Korsmeyer, R.W., E. Von Meerwall, and N.A. Peppas, *Solute and penetrant diffusion in swellable polymers. II. Verification of theoretical models.* Journal of Polymer Science Part B: Polymer Physics, 1986. **24**(2): p. 409-434.
75. Burke, T.G. and Z. Mi, *The structural basis of camptothecin interactions with human serum albumin: impact on drug stability.* Journal of Medicinal Chemistry, 1994. **37**(1): p. 40-46.

CHAPTER 5

A scale-up strategy for the synthesis of chitosan derivatives used in micellar nanomedicines

The information provided in this chapter was based in the following publication:

Almeida, A., Günday-Türeli, N. & Sarmento, B., 2021. A scale-up strategy for the synthesis of chitosan derivatives used in micellar nanomedicines, *submitted*.

In this paper, I was responsible for the conception, execution and revision of the manuscript. Nazende Günday-Türeli was responsible for the methodology and the supervisor was responsible for reviewing and submit the manuscript. This paper was not previously included in other thesis and it is partially reproduced in this section.

5.1. Abstract

Nanomedicines have been increasingly investigated and used by pharmaceutical industry due to their potential in solving various public health problems. However, standardizing and approving nanomedicines remains a significant challenge, as the translation from the laboratory to the market is still limited. These constraints are due to a lack of reproducibility and standardization of procedures, small batch sizes due to inability to scale-up, or the associated production costs as a result of the production methods chosen. In this work, two chitosan derivatives, methoxypolyethylene glycol-chitosan (mPEG-CS) and methoxypolyethylene glycol-chitosan-oleic acid (mPEG-CS-OA), produced at the lab scale were implemented in a pharmaceutical industry to achieve the scale-up production using cross flow filtration (CFF). The two copolymers were shown to be capable of retaining their physicochemical properties when produced in larger batch sizes, with reduced production time and increased yield. Also, both chitosan derivatives presented no *in vitro* cytotoxicity independent of the method of production. Furthermore, after scale-up, polymeric micelles produced from mPEG-CS-OA were tested for storage stability, demonstrating that micelles remained stable at – 20 ºC for at least 6 months. This study demonstrated the feasibility of producing polymers and polymeric micelles closer to the bedside due to their suitability for GMP production.

5.2. Introduction

Among the various existing routes of administration, the oral route is the one that attracts more researchers and clinicians due to its advantages such as ease of administration, patient acceptance and the practicality of solid formulations [1, 2]. However, and unlike other administration routes, oral delivery becomes more complex when it comes to drug transport and absorption.

Several factors may affect the intestinal transport of drugs as the solubility, must be resistant to the physical and biochemical barriers of the gastrointestinal tract (GIT) such as the presence of mucus, enzymes, pH differences along the GIT and, must resist metabolic degradation to be absorbed into the blood when systemic treatment is desired [3-5].

Nanotechnology has evolved to respond to the existing limitations of oral drug transport and absorption. The production of drug carrier vehicles, such as nanoparticles, liposomes or polymeric micelles, has allowed the release of drugs at their target site, overcoming the physical and biochemical limitations mentioned above. Furthermore, nanomedicines have allowed for the optimization of drug dosage in order to reduce side effects, as nanoformulations are more stable than free drugs, with a longer residence time and the ability to transport a large amount of drug into the intestine [6, 7]. However, although

nanotechnology is highly attractive and promising compared to conventional therapies, there is still a major flaw in the translation of new formulations to clinical phases or even to the market.

The translation of nanomedicines from the lab scale into clinical trials or even the market has been limited by the industrial-scale production quantities and quality required [8]. As a result, establishing good manufacturing practices (GMP) for large-scale production of nanoformulations is critical for the successful transfer from bench to bedside. Other factors such as the starting material, namely the type of excipient, the active molecule, or the formulation design, all play an important role in the regulatory compliance of nanoformulations [9]. Manufacturing process issues such as scale-up, batch-to-batch irreproducibility, low production rate, and high production costs are other factors that contribute to the formulation not reaching the market, which is primarily due to the lack of implemented GMP. The physicochemical characterization of the nanoformulation should be kept before and after the scale-up, however, at the lab scale, it is difficult to maintain the same properties with the available equipment [8].

Purification of the nanoformulation is a critical step in the development process. Conventional methods, such as dialysis or centrifugation, are time-consuming processes that can not be applied on an industrial scale. Cross flow filtration (CFF) is a purification method in which the tangential flow of the medium is applied to improve the filtration process without clogging [9]. This method enables scaling-up and sterility of the process, reducing time and cost, and, once established, it can be used in a GMP environment without lot size limitations due to its continuous processing. We hypothesized in this study that bench-scale production of two chitosan derivatives could be scaled-up to industrial batch production, while retaining the same physicochemical properties. Furthermore, polymeric micelles were formed from the mPEG-CS-OA polymer, and their stability and properties were maintained for 6 months. Thus, CFF pioneered the synthesis of these copolymers, biomaterials with exceptional properties for the development of nanomedicines [10], as an alternative to the traditional method [11]. In this sense, it was possible to improve manufacturing time, reduce batch-to-batch irreproducibility, and achieve large-scale production while adhering to the International Conference on Harmonization (ICH) guidelines as closely as possible. These factors are critical not only for *in vitro* and *in vivo* testing, but also for determining the formulation's future to the bedside.

5.3. Materials and Methods

5.3.1. Materials

Chitosan (CS, 112 kDa, 15% acetylated), N-(3-dimethylaminopropyl)-N′- ethylcarbodiimide hydrochloride (EDC·HCl), 1-hydroxybenzotriazole hydrate (HOBt), oleic acid (OA) and *O*-methyl-*O*′-succinyl polyethylene glycol 5′000 (mPEG-COOH), were all purchased from Sigma-Aldrich. Ultracel® 30 kDa ultrafiltration discs (PLTK04310, 44.5 mm diameter, Merck Millipore) and a 3.5 kDa cutoff dialysis membrane (regenerated cellulose, Spectra/Por® 3 Dialysis Tubing, Fisher Scientific) were used to purify the mPEG-CS and mPEG-CS-OA polymers, respectively, by the bench method. CFF membranes (Spectra/Por®, 10 and 50 kDa) was used to purify the polymers by the continuous manufacturing method. Camptothecin (CPT) was purchased from Hangzhou ROYAL Import & Export Co., Ltd. 3-(4,5-Dimethylthiazol-2-yl)-2,5-diphenyltetrazolium bromide (MTT) and dimethyl sulfoxide (DMSO) were obtained from Sigma-Aldrich, triton X-100 from Spi-Chem.

5.3.2. Polymer synthesis at bench scale

5.3.2.1. Synthesis of methoxypolyethylene glycol-chitosan

The synthesis and purification of methoxypolyethylene glycol-chitosan (mPEG-CS) at the bench side was previously described [13]. Briefly, 250 mg of CS was solubilized in 10 mL of HCl and the pH adjusted to 5.5 with NaOH. mPEG-COOH was mixed with CS at a stoichiometric ratio of 5%, following the addition of HOBt. The pH was again adjusted to 5.5 and EDC·HCl was added to the solution, which was left under stirring at RT overnight. The final product was purified by ultrafiltration with a 30 kDa membrane with 5 washing steps with HCl 10^{-3} M and 3 washing steps with MilliQ water to exclude the unreacted mPEG-COOH, HOBt and EDC·HCl and the reaction byproducts. The new product, mPEG-CS, was freeze-dried and stored at -20 ºC until further utilization.

5.3.2.2. Synthesis of methoxypolyethylene glycol-chitosan-oleic acid

The synthesis and purification of methoxypolyethylene glycol-chitosan-oleic acid (mPEG-CS-OA) was also previously described [13]. Briefly, 300 mg mPEG-CS was solubilized with 60 mL of HCl and the pH adjusted to 5.5 with NaOH. Ethanol was added to the solution following the addition of OA at a stoichiometric ratio of 5%. Then, HOBt was added to the mixture and the pH was again adjusted to 5.5 following the addition of EDC·HCl. The mixture was left under stirring overnight at RT and the polymer purification was performed by dialysis method against water during 3 days with 3 water-cycles renewal in order to exclude the unreacted OA, HOBt, EDC·HCl and the reaction byproducts. The new product, mPEG-CS-OA, was freeze-dried and stored at -20 ºC until further utilization.

5.3.3. Polymer synthesis by scale-up continuous manufacturing

CFF is a fast and effective method for separating and purifying substances in which the fluid is pumped tangentially over the membrane's surface. As the fluid is pumped against the membrane walls, everything smaller than the membrane pore size is permeated and eliminated from the filtration system, and everything bigger than the membrane molecular weight continues to be pumped until all impurities and by-products of a synthesis for example, are eliminated. CFF membranes constituted by hollow fibers are easy to set-up and the loss of product is negligible. The graphical abstract describes the operation of the CFF.

5.3.3.1. Synthesis of methoxypolyethylene glycol-chitosan

The synthesis of mPEG-CS occurred in the same way as described in Section 5.3.2.1, with a ten-time fold increase on the amount of the polymer used for the carbodiimide reaction. Additionally, the purification process was changed from the ultrafiltration to the CFF method. Briefly, the mixture of the previous reaction was purified against water using a 50 kDa CFF membrane in a close loop and, the water volume to wash the polymer was 10-fold more, compared to the bench method. The new product, mPEG-CS, was concentrated to a minimum, collected to be freeze-dried and stored at -20 ºC until further utilization.

5.3.3.2. Synthesis of methoxypolyethylene glycol-chitosan-oleic acid

The synthesis of mPEG-CS-OA occurred in the same way as described in Section 5.3.2.2, however, the amount of the polymer used for the carbodiimide reaction was also 10-fold more. Additionally, the purification process was changed from dialysis to the CFF method. Briefly, the mixture of the previous reaction was purified against water using a 10 kDa CFF membrane in a close loop and, the water volume to wash the polymer was 10-fold more, compared to the bench method. The new product, mPEG-CS-OA, was concentrated to a minimum, collected to be freeze-dried and stored at -20 ºC until further utilization.

5.3.4. Physicochemical characterization of the copolymers

Both mPEG-CS and mPEG-CS-OA produced either by the bench or by the continuous manufacturing method were characterized by FTIR and ^{1}H NMR spectroscopy as previously described [13, 14]. The mPEG substitution degree was calculated from the ratio between integrals of the mPEG methylene group peaks and the number of mPEG protons by the H1 of the chitosan glucosamine residue in the ^{1}H NMR spectra. The oleic acid substitution degree was determined using the ratio between the integrals of the oleic acid peaks and

the total number of oleic acid protons by the H1 of monosaccharide residue in the ^{1}H NMR spectra.

5.3.5. Cell culture

C2BBe1 [Caco-2 clone] (human colorectal adenocarcinoma) cells were acquired from ATCC and HT29-MTX mucus-producing cells were kindly provided by Dr. T. Lesuffleur (INSERM U178, Villejuif, France). Dulbecco's Modified Eagle's Medium (DMEM, ATCC) supplemented with 10% (v/v) Fetal Bovine Serum (FBS, Biochrom) and 1% (v/v) antibiotic-antimitotic mixture (final concentration of 100 U/mL penicillin and 100 U/mL streptomycin, Biowest) was used to culture both cell lines. Caco-2 and HT29-MTX were cultured in 75 cm^2 T-flasks, inside an incubator at 37 ºC and 5% CO_2 and 95% relative humidity.

5.3.6. Cell viability assessment of the produced polymers

To assess the safety of the polymers produced either by the bench or the continuous manufacturing method, a cell metabolic assay was performed. Briefly, 2×10^4 Caco-2 cells and 1×10^4 HT29-MTX cells were seeded in 96-well plates and incubated at 37 ºC and 5% CO_2 and 95% relative humidity (RH) so that the cells adhere to the bottom of the well. The culture medium was removed after 24 h, and the cells were washed twice with pre-warmed PBS before being treated with 200 µL of mPEG-CS (0.31 to 10 mg/mL) or 200 µL of mPEG-CS-OA (0.16 to 5.00 mg/mL) for 4 and 24 hours at 37 ºC. Then, the medium was removed and the remaining cells were washed twice with pre-warmed PBS and incubated MTT solution at 0.5 mg/mL for 4 h in the dark at 37 ºC. After that, MTT solution was removed and DMSO was added to each well to dissolve the formazan crystals formed as product of the reaction and plates were placed under shaking to facilitate the dissolution of the crystals. The absorbance was measured using a microplate reader SynergyTM Mx HM550 (Biotek) set at 570 and 630 nm. A negative and a positive control were also included in the experiment, which corresponds to Triton X – 100 1% (v/v) and cell culture medium, respectively. A number of three replicates were performed for each group and, the cell viability was quantified according to Equation 5.1:

$$Cellular\ viability\ (\%) = \frac{absorbance\ (experimental\ value) - absorbance\ (positive\ control)}{absorbance\ (negative\ control) - ababsorbance\ (positive\ control)} \times 100 \qquad (5.1)$$

5.3.7. Production and characterization of chitosan-based polymeric micelles

Using the industrial pilot batch of the polymer mPEG-CS-OA, which has amphiphilic properties, chitosan micelles were produced by self-assembly as previously described [11], to test its stability overtime. Briefly, mPEG-CS-OA was dissolved in a mixture of DMSO:HCl 0.1 M (9:1) overnight. The copolymer was dialyzed against water with three cycles of water renewal and then centrifugated at 3110 g for 20 min. After, polymeric micelles were cryopreserved with 0.5 % (w/v) trehalose and freeze-dried.

5.3.8. Long-term storage study

In other to assess the stability of the micelles over time, a 6-month long-term stability study was performed with freeze-dried micelles following the ICH guidelines [13]. Micelles were placed at four different conditions: -20 ± 2 ºC, 4 ± 2 ºC, 25 ± 2 ºC/60 ± 5% RH and, 40 ± 2 ºC/75 ± 5% RH in a Climacell chamber from MMM Medcenter Einrichtungen GmbH (Planegg, Germany). The size, polydispersity index, surface charge and morphology were assessed by DLS and TEM, as previously described [11, 12] at four different times after 0 (t0), 1 (t1), 3 (t3) and 6 (t6) months of storage (n=3).

5.3.9. Statistical analysis

Statistical analysis was performed using the GraphPad Prism Software vs. 6.0 (GraphPad Software Inc) using two-way analysis of variance (ANOVA) Sidak's or Dunnett's multiple comparison test. All data were presented as mean ± standard deviation.

5.4. Results and Discussion

5.4.1. Characterization of the polymers

Chitosan grafted with mPEG (mPEG-CS) and mPEG-CS grafted with oleic acid (mPEG-CS-OA) were synthesized via a carbodiimide amidation reaction of chitosan amine groups with mPEG and oleic acid carboxylic groups. Both syntheses were performed following the bench procedure [11], but the purification method was changed for the CFF. The success of the reaction of mPEG-CS and mPEG-CS-OA was confirmed by ^{1}H NMR and ATR-FTIR and it is presented below, Figure 5.1 and 5.2, respectively.

As can be seen in Figure 5.1A, the ^{1}H NMR spectra demonstrated that both bench and scaled-up polymers presented the characteristic peaks of chitosan: peak at δ = 4.88 ppm (H-1) was referred to the hydrogen-bonded of the anomeric carbon of N-glucosamine units in chitosan, peaks at δ = 3.5–4.0 ppm (H-3, H-4, H-5, and H-6), were referred to the

methylene chitosan protons, δ = 2.05 (H-7) and peaks at δ = 3.18 (H-2) ppm were referred to $-COCH_3$ and proton in $CHNH_2$ protons in the chitosan backbone, respectively. Furthermore, the mPEG-COOH characteristic peaks were shown in the mPEG-CS bench and scaled-up spectra, such as the peaks at δ = 3.70 ppm (H-b and H- c) and at δ = 3.52 ppm (H-d) [14]. Thus, the presence of both chitosan and mPEG-COOH characteristic peaks in the copolymer spectra confirms not only the success of the reaction, but also the success of the up-scaling, as the same chemical shifts were demonstrated for the two mPEG-CS bench and scaled-up syntheses. The ATR-FTIR analysis corroborate with the ^{1}H NMR study. In Figure 5.1B, it is possible to observe the characteristic bands of chitosan and mPEG-COOH in the mPEG-CS bench and scaled-up spectra, such as the assigned bands at 2780-3000 cm^{-1}, referred to the overlap of C-H stretching vibrations of chitosan and mPEG-COOH [15], and the bands at 1637 and 1522 cm^{-1}, referred to chitosan chemical shift of the amide I and II bands, as result of the successful reaction between chitosan and mPEG-COOH. Furthermore, the peak at 1731 cm^{-1} corresponding to the (C=O stretching) does not appear on the copolymer spectra in the physical mixture of chitosan and mPEG-COOH (mPEG+CS), demonstrating that the polymer purification (either ultrafiltration or CFF) was carried out successfully, with no free mPEG present.

The same was demonstrated for the mPEG-CS-OA modification. In Figure 5.2A, the spectrum of mPEG-CS-OA bench and scaled-up polymers demonstrated the characteristic peaks of chitosan and mPEG, as previously detailed and, the oleic acid characteristic peaks at δ = 0.75 ppm (H-30), at δ = 1.15 ppm (H-15 to H-19 and H-25 to H-28) and at δ = 5.20 ppm (H-21 and H-22) referred to the methyl group of oleic acid, the oleic acid methylene groups and the ethylene group of oleic acid, respectively [16]. Both mPEG-CS-OA bench and scaled-up presented same chemical shifts, which means that changing the purification method did not change the structure of the polymer or the success of the synthesis.

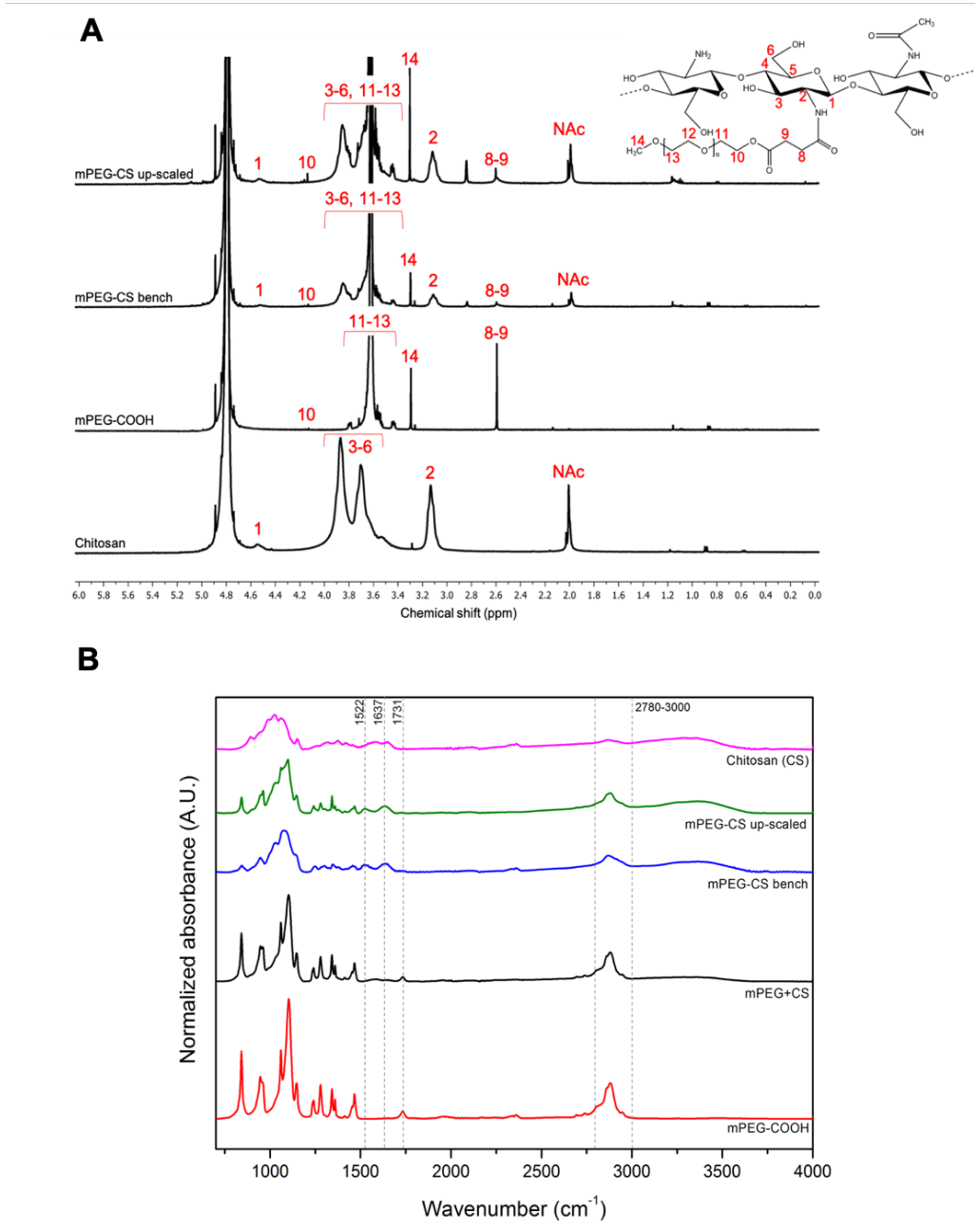

Figure 5.1. (A) ^{1}H NMR spectra of chitosan, mPEG-COOH and mPEG-CS bench scale and mPEG-CS scaled-up in 2% DCl (1 mg/mL, 400 MHz) and (B) ATR-FTIR spectra of mPEG-COOH, physical mixture of mPEG-COOH and CS, mPEG-CS bench scale, mPEG-CS scaled-up and chitosan (CS).

The same pattern can be seen in Figure 5.2B. The ATR-FTIR analysis demonstrated the characteristic bands of chitosan and mPEG, already enumerated, as the characteristic band of oleic acid between 2800-3000 cm^{-1} referred to the CH_2 stretching in the alkyl chain of oleic acid. Moreover, the oleic acid band at 1700 cm^{-1}, referred to the carboxylic group, was present in the physical mixture of mPEG-CS and oleic acid (mPEG-CS+OA), but was not present in the spectra of mPEG-CS-OA copolymers, as result of the amide reaction. Additionally, it was possible to verify the chemical shift of the amide I and II of chitosan

(1635 and 1540 cm^{-1}), as a result of the reaction between the chitosan amine groups with the oleic acid carboxyl groups [17]. This indicates that the purification method did not alter the polymer structurally since scaled-up mPEG-CS-OA synthesis could reproduce the same chemical structure as bench synthesis.

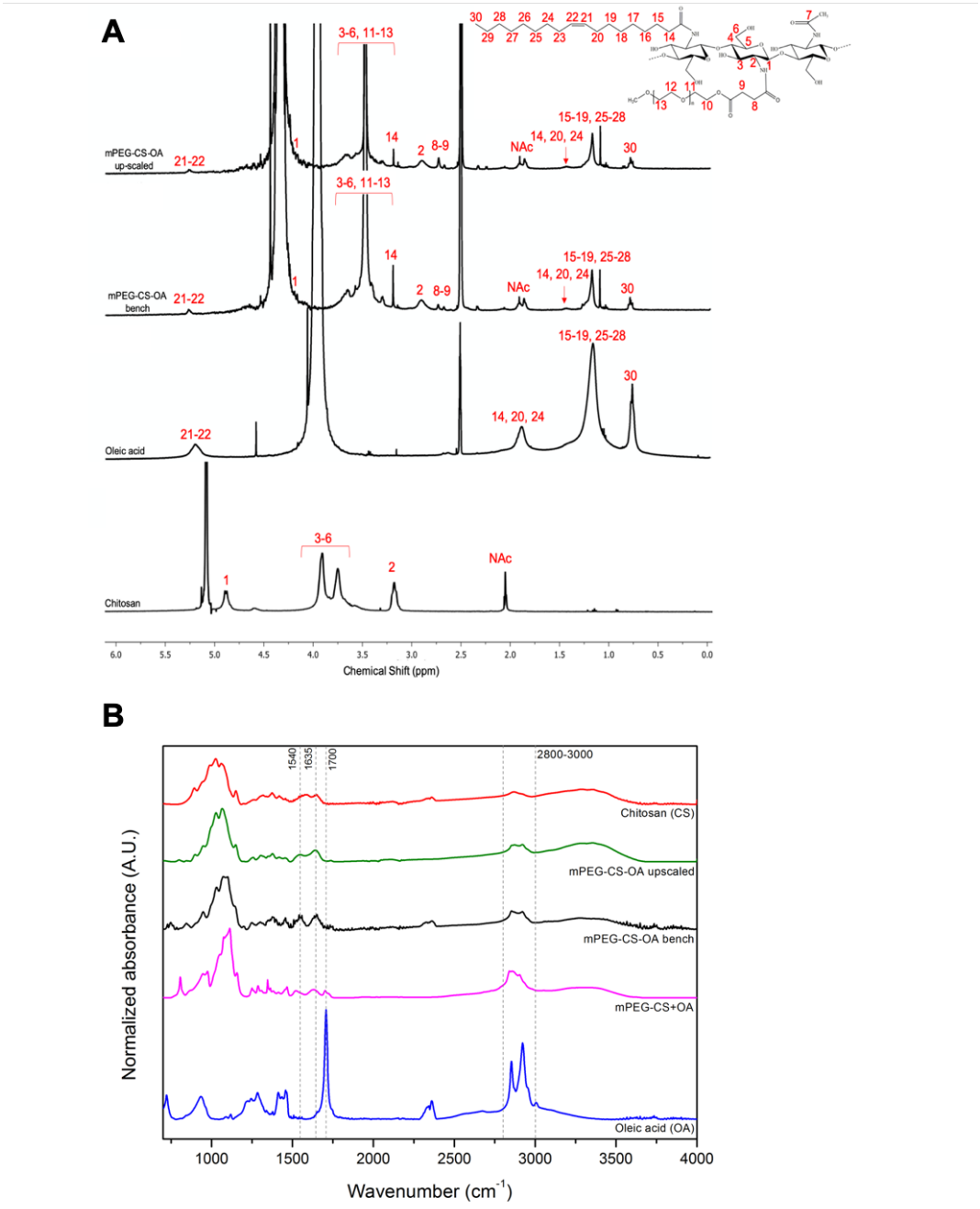

Figure 5.2. (A) ^{1}H NMR spectra of chitosan, oleic acid and mPEG-CS-OA bench scale and mPEG-CS-OA scaled-up in 2% DCl (1 mg/mL, 400 MHz) and (B) ATR-FTIR spectra of oleic acid, physical mixture of mPEG-CS and oleic acid, mPEG-CS-OA bench scale, mPEG-CS-OA scaled-up and chitosan (CS).

It is interesting to note that, although there are no structural differences in the chemical synthesis of the two polymers, it is possible to identify other differences such as the time of synthesis, the yield and the degree of substitution (Table 5.1). With the modification of the purification method for the CFF, the time required for the synthesis of mPEG-CS decreased almost 3 times and the yield improved from 67 to 85%. The same was observed for the mPEG-CS-OA reaction, where the time required to complete the synthesis decreased almost 2 times and the yield increased from 59 to 87%. This was a great advantage compared to the traditional bench method of production, since the time needed to produce the polymers is much less and the yield is much higher. It is important to note that, in addition to being a continuous process, the starting amount of the copolymer in the CFF method is greater; nevertheless, its purification takes less time and produces a higher yield. Thus, the time of production was essentially improved by the purification method, which also contributed to a greater recovery of the copolymer. These features are essential when translating a product from the bench to the market. The mPEG-COOH and oleic acid substitution degree did not change significantly, which means that polymers purified by different methods and in different amounts present the same physicochemical structure after production.

Table 5.1. Relationship between bench synthesis and continuous manufacturing method methods regarding the manufacturing time, substitution degree calculated by ^{1}H NMR and the yield.

Polymer	Method	Time of production (days)	Yield (%)	Substitution degree (%)
mPEG-CS	Bench synthesis	8	67 ± 2	4.3 ± 0.2
	Continuous manufacturing method	3	85 ± 3	4.8 ± 0.3
mPEG-CS-OA	Bench synthesis	5	59 ± 4	5.8 ± 2.9
	Continuous manufacturing method	3	87 ± 3	5.3 ± 1.2

5.4.3. In vitro safety of the produced polymers

Both mPEG-CS and mPEG-CS-OA produced by the bench or continuous manufacturing methods were evaluated regarding its safety profile. mPEG-CS (0.32 to 10 mg/mL) and

mPEG-CS-OA (0.16 to 5.00 mg/mL) were tested against Caco-2 and HT29-MTX cells for 4 and 24h of incubation. As can be seen in Figure 5.3, all the polymers presented a cellular viability close to the 100%. Indeed, according to the ISO 10993-5 guideline [18], it is reported that above 70% of cell viability is considered as safe, when testing in vitro formulations. As a result, none of the polymers demonstrated a cytotoxic profile at all concentrations tested. On the other hand, it was possible to verify a slight decrease on the cellular viability after 24h of incubation compared with 4 h of incubation. Inclusively, in Figure 5.3D this decrease was statistically significant, however, it is not biological relevant regarding the safety of the polymer since the cellular viability is still high. The same pattern was found in both cell lines and, these results agree with other published works where polymer-based chitosan were used [19-21].

More importantly, it should be noted that the polymers produced by the traditional method (Figure 5.3A and C) compared to the industrial method (Figure 5.3B and D), had very comparable cellular viability values. This means that the purification process was efficient and could remove the organic solvents used in the synthesis, and so, a safe polymer is obtained in the same way as in the laboratory, but in a much higher amount.

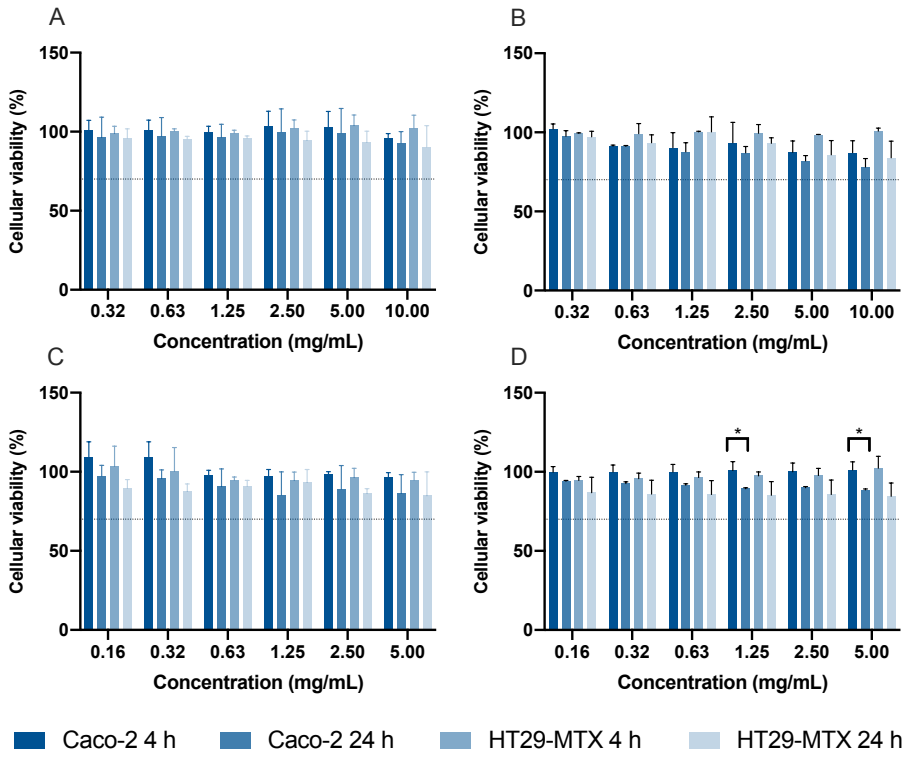

Figure 5.3. Cellular viability of (A) mPEG-CS from the bench synthesis (B) mPEG-CS from the continuous manufacturing method (C) mPEG-CS-OA from the bench synthesis (D) from the continuous manufacturing method tested in Caco-2 and HT29-MTX colorectal cancer cell lines during 4 and 24 h of incubation. Error bars represent mean ± SD (n = 3). *p<0.05 denotes a significant difference between 4 and 24 h of incubation by two-way analysis of variance (ANOVA) Sidak's multiple comparison test.

5.4.5. Long-term stability study

As previously mentioned, the synthesized polymers were used to produce polymeric micelles. For the long-term storage stability study, mPEG-CS-OA from the continuous manufacturing method was used to produce polymeric micelles. Empty micelles were frozen with 0.5% (w/v) trehalose [11], and stored at -20 ºC, 4ºC, 25 ºC/60% RH and 40 ºC/75% RH and physicochemically characterized after 0, 1, 3 and 6 months.

As can be seen in Figure 5.4A, the micelle size remained the same after 6 months when stored at -20 ºC. On the other hand, when increasing the storage temperatures, micelles size started to get bigger, indicating aggregation, meaning the micelles cannot maintain their architecture at the temperature of 25 ºC/60% RH for more than 1 month and at 40 ºC/75% RH micelles aggregate in the first month. These results agree with the polydispersity index (PdI, Figure 5.4B), where at -20 and 4 ºC the PdI was maintained, along with the particle size. Micelles stored at 25 ºC/60% RH and 40 ºC/75% RH increased their PdI values close to 1. In contrast, the zeta potential did no present significant changes, except for the 40 ºC/75% RH condition.

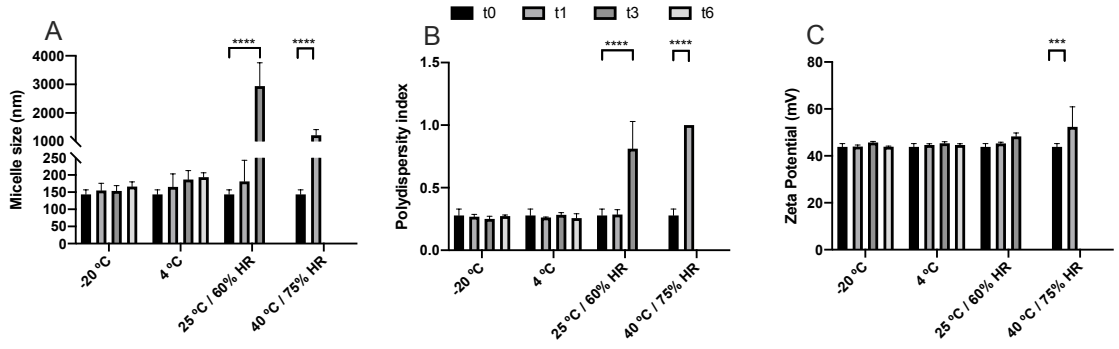

Figure 5.4. Characterization and stability of the chitosan micelles after long-term storage: (A) Average of micelle size, (B) polydispersity index, and (C) zeta potential for empty micelles placed at -20 ºC, 4 ºC, 25 ºC/60% HR and 40 ºC/75% HR after 0, 1, 3 and 6 months of storage. Error bars represent mean ± SD (n = 3). ***p< 0.001 and ****p<0.0001 denotes a significant difference denotes a significant difference compared with the formulation at time 0 by two-way analysis of variance (ANOVA) Dunnett's multiple comparison test.

The morphology of micelles during the storage stability study was also evaluated. As depicted in Figure 5.5, micelles preserved the micellar round shape and smooth surface after 1 month of storage, with the exception of the 40 ºC/75% RH condition. After 3 months of store, only micelles stored at -20 and 4 ºC preserved its structure. Furthermore, after 6 months, the conditions at -20 and 4 ºC best maintained the micellar structure, however,

when these results were compared to the particle diameter, it appears that the temperature of -20 ºC was the most appropriate condition to store the micelles for a long period of time. In Figure 5.6, it is possible to visualize the macroscopic changes of the freeze-dried micelles after 6 months of storage at different temperatures. At -20 and 4 ºC, the micelle 'cake' is preserved, whereas at 25 ºC/60% RH and 40 ºC/75% RH the 'cake' collapsed, which was more evident at the 40 ºC/75% RH condition. Micelles lose their resuspension capacity, due to the degradation of the polymer when subjected to higher temperatures [22]. All of these findings corroborate the hypothesis that -20 ºC was the most suitable storage condition for these chitosan-based micelles.

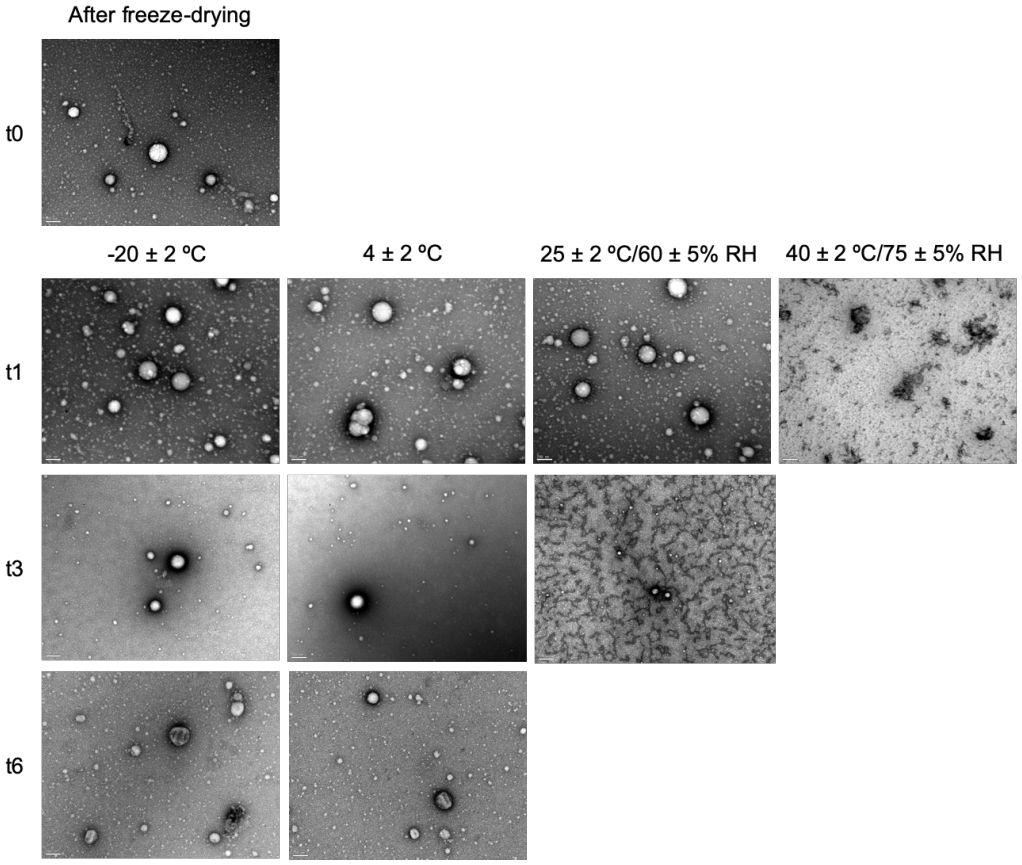

Figure 5.5. TEM microphotographs of chitosan micelles after freeze-drying and after 1, 3 and 6 months of storage at -20 ºC, 4 ºC, 25 ºC/60% HR and 40 ºC/75% HR. Scale bar corresponding to 200 nm.

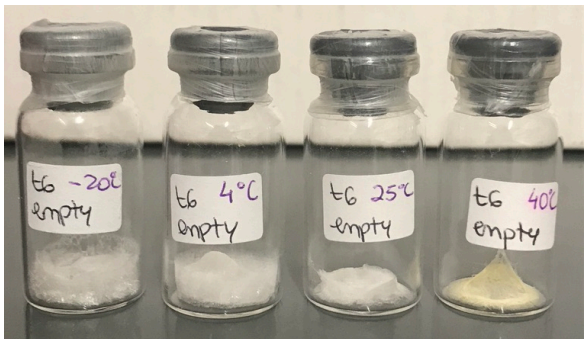

Figure 5.6. Macroscopic differences of chitosan micelles when subjected at different storage temperatures after 6 months.

5.5. Conclusion

To achieve a final product for oral administration to patients, the first stages of product development must be taken into consideration. It is necessary to implement scale-up strategies and follow standardized methods in order to decrease irreproducibility and put the formulation close to a suitable industrial production. The overall goals of this work were to benefit from a method and technology transfer to a pilot batch (representing an industrial batch) of two chitosan derivatives and use one polymer to produce polymeric micelles. The copolymers' scalability in less time and higher yield, while maintaining physicochemical properties, was demonstrated, and polymeric micelles produced by the continuous manufacturing method exhibited long-term storage stability. These accomplishments have narrowed the gap between bench and bedside, making the prospect of translating laboratory research to market production more realistic.

References

1. Araújo, F., et al., *Functionalized materials for multistage platforms in the oral delivery of biopharmaceuticals.* Progress in Materials Science, 2017. **89**: p. 306-344.
2. Azevedo, C., et al., *Engineered albumin-functionalized nanoparticles for improved FcRn binding enhance oral delivery of insulin.* Journal of Controlled Release, 2020. **327**: p. 161-173.
3. Knipe, J.M., F. Chen, and N.A. Peppas, *Enzymatic biodegradation of hydrogels for protein delivery targeted to the small intestine.* Biomacromolecules, 2015. **16**(3): p. 962-972.
4. Schenk, M. and C. Mueller, *The mucosal immune system at the gastrointestinal barrier.* Best Practice & Research Clinical Gastroenterology, 2008. **22**(3): p. 391-409.
5. Ensign, L.M., R. Cone, and J. Hanes, *Oral drug delivery with polymeric nanoparticles: the gastrointestinal mucus barriers.* Advanced Drug Delivery Reviews, 2012. **64**(6): p. 557-570.
6. Chivere, V.T., et al., *Nanotechnology-based biopolymeric oral delivery platforms for advanced cancer treatment.* Cancers, 2020. **12**(2): p. 522.
7. Jin, Y., et al., *Intestinal oligopeptide transporter PepT1-targeted polymeric micelles for further enhancing the oral absorption of water-insoluble agents.* Nanoscale, 2019. **11**(44): p. 21433-21448.
8. Türeli, N.G. and A.E. Türeli, *Upscaling and GMP production of pharmaceutical drug delivery systems*, in *Drug Delivery Trends*. 2020, Elsevier. p. 215-229.
9. Türeli, N.G. and A.E. Türeli, *Industrial perspectives and future of oral drug delivery*, in *Nanotechnology for Oral Drug Delivery*. 2020, Elsevier. p. 483-502.
10. Silva, D.S., et al., *Synthesis and applications of amphiphilic chitosan derivatives for drug delivery applications.* Nanoparticles in Life Sciences and Biomedicine, 2018: p. 45.
11. Almeida, A., et al., *Novel amphiphilic chitosan micelles as carriers for hydrophobic anticancer drugs.* Materials Science and Engineering: C, 2020. **112**: p. 110920.
12. Almeida, A., et al., *Synthesis and characterization of chitosan-grafted-polycaprolactone micelles for modulate intestinal paclitaxel delivery.* Drug Delivery and Translational Research, 2018. **8**(2): p. 387-397.
13. *International Conference on Harmonisation (ICH) guidelines* in *ICH Q1A (R2) : Stability Testing of new Drug Substances and Products*. 2003: London, UK.

14. Maisel, K., et al., *Nanoparticles coated with high molecular weight PEG penetrate mucus and provide uniform vaginal and colorectal distribution in vivo.* Nanomedicine, 2016. **11**(11): p. 1337-1343.
15. Bhattarai, N., et al., *PEG-grafted chitosan as an injectable thermosensitive hydrogel for sustained protein release.* Journal of Controlled Release, 2005. **103**(3): p. 609-624.
16. Li, Y.Y., et al., *Aggregation of hydrophobically modified chitosan in solution and at the air–water interface.* Journal of Applied Polymer Science, 2006. **102**(2): p. 1968-1973.
17. Shukla, N., et al., *FTIR study of surfactant bonding to FePt nanoparticles.* Journal of Magnetism and Magnetic materials, 2003. **266**(1-2): p. 178-184.
18. *ISO/EN10993-5. International Standard ISO 10993-5 Biological Evaluation of Medical Devices—Part 5: Tests for Cytotoxicity: In Vitro Methods*. 2009, International Organization for Standardization: Geneva, Switzerland.
19. Silva, D.S., et al., *Synthesis and characterization of 3, 6-O, O'-dimyristoyl chitosan micelles for oral delivery of paclitaxel.* Colloids and Surfaces B: Biointerfaces, 2017. **152**: p. 220-228.
20. Silva, D.S., et al., *Self-aggregates of 3, 6-O, O'-dimyristoylchitosan derivative are effective in enhancing the solubility and intestinal permeability of camptothecin.* Carbohydrate Polymers, 2017. **177**: p. 178-186.
21. Silva, D.S., et al., *N-(2-hydroxy)-propyl-3-trimethylammonium, o-mysristoyl chitosan enhances the solubility and intestinal permeability of anticancer curcumin.* Pharmaceutics, 2018. **10**(4): p. 245.
22. Szymańska, E. and K. Winnicka, *Stability of chitosan—a challenge for pharmaceutical and biomedical applications.* Marine Drugs, 2015. **13**(4): p. 1819-1846.

CHAPTER 6

3D printed systems for specific colonic delivery of camptothecin-loaded chitosan micelles

The information provided in this chapter was based in the following publication:

Almeida, A.*, Linares, V.*, Mora-Castaño, G., Casas, M., Caraballo, I. & Sarmento, B., 2021. 3D printed systems for specific colonic delivery of chitosan micelles for a better intestinal absorption, *European Journal of Pharmaceutics and Biopharmaceutics.* (*equal contribution)

In this paper, I was responsible for the conception, execution and revision of the manuscript. Vicente Linares was also responsible for the conception, execution and revision of the manuscript. Gloria Mora-Castaño and Marta Casas were responsible for the methodology and the supervisors were responsible for reviewing and submit the manuscript. This paper was not previously included in other thesis and it is partially reproduced in this section.

6.1. Abstract

The use of 3D printing technology in the manufacturing of drug delivery systems has expanded and benefit of a customized care. The ability to create tailor-made structures filled with drugs/delivery systems with suitable drug dosage is especially appealing in the field of nanomedicine. In this work, chitosan-based polymeric micelles loaded with camptothecin (CPT) were incorporated into 3D printing systems (printfills) sealed with an enteric layer, aiming to protect the nanosystems from the harsh environment of the gastrointestinal tract (GIT). Polymeric micelles and printfills were fully characterized and, a simulated digestion of the 3D systems upon an oral administration was performed. The printfills maintained intact at the simulated gastric pH of the stomach and, only released the micelles at the colonic pH. From there, the dissolution media was used to recreate the intestinal absorption and, chitosan micelles showed a significant increase of the CPT permeability compared to the free drug, reaching an apparent permeability coefficient (P_{app}) of around 8×10^{-6} cm/s in a 3D intestinal cell-based model. The combination of 3D printing with nanotechnology appears to have great potential for the colon-specific release of polymeric micelles, thereby increasing intestinal absorption while protecting the system/drug from degradation throughout the GIT.

6.2. Introduction

The oral route is the most preferred via of administration of drugs due to the greatest patient compliance and ease of administration. In the market, drugs for oral administration are the most used worldwide, however, some drugs present poor oral availability and cannot be administered orally. This is the case of several anticancer drugs, that despite being effective against cancer, cannot be administered orally due to the poor aqueous solubility and low intestinal permeability [1, 2].

CPT was found in the bark of the Chinese tree, *Camptotheca acuminate* [3] and, is a potent anticancer drug against several types of cancer, including colorectal cancer. Its mechanism of action is based on the inhibition of the nuclear DNA topoisomerase I (TOP1) by binding the complex DNA-TOP1, leading to DNA damage and, subsequently, to cell apoptosis [4]. CPT belongs to the Class IV of the Biopharmaceutical Classification System (BCS), which means to have low solubility and low permeability. Indeed, CPT present some toxicity, its physical-chemical stability is pH dependent and can suffer hydrolysis if administered orally due to the chemical and enzymatical barriers of the gastrointestinal tract (GIT). Additionally, the poor oral bioavailability is a result of the high level of the first pass metabolism and the action of drug efflux transporters, as the P-glycoproteins (P-gp) [5]. Thus, there is a great

need to overcome these drawbacks in order to be able to deliver CPT efficiently after an oral administration.

Nanotechnology has changed the field of drug delivery and, particular attention has been given to oral administration of drugs [6-8]. Polymeric micelles are nanosystems constituted by a hydrophobic core and a hydrophilic shell widely used in the encapsulation of hydrophobic drugs. These systems are described as potential oral vehicle of delivery since they can protect the drug from the harsh environment of the GIT, increasing its stability. Polymeric micelles are attractive also due to the high drug encapsulation capacity, where a therapeutic dose can be reached easily, avoiding side-effects and avoid efflux pumps of the epithelium [9-11].

Chitosan is a natural polymer extensively used in the production of polymeric micelles due to the ease of modification into an amphiphilic polymer with self-assembly properties. Moreover, chitosan has mucoadhesive properties and has the ability to temporarily open the tight junctions of the epithelium, properties that can enhance the intestinal permeability of drugs [8].

Three-dimensional printing (3DP) is gaining interest in pharmaceuticals by virtue of its ability to manufacture medicines with freeform geometries and flexibility in dose, drug release, etc. Thanks to its versatility, 3DP for medicines has become an interesting tool for drug personalization specially for paediatric and geriatric population due to their particular physiological needs [12-15].

Several 3DP techniques have been successfully employed for medicine manufacturing. Between them, fused deposition modelling (FDM) is one of the most common for its easy use, acceptable level of accuracy and good reproducibility. However, one of the main drawbacks is the impossibility to print thermolabile drugs due to the high temperatures achieved both during the drug loading process of the thermoplastic filament, and the 3D printing process [16]. Consequently, for thermo-sensitive pharmaceutical formulations, FDM does not appear to be the best option. Nevertheless, we have already shown the potential of combining two 3DP techniques (FDM and injection volume filling (IVF)) in one bioprinter to overcome this limitation [17]. IVF is based on a syringes system which works with low pressure injections, being useful for dispersions, suspensions, and low-viscosity pastes. As a result, 3D printed systems filled with a liquid or semisolid pharmaceutical formulation, called printfills, were developed. Thanks to the combination of FDM and IVF, the drug and a pH-sensitive polymer were incorporated in the scaffold produced by FDM at once, in a continuous and automated process.

Targeted drug delivery together with dose personalization can improve the patient´s standard of living [18, 19]. Therefore, the ease to design modified drug release systems is a valuable advantage of 3DP for medicines. In this sense, colonic drug release becomes a

potential area for 3DP, especially for the treatment of colonic diseases like Crohn disease, cancer, or ulcers [20, 21].

The aim of this study was to protect chitosan-based micelles loading CPT from the harsh environment of the GIT, allowing the release of micelles in the colon, improving the intestinal permeability of CPT. Free CPT and loaded into micelles [22] were incorporated in printfills manufactured through an automated manufacturing 3D printing process.

6.3. Materials and Methods

6.3.1. Materials

Polylactic acid (PLA) was chosen as biodegradable thermoplastic filament for FDM (melting point 220ºC, density 1.25 g/cm^3), supplied by Leon3D (Spain). Eudragit FS30D (Evonik, Germany) was employed as delayed release polymer. CPT was purchased from Hangzhou ROYAL Import & Export Co., Ltd; 3.5 kDa cutoff dialysis membrane (regenerated cellulose, Spectra/Por® 3 Dialysis Tubing, Fisher Scientific) was used to produce the micelles.

6.3.2. Production of camptothecin-loaded polymeric micelles

Polymeric micelles based on chitosan were obtained by a dialysis method, as previously described [22, 23], however, the CPT AE was optimized and improved from the last published work [22]. Briefly, 10 mg of *O*-methyl-*O'*-succinyl polyethylene glycol-chitosan-oleic acid (mPEG-CS-OA polymer) were dissolved in 4 mL of dimethyl sulfoxide (DMSO):HCl 0.1 M (9:1) in a glass tube and left overnight at RT until its complete dissolution. CPT, previously dissolved in DMSO at 1 mg/mL, was added to the prior solution at different drug loadings (w/w). The mixture continued under stirring and, after 6 h, dialyzed with three-cycle renewal against water to remove the DMSO and the non-associated CPT. Afterwards, CPT-loaded micelles were centrifuged during 20 min at 3110 g to remove the drug precipitate during dialysis, frozen with 0.5% (w/v) trehalose as a cryoprotectant, and freeze-dried to achieve the micellar powder.

6.3.3. Characterization of camptothecin-loaded micelles

Mean particle size, polydispersity index (PdI), and surface charge were assessed by DLS and Laser Doppler Micro-electrophoresis (ZetaSizer Nano ZS, Malvern, UK), respectively, with an angle of 173° at 25 °C. Polymeric micelles were analyzed freeze-drying resuspended in MilliQ water at 1% (w/v) concentration. The AE was determined by the indirect method by high-performance liquid chromatography (HPLC) and calculated as described in Equation 6.1. Drug loading (DL) was obtained according to Equation 6.2.

Briefly, the HPLC analysis was performed in a Shimadzu UFLC Prominence System (USA) equipped with two Pumps LC-20AD, a column oven CTO-20AC, an autosampler SIL-20AC, a System Controller CBM-20A, a degasser DGU- 20A5, a RF-10Axl fluorescence detector coupled to the LC System and a LC Solution, Version 1.24 SP1 (Shimadzu), and the method used for CPT quantification was described by Martins *et al*., [24].

$$AE\% = \frac{weight\ of CPT\ added - weight\ of\ free\ CPT}{weight\ of\ CPT\ added} \times 100 \quad (6.1)$$

$$DL\% = \frac{weight\ of\ CPT\ added - weight\ of\ free\ CPT}{total\ micelles\ weight} \times 100 \quad (6.2)$$

6.3.4. 3D printed systems production

Printfills (3D printed systems) were manufactured employing a bioprinter (Regemat 3D S.L., Spain) which combines FDM and IVF techniques. Two different batches of printfills were designed by the software Regemat 3D DESIGNER. First batch contained free CPT, whereas the second one CPT encapsulated within polymeric micelles.

6.3.4.1. Preparation of drug printable ink

Suitable drug printable inks were prepared for each batch: Firstly, free CPT dissolved in DMSO with a concentration of 5 mg/mL was diluted in a dissolution of 10 mL DMSO:dH_2O at a ratio of 7:3. Secondly, to obtain printable ink with lyophilized CPT loaded-micelles, 4.5 mL of dH_2O were employed to rehydrate and resuspend the micelles. Both printable inks were prepared with the minimum light exposure to reduce the interaction with the drug.

6.3.4.2. 3D printing process

Printing settings for each batch are shown in Tables A3.1 and A3.2 in the supplementary information. Due to the different composition of the two drug inks, systems prepared with micelles required more injection points and lower deposit speed in order to ensure the same volume incorporated in the structure. Also, the amount of Eudragit FS30D was higher to ensure the top face sealing of the printfill (Table A3.1 and Table A3.2).

According to the digital design of the 3D printed system, printfills were built layer by layer (Figure A3.1, supporting information). FDM starts the printing process building the scaffold in the platform by extruding 2 bottom solid layers. The extrusion continues with parallels lines separated by 1.8 mm and 2 mm for free CPT batches and CPT encapsulated, respectively. The next layer is built with perpendicular lines respect to the lower one, resulting in a quadrilateral mesh of 1.8×1.8 mm and 2×2 mm for each batch. This process

continues until the18th layer of the scaffold when the two automated syringes of IVF inject inside the scaffold. The first syringe contained printable ink with the free CPT and injected 200 µL in the 18th layer in 4 different points of the mesh, whereas 12 injection points were necessary for micelles. Again, FDM continues extruding a couple of layers to finish the scaffolds. Finally, IVF with the second syringe injected the set volume of the delaying polymer in the last layer of the system sealing the top face of the printfill.

All 3DP process from the FDM extrusion until the last injection of IVF was a continuous and automatic manufacturing. Once the printfills were finished, were dried in a drying oven (632 plus Nahita, Auxilab S.L., Navarra, Spain) at 29 ºC for 24 h to evaporate the solvent (Figure A3.2 in the supplementary information).

6.3.5. Characterization of the 3D printed systems

6.3.5.1. Physical characteristics of 3D printed systems

Printfills were weighed in a precision balance (Scaltec, type SBC31) and thickness and diameter were measured using a digital micrometer (Comecta, SA).

6.3.5.2. Scanning electron microscopy

The interior mesh and transversal section of the delaying polymer were evaluated in the Microscopy Service of the CITIUS in the University of Seville by using scanning electron microscopy (SEM) with a FEI TENEO electronic microscope (FEI Company, USA), operating at 5 kV. Printfills were coated with a 12 nm thin Pt/Pd layer with Leica EM SCD500 high vacuum sputter coater.

6.3.6. Camptothecin release from the printfills

The dissolution studies were carried out using a USP Apparatus I Sotax AT7 smart (Allschwil, Switzerland) at 37 ± 0.5 °C with a rotation speed of 50 rpm. Printfills were exposed to different switch solutions (SS) to mimic the intestinal transit according to Schellekens *et al*., [25]. Their methodology was modified to prolong the colon residence time, as shown in Table A3.3 in the supplementary information. The different SS (Table A3.4 in the supplementary information) were added from one phase to another to obtain the required pH. Samples were withdrawn at specific interval times: 1, 2, 2.5, 3.5, 4.0, 4.2, 4.3, 4.5, 4.8, 5.0, 5.3, 5.5, 6.0, 6.5, 7.0, 7.5, 8 hours. The amount of CPT released from the printfills at each time-point was quantified by HPLC, as previously described [24]. The results are present as a cumulative percentage of CPT released at each analyzed time (*n=6*). Drug release data ($M_t/M_\infty \leq 0.8$) was also analyzed using Microsoft Excel 2010

(Microsoft, Albuquerque, NM, USA) according to zero order, Higuchi [26], Korsmeyer *et al.*, [27] and Peppas and Sahlin [28], following the Equations 6.3 –6.5:

$$\frac{M_t}{M_\infty} = bt^{1/2} \quad (6.3)$$

$$\frac{M_t}{M_\infty} = k_k t^n \quad (6.4)$$

$$\frac{M_t}{M_\infty} = k_d t^m + k_r t^{2m} \quad (6.5)$$

where M_t/M_∞ is the drug released fraction at time *t* (the drug loading was considered as M_∞), *b* and k_k are kinetic constants characteristic of the drug/polymer system, *t* is the release time, *n* is the release exponent that depends on the release mechanism and the shape of the matrix tested, k_d and k_r are the diffusion and relaxation rate constants, respectively, *m* is the purely Fickian diffusion exponent for a device of any geometrical shape which exhibits controlled release. Determination coefficient (r_2) was used to test the applicability of the release models, calculated in linear regression for zero order, Higuchi and Korsmeyer equations or quadratic regression for Peppas and Sahlin model.

6.3.7. Cell culture

C2BBe1 [Caco-2 clone] (human colorectal adenocarcinoma) cells were acquired from ATCC and HT29-MTX mucus-producing cells were kindly provided by Dr. T. Lesuffleur (INSERM U178, Villejuif, France). Both cell lines were maintained in complete medium comprising Dulbecco's Modified Eagle's Medium (DMEM, ATCC) supplemented with 10% (v/v) Fetal Bovine Serum (FBS, Biochrom) and 1% (v/v) antibiotic-antimitotic mixture (final concentration of 100 U/mL penicillin and 100 U/mL streptomycin, Biowest). Human intestinal fibroblast (HIF) primary cells were obtained from ScienCell and maintained in culture with Fibroblast Medium (FM) supplemented with 2% FBS, 1% of Fibroblast Growth Supplement (FGS), and 1% penicillin/streptomycin solution (all supplements from ScienCell). HPMEC-St1.6R cells were kindly provided by Professor C. James Kirkpatrick (Institute of Pathology, Johannes Gutenberg University of Mainz, Germany) and were maintained with M199 medium (Sigma), supplemented with 20% FBS (Biochrom), 1% (v/v) antibiotic-antimitotic mixture (final concentration of 100 U/mL penicillin and 100 U/mL streptomycin, Biowest), 25 µg/mL of Endothelial Cell Growth Supplement (ECGS) and 25 µg/mL of heparin (both from Sigma), and 100 µg/mL L-glutamine (LabClinics). All the cells were cultures in 75 cm^2 T-flasks, inside an incubator at 37 ºC and 5% CO_2 and 95% relative humidity.

6.3.8. Metabolic assay using drug and micelle released medium

To assess the safety of the micelles and the free drug to be placed in the permeability assay, the released media from the printfills of the CPT and CPT-loaded micelles was used to perform a resazurin assay. Briefly, 2×10^4 Caco-2 cells were seeded in 96-well plates and incubated at 37 ºC and 5% CO_2 and 95% relative humidity during 24 h to allow the cells to adhere to the wells. Then, the medium was removed and cells were washed twice with pre-warmed PBS and, treated with 200 µL of the release media from the printfills of the free CPT and CPT-loaded micelles diluted 1:1 with DMEM complete medium and, allowed to incubate for 4, 6 and 24 h. After that, the medium was removed and cells were washed twice with pre-warmed PBS and incubated with DMEM complete medium with 20% resazurin (0.1 mg/mL; Merck) during 2 h at 37 ºC, 5% CO_2 and 95% relative humidity, protected from the light, to allow viable cells reduce resazurin into the resorufin, which the pink and fluorescent product of the reaction. The fluorescence was measured by the relative fluorescence units (RFUs) by removing the supernatant of the previous plate into black 96-well plates using a microplate reader SynergyTM Mx HM550 (Biotek) set at 530/590 (excitation/emission wavelength, respectively). A negative control consisting in cells incubated with 1% (v/v) of Triton X-100 in complete medium and a positive control consisting in cells incubated with complete medium were also included in the experiment. A number of six replicates were performed for each group and, the metabolic activity was quantified according to Equation 6.6:

$$Cellular\ viability\ (\%) = \frac{fluorescence\ (experimental\ value) - fluorescence\ (positive\ control)}{fluorescence\ (negative\ control) - fluorescence\ (positive\ control)} \times 100 \quad (6.6)$$

6.3.9. Intestinal permeability models

Two different intestinal models were used to evaluate the intestinal permeability of CPT released from the printfills with free CPT and CPT-loaded micelles after passing through the simulated gastrointestinal fluids. The first one, constituted only by Caco-2 cells, which is the standard model to study the intestinal permeability of molecules; and the second one, constituted by Caco-2 cells, HT29-MTX mucus-producing cells, HIF embedded in a collagen coating and endothelial cells, a 3D model that better mimic what happens in an *in vivo* situation [29]. For the Caco-2 model, 1×10^5 cells per cm^2 were seeded in a 12-Transwell® cell culture inserts (pore size of 1 µm, MilliceII) and allowed to grow and differentiate for 21 days inside an incubator at 37 ºC, 5% CO_2 and 95% relative humidity. The 3D intestinal model is similar to the previously published work of our group [30], but it was improved for the presence of an endothelial layer mimicking the passage into the blood

vessels [29]. Thus, in the 3D intestinal model, HPMEC-St1.6R cells were firstly seeded in a 0.2% gelatin coating in the basolateral side of the Transwell® insert at density of 5×10^4 cells/cm^2 and waited 2 h for the cells to adhere to the coating. After that, the inserts were placed in a 12-well plate and the apical side was coated with collagen with HIF embedded, which were incubated as previously described for 30 min. Then, 1×10^5 cells/cm^2 in a ratio of 9:1 (Caco-2:HT29-MTX) were seeded in the apical side of the inserts over the collagen coating. Both models used DMEM complete medium to culture the cells in the Transwell® inserts for 21 days, incubated as previously described and, the medium was changed every two/three days from the apical and basolateral sides. During 21 days, both models were monitored by the transepithelial electrical resistance (TEER) using an EVOM2 epithelial voltohmmeter equipped with a STX2 electrode (World Precision Instruments, Inc.), which gives the information about the integrity of the monolayer.

6.3.10. Camptothecin intestinal permeability

After 21 days the models sown, the medium was removed from both compartments and cells were washed twice with pre-warmed Hank's Balanced Salt Solution (HBSS) buffer and left to equilibrate with HBSS during 30 min at 37 ºC and 100 rpm in an orbital shaker (KS 4000 ic control orbital shaker, IKA). After 30 min, the HBSS was removed from the apical side and the released medium from the printfills from both free CPT and CPT-loaded micelles were added to the apical side of the insert (0.5 mL) and plates were again incubated at 37 ºC and 100 rpm. At predetermined time points (15, 30, 60, 180, and 240 min), a 200 µL sample was taken from the basolateral side and the same volume of pre-warmed HBSS was added to the insert. The TEER was measured at each time-point in order to assess the monolayer integrity. The CPT permeated through the monolayers was quantified by HPLC, as previously described [24] and, the permeability percentage and apparent permeability coefficient (P_{app}) were determined through the Equation 6.7 and Equation 6.8, respectively.

$$CPT\ permeated\ \% = \frac{total\ mass}{theoretic\ mass} \times 100 \quad (6.7)$$

$$Papp = \frac{dQ}{A \times C_0 \times dt} \quad (6.8)$$

where dQ (µg) is the total amount of compound in the basolateral side, A is the surface area of the insert (cm^2), C_0 is the initial concentration in the apical side (µg/mL) and *dt* (s) is the time of the experiment. The assay was performed in triplicate.

6.3.11. Cellular integrity by hematoxylin and eosin staining

To assess the integrity of the monolayers of the intestinal models after the permeability assay and, to ensure the permeability found was not due to the monolayer disruption, H&E staining was performed. Transwell® inserts were washed twice with PBS for 5 min and then fixed with 2% PFA in PBS during 20 min at RT. Then, the intestinal models were washed thrice with PBS during 5 min and kept at 4 ºC in PBS until further processing for paraffin embedding. Sections of 3 mm were collected using an RM2255 microtome (Leica) and then stained for H&E. Briefly, sections were deparaffinized and rehydrated, stained for 3 min in Gil's Hematoxylin (Thermo Scientific), 6 min in running water, dehydrated, stained for 1 min in Eosin Y (Thermo Scientific), cleared, and mounted in Entellan (Merck). Demonstrative images of each condition of the intestinal permeability were acquired with a Light microscope Olympus DP 25 Camera Software Cell B.

6.3.12. Statistical analysis

Statistical analysis was performed using the GraphPad Prism Software vs. 6.0 (GraphPad Software Inc). All data were presented as mean ± SD.

6.4. Results and Discussion

6.4.1. Characterization of camptothecin-loaded micelles

In this study, CPT was associated to chitosan micelles by dialysis method and characterized by the average size, PdI and surface charge. The AE and DL was also calculated, where the last was optimized from our last work [22]. As can be seen from Table 6.1, empty micelles presented an average size of around 130 nm and, as the CPT was physical entrapped to the system with the DL increasing, the average size of the micelles also increased. This expansion volume of the micelles can be due to the accumulation of large amounts of hydrophobic groups on the micelle core, which means the CPT encapsulation have a direct influence on micelle average size. At the same time, the PdI also increased with DL increasing. Taking into consideration the data found in the literature, systems with PdI values below 0.3 represent monodispersed systems [31, 32]. Therefore, the formulation with 20% (w/w) CPT did not represent a monodispersed distribution and, thus, should not proceed for the further studies. The high PdI is typically found on chitosan-based micelles due to the heterogeneity of the polymer and the non-uniform distribution of the acyl chains on the chitosan backbone as result of the reaction with the substituent groups to obtain new chitosan derivatives. Nevertheless, the values found agree with the literature for other chitosan derivatives [33, 34].

The micelles surface charge also presented a direct influence with the DL increasing. As CPT is entrapped into the mPEG-CS-OA micelles, their surface charge changed from +37 mV to +44 mV (Table 6.1). This comportment may be explained by the fact that micelles were formed by the interaction of the hydrophobic moieties of the polymer chain with the hydrophobic segments of the drug. Thus, with the DL increasing, the hydrophobic moieties also increased, leading to a higher exposure of the hydrophilic segments of chitosan, which is positively charged. The fact the micelles presented a highly positive surface charge may favor the interaction with epithelial cells, leading to a higher CPT absorption.

Regarding the AE of mPEG-CS-OA micelles, it was verified a decreased with the DL increasing, due to the saturation of the nanosystems. Indeed, despite the decrease on the AE, the DL of the micelles increased until the DL_T of 15% (w/w), where an 8% DL was found, as previously observed [1, 35]. Since it was demonstrated the monodispersed character of this formulation together with the higher amount of CPT associated into the micelles, the formulation of mPEG-CS-OA micelles with 15% (w/w) DL_T was chosen for further experiments.

Table 6.1. The theoretical drug loading (DL_T), association efficiency (AE), the drug loading (DL), particle size, PdI and micelles surface charge empty and CPT-loaded mPEG-CS-OA micelles. Values are represented as mean ± SD (n = 3).

DL_T (%)	AE (%)	DL (%)	Size (nm)	PdI	Zeta potential (mV)
0	-	-	132 ± 3	0.262 ± 0.026	37.5 ± 0.2
5	78.4 ± 2.2	3.9 ± 0.1	155 ± 15	0.272 ± 0.033	41.3 ± 2.8
10	62.7 ± 5.5	6.3 ± 0.5	174 ± 26	0.286 ± 0.015	42.3 ± 3.6
15	55.5 ± 8.9	8.3 ± 1.3	178 ± 6	0.281 ± 0.016	42.8 ± 4.3
20	45.4 ± 2.9	9.1 ± 0.6	262 ± 25	0.324 ± 0.021	43.9± 3.3

6.4.2. Characterization of the 3D printed systems

6.4.2.1. Physical characteristics of 3D printed systems

Table 6.2 show the weights and dimensions of printfills according to the digital design. As expected, FDM technology worked with accuracy and precision during 3DP systems manufacturing.

Table 6.2. Physical characteristics of printfills with free CPT and CPT-loaded micelles.

	Experimental			Theoretical	
Printfill with free CPT	**Weight (mg)**	**Height (mm)**	**Diameter (mm)**	**Height (mm)**	**Diameter (mm)**
Mean	1523.85	7.403	14.867	7.35	14
SD	79.116	0.204	0.053	0.038[a]	0.613[a]
CV	5.1918	2.758	0.358	0.513[a]	4.381[a]
Printfill with CPT-loaded micelles	**Weight (mg)**	**Height (mm)**	**Diameter (mm)**	**Height (mm)**	**Diameter (mm)**
Mean	1364.0	7.643	14.811	7.35	14
SD	63.746	0.250	0.080	0.207[a]	0.574[a]
CV	4.6736	3.266	0.538	2.820[a]	4.098[a]

[a] Calculated between theoretical and mean of experimental data.

6.4.2.2. Scanning electron microscopy

SEM images depict the internal structure of printfills (Figure 6.1). The cross section of the 3DP system reveals a homogenous film of Eudragit FS30D at the top confirming a sealing layer with a thickness of about 50 µm in the narrowest part. (Figure 6.1A). Furthermore, evidence of the perimeter sealing of the scaffold can be found on supplementary material (Figure A3.3). Thus, the only water inlet available is through the upper face of the printfill, once the delaying polymer is dissolved at enteric pH. SEM cross section images of printfills with free drug showed recrystallized CPT on PLA after the drying process (Figure 6.1B). Although printing settings were modified in order to inject the printable ink reducing the interaction between both delaying polymer and micelles, part of the printable ink remained embedded in the polymer after the drying process. Soaked micelles in the polymer Eudragit FS 30D can be seen in Figure 6.1C and 6.1D.

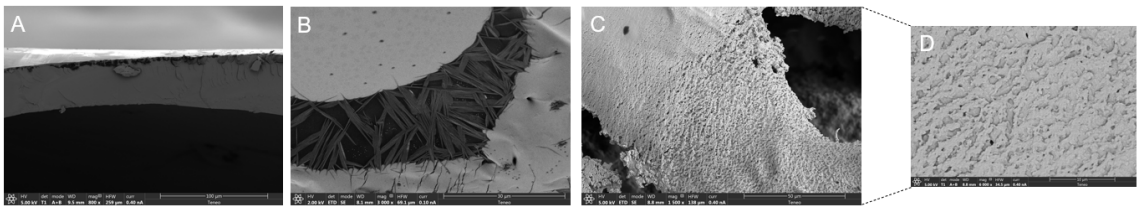

Figure 6.1 – Scanning electron microscopy images of (A) Eudragit top layer of the printfill; (B) CPT crystals inside of the printfill; (C) CPT-loaded micelles inside of the printfill; (D) amplification of the printfill with polymeric micelles inside. Scale bar corresponding to 100, 30, 50 and 10 µm, respectively.

6.4.3. *In vitro* release profile of camptothecin from the printfills loaded with polymeric micelles

As can be seen in the Figure 6.2, printfills with free drug and micelles were able to control the drug release. Thus, there was no drug release from the printfills during 2 h in pH 1.2. Once SS was added changing the pH to 6.8, the delaying polymer started to dissolve allowing the entrance of the water.

Printfills with free drug released 70% of CPT in less than 30 minutes at pH 6.8. The total amount of CPT obtained for this batch confirms the precision of IVF technology injecting the printable ink. On the other hand, printfills with CPT-loaded micelles showed a slower drug release (approximately 3%) due to the drug encapsulation within the polymeric micelles. Furthermore, it was evident the shape changes of release profiles, showing the micelles a sigmoid profile, typically of erosive systems.

Drug release data ($M_t/M_\infty < 0.8$) from printfills were analyzed according to zero order, Higuchi, Korsmeyer–Peppas and, Peppas and Sahlin equations (Table 6.3). In the case of printfills with free CPT, since it was showed a similar fast drug release as previously described in Chapter 4, it was not described again in this chapter. Determination coefficient values indicates a poor fit for the different kinetic models, that can be explained because drug release profile reaches an asymptote at around 35% w/w. Thus, in order to obtain information about drug release mechanism from this profile, data has been analyzed until 260 min, i.e., before reaching asymptote. In this case, the best fit corresponds to Peppas and Sahlin equation, with a clear prevalence of K_r over K_d. This indicates that the drug release mechanism was controlled mainly by erosion. The *n* value from Korsmeyer equation indicates a super case II transport, confirming that the mechanism of drug release was erosion/relaxation controlled. This data is corroborated with the previously described results on Chapter 4 (Table 4.4), where it is stated the CPT release from chitosan micelles following the Fickian diffusion combined with case II transport. As a result, there was no difference in the drug release kinetics from polymeric micelles whether they were free or inside a 3D system. This means that, following the degradation of the Eudragit top layer of the *printfills*, CPT from the polymeric micelles follows the same release kinetic pattern as already mentioned.

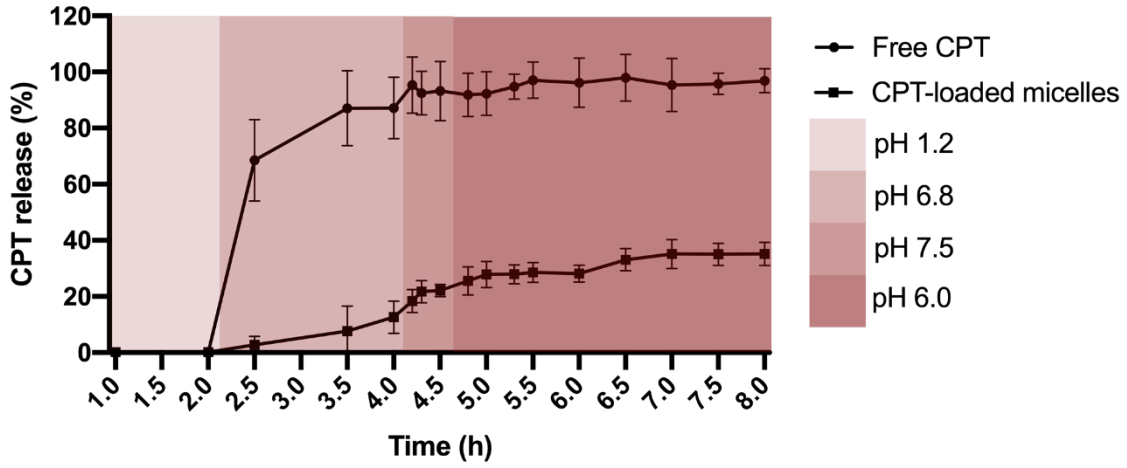

Figure 6.2. Cumulative CPT release from the printfills in simulated gastrointestinal fluids. *Squares* represent the release of CPT-loaded micelles and *circles* represent the release of free CPT. Error bars represent mean ± SD (n = 6).

Table 6.3. Mathematical modelling and drug release kinetics from enteric printfills.

	Zero order	Higuchi		Korsmeyer			Peppas and Sahlin		
	r^2	b ($min^{-0.5}$)	r^2	K_k (min^{-n})	n	r^2	K_d(min^{-m})	K_r(min^{-2m})	r^2
Printfills with CPT-loaded micelles*	0.8586	0.0362	0.8995	$1.9113x10^{-6}$	2.0311	0.818	0.1245	-0.0025	0.9417
Prinfills with free CPT*	0.8699	0.0451	0.8476	$3.0705x10^{-10}$	3.6433	0976	-0.4697	0.0182	0.9798

*Drug release kinetics up to 260 min.

b, Higuchi kinetic constant; n, release exponent; k_k, Korsmeyer kinetic constant; k_d, Peppas diffusion kinetic constant; k_r, Peppas relaxation kinetic constant; r_2, determination coefficient.

6.4.4. *In vitro* cytocompatibility of polymeric micelles

In order to assess the safety and biocompatibility of the micelles and free CPT loaded in the printfills and released in the simulated GIT fluids, a resazurin assay was performed in Caco-2 cells during 4, 6 and 24 h of incubation. The micelles and free drug present in the dissolution medium after 6h were used to evaluate its cytotoxic potential. As we described before, the release of the micelles and drug only occurs at intestinal pH, thus, it only makes sense to evaluate safety by this way.

As can be seen in Figure 6.3, both polymeric micelles and free drug present in the dissolution media showed no cellular cytotoxicity against Caco-2 cells, a colorectal cancer cell line. Moreover, the metabolic activity of these cells increased up to 100%, which may

be due to the presence of simulated GIF. Actually, according to the ISO 10993-5 guideline [36], it is reported that above 70% of cell viability is considered as safe, when testing *in vitro* formulations. Moreover, since we are working with a relatively low CPT concentration (< 10 µg) due to the slow CPT release and, based on previous published works [34, 37-39], it was expected no cytotoxic effect of the free CPT and CPT-loaded micelles present in the dissolution medium of the *in vitro* CPT release.

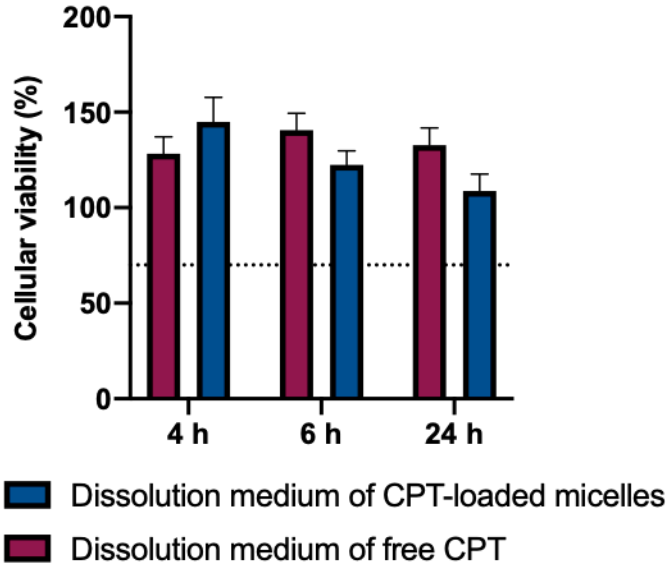

Figure 6.3. Cellular viability of the dissolution medium from the printfills containing CPT-loaded micelles (blue columns) and free CPT (pink columns) after 4, 6 and 24 h of incubation with Caco-2 cells. Error bars represent mean ± SD (n = 6).

6.4.5. Permeability of camptothecin after simulated gastrointestinal passage

Printfills were prepared and filled with CPT-loaded micelles and free CPT. Then, they were placed in a simulated GIT fluid to release both micelles and drug at the intestine to mimic oral intake. The dissolution medium at 6 h since the dissolution assay started was used to perform the permeability study.

To evaluate the CPT permeability, two different intestinal models were used, the 2D Caco-2 standard model and a 3D model, as previously described. As can be seen in Figure 6.4, the CPT permeability from the micelles was higher than the free drug in both models with significative differences at the last incubation times. The CPT permeability in the 3D model was around 27% which, compared to the standard model (20%), an enhanced intestinal permeability was verified. Since the 3D model represents the human intestine more closely, we are facing a drug permeability closer to the *in vivo* situation. Moreover, the P_{app} presented significative differences between micelles and free drug, where in the 3D model the P_{app} of CPT from the micelles reached values around 9×10^{-6} cm/s, which represents a

great increase of the CPT permeability and bioavailability (Figure 6.4C). The free drug maintained the P_{app} around 5×10^{-6} cm/s in both models, which also describes the permeability of the free drug as being almost half of the permeability of the drug by the micelles, in the case of the 3D model. Silva *et al*., described CPT permeability of 4×10^{-6} cm/s and 8×10^{-6} cm/s for a similar system in a Caco-2 and a co-culture 2D model, respectively [34], which is very close to the results found in this work.

As it is widely known, chitosan has the ability to open the tight junctions of the epithelium [40]. In addition, chitosan has mucoadhesive properties and, in a more realistic model, as the 3D model, chitosan micelles can stick to the mucus layer and release the drug, also contributing to the CPT permeability enhancement and bioavailability. Indeed, other authors already described the interaction of chitosan with mucus layer, leading to a permeability increase [33, 41].

The TEER maintained stable during the experiment for both micelles and free drug, which is an indicative of the safety of the tested formulation [42]. The slight decrease observed after 1 h of the experiment starting may be related to the permeability increase, possible due to the opening of the tight junctions of the epithelium [43], which then increasing again in the end in the experiment.

Overall, chitosan micelles and free drug were maintained stable after simulated oral administration and were protected within the printfills and only released at the intestinal pH, where the permeability was tested. Micelles significantly increased the CPT permeability in both models, especially in the 3D model, that better mimics what occurs *in vivo*. We are facing an increase in the bioavailability of CPT after an oral administration, which can be very useful for the treatment of various diseases, as the cancer therapy.

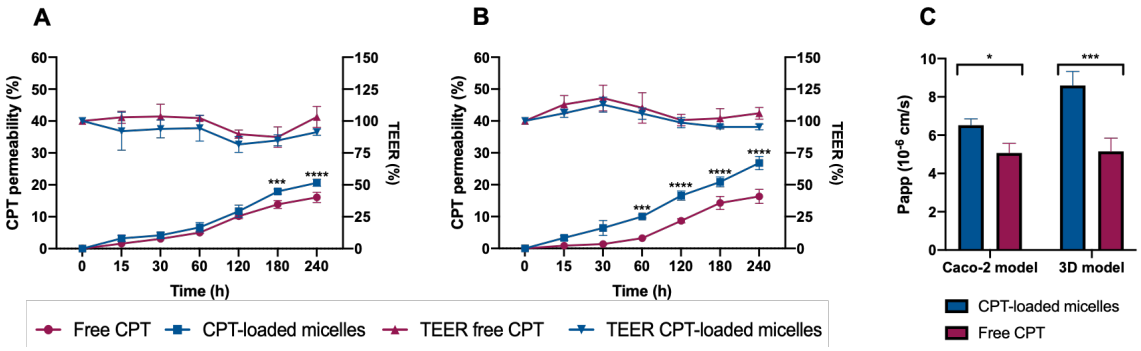

Figure 6.4. Intestinal permeability and respective TEER values of the CPT-loaded micelles and free CPT after being released in the simulated GIT fluid. (A) CPT permeability across Caco-2 standard model; (B) CPT permeability across a 3D intestinal model; (C) apparent permeability coefficients (P_{app}) of CPT-loaded micelles and free CPT across Caco-2 monoculture model and across the 3D model. All experiments were conducted from the apical to basolateral side in HBSS at 37 °C. Error

bars represent mean ± SD (n = 3). *p<0.05, ***p<0.001 and ****p<0.0001 denotes a significant difference by two-way analysis of variance (ANOVA) Sidak's multiple comparison test.

6.4.6. Cellular integrity of the intestinal models

The TEER represents the integrity of the monolayer as previously mentioned, and thus, TEER values during 21 days of culture can be seen in the supplementary material (Figure A3.4). This can guarantee that the monolayer was formed and ready for the permeability studies. Also, during the permeability assay, the TEER was registered and, as described above, the values were maintained at the end of the experiment, meaning the permeability obtained was not due to the monolayer disruption. Moreover, to ensure the integrity of the membrane after the permeability experiment, hematoxylin and eosin (H&E) staining was performed for both models and conditions (Figure 6.5). For this assay, two dyes were used, hematoxylin and eosin, which are basic and acidic dyes, respectively. Hematoxylin stains acidic structures in purple, as the nucleus and, eosin dyes basic structures in pink, as the cytoplasm and extracellular matrix [44]. Taking this into account, in Figure 6.6 is possible to observe a continuous monolayer in both models, corroborating with the TEER values, i. e., the cellular membrane integrity was maintained. Also, it is possible to visualize some portions of the monolayer where the membrane suffered disruption, but it was due to the handling procedure, which happens sometimes. In the case of the 3D model, it is possible to see a collagen layer with fibroblast embedded, as described in the methods section. Absence of cytotoxicity of chitosan-based micelles was also demonstrated by others authors [39, 45, 46]. Overall, the TEER values and the H&E staining support the hypothesis that the increased permeability is not due to the membrane disruption because, as demonstrated, it remains intact and tightly formed during and after the permeability assay.

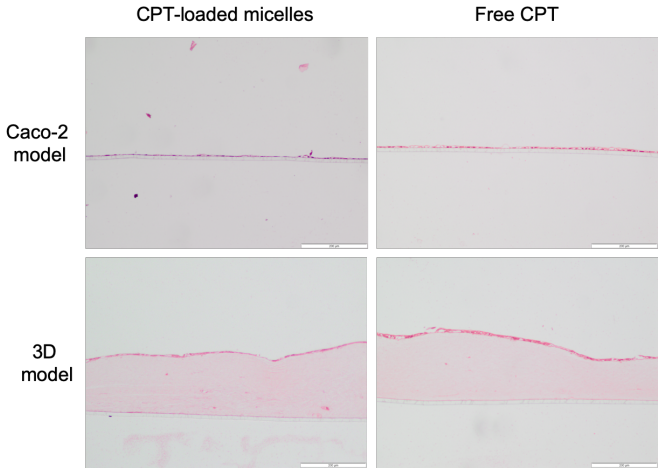

Figure 6.5. H&E staining to address the cellular integrity when cells were exposed to the dissolution medium containing CPT-loaded micelles and free CPT for the permeability assay. Cytoplasm stained

with pink and nucleus with purple. The Transwell® membrane is transparent and is right below the cellular monolayer. Scale bar = 100 µm.

6.5. Conclusion

Chitosan-based micelles loaded with CPT presenting an average diameter <200 nm were efficiently filled into 3D systems covered by an enteric layer. It was possible to verify the Eudragit top layer by SEM, as well as, the presence of the polymeric micelles and free drug inside of the printfills. The dissolution assay demonstrated the printfills are able to maintain the micelles intact until they reach the intestinal pH. From the dissolution media mimicking a digestion upon oral administration of the printfills, it was possible to verify a significant increase of the intestinal permeability in both Caco-2 and 3D intestinal models. Thus, printfills filled with polymeric micelles were able to maintain them intact along the simulated GIT digestion and, specifically delivered it at the colonic pH. In this regard, it was possible to substantially increase the CPT intestinal absorption and, consequently, its oral availability avoid the enzymatic degradation and metabolization. This work showed a tremendous potential for a colonic-specific delivery of CPT-loaded micelles with proven improved intestinal absorption.

References

1. Tu, L., et al., *Multi-functional chitosan polymeric micelles as oral paclitaxel delivery systems for enhanced bioavailability and anti-tumor efficacy.* International Journal of Pharmaceutics, 2020. **578**: p. 119105.
2. Qu, G., et al., *Self-assembled micelles based on N-octyl-N'-phthalyl-O-phosphoryl chitosan derivative as an effective oral carrier of paclitaxel.* Carbohydrate Polymers, 2019. **207**: p. 428-439.
3. Wall, M.E. and M.C. Wani, *Camptothecin and taxol: discovery to clinic—thirteenth Bruce F. Cain Memorial Award Lecture.* Cancer Research, 1995. **55**(4): p. 753-760.
4. Pommier, Y., *Topoisomerase I inhibitors: camptothecins and beyond.* Nature Reviews Cancer, 2006. **6**(10): p. 789-802.
5. Xue, Y., et al., *Intestinal transporter-associated drug absorption and toxicity.* Drug Transporters in Drug Disposition, Effects and Toxicity, 2019: p. 361-405.
6. Chen, G., et al., *N-trimethyl chitosan nanoparticles and CSKSSDYQC peptide: N-trimethyl chitosan conjugates enhance the oral bioavailability of gemcitabine to treat breast cancer.* Journal of Controlled Release, 2018. **277**: p. 142-153.
7. He, R. and C. Yin, *Trimethyl chitosan based conjugates for oral and intravenous delivery of paclitaxel.* Acta Biomaterialia, 2017. **53**: p. 355-366.
8. Kumar, R., et al., *Polymeric micelles based on amphiphilic oleic acid modified carboxymethyl chitosan for oral drug delivery of bcs class iv compound: Intestinal permeability and pharmacokinetic evaluation.* European Journal of Pharmaceutical Sciences, 2020. **153**: p. 105466.
9. Hu, W.Y., et al., *Smart pH-responsive polymeric micelles for programmed oral delivery of insulin.* Colloids and Surfaces B: Biointerfaces, 2019. **183**: p. 110443.
10. Wang, X., et al., *Preparation and evaluation of carboxymethyl chitosan-rhein polymeric micelles with synergistic antitumor effect for oral delivery of paclitaxel.* Carbohydrate Polymers, 2019. **206**: p. 121-131.
11. He, C., et al., *Efficient oral delivery of poorly water-soluble drugs using carnitine/organic cation transporter 2-mediated polymeric micelles.* ACS Biomaterials Science & Engineering, 2020. **6**(4): p. 2146-2158.
12. Aguilar-de-Leyva, Á., et al., *3D printed drug delivery systems based on natural products.* Pharmaceutics, 2020. **12**(7): p. 620.
13. Karavasili, C., et al., *Pediatric-friendly chocolate-based dosage forms for the oral administration of both hydrophilic and lipophilic drugs fabricated with extrusion-*

based 3D printing. European Journal of Pharmaceutical Sciences, 2020. **147**: p. 105291.

14. Xu, X., et al., *Stereolithography (SLA) 3D printing of an antihypertensive polyprintlet: Case study of an unexpected photopolymer-drug reaction.* Additive Manufacturing, 2020. **33**: p. 101071.
15. Herrada-Manchón, H., et al., *3D printed gummies: Personalized drug dosage in a safe and appealing way.* International Journal of Pharmaceutics, 2020. **587**: p. 119687.
16. Kollamaram, G., et al., *Low temperature fused deposition modeling (FDM) 3D printing of thermolabile drugs.* International Journal of Pharmaceutics, 2018. **545**(1-2): p. 144-152.
17. Linares, V., M. Casas, and I. Caraballo, *Printfills: 3D printed systems combining fused deposition modeling and injection volume filling. Application to colon-specific drug delivery.* European Journal of Pharmaceutics and Biopharmaceutics, 2019. **134**: p. 138-143.
18. Govender, R., et al., *Therapy for the individual: Towards patient integration into the manufacturing and provision of pharmaceuticals.* European Journal of Pharmaceutics and Biopharmaceutics, 2020. **149**: p. 58-76.
19. Okwuosa, T.C., et al., *On demand manufacturing of patient-specific liquid capsules via co-ordinated 3D printing and liquid dispensing.* European Journal of Pharmaceutical Sciences, 2018. **118**: p. 134-143.
20. Goyanes, A., et al., *Fabrication of controlled-release budesonide tablets via desktop (FDM) 3D printing.* International Journal of Pharmaceutics, 2015. **496**(2): p. 414-420.
21. Gioumouxouzis, C.I., et al., *Controlled release of 5-fluorouracil from alginate beads encapsulated in 3D printed pH-responsive solid dosage forms.* AAPS PharmSciTech, 2018. **19**(8): p. 3362-3375.
22. Almeida, A., et al., *Novel amphiphilic chitosan micelles as carriers for hydrophobic anticancer drugs.* Materials Science and Engineering: C, 2020. **112**: p. 110920.
23. Almeida, A., et al., *Synthesis and characterization of chitosan-grafted-polycaprolactone micelles for modulate intestinal paclitaxel delivery.* Drug Delivery and Translational Research, 2018. **8**(2): p. 387-397.
24. Martins, S.M., et al., *Development and validation of a simple reversed-phase HPLC method for the determination of camptothecin in animal organs following administration in solid lipid nanoparticles.* Journal of Chromatography B, 2012. **880**: p. 100-107.

25. Schellekens, R., et al., *A novel dissolution method relevant to intestinal release behaviour and its application in the evaluation of modified release mesalazine products.* European Journal of Pharmaceutical Sciences, 2007. **30**(1): p. 15-20.
26. Higuchi, T., *Mechanism of sustained-action medication. Theoretical analysis of rate of release of solid drugs dispersed in solid matrices.* Journal of Pharmaceutical Sciences, 1963. **52**(12): p. 1145-1149.
27. Korsmeyer, R.W., et al., *Mechanisms of solute release from porous hydrophilic polymers.* International Journal of Pharmaceutics, 1983. **15**(1): p. 25-35.
28. Ritger, P.L. and N.A. Peppas, *A simple equation for description of solute release II. Fickian and anomalous release from swellable devices.* Journal of Controlled Release, 1987. **5**(1): p. 37-42.
29. Macedo, M.H., et al., *All layers matter: Innovative three-dimensional epithelium-stroma-endothelium intestinal model for reliable permeability outcomes.* Submitted, 2021.
30. Macedo, M.H., et al., *Development of an improved 3D in vitro intestinal model to perform permeability studies of paracellular compounds.* Frontiers in Bioengineering and Biotechnology, 2020. **8**: p. 1076.
31. Rao, J.P. and K.E. Geckeler, *Polymer nanoparticles: preparation techniques and size-control parameters.* Progress in Polymer Science, 2011. **36**(7): p. 887-913.
32. Hickey, J.W., et al., *Control of polymeric nanoparticle size to improve therapeutic delivery.* Journal of Controlled Release, 2015. **219**: p. 536-547.
33. Yuan, H., et al., *Stearic acid-g-chitosan polymeric micelle for oral drug delivery: in vitro transport and in vivo absorption.* Molecular Pharmaceutics, 2011. **8**(1): p. 225-238.
34. Silva, D.S., et al., *Self-aggregates of 3, 6-O, O'-dimyristoylchitosan derivative are effective in enhancing the solubility and intestinal permeability of camptothecin.* Carbohydrate Polymers, 2017. **177**: p. 178-186.
35. Li, L., et al., *Amphiphilic polymeric micelles based on deoxycholic acid and folic acid modified chitosan for the delivery of paclitaxel.* International Journal of Molecular Sciences, 2018. **19**(10): p. 3132.
36. *ISO/EN10993-5. International Standard ISO 10993-5 Biological Evaluation of Medical Devices—Part 5: Tests for Cytotoxicity: In Vitro Methods*. 2009, International Organization for Standardization: Geneva, Switzerland.
37. Laskar, P., et al., *In vitro evaluation of pH-sensitive cholesterol-containing stable polymeric micelles for delivery of camptothecin.* Journal of Colloid and Interface Science, 2014. **430**: p. 305-314.

38. Luo, P., et al., *Incorporation of camptothecin into reduction-degradable supramolecular micelles for enhancing its stability.* Colloids and Surfaces B: Biointerfaces, 2013. **109**: p. 167-175.
39. Du, Y., et al., *Redox sensitive lipid-camptothecin conjugate encapsulated solid lipid nanoparticles for oral delivery.* International Journal of Pharmaceutics, 2018. **549**(1-2): p. 352-362.
40. Yeh, T.-H., et al., *Mechanism and consequence of chitosan-mediated reversible epithelial tight junction opening.* Biomaterials, 2011. **32**(26): p. 6164-6173.
41. Mo, R., et al., *The mechanism of enhancement on oral absorption of paclitaxel by N-octyl-O-sulfate chitosan micelles.* Biomaterials, 2011. **32**(20): p. 4609-4620.
42. Narai, A., S. Arai, and M. Shimizu, *Rapid decrease in transepithelial electrical resistance of human intestinal Caco-2 cell monolayers by cytotoxic membrane perturbents.* Toxicology in vitro, 1997. **11**(4): p. 347-354.
43. Behrens, I. and T. Kissel, *Do cell culture conditions influence the carrier-mediated transport of peptides in Caco-2 cell monolayers?* European Journal of Pharmaceutical Sciences, 2003. **19**(5): p. 433-442.
44. Fischer, A.H., et al., *Hematoxylin and eosin staining of tissue and cell sections.* Cold Spring Harbor Protocols, 2008.
45. Woraphatphadung, T., et al., *pH-Responsive polymeric micelles based on amphiphilic chitosan derivatives: Effect of hydrophobic cores on oral meloxicam delivery.* International Journal of Pharmaceutics, 2016. **497**(1-2): p. 150-160.
46. Dramou, P., et al., *Folic acid-conjugated chitosan oligosaccharide-magnetic halloysite nanotubes as a delivery system for camptothecin.* Carbohydrate Polymers, 2018. **197**: p. 117-127.

CHAPTER 7

Oral delivery of camptothecin-loaded in chitosan-based micelles is effective in reducing colorectal cancer

The information provided in this chapter was based in the following publication:

Almeida, A., Castro, F., Resende, C. Lúcio, M., Schwartz Jr, S. & Sarmento, B., 2021. Oral delivery of camptothecin-loaded in chitosan-based micelles is effective in reducing colorectal cancer, *submitted.*

In this paper, I was responsible for the conception, execution and revision of the manuscript. Flávia Castro was also responsible for the methodology and revision of the manuscript. Carlos Resende was responsible for the methodology and the supervisor was responsible for reviewing and submit the manuscript. This paper was not previously included in other thesis and it is partially reproduced in this section.

7.1. Abstract

Colorectal cancer (CRC) is a heterogeneous disease with a high incidence and mortality worldwide. Conventional CRC chemotherapy is still ineffective in eradicating the disease, and novel approaches with improved therapeutic results are needed. Camptothecin (CPT), a powerful anticancer agent, was incorporated into chitosan-based polymeric micelles in this study with the goal of reducing CRC development by oral administration. Empty micelles demonstrated a safe profile when incubated with human blood cells, while CPT-loaded micelles presented anticancer activity against HCT116, Caco-2 and HT29 CRC cell lines. When tested against 3D CRC multicellular spheroids, CPT-loaded micelles were effective in reducing spheroid's metabolic activity and size. *In vivo* studies in an HCT116 xenograft model revealed that the group treated subcutaneously with CPT-loaded micelles had a significant reduction in tumor growth when compared to non-treated animals. Moreover, in a more biological relevant *in vivo* model based on CRC developed by chemical induction, orally administered CPT-loaded micelles demonstrated a significant effect on CRC lesions reduction. Additionally, the tumors found in the animals treated with CPT-loaded micelles presented smaller tumors than the other treatment groups. The findings presented here suggest that CPT-loaded chitosan-based micelles, by improving drug solubility and oral bioavailability, as well as their safety profile for normal tissues, strongly support their use for CRC chemotherapy.

7.2. Introduction

Cancer is a leading cause of death worldwide and the number of deaths is expected to rise in the next decades. Particularly, CRC is the third most common cancer and the second with highest mortality, according to 2020 data [1]. The current available treatments are dependent on the stage of the disease, but surgery, radiotherapy, immunotherapy and chemotherapy can be one or some of the approaches used on CRC treatment. Adjuvant chemotherapy, given after surgery, is the approach that most prolongs the patient's life, but on the other hand, it is also the treatment that causes the most adverse effects due to non-specific biodistribution and the development of drug resistance [2].

In the last few years, several anticancer oral drug formulations have been developed since the oral route is preferred for patients and clinicians over intravenous administration. This is due to its non-invasive character, associated with better patient compliance, facility of administration and reduced cost of treatment. However, several anticancer drugs have low aqueous solubility and bioavailability, resulting in poor therapeutic outcome and significant side-effects resulting of the need of high doses of drug for the treatment [3].

CPT is a potent anticancer drug used in the treatment of several types of cancer, including CRC [4-6]. Its mechanism of action is based on the CPT binding to the topoisomerase I-DNA complex during the S-phase of the cell cycle, leading to the cell cycle arrest and, consequently, cell death [7, 8] Its therapeutic potential is hampered by the low aqueous solubility and permeability, belonging to the Class IV of the Biopharmaceutical Classification System (BCS). Also, the pharmacological action of CPT is pH-dependent, where at pH < 5.5 is stable in the lactone form and biologically active, but at higher pH the molecule turns the conformation to the carboxylated form, which has limited biological effect [9]. Thus, many efforts have been made over the last decades to improve CPT stability and solubility through the synthesis of new CPT analogues, such as topotecan (Hycamtin®), irinotecan (Camptosar®) and belotecan (Camtobell®), the only three analogues approved for clinical administration. These CPT analogues still present high lipophilicity and cytotoxicity, being, thus, intravenously administered. They are substrates of efflux-systems as the P-glycoprotein (P-gp), which contributes for its reduced oral absorption [10]. Hence, encapsulating CPT in nanocarriers may be a way to improve its solubility and stability while avoiding efflux pumps, which are critical points for improved bioavailability after oral administration.

Polymeric micelles, structures at the nanometric scale produced by amphiphilic polymers, offer several advantages such as encapsulation of drugs with high stability and encapsulation efficiency and, ability to penetrate in cancer tissues due to their small size [11, 12]. Many anticancer drugs have been tested using these nanocarriers as solubility enhancers and delivery systems, with some formulations undergoing clinical trials and others already on the market [13-16]. CPT oral bioavailability can be increased by the encapsulation into polymeric micelles, which can increase the drug's intestinal tract residence time via mucoadhesion and mucodiffusion, resulting in an improved therapeutic activity. We previously described chitosan-based polymeric micelles with properties suitable for oral delivery of CPT [17]. Here, we aim to investigate the therapeutic potential of CPT-loaded chitosan-based polymeric micelles in CRC context. Thus, CPT-loaded micelles were deeply studied regarding its anticancer activity using 2D CRC cancer cells and 3D multicellular CRC spheroids. Further, HCT116 xenograft and azoxymethane (AOM)/dextran sodium sulfate (DSS) mouse models of inflammatory CRC were established to evaluate the pharmacokinetics and therapeutic response to CPT-loaded chitosan-based polymeric micelles. Overall, this work highlights the efficacy of the mentioned micelles in reducing the tumor growth over time in a safe manner, as well as, reducing the tumor score in mice, after oral administration, which can potentially be used as a promising therapeutic option.

7.3. Materials and Methods

7.3.1. Ethics statement

Human samples were obtained in agreement with the principles of the Declaration of Helsinki. Monocytes used to produce CRC spheroids were harvested from surplus buffy coats from healthy blood donors, which were generously given by the Immunochemotherapy Department of Centro Hospitalar Universitário São João (CHUSJ) Porto, Portugal. The CHUSJ Ethics Committee approved the procedures (protocol 90/19) and blood donors gave their written permission for the by-products of their blood samples to be used for research purposes. Regarding the animal studies, all experiments were approved by the Animal Welfare Body at i3S (ref. BSm_2017_10) and conducted under FELASA and the European Directive 2010/63/EU guidance. At the defined endpoints, mice were euthanized by cervical dislocation by trained personal, certified by the Portuguese Direção-Geral de Alimentação e Veterinária, to minimize suffering. Male C57BL/6 mice were acquired from Charles River (France) and male N:NIH(S)II-*nu/nu* mice were developed by successive crossings and backcrossing's between athymic nu/nu mice, on an N:NIH(S) background, and female CBA/N mice that have an X-linked immune defect in B-lymphocyte function [18]. Male N:NIH(S)II-*nu/nu* mice aged 4–6 weeks and weighing 16–20 g were breed and cared at the i3S Animal Facility (Porto, Portugal).

7.3.2. Materials

Chitosan with 15% DA and weight-average molecular weight value (Mw) of 112 kDa, oleic acid, 1-hydroxybenzotriazole hydrate (HOBt), *N*-(3-dimethylaminopropyl)-*N*′-ethylcarbodiimide hydrochloride (EDC·HCl), trehalose, *O*-methyl-*O*′-succinylpolyethylene glycol 5′000 (mPEG-COOH), Histopaque-1077 and resazurin were all purchased from Sigma-Merck. Ultracel® 30 kDa ultrafiltration discs (PLTK04310, 44.5 mm diameter, Merck Millipore) were used to purify the mPEG-CS polymer and 3.5 kDa cutoff dialysis membrane (Spectra/Por® 3 Dialysis Tubing, Fisher Scientific) was used to purify the polymer mPEG-CS-OA and to produce the polymeric micelles. CPT was purchased from Hangzhou ROYAL Import & Export Co., Ltd,

7.3.3. Production of camptothecin-loaded polymeric micelles

Polymeric micelles based on chitosan were obtained by a dialysis method, as previously described [17, 19, 20]. Briefly, *O*-methyl-*O*′-succinyl polyethylene glycol-chitosan-oleic acid (mPEG-CS-OA copolymer) was dissolved in dimethyl sulfoxide (DMSO):HCl 0.1 M (9:1) in a glass vial until its complete dissolution. Then, mixture was transferred to a dialysis bag to remove the organic solvent and dialyzed against water during 3 cycles of water renewal.

mPEG-CS-OA micelles were centrifuged during 20 min at 3110 g to remove possible insoluble polymer segments and/or the non-encapsulated drug and, then cryopreserved with 0.5% (w/v) trehalose, freeze-dried and stored at -20 ºC until further utilization. To obtain CPT-loaded micelles, CPT was previously dissolved in DMSO at 1 mg/mL and added to the polymer solutions under stirring at 15% (w/w) drug loading. After 6 h, micelles were dialyzed, centrifugated, cryopreserved in the presence of trehalose as cryoprotectant, freeze-dried and stored as previously described [17, 20].

7.3.4. Characterization of camptothecin-loaded polymeric micelles

After freeze-drying, polymeric micelles were resuspended in MilliQ water at 1% (w/v) concentration and the mean diameter, polydispersity index (PdI), and surface charge were assessed by DLS and Laser Doppler Micro-electrophoresis (ZetaSizer Nano ZS, Malvern, UK), respectively, with an angle of 173° at 25 °C. The CPT association efficiency (AE) was determined using the indirect method by high-performance liquid chromatography (HPLC) [21] and calculated as described in Equation 7.1. The drug loading (DL) was calculated according to Equation 7.2. Succinctly, the HPLC analysis was performed in a Shimadzu UFLC Prominence System (USA) equipped with two Pumps LC-20AD, a column oven CTO-20AC, an autosampler SIL-20AC, a System Controller CBM-20A, a degasser DGU- 20A5, a RF-10Axl fluorescence detector coupled to the LC System and a LC Solution, Version 1.24 SP1 (Shimadzu).

$$AE\% = \frac{weight\ of CPT\ added - weight\ of\ free\ CPT}{weight\ of\ CPT\ added} \times 100 \quad (7.1)$$

$$DL\% = \frac{weight\ of\ CPT\ added - weight\ of\ free\ CPT}{total\ micelles\ weight} \times 100 \quad (7.2)$$

7.3.5. Cell culture conditions

HCT116 human colorectal carcinoma, C2BBe1 [Cacao-2 clone] and HT29 (human colorectal adenocarcinoma) cells were obtained from American Type Culture Collection (ATCC, USA). HCT116 cells were cultured in Roswell Park Memorial Institute (RPMI)-1640 media, supplemented with 10% of heat inactivated fetal bovine serum (FBS), penicillin (100 IU/mL) and streptomycin (100 mg/mL). HT29-MTX mucus-producing cells were kindly provided by Dr. T. Lesuffleur (INSERM U178, Villejuif, France). Caco-2, HT29 and HT29-MTX cell lines were cultured in Dulbecco's Modified Eagle's Medium (DMEM) supplemented with 10% (v/v) FBS, penicillin (100 IU/mL) and streptomycin (100 mg/mL). Human intestinal fibroblast (HIF) primary cells were acquired from ScienCellTM Research Laboratories (USA) and cultured with Fibroblast Medium (FM) supplemented with 2% FBS,

1% of Fibroblast Growth Supplement (FGS), and 1% penicillin/streptomycin solution (all supplements from ScienCell). Human monocytes were isolated from buffy coats from healthy blood donors using RosetteSep-Human Monocyte Enrichment Cocktail (StemCell Technologies, France), following the manufacturer's instructions. HPMEC-St1.6R cells were kindly provided by Professor C. James Kirkpatrick (Institute of Pathology, Johannes Gutenberg University of Mainz, Germany) and cultured in M199 medium (Sigma), supplemented with 20% FBS, penicillin (100 IU/mL) and streptomycin (100 mg/mL), 25 µg/mL of Endothelial Cell Growth Supplement (ECGS) and 25 µg/mL of heparin and 100 µg/mL L-glutamine. All the cells were cultured in 75 cm^2 T-flasks, inside an incubator at 37 ºC and 5% CO_2 and 95% relative humidity.

7.3.6. Polymeric micelles cytocompatibility in human peripheral blood mononuclear cells

Peripheral blood mononuclear cells (PBMCs) were isolated from buffy coats from healthy blood donors [22]. Briefly, blood collected from the buffy coats was diluted with PBS (1:4) and added over the same volume of Histopaque-1077 and centrifuged (30 min, 800 g, 22 ºC, without brake). The PBMCs layer formed after centrifugation was transferred for new centrifuge tubes and cells were washed with PBS and centrifugated as previously described. The washing and centrifugation steps were repeated until the supernatant has become transparent. Then, PBMCs were counted and 2×10^4 cells were seeded per well in 96-well plates cultures with RPMI-1640 medium. Afterwards, cells were treated with empty and loaded micelles and free CPT at concentrations ranging from 0.025 to 250 µg/mL during 24, 48 and 72 h. At each time-point, the medium was removed and cells were washed twice with PBS and incubated with complete RPMI-1640 medium containing 20% resazurin (0.1 mg/mL) during 2 h at 37 ºC, 5% CO_2 and 95% relative humidity. The fluorescence was measured by the relative fluorescence units (RFUs) using a microplate reader SynergyTM Mx HM550 (Biotek) set at 530/590 (excitation/emission wavelength, respectively) and a negative control consisting in cells incubated with 1% (v/v) of Triton X-100 in complete medium and a positive control consisting in cells incubated with complete medium were also included. The experiment was performed in triplicate and, the cytocompatibility was obtained regarding the cellular metabolic activity, which was quantified according to Equation 7.3:

$$Metabolic\ activity\ (\%) = \frac{fluorescence\ (experimental\ value) - fluorescence\ (positive\ control)}{fluorescence\ (negative\ control) - fluorescence\ (positive\ control)} \times 100 \qquad (7.3)$$

7.3.7. *In vitro* antitumor efficacy studies in 2D colorectal cancer cell lines

To assess the antitumor efficacy of CPT-loaded micelles, a resazurin assay was performed in Caco-2, HT29 and HCT116 cells. Briefly, 2×10^4 Caco-2 cells and 1×10^4 HT29 and 1×10^4 HCT116 cells were seeded in 96-well plates and incubated at 37 ºC and 5% CO_2 and 95% relative humidity during 24 h allowing cells to adhere to the plate. Culture medium was then removed and cells were washed twice with PBS and, treated with empty and loaded micelles and free drug in a range of concentrations from 0.025 to 250 µg/mL, in function of CPT concentration. Samples were allowed to incubate during 24, 48 and 72 h. At each time-point, the medium was removed and cells were washed twice with PBS and incubated with complete DMEM or RPMI-1640 medium containing 20% resazurin (0.1 mg/mL) during 2 h at 37 ºC, 5% CO_2 and 95% relative humidity. The fluorescence was measured as described in Section 2.5, as well as the controls and, the anticancer activity was obtained regarding the cellular metabolic activity, quantified according to Equation 7.3.

7.3.8. *In vitro* antitumor efficacy studies using multicellular tumor spheroids

7.3.8.1. Multicellular tumor spheroids formation

Multicellular tumor spheroids (MCTSs) were prepared as previously described [23]. Briefly, MCTS were formed using commercially available micro-molds (3D Petri Dish®, from MicroTissues Inc.) filled with agarose (2%, w/v) dissolved in NaCl (0.9%, w/v) until their solidification. Then, molds were placed in 12-well plates and RPMI-1640 media (2 mL) was added to each well to equilibrate the molds overnight before cell seeding. Afterwards, cell suspension (190 µL; corresponding to 5000 total cells per MCTS) was added to each mold and allowed to settle for 30 min, before adding RPMI-1640 media (2 mL) to each well. MCTS were produced in triple culture at a ratio of 4:1:4 (monocytes:HCT116:HIF) and cultured until day 7 media. Culture media was replaced every other day and supplemented with M-CSF (50 ng/mL) for macrophage differentiation. Monocytes were isolated from buffy coats of health blood donors as previously described [24].

7.3.8.2. Multicellular tumor spheroids size measurement

After MCTS formation, empty and loaded micelles and free CPT were added to the spheroids at 0.25, 2.5 and 25 µg/mL (regarding CPT concentration) and incubated during 24, 48 and 72 h. A mold containing 81 spheroids was used for each condition in triplicate and MCTS without treatment were used as control. After the incubation time, MCTS images were taken using an optical microscope (Leica DMi1). The size was determined by measuring the diameter of the MCTS, using ImageJ software and, the average size of each

condition was reached by the average of two diameters measurements per MCTS, performed in at least ten different spheroids.

7.3.8.3. Multicellular tumor spheroids metabolic activity

The MCTS metabolic activity after incubation with empty and loaded micelles and free CPT was measured by the ATP content of the cells, which is directly proportional to the number of viable cells in culture [25]. After spheroids formation, spheroids were collected and placed in each well Corning® spheroid microplates with 96-well plates cultured with 100 µL of RPMI-1640 media. Then, 100 µL of empty and loaded micelles and free CPT at 0.25, 2.5 and 25 µg/mL (in function of CPT concentration) were added to each well and incubated at 37 °C, under stirring (30 rpm) during 24, 48 and 72 h. At each time-point, 100 µL of medium was removed and 100 µL of CellTiter-Glo® 3D Reagent (Promega Corporation, USA) were added. Then, plates were shaken (100 rpm) during 5 min and incubated during 25 min at RT. Luminescence was measured using a microplate reader SynergyTM Mx HM550 (Biotek). Each condition was performed in triplicate.

7.3.9. *In vitro* permeability studies

The intestinal permeability of CPT delivered from chitosan micelles (CS-OA and mPEG-CS-OA) was assessed using two different intestinal models. The first, the standard model to study the intestinal permeability of molecules constituted only by Caco-2 cells; and the second, a 3D model that better mimics what happens *in vivo*, constituted by Caco-2 cells, HT29-MTX mucus-producing cells, HIF embedded in a collagen coating and HPMEC-St1.6R cells. In the Caco-2 model, 1×10^5 cells/cm^2 were seeded in a 12-Transwell® cell culture inserts (pore size of 1 µm, Millicell) and allowed to grow and differentiate for 21 days inside an incubator at 37 ºC, 5% CO_2 and 95% relative humidity. For the 3D intestinal model, HPMEC-St1.6R cells were seeded in a gelatin coating in the basolateral side of the Transwell® insert at density of 5×10^4 cells/cm^2 and left to adhere during 2 h. Then, the inserts were placed in a 12-well plate and the apical side was coated with collagen with HIF embedded for 30 min. After, 1×10^5 cells/cm^2 of Caco-2:HT29-MTX in a 9:1 ratio were seeded in the apical side of the inserts over the collagen coating [26]. To maintain and culture both models, DMEM complete medium was used for 21 days and the medium was changed every two/three days from both sides if the Transwell®. Also, the models were monitored by the transepithelial electrical resistance (TEER) using an EVOM2 epithelial voltohmmeter equipped with a STX2 electrode (World Precision Instruments, Inc.), that provides information about the monolayer's integrity. 21 days after the complete growth and

differentiation of the intestinal models, the culture medium was removed from the transwells® and cells were washed twice with pre-warmed Hank's Balanced Salt Solution (HBSS) buffer and left to equilibrate with HBSS during 30 min at 37 ºC and 100 rpm in an orbital shaker (KS 4000 ic control orbital shaker, IKA). Then, HBSS was removed from the apical side and free CPT, CPT-loaded CS-OA micelles and CPT-loaded mPEG-CS-OA micelles were added to the apical side (0.5 mL) at 2 µg/mL (in function of CPT concentration) and plates were incubated at 37 ºC and 100 rpm. During predetermined time points (15, 30, 45, 60, 120, 180, and 240 min), 200 µL aliquot was taken from the basolateral side and the volume withdrawn was replaced by HBSS. To determine the monolayer integrity, the TEER was measured at each time-point. The amount of CPT permeated through the monolayers was quantified by HPLC, as previously described [21] and, the permeability percentage and apparent permeability coefficient (P_{app}) were determined through the Equation 7.4 and 7.5, respectively.

$$CPT\ permeated\ \% = \frac{total\ mass}{theoretic\ mass} \times 100 \quad (7.4)$$

$$Papp = \frac{dQ}{A \times C_0 \times dt} \quad (7.5)$$

where dQ (µg) is the total amount of compound in the basolateral side, A is the surface area of the insert (cm^2), C_0 is the initial concentration in the apical side (µg/mL) and dt (s) is the time of the experiment. The assay was performed in triplicate.

7.3.10. *In vivo* studies

7.3.10.1. Pharmacodynamic study in a xenograft model

CBA nude mice (6-8 week old) were maintained in a temperature and humidity-controlled in the facility under a 12 h light/dark cycle and, water and standard diet were given ad libitum. For tumor inoculation, mice were anaesthetized with isoflurane by inhalation and each animal was injected subcutaneously in the right lateral flank with 100 µL of serum free RPMI-1640:Matrigel (1:1) containing 1×10^6 of HCT116 cells. Treatment started when tumors reached approximately 100 mm^3. Animals were randomized in five groups of six mice: (i) CPT-loaded micelles, (ii) empty micelles, (iii) free CPT (iv) free CPT administered intravenously (i.v.) (v) untreated control group. All groups were injected subcutaneously close to the tumor, except for the group where CPT was administered i.v.. Animals treated with CPT-loaded micelles and free CPT received a dose of 1 mg/kg and animals treated with free CPT i.v. received a dose of 0.075 mg/kg (maximum dose of CPT dissolved for i.v. administration) three times per week for two weeks. During the study, tumor size (V) was

measured using a caliper in two dimensions, width (W) and length (L) with a caliper. The final volume (V) was calculated using the Equation 7.6:

$$V(mm^3) = length \times (width)^2 \times 0.5 \quad (7.6)$$

Tumor growth was measured until day 30 and a survival study was performed until day 60. Once mice achieved a tumor volume >1800 mm^3 the animals were euthanized. The area under the curve (AUC) was calculated by GraphPad Prism Software vs. 6.0 (GraphPad Software Inc).

7.3.10.2. Colorectal cancer disease model

C57BL/6 mice (6-8 week old) were maintained in a temperature and humidity-controlled in the facility under a 12 h light/dark cycle and, water and standard diet were given ad libitum. After 1 week of adaptation, animals were chemically induced to develop CRC by the administration of AOM (Sigma) and DSS (MP Biomedicals, 36,000–50,000 Da) [26, 27]. Thus, animals were injected intraperitoneally with AOM (10 mg/kg body weight) with a sterile syringe in a laminar airflow hood. After 48 h, 1.5% (w/v) DSS was given in drinking water over 5 days followed by regular drinking water for 14 days. This DSS cycle was repeated twice and, lesions were evaluated after the first and second DSS cycle by colonoscopy. The animals were monitored and checked for their weight and some abnormalities and registered in the score sheet every other day.

7.3.10.3. In vivo pharmacokinetic study

C57BL/6 mice induced with CRC were used to perform a pharmacokinetic study of CPT-loaded chitosan micelles. The different formulations (CPT in suspension and CPT-loaded micelles) were administered by oral gavage (1.5 mg/kg) and CPT i.v. was administered intravenously via the lateral tail vein (0.1 mg/kg). Blood samples were collected at 1, 2, 4, 6 and 24 h after CPT injection via facial vein and, the animals at the last timepoint were sacrificed with lethal dose of anesthesia followed cervical dislocation. The blood samples were processed and quantified by HPLC as previously described [21].

7.3.10.4. In vivo biodistribution of polymeric micelles

C57BL/6 mice induced with CRC were used to perform a biodistribution study of the chitosan micelles. Fluorescent mPEG-CS-OA micelles were produced following the protocol described in Section 2.2., but instead of using CPT, 2 µg of cyanine7.5 carboxylic

acid (Cy7.5, Lumiprobe) dissolved in DMSO were loaded into the micelles. Fluorescent chitosan micelles were orally administered and, at different time-points, the fluorescence was acquired in an IVIS Lumina LT system (Perkin Elmer, Waltham, MA, USA) after brief anesthetization with inhalational isoflurane. Before imaging, the abdominal fur was shaved with a hair clipper, and the background signal from non-treated animals was used to determine the correct radiance signal. Animals were sacrificed by cervical dislocation after 12 or 24 hours. Following necropsy, the colon and tissues were placed in petri dishes and examined using the IVIS system. The relevant radiance signal was determined using the background signal from the colon of non-treated animals and, the radiant efficiency from the same sized regions was quantified using Living Image® software v. 4.4.

7.3.10.5. In vivo pharmacodynamic study

Male C57BL/6 mice induced with CRC were used to assess the therapeutic efficacy of CPT-loaded chitosan micelles. After tumor growth confirmation and evaluation by colonoscopy, animals were equally distributed regarding their tumor development by the different groups (saline, CPT i.v., CPT suspension, empty micelles and CPT-loaded micelles, n=7) and formulations were administered by oral gavage three times per week along two weeks, with the exception of CPT i.v., which was administered intravenously. CPT suspension and CPT-loaded micelles were administered at 1.5 mg/kg, while CPT i.v. was administered at 0.1 mg/kg. After receiving the treatment, animals were sacrificed by cervical dislocation and the intestine and colon were measured, the spleen index calculated by the spleen weight/body weight of each animal, the macroscopic tumors were counted and measured using a caliper.

7.3.11. Statistical analysis

Statistical analysis was performed using the GraphPad Prism Software vs. 6.0 (GraphPad Software Inc). All data are presented as mean ± SD. Statistical significance of the difference between two groups was evaluated by the Student's t-test. Differences between groups were compared using one-way or two-way analysis of variance (ANOVA) using Tukey's, Sidak's or Dunnet's multiple comparison test. Results are expressed as mean ± standard deviation and geometric means with 95% confidence intervals.

7.4. Results and Discussion

7.4.1. Characterization of chitosan-based micelles

The chitosan amphiphilic derivative was previously synthesized through the grafting of mPEG and oleic acid on the chitosan chains [17]. Polymeric micelles were obtained by

dialysis method and its size, PdI, surface charge and AE were investigated (Table 7.1). CPT-loaded micelles of a theoretical loading of 15% (w/w) were of 180 nm in size and slightly heterogeneous with PdI close to 0.25, as commonly reported [19]. These findings are consistent with the TEM analysis, where CPT-loaded micelles appear to be larger in diameter than empty micelles (Figure A4.1, supplementary material).

Micelles presented a positive surface charge, due to the cationic feature of chitosan and, the surface charge tend to increase with the encapsulation of CPT [17, 29]. Moreover, highly positively charged micelles are favorite since they can increase cell interaction, since cellular membranes are negatively charged and, thus, improve the micelles adhesion and control the release of CPT to the cells.

Regarding the AE, CPT presented a 55% of association to the micelles, which is translated in 8% (w/w) DL in the whole formulation. Despite the high DL obtained for these micelles, it was possible to observe a smooth and spherical shape in both empty and loaded micelles, as well as, the absence of aggregation (Figure A4.1, supplementary material). Thus, this system, present high potential for oral drug delivery since it was possible to associate into the micelles a high amount of drug.

Table 7.1. The particle size, polydispersity index (PdI), micelles surface charge, association efficiency (AE) and drug loading (DL) of empty chitosan micelles and CPT-loaded micelles. Values are represented as mean ± SD (n = 3).

	Size (nm)	PdI	Zeta potential (mV)	AE (%)	DL (%)
Empty micelles	132 ± 3	0.262 ± 0.026	37.5 ± 1.2	-	-
CPT-loaded micelles	178 ± 6	0.281 ± 0.016	42.8 ± 4.3	55.5 ± 8.9	8.3 ± 1.3

7.4.2. Polymeric micelles cytocompatibility

The cytocompatibility of empty chitosan micelles was investigated using PBMC's and the CRC HCT116 cell line after pre-determined times of incubation. As depicted in Figure 7.1, empty micelles presented no cytotoxicity against PBMC's and HCT116 cells to all the tested concentrations indicating a safe profile. However, a small decrease in cell viability with increasing incubation time can be observed. Still, this decrease is not biologically significant for assuming that the empty micelles, as a drug transport vehicle, have a toxic profile. [30]. Indeed, chitosan is recognized as a well-known and safe biomaterial [31, 32] and, other similar chitosan derivatives described in the literature also demonstrated good cytocompatibility, correlating with the findings in this study [33, 34].

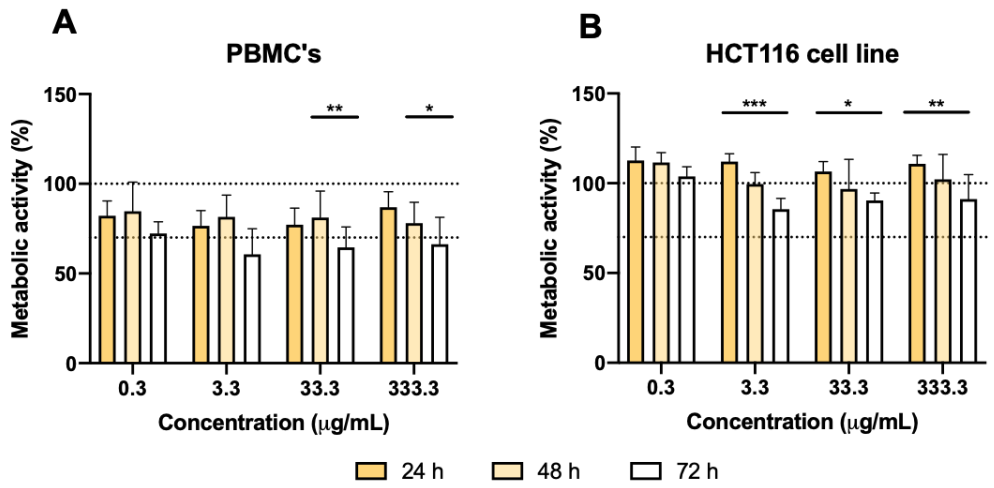

Figure 7.1. Cytocompatibility of empty chitosan-based polymeric micelles during 24, 48 and 72 h of incubation. (A) metabolic activity of PBMC's; (B) metabolic activity of HCT116 cell line. Concentration is represented in function to the micelle mass. Error bars represent mean ± SD (n = 3). *p<0.05, **p<0.01 and ***p<0.001 denotes a significant difference between incubation times by two-way analysis of variance (ANOVA) Tukey's multiple comparison test.

We also investigated the possible protection effect of the chitosan micelles when loaded with CPT in contact with human blood cells. Figure 7.2 shows the metabolic activity of PBMC's after incubation with free and CPT-loaded micelles during 24 h, 48 h and 72 h of incubation. It is possible to observe a higher metabolic activity of CPT-loaded micelles to all the tested concentrations and during all the incubation times. When freely incubated, CPT presented significant levels of cytotoxicity dependent on the concentration and the time of incubation. After 24 h, free CPT presented high cytotoxicity to the blood cells at the higher concentrations, while CPT-loaded micelles presented a cellular viability around 70% at the highest concentration. The same pattern was followed after 48 h of incubation, where free CPT became cytotoxic even at the lowest concentrations, while CPT-loaded micelles presented a good cellular viability. This is even more evident after 72 h of incubation, however, at the highest concentration CPT-loaded micelles presented a cytotoxic effect. These results may be explained by the slow and controlled release of CPT from the chitosan micelles, which becomes greater after 72 h of release [17]. Because CPT is released slowly into the medium, cell metabolic activity is not adversely affected as much as it is with free CPT, which can interact with blood cells at any time.

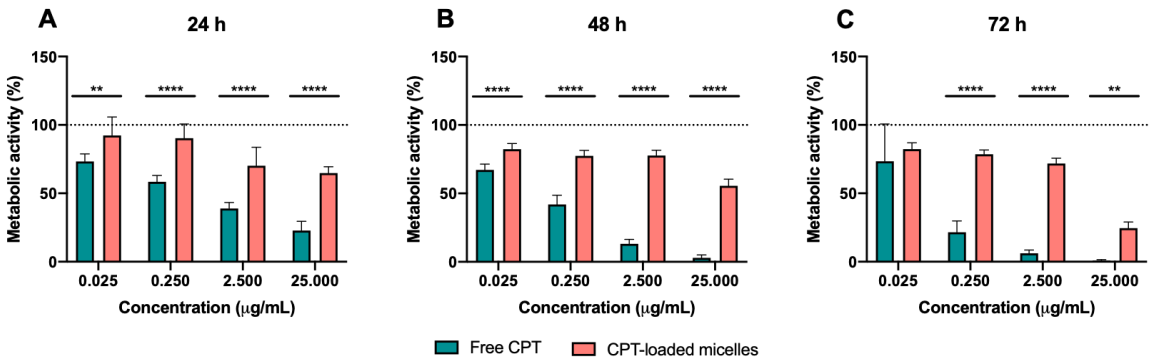

Figure 7.2 Cytotoxicity of free CPT and CPT-loaded micelles tested in PBMC's during (A) 24 h; (B) 48 h and (C) 72 h of incubation. Concentrations are represented in function of CPT. Error bars represent mean ± SD (n = 3). **p<0.01, ***p<0.001 and ****p<0.0001 denotes a significant difference between free CPT and CPT-loaded micelles by two-way analysis of variance (ANOVA) Sidak's multiple comparison test.

7.4.3. *In vitro* antitumor efficacy of camptothecin-loaded micelles

To evaluate the therapeutic effect of CPT-loaded micelles, HCT116 cells were incubated with free CPT or CPT-loaded micelles, and their viability was assessed at different time points. As depicted in Figure 7.3, both CPT and CPT-loaded micelles presented a decrease on the metabolic activity, which was dependent on CPT concentration and time of incubation. After 48 h and 72 h of, free and CPT-loaded micelles presented a similar behaviour - the cellular viability decreased with the increase of CPT concentration. Nevertheless, CPT-loaded micelles presented a significant difference compared with free CPT in the decrease of the cellular viability, which demonstrates the anticancer potential of CPT-loaded micelles. This pattern was also observed for Caco-2 and HT29 CRC cell lines (Figure A4.2, supplementary material). Polymeric micelles presented a significative reduction on the metabolic activity of these cells at the high concentrations after 48 h and 72 h of incubation (Figure 7.3). The *in vitro* antitumor activity of CPT micelles based on chitosan has been described in the literature, demonstrating the effectiveness of this type of vehicle in the release of anticancer drugs and its potential effect on cell proliferation reduction [35, 36].

Conversely, the same pattern was not verified PBMC's when incubated with CPT-loaded micelles. Their differential impact on metabolic activity of CRC cell lines, but not in PBMC's, may be explained by the CPT mechanism of action. As previously described, CPT binds to the topoisomerase I, which is overexpressed in solid tumors. Therefore, the CPT encapsulation into chitosan micelles can provide targeting and accumulation in the tumor, which was not observed in blood cells, considering that there is no overexpression of topoisomerase I [37].

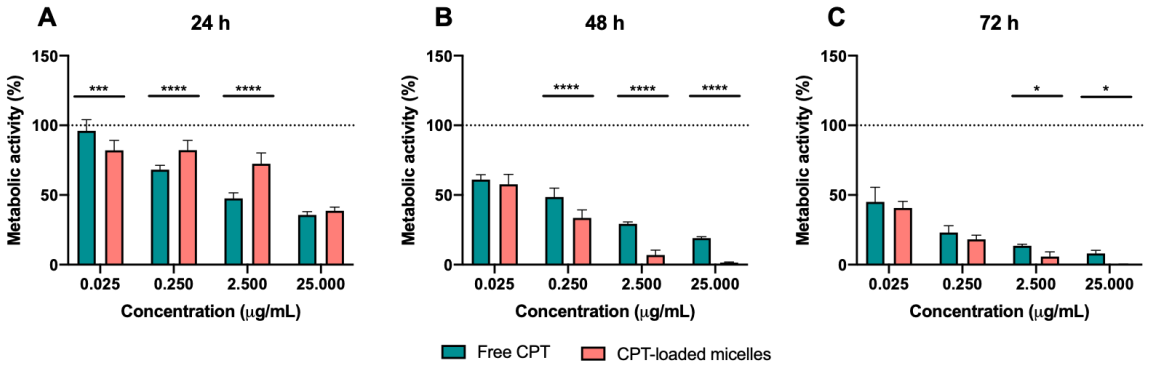

Figure 7.3 *In vitro* therapeutic efficacy of free CPT and CPT-loaded micelles against HCT116 cell line during (A) 24 h; (B) 48 h and (C) 72 h of incubation. Concentrations are represented in function of CPT. Error bars represent mean ± SD (n = 3). *p<0.05, ***p<0.001 and ****p<0.0001 denotes a significant difference between free CPT and CPT-loaded micelles by two-way analysis of variance (ANOVA) Sidak's multiple comparison test.

The *in vitro* anticancer activity of CPT-loaded mPEG-CS-OA micelles was also tested in a more complex model, 3D multicellular CRC spheroids. These spheroids were previously described in our group [23], and are constituted by HCT116 CRC cell line, intestinal fibroblasts and macrophages (Figure 7.4A and B). Firstly, the metabolic activity of the spheroids was measured by the ATP content of the cells, which is directly proportional to the number of viable cells [25], after incubation with free CPT and CPT-loaded and empty micelles. CPT-loaded micelles presented a significative reduction of the cellular viability after 24 h of incubation at the highest concentration, similar to what happens with free CPT (Figure 7.4C). This decrease on the cellular viability was prolonged overtime, where after 48 h and 72 h of incubation (Figure 7.4D and E), CPT-loaded micelles were significantly more effective than free CPT. Despite CPT-loaded micelles showed a similar effect as the obtained for the CRC cell lines regarding the anticancer activity, free CPT presented less efficacy compared with the 2D studies. This difference may be explained by the presence of other cell types, as fibroblasts and macrophages. On the other hand, polymeric micelles, due to their cationic character and small size, favor the interactions with the cell membranes, leading to a better cell penetration, supporting the spheroid size reduction results. Regarding the effect of the empty micelles, it was shown high cellular viability values, corroborating with the previous results, where empty micelles showed no cytotoxic effects in CRC cell lines.

The reduction in metabolic activity can be related to the size of the spheroid [23, 38]. In fact, it was demonstrated a slight decrease on the spheroid diameter when incubated with CPT-loaded micelles (Figure 7.4F-H). This decrease is more relevant after 72 h of incubation

with the CPT-loaded micelles (Figure 7.4H), in agreement with previous effect of CPT-loaded micelles in metabolic activity.

The *in vitro* anticancer activity of CPT-loaded micelles was also demonstrated by the wound healing assay (Figure A4.3) [39, 40]. Drug-loaded micelles were able to significantly reduce the wound closure even after 48 h of incubation, demonstrating a better inhibition effect than the free CPT. Its efficacy was more evident at the highest CPT concentration (25 µg/mL). Thus, CPT-loaded chitosan micelles showed an in vitro potential to reduce the cellular viability of CRC cells in 2D cultures and 3D multicellular spheroids, model that better represent the tumor microenvironment.

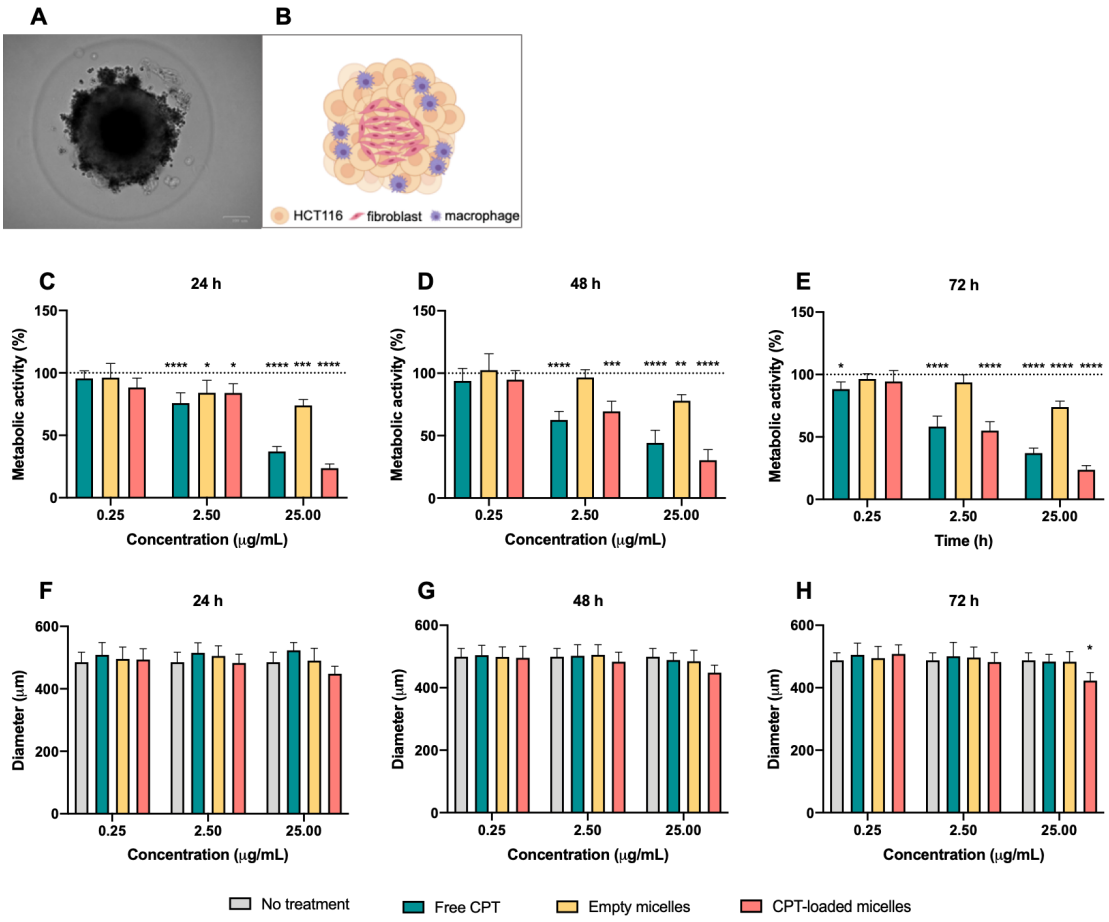

Figure 7.4. Metabolic activity and diameter measurement of 3D multicellular CRC spheroids after incubation with free CPT, empty micelles and CPT-loaded micelles. (A) 3D multicellular CRC spheroid; (B) schematic representation of the 3D multicellular CRC spheroid; spheroids metabolic activity after (A) 24 h, (B) 48 h and (C) 72 h of incubation with free CPT, empty micelles and CPT-loaded micelles; spheroids diameter after (A) 24 h, (B) 48 h and (C) 72 h of incubation with free CPT, empty micelles and CPT-loaded micelles. Concentrations are represented in function of CPT. Error bars represent mean ± SD (n = 3). *p<0.05, **p<0.01, ***p<0.001 and ****p<0.0001 denotes a significant difference when compared with the control (non-treated spheroids) by two-way analysis of variance (ANOVA) Tukey's (C, D and E) and Dunnet's (F, G and H) multiple comparison test.

7.4.4. *In vitro* intestinal permeability of CPT from chitosan micelles

The *in vitro* intestinal permeability of CPT was assessed in a Caco-2 monoculture model and in a 3D epithelium-stroma-endothelium intestinal model that better mimics the *in vivo* situation [26]. As depicted in Figure 7.5, CPT from polymeric micelles was able to cross the epithelial and endothelial barriers of the Caco-2 and 3D intestinal models, respectively, reaching a P_{app} of 4.5×10^{6} cm/s for the Caco-2 model and a P_{app} of 5.4×10^{6} cm/s in the more complex and realistic model. The TEER values were kept high throughout the experiment, which indicates that the integrity of the cell layers was maintained.

Relatively low P_{app} of CPT freely incubated in Caco-2 cells are well described in the literature [41, 42]. However, the association of CPT into polymeric micelles tend to increase its intestinal permeability since the drug can remain stable along the GIT, being only released at the intestine at high concentration [29, 43]. Moreover, chitosan-based systems tend to increase the drug absorption due to the ability to open the tight junctions of the epithelium [44, 45]. However, the fact that only about 20% of CPT has permeated is indicative that CPT could be retained in the luminal side of intestine due to the mucoadhesive character of chitosan and, thus, delivering the drug to the site of interest. This can be corroborated by confocal microscopy, where it was shown CPT accumulation in the apical side of the epithelial cells when encapsulated into micelles (Figure A4.4, supplementary material).

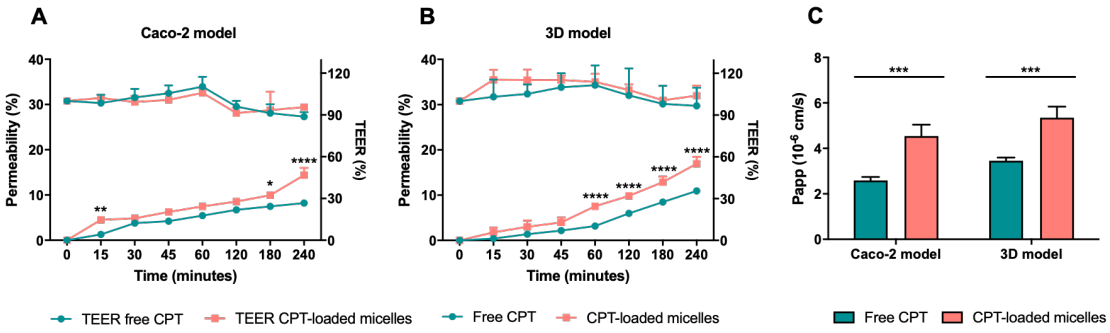

Figure 7.5. Intestinal permeability and respective TEER values of free CPT and CPT-loaded mPEG-CS-OA micelles. (A) CPT permeability across Caco-2 standard model; (B) CPT permeability across a 3D intestinal model; (C) Apparent permeability coefficients (P_{app}) of free CPT and CPT-loaded mPEG-CS-OA micelles across Caco-2 monoculture model and the 3D intestinal model. All experiments were conducted from the apical to basolateral side in HBSS at 37 °C. Error bars represent mean ± SD (n = 3). *p<0.05, **p<0.01, ***p<0.001 and ****p<0.0001 denotes a significant difference by two-way analysis of variance (ANOVA) Sidak's multiple comparison test.

7.4.5. *In vivo* antitumor activity in HCT116 xenograft mouse model

To establish a proof-of-concept of the therapeutic efficacy of CPT-loaded micelles *in vivo,* N:NIH(S)II-*nu/nu* mice were injected with CRC HCT116 cells into the right flank and, when tumors reached 100 mm^3, the different formulations were subcutaneously administered three times per week along two weeks (Figure 7.6A). The body weight of the animals was monitored for the 40 days of study. Mice maintained their initial weight until the end of the treatment and, non-relevant changes were observed afterwards, which may suggest the safe character of these micelles [46, 47], confirming the demonstrated previous *in vitro* results (Figure 7.6B).

CPT-loaded micelles and CPT suspension were administered at a dose of 1 mg/kg, while CPT i.v. was administered at a dose of 0.075 mg/kg. CPT-loaded micelles showed a significant delay in the tumor growth during the treatment comparing to the control group. Also, at the end of treatment setting, CPT-loaded micelles significantly delayed tumor growth (no treatment, ***$p<0.001$; CPT suspension *$p<0.05$ and CPT i.v. **$p<0.01$) for at least another 10 days. Regarding the tumor volume, at the end of the treatment (Figure 7.6D), CPT-loaded micelles revealed a 50% tumor reduction when compared with the control (no treatment) (**$p<0.01$). Previously, a dose of 7-ethyl-10-hydroxycamptothecin (SN-38, a CPT analogue) of 20 mg/kg demonstrated better inhibition of the tumor growth among all formulations studied (empty and loaded nanoparticles with or without PEG and irinotecan), including irinotecan at 25 mg/kg [48]. Thus, as a future perspective, higher doses of CPT-loaded micelles can be evaluated in order to identify the most effective dose formulation for tumor inhibition.

The animals were then subjected to a survival study (Figure 7.6E). Animals treated with CPT-loaded micelles presented the most favorable survival rate, related with the tumor growth delay.

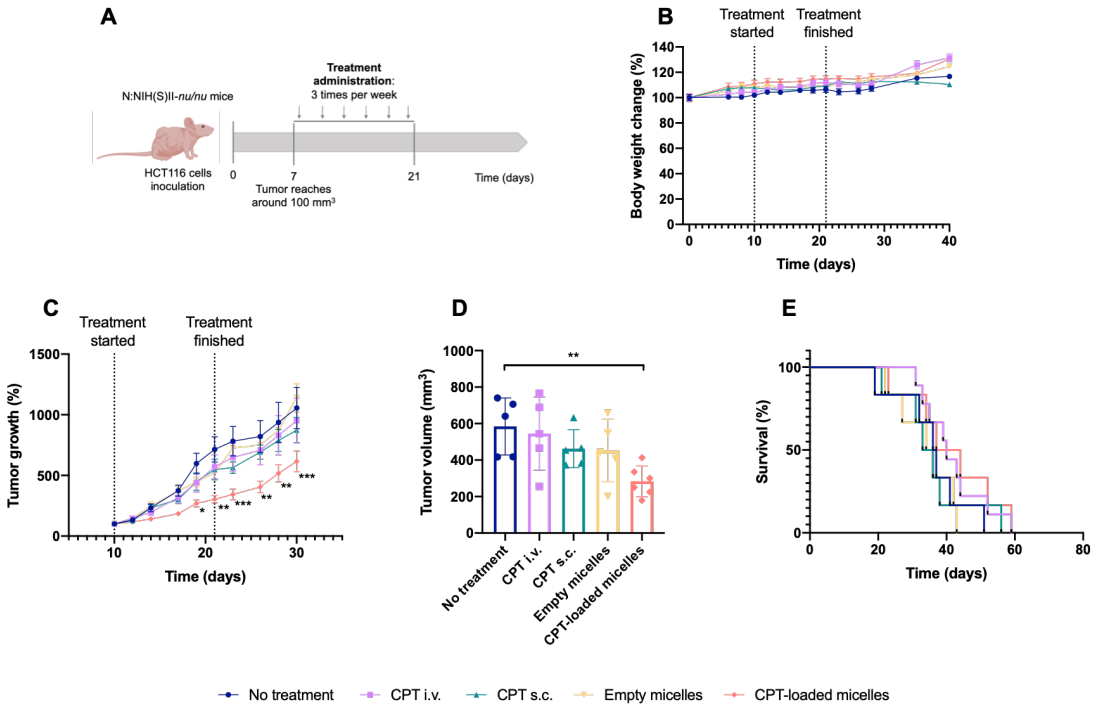

Figure 7.6. (A) Experimental timeline. N:NIH(S)II-*nu/nu* mice were injected with colorectal cancer HCT116 cells into the right flank of the mice. After 7 days of tumor inoculation, animals were subcutaneously (saline, CPT s.c., empty micelles, CPT-loaded micelles) and intravenously (CPT i.v.) treated three times per week, during two weeks. Saline-treated animals were used as experimental control (no treatment). After 21 days, animals were maintained for survival curve. (B) Change in the animal body weight was evaluated until day 40 after tumor cells inoculation. (C) Tumor growth (%) was measured using a caliper and normalized to the initial tumor volume for each animal, before any treatment. (D) Tumor volume (mm^3) in a HCT116 xenograft model after the end of the treatment. (E) Survival curves of tumor bearing mice. Error bars represent mean ± SD (n = 5-6). **p<0.01, ***p<0.001 and ****p<0.0001 denotes a significant difference when compared with the control (no treatment) by one-way (D) or two-way (C) analysis of variance (ANOVA) Dunnet's or Tukey's multiple comparison test, respectively.

7.4.6. Pharmacokinetic and biodistribution studies in a chemically-induced colorectal cancer model

The pharmacokinetic parameters of CPT from the micelles and CPT suspension after oral administration and CPT after intravenous administration at CPT equivalent dose of 1.5 mg/kg and 0.5 mg/kg, respectively, were evaluated in male C57BL/6 mice chemically induced to develop CRC. As present in Table 7.2, CPT from the chitosan micelles demonstrated a maximum drug concentration (C_{max}) of 0.74 ± 0.11 ng/mL after 1 h of administration. CPT suspension and CPT i.v., also reached the C_{max} after 1 h of administration, but in a significant lower concentration (0.32 ± 0.10 ng/mL for CPT suspension and 0.37 ± 0.07 ng/mL for CPT i.v. compared with CPT from chitosan micelles

($p<0.001$). Higher CPT absorption values are reported in the literature for other drug carriers [49, 50], however, it is not favorable for local cancer therapy.

When comparing AUC values, CPT-loaded micelles also resulted in higher bioavailability for CPT in 24 h, where close to 10% of CPT from the micelles was absorbed, compared to the 6% of free CPT. These results differed slightly from the *in vitro* intestinal permeability, as expected given the large difference between the *in vitro* and *in vivo* models. Nonetheless, CPT from chitosan micelles had higher bioavailability, which is consistent with the referred data. As previously stated, encapsulating CPT into nanocarriers increases its solubility and, as a consequence, its oral absorption. As a result, there are numerous examples of polymeric micelles loaded with CPT that have increased oral bioavailability [50-52].

The biodistribution of chitosan micelles was assessed by NIR imaging after the encapsulation of Cy7.5 (Figure 7.7). Micelles were administered orally, and after 3 hours, a maximum intensity was observed at the luminal site of the intestine. Following that, the signal fall close to zero after 12 hours (Figure 7.7B), which we attributed to micelle retention in the intestine, where the signal is not detectable due to the depth of the colon. This is supported by measurements performed after 12 hours in the organs of the animals, which revealed an increase in fluorescent signal in the colon (Figure 7.7D). This means that the micelles were in direct contact with the tumors where CPT is released, which could lead to a more effective therapeutic effect. The fluorescent signal from the micelles was absent in all other organs (liver, spleen, kidneys, heart and lungs), indicating that the micelles did not pass through the intestine.

Table 7.2. Pharmacokinetic parameters of CPT-loaded micelles and CPT suspension in C57BL/6 CRC induced mice.

	Dose (mg/kg)	**Route**	**C_{max} (ng/mL)**	**T_{max} (h)**	**$AUC_{0\rightarrow24}$ (ng h/mL)**	**Fr (%)**
CPT-loaded micelles	1.5	Oral	0.74±0.11	1	4.79±0.42	9.8
CPT suspension	1.5	Oral	0.32±0.10	1	2.73±0.86	5.6
CPT suspension	0.1	i.v.	0.37±0.07	1	3.27±0.33	100.0

C_{max}: maximum concentration; T_{max}: time in which C_{max} is reached; AUC: area under the curve; Fr: relative bioavailability.

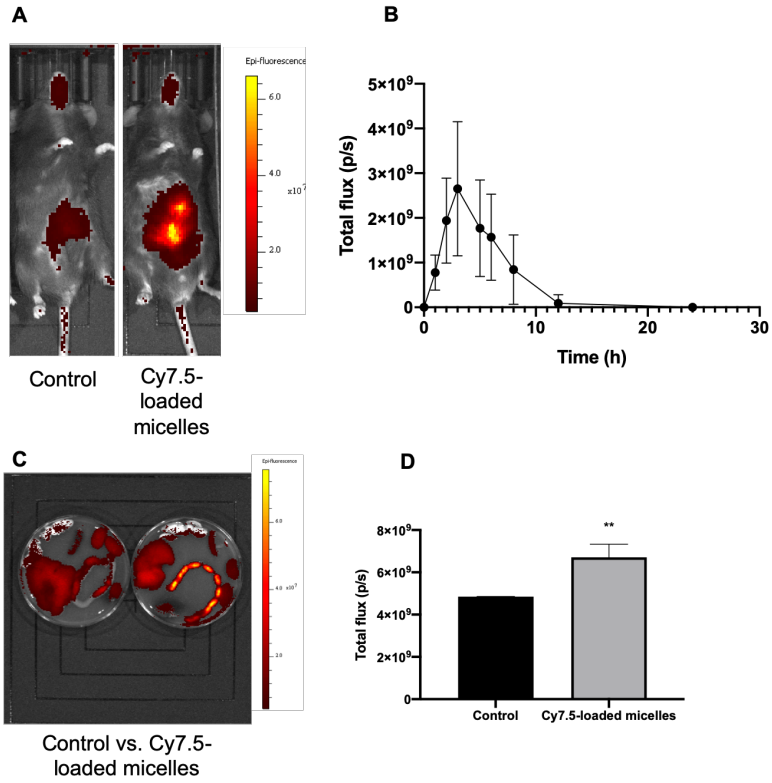

Figure 7.7 – Assessment of the distribution and retention of fluorescent chitosan micelles following oral administration by NIR imaging. (A) Representative fluorescence signal obtained from full body, live animals in supine position after 3 h of administration Cy7.5-loaded micelles (B) total efflux (photons/second) of Cy7.5-loaded chitosan micelles overtime after oral administration. (C) Representative fluorescence signal of animal *ex vivo* organs and colon after 12 h of administration. (D) total efflux (photons/second) of Cy7.5-loaded chitosan micelles distributed by the organs and colon after 12 of the oral administration. Error bars represent mean ± SD (n = 3). **p<0.01 denotes a significant difference t-test.

7.4.7. Antitumor efficacy of camptothecin-loaded micelles in chemically induced colorectal cancer model

Upon the validation of the tumor-growth retention in a xenograft, where CPT-loaded micelles presented a therapeutic effect when locally administrated in the tumor site, we evaluated their efficacy in a more biological relevant *in vivo* model - the AOM/DSS-induced inflammatory CRC through oral route. AOM is responsible for reducing apoptosis and increase the cell cycle by causing mutations in DNA [53]. DSS leads to CRC formation by causing inflammation and oxidative stress in the intestinal mucosa [54]. This model closely recapitulates human colon adenocarcinoma in terms of disease characteristics and pathology [55]. After the confirmation of the colon tumors formation by colonoscopy (Figure A4.6, supplementary material), animals were treated orally three times per week during two weeks with different formulations (Figure 7.8A). After treatment, animals were euthanized

and the intestines evaluated. The animals were monitored regarding their body weight and behavior. There was a slight decrease on the weight on animals during tumor induction (Figure A4.5, supplementary material), as commonly observed [27, 28]. Nevertheless, after finishing the DSS cycles, animals were able to recover their initial weight. Also, during treatment with the different formulations, animals did not present a significant change in their body weight, which could be an indication of the safety of the formulations administered (Figure 7.8B) [46, 47].

After euthanasia, colon was excised and opened to count the tumor number. As shown in Figure 7.8C, animals treated with CPT-loaded micelles had the lowest tumor score (*$p<0.05$), indicating that this group of animals had fewer tumors in the colon and a small tumor area after the sum of all tumor areas in each mouse, when compared to non-treated animals. (Figure 7.8D). CPT alone had no effect on tumor score when compared to the non-treated group, indicating a negligible therapeutic effect of the free drug, whereas polymeric micelles inhibited the progression of CRC and the formation of new lesions. Close to 50% of the tumors in the animals treated with CPT-loaded micelles were <2 mm in size and only 10% were larger than >3 mm (Figure A4.7). All of the other formulations and non-treated animals had similar larger tumors, with 20-30% of the tumors being <2 mm, 30-40% of the tumors between 2-3 mm, and 30-40% of the tumors being >3 mm. Moreover, CPT oral suspension or CPT administrated i.v. did not feature any difference in the tumor score or area when compared with the control, evidencing the therapeutic benefits of chitosan micelles for CPT delivery.

Liu *et al*. described chitosan nanoparticles loaded with a CPT analogue for CRC using a systemic approach to deliver the drug [56]. In this study, the authors demonstrated a tumor score reduction at the colon, as well as, a decrease on the TNF-α and IL-1β levels in the tumor tissues, which were mainly due to the surface modification of chitosan with chondroitin sulfate. At the same time, it was evaluated the nanoparticle accumulation at the colon, where surface modified nanoparticles showed an accumulation after oral administration, however, the authors did not test the therapeutic effect of the system after oral administration for CRC treatment [56]. Thus, although beneficial effects have been demonstrated in the treatment of CRC by i.v. administration, its effect after oral administration is unknown. Therefore, to the best of our knowledge, a chitosan-based polymeric system for oral delivery of CPT for CRC treatment has never been described before. The data here described support the excellent activity of CPT-loaded micelles reducing CRC by oral administration, which can be a powerful system for the oral chemotherapy of CRC. Similar reports also demonstrate the effectiveness of the drug encapsulation into nanocarriers in reducing the tumor number and size in CRC treatment. For instance, Wang *et al*. used SN38-loaded nanoparticles covalently linked to oligo-ε-

caprolactone [57] and Pan *et al*. used hyaluronic acid–doxorubicin nanoparticles [58] to treat CRC and decrease inflamation.

An illustrative image from the colonoscopy of each group is demonstrated in Figure A4.6, supplementary material. It was noticed the tumor growth, particularly in the non-treated animals, presenting obstructive tumors, while a non-inflamed mucosa with less and much smaller tumors was observed in the animals treated with CPT-loaded micelles. These results are also in concordance with tumor score and area, assessed at the end of the treatment (Figure 7.8C and D).

By causing cell mutation and differentiation, inflammation contributes to the initiation and development of CRC [59]. The intestine and colon length, as well as, spleen index were measured as it is an indication of the tissue inflammation [60, 61]. Animals treated with CPT-loaded micelles presented a larger intestine and colon comparing to non-treated ones (*$p<0.05$). The shortening of colon length upon administering empty micelles, CPT suspension or CPT i.v. was observed due to the tumor burden in the colon. Further, CPT-loaded micelles presented a low spleen index compared with non-treated animals (**$p<0.01$), corroborating with the previous results, where an increase on intestine and colon length was verified (Figure 7.8C, D and E). The enlargement of the colon and intestines, as well as the low spleen index, are consistent with reports in which the reduction of inflammation and tumor development was also observed in CRC treatment using nanosystems [58, 62]. Thus, our findings suggest that CPT-loaded micelles may exert an anti-inflammatory effect, although a deeper characterization of immune cells at the intestine and spleen and systemic inflammatory cytokines is required. It is, also, well-documented the anti-inflammatory character of chitosan [63-65], associated with the mechanism of action of CPT derivatives [66], synergically contributing to the reduction in intestine inflammation. Also, with the reduction of the tumor progression, the inflammation retreat, which agrees with the results obtained for the animals treated with CPT-loaded micelles.

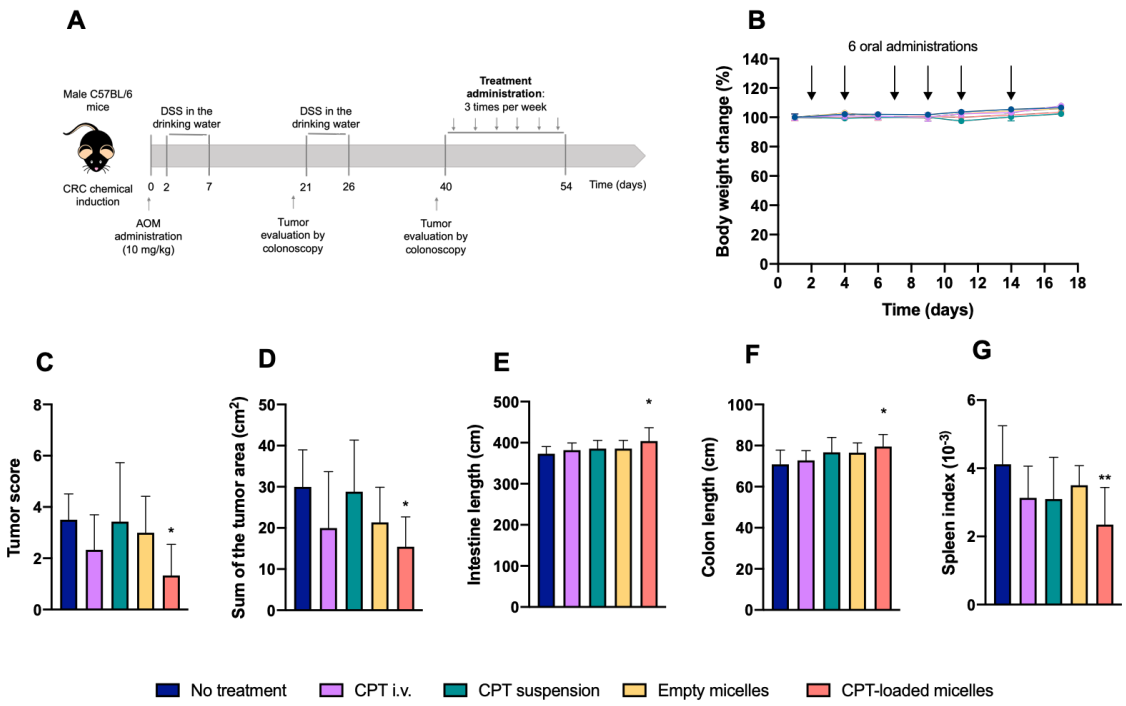

Figure 7.8. (A) Experimental timeline. C57BL/6 mice were chemically induced to develop colorectal cancer through the intraperitoneal injection of AOM, and DSS in the drinking water. After confirmation of the tumor formation by colonoscopy, animals were orally (saline, CPT suspension, empty micelles, CPT-loaded micelles) and intravenously (CPT i.v.) treated three times per week, during two weeks. Saline-treated animals were used as experimental control (no treatment). After the end of the treatment, animals were euthanized and the tumors counted. (B) Change in the animal body weight during treatment. (C) tumor score and (D) sum of the tumor area, (E) Intestine length (cm), (F) colon length (cm) and (G) spleen index were calculated after the euthanasia of animals. Error bars represent mean ± SD (*n* = 7). *p<0.05 and **p<0.01 denotes a significant difference when compared with the control (no treatment) by one-way analysis of variance (ANOVA) Dunnet's multiple comparison test.

7.5. Conclusion

In this work, CPT-loaded micelles were produced by dialysis method and characterized demonstrating an average size <200 nm, positive surface charge around 43 mV and a drug loading of 8% (w/w). CPT-loaded micelles demonstrated a protective effect of CPT against PBMC's and empty micelles exhibited no cytotoxicity when in contact with the same cells. The *in vitro* anticancer activity was evaluated in CRC cell lines and in 3D multicellular CRC spheroids, where drug-loaded micelles revealed a significant potential effect on the metabolic activity reduction. *In vivo* studies suggested that CPT-loaded micelles locally administered had a significant effect in the tumor growth, where a 50% tumor volume reduction was achieved. In the *in vivo* colitis associated CRC model, a more complex model that better mimics the disease on humans, biodistribution studies demonstrated the

accumulation of the chitosan micelles in the colon, as an indicative of the micelles retention for consequent CPT delivery near the tumors. This was in agreement with the tumor score reduction, as well as, the enlargement of the colon and intestine due to the reduced tumor burden when CPT-loaded micelles were administered. Overall, these findings show that CPT-loaded chitosan-based micelles had a significant and effective effect on the reduction of CRC development and progression, as well as, being a safe therapeutic option for oral CRC chemotherapy.

References

1. Sung, H., et al., *Global cancer statistics 2020: GLOBOCAN estimates of incidence and mortality worldwide for 36 cancers in 185 countries.* CA: A Cancer Journal for Clinicians, 2021. **71**(3): p. 209-249.
2. Banerjee, A., et al., *Strategies for targeted drug delivery in treatment of colon cancer: current trends and future perspectives.* Drug Discovery Today, 2017. **22**(8): p. 1224-1232.
3. Stuurman, F.E., et al., *Oral anticancer drugs: mechanisms of low bioavailability and strategies for improvement.* Clinical Pharmacokinetics, 2013. **52**(6): p. 399-414.
4. Ünal, S., et al., *Cyclodextrin nanoparticle bound oral camptothecin for colorectal cancer: Formulation development and optimization.* International Journal of Pharmaceutics, 2020. **584**: p. 119468.
5. Chen, M., et al., *Ultrasound triggered conversion of porphyrin/camptothecin-fluoroxyuridine triad microbubbles into nanoparticles overcomes multidrug resistance in colorectal cancer.* ACS Nano, 2018. **12**(7): p. 7312-7326.
6. Patel, H., et al., *Phase II study of rubitecan, an oral camptothecin in patients with advanced colorectal cancer who have failed previous 5-fluorouracil based chemotherapy.* Investigational New Drugs, 2006. **24**(4): p. 359-363.
7. Pizzolato, J.F. and L.B. Saltz, *The camptothecins.* The Lancet, 2003. **361**(9376): p. 2235-2242.
8. Liu, L.F., et al., *Mechanism of action of camptothecin.* Annals of the New York Academy of Sciences, 2000. **922**(1): p. 1-10.
9. Fassberg, J. and V.J. Stella, *A kinetic and mechanistic study of the hydrolysis of camptothecin and some analogues.* Journal of Pharmaceutical Sciences, 1992. **81**(7): p. 676-684.
10. Rahier, N.J., C.J. Thomas, and S.M. Hecht, *Camptothecin and its analogs.* Anticancer Agents from Natural Products, 2005. **5**: p. 22.
11. Ghosh, B. and S. Biswas, *Polymeric micelles in cancer therapy: State of the art.* Journal of Controlled Release, 2021.
12. Ghezzi, M., et al., *Polymeric micelles in drug delivery: An insight of the techniques for their characterization and assessment in biorelevant conditions.* Journal of Controlled Release, 2021.
13. *A phase II trial of Genexol-PM and gemcitabine in patients with advanced non-small-cell lung cancer*. 2016; Available from: https://clinicaltrials.gov/ct2/show/NCT01770795.

14. *A phase III study of NK105 in patients with breast cancer*. 2016; Available from: https://clinicaltrials.gov/ct2/show/NCT01644890.
15. *Combination therapy with NC-6004 and gemcitabine versus gemcitabine alone in pancreatic cancer*. 2016; Available from: https://clinicaltrials.gov/ct2/show/NCT02043288.
16. *Dose-escalation and expansion trial of NC-6300 in patients with advanced solid tumors or soft tissue sarcoma*. 2017; Available from: https://clinicaltrials.gov/ct2/show/record/NCT03168061.
17. Almeida, A., et al., *Novel amphiphilic chitosan micelles as carriers for hydrophobic anticancer drugs.* Materials Science and Engineering: C, 2020. **112**: p. 110920.
18. Azar, H.A., C.T. Hansen, and J. Costa, *N: NIH (S) II-nu/nu mice with combined immunodeficiency: a new model for human tumor heterotransplantation.* Journal of the National Cancer Institute, 1980. **65**(2): p. 421-430.
19. Almeida, A., et al., *Synthesis and characterization of chitosan-grafted-polycaprolactone micelles for modulate intestinal paclitaxel delivery.* Drug Delivery and Translational Research, 2018. **8**(2): p. 387-397.
20. Almeida, A., et al., *3D printed systems for specific colonic delivery of camptothecin-loaded chitosan micelles* Submitted 2021.
21. Martins, S.M., et al., *Development and validation of a simple reversed-phase HPLC method for the determination of camptothecin in animal organs following administration in solid lipid nanoparticles.* Journal of Chromatography B, 2012. **880**: p. 100-107.
22. Castro, F., et al., *Chitosan/poly (γ-glutamic acid) nanoparticles incorporating IFN-γ for immune response modulation in the context of colorectal cancer.* Biomaterials Science, 2019. **7**(8): p. 3386-3403.
23. Bauleth-Ramos, T., et al., *Colorectal cancer triple co-culture spheroid model to assess the biocompatibility and anticancer properties of polymeric nanoparticles.* Journal of Controlled Release, 2020. **323**: p. 398-411.
24. Cardoso, A., et al., *Macrophages stimulate gastric and colorectal cancer invasion through EGFR Y 1086, c-Src, Erk1/2 and Akt phosphorylation and smallGTPase activity.* Oncogene, 2014. **33**(16): p. 2123-2133.
25. Crouch, S., *Kozlowski R, Slater K, and Fletcher J.* The use of ATP bioluminescence as a measure of cell proliferation and cytotoxicity. Journal of Immunological Methods, 1993. **160**: p. 81-88.
26. Macedo, M.H., et al., *All layers matter: innovative three-dimensional epithelium-stroma-endothelium intestinal model for reliable permeability outcomes.* Submitted, 2021.

27. Neufert, C., C. Becker, and M.F. Neurath, *An inducible mouse model of colon carcinogenesis for the analysis of sporadic and inflammation-driven tumor progression.* Nature Protocols, 2007. **2**(8): p. 1998.
28. Parang, B., C.W. Barrett, and C.S. Williams, *AOM/DSS model of colitis-associated cancer*, in *Gastrointestinal Physiology and Diseases*. 2016, Springer. p. 297-307.
29. Silva, D.S., et al., *Self-aggregates of 3, 6-O, O'-dimyristoylchitosan derivative are effective in enhancing the solubility and intestinal permeability of camptothecin.* Carbohydrate Polymers, 2017. **177**: p. 178-186.
30. *ISO/EN10993-5. International Standard ISO 10993-5 Biological Evaluation of Medical Devices—Part 5: Tests for Cytotoxicity: In Vitro Methods*. 2009, International Organization for Standardization: Geneva, Switzerland.
31. Li, P., et al., *Fully bio-based coating from chitosan and phytate for fire-safety and antibacterial cotton fabrics.* Carbohydrate Polymers, 2020. **237**: p. 116173.
32. Li, Y., et al., *Shelf-life, quality, safety evaluations of blueberry fruits coated with chitosan nano-material films.* Scientific Reports, 2021. **11**(1): p. 1-10.
33. He, R. and C. Yin, *Trimethyl chitosan based conjugates for oral and intravenous delivery of paclitaxel.* Acta Biomaterialia, 2017. **53**: p. 355-366.
34. Huo, M., et al., *Redox-sensitive micelles based on O, N-hydroxyethyl chitosan–octylamine conjugates for triggered intracellular delivery of paclitaxel.* Molecular Pharmaceutics, 2016. **13**(6): p. 1750-1762.
35. Zhu, H., et al., *Enhanced tumor targeting and antitumor efficacy via hydroxycamptothecin-encapsulated folate-modified N-succinyl-N'-octyl chitosan micelles.* Journal of Pharmaceutical Sciences, 2013. **102**(4): p. 1318-1332.
36. Dramou, P., et al., *Folic acid-conjugated chitosan oligosaccharide-magnetic halloysite nanotubes as a delivery system for camptothecin.* Carbohydrate Polymers, 2018. **197**: p. 117-127.
37. Heestand, G.M., et al., *Topoisomerase expression and amplification in solid tumours: Analysis of 24,262 patients.* European Journal of Cancer, 2017. **83**: p. 80-87.
38. Zhang, X., et al., *Development of an in vitro multicellular tumor spheroid model using microencapsulation and its application in anticancer drug screening and testing.* Biotechnology Progress, 2005. **21**(4): p. 1289-1296.
39. Valster, A., et al., *Cell migration and invasion assays.* Methods, 2005. **37**(2): p. 208-215.
40. M Ashraf, S. and K. Rathinasamy, *Antibacterial and anticancer activity of the purified cashew nut shell liquid: implications in cancer chemotherapy and wound healing.* Natural Product Research, 2018. **32**(23): p. 2856-2860.

41. Rodríguez-Berna, G., et al., *A promising camptothecin derivative: Semisynthesis, antitumor activity and intestinal permeability.* European Journal of Medicinal Chemistry, 2014. **83**: p. 366-373.
42. Martínez-Martínez, M., et al., *Covalently crosslinked organophosphorous derivatives-chitosan hydrogel as a drug delivery system for oral administration of camptothecin.* European Journal of Pharmaceutics and Biopharmaceutics, 2019. **136**: p. 174-183.
43. Yuan, H., et al., *Stearic acid-g-chitosan polymeric micelle for oral drug delivery: in vitro transport and in vivo absorption.* Molecular Pharmaceutics, 2011. **8**(1): p. 225-238.
44. Li, L., et al., *Amphiphilic polymeric micelles based on deoxycholic acid and folic acid modified chitosan for the delivery of paclitaxel.* International Journal of Molecular Sciences, 2018. **19**(10): p. 3132.
45. Mo, R., et al., *The mechanism of enhancement on oral absorption of paclitaxel by N-octyl-O-sulfate chitosan micelles.* Biomaterials, 2011. **32**(20): p. 4609-4620.
46. Sepehri, N., et al., *SN38 polymeric nanoparticles: in vitro cytotoxicity and in vivo antitumor efficacy in xenograft balb/c model with breast cancer versus irinotecan.* International Journal of Pharmaceutics, 2014. **471**(1-2): p. 485-497.
47. Wang, L., et al., *Docetaxel-loaded-lipid-based-nanosuspensions (DTX-LNS): preparation, pharmacokinetics, tissue distribution and antitumor activity.* International Journal of Pharmaceutics, 2011. **413**(1-2): p. 194-201.
48. Mosallaei, N., et al., *Solid lipid nanoparticles containing 7-ethyl-10-hydroxycamptothecin (SN38): Preparation, characterization, in vitro, and in vivo evaluations.* European Journal of Pharmaceutics and Biopharmaceutics, 2016. **104**: p. 42-50.
49. Wang, T., et al., *A novel core-shell lipid nanoparticle for improving oral administration of water soluble chemotherapeutic agents: inhibited intestinal hydrolysis and enhanced lymphatic absorption.* Drug Delivery, 2017. **24**(1): p. 1565-1573.
50. Sadekar, S., et al., *Poly (amido amine) dendrimers as absorption enhancers for oral delivery of camptothecin.* International Journal of Pharmaceutics, 2013. **456**(1): p. 175-185.
51. Du, Y., et al., *Redox sensitive lipid-camptothecin conjugate encapsulated solid lipid nanoparticles for oral delivery.* International Journal of Pharmaceutics, 2018. **549**(1-2): p. 352-362.
52. Huarte, J., et al., *Oral delivery of camptothecin using cyclodextrin/poly (anhydride) nanoparticles.* International Journal of Pharmaceutics, 2016. **506**(1-2): p. 116-128.

53. Chen, J. and X.-F. Huang, *The signal pathways in azoxymethane-induced colon cancer and preventive implications.* Cancer Biology and Therapy, 2009. **8**(14): p. 1313-1317.
54. Mladenova, D. and M.R. Kohonen-Corish, *Mouse models of inflammatory bowel disease-insights into the mechanisms of inflammation-associated colorectal cancer.* In Vivo, 2012. **26**(4): p. 627-646.
55. Cooks, T., et al., *Mutant p53 prolongs NF-κB activation and promotes chronic inflammation and inflammation-associated colorectal cancer.* Cancer Cell, 2013. **23**(5): p. 634-646.
56. Liu, Z.-L., et al., *Chondroitin sulfate modification enhances the targeting and therapeutic effect of nanomedicine on AOM/DSS-induced mouse colon cancer.* Journal of Drug Delivery Science and Technology, 2019. **52**: p. 1-7.
57. Wang, Y., et al., *Tuning the efficacy of esterase-activatable prodrug nanoparticles for the treatment of colorectal malignancies.* Biomaterials, 2021. **270**: p. 120705.
58. Pan, D.C., et al., *Hyaluronic acid–doxorubicin nanoparticles for targeted treatment of colorectal cancer.* Bioengineering and Translational Medicine, 2021. **6**(1): p. e10166.
59. Grivennikov, S.I. *Inflammation and colorectal cancer: colitis-associated neoplasia*. in *Seminars in Immunopathology*. 2013. Springer.
60. Chassaing, B., et al., *Dextran sulfate sodium (DSS)-induced colitis in mice. Current Protocols in Immunology 104.* Unit, 2014. **15**: p. 25.
61. Singh, K., et al., *Ornithine decarboxylase in macrophages exacerbates colitis and promotes colitis-associated colon carcinogenesis by impairing M1 immune responses.* Cancer Research, 2018. **78**(15): p. 4303-4315.
62. Shen, C., et al., *Smart responsive quercetin-conjugated glycol chitosan prodrug micelles for treatment of inflammatory bowel diseases.* Molecular Pharmaceutics, 2021. **18**(3): p. 1419-1430.
63. Azuma, K., et al., *Anticancer and anti-inflammatory properties of chitin and chitosan oligosaccharides.* Journal of Functional Biomaterials, 2015. **6**(1): p. 33-49.
64. Kim, S., *Competitive biological activities of chitosan and its derivatives: antimicrobial, antioxidant, anticancer, and anti-inflammatory activities.* International Journal of Polymer Science, 2018. **2018**.
65. Ahmed, S. and S. Ikram, *Chitosan based scaffolds and their applications in wound healing.* Achievements in the Life Sciences, 2016. **10**(1): p. 27-37.
66. Du, H., et al., *Two novel camptothecin derivatives inhibit colorectal cancer proliferation via induction of cell cycle arrest and apoptosis in vitro and in vivo.* European Journal of Pharmaceutical Sciences, 2018. **123**: p. 546-559.

CHAPTER 8

Conclusions and Future Perspectives

8.1. Conclusions

CRC is a disease whose prevalence is expected to rise in the coming years. Many efforts have been made in the scientific and medical communities to develop a more effective treatment with fewer side effects. Oral chemotherapy has been proposed as a potential therapeutical approach, in combination with nanotechnology, for increasing the solubility of anticancer drugs such as CPT and extending their retention time in the intestine to exert therapeutic action. Polymeric micelles have been widely used in this context because they can encapsulate a large amount of drug while maintaining high stability during passage through the GIT.

Taking all of this in consideration, PK and physicochemical studies of CPT were performed *in silico* and *in vitro* to understand how the drug can behave after oral administration. It was demonstrated that, when administered freely, CPT is poorly absorbed and, when absorbed demonstrated a large biodistribution, resulting in a lack of selectivity. This was corroborated with the interaction with cellular membranes, where CPT did not present any specificity to the cancer cells. Furthermore, CPT had high affinity for plasmatic proteins, with only a small portion of the drug free to interact with the target site. As a result, it was demonstrated that CPT should be encapsulated in DDS to improve these PK issues and reach the tumor site via the nanosystem's mucoadhesion and mucopenetration. Gathering all of this, chitosan was used due its biological and chemical properties to produce amphiphilic polymers with ability to form polymeric micelles by self-assembly. Thus, mPEG was used to improve the mucodiffusion of the system and OA was used to confer the hydrophobic segments of the micelles. The SD of both segments was carefully considered so that the mucoadhesive properties of chitosan were not lost. After the synthesis and physicochemical characterization, the amphiphilic copolymer obtained, mPEG-CS-OA, was used to produce micelles and encapsulate CPT. Polymeric micelles with an average diameter of <180 nm, a 55% AE and 8% (w/w) DL of CPT were obtained. The micelles allowed a slow and sustained release of CPT up to 50% after 72 h and were able to protect around 80% of the drug from hydrolysis in simulated gastrointestinal fluids.

It was critical to determine whether the new chitosan derivatives could be synthesized on an industrial scale and how stable these micelles are over time. Thus, mPEG-CS and mPEG-CS-OA were produced in a larger scale and purified by CFF, where the physicochemical properties, as well as the ability to produce polymeric micelles were confirmed to be maintained. It was also demonstrated that micelles obtained from the scaled-up copolymer presented an *in vitro* cytocompatibility independent of the batch size and its stability was preserved for 6 months at -20 ºC, demonstrating its shelf storage potential.

As a strategy to provide a handling oral macroplatform for a colon-specific release of CPT, drug-loaded micelles were associated to 3D printing systems sealed with an enteric polymeric layer. It was possible to simulate the tablet digestion in simulated gastrointestinal fluids, where CPT from the chitosan micelles were only released at the colon pH, and, subsequently, the CPT, improving the amount of CPT in the colon without being hydrolyzed. This could be an alternative for the oral administration of the micelles if there was no therapeutic effect of its oral administration, which could be due to some degradation during passage through the GIT.

The *in vitro* cytocompatibility and anticancer efficacy of the polymeric micelles was evaluated in PBMC's and in CRC cell lines. Results demonstrated a good cytocompatibility of the empty micelles when incubated with PBMC's and with CRC cell lines. On the other hand, CPT-loaded micelles presented a cytotoxic effect on the CRC cell lines tested, but interestingly, the same was not verified when in contact with PBMC's. The same pattern was verified when the anticancer activity was study in a more complex model, in 3D MCTS. A preliminary *in vivo* study was performed in HCT116 xenograft model aiming to evaluate the local efficacy of these micelles. The data showed promisor results since CPT-loaded micelles were able to significantly reduce the tumor growth overtime, which is translated in the tumor volume. Thus, thinking in the evaluation of the oral chemotherapeutic potential of these micelles, a CRC orthotopic model was developed by the chemical induction with AOM/DSS. Biodistribution studied demonstrated that chitosan micelles were not accumulated in the tissues of the body, suggesting the safety of this system, but were instead accumulated at the intestine. This favored our study since we are looking for a local therapy of CRC. Indeed, pharmacodynamic studies in CRC induced mice showed the therapeutic potential of CPT-loaded micelles after oral administration. It was demonstrated a significantly reduction on the tumor score, as well as, the tumor size in animals treated with CPT-loaded micelles, whereas all the other formulations tested did not present any therapeutic effect. Additionally, animals treated with CPT-loaded micelles showed larger intestine and colon and, lower spleen index, factors related with the reduction of inflammatory activity, which may be due to the efficacy of the nanosystems to slow down the progression and development of CRC.

Overall, the micelles developed in this thesis holds an enormous potential to address the PK issues of CPT, but more importantly, CPT-loaded micelles demonstrated a significant therapeutic effect on CRC treatment in an orthotopic mice model. The oral administration of this carrier may be a powerful tool for CRC treatment as means of oral chemotherapy.

A parallel study was performed in collaboration with ESA aiming to understand the effect of HG in the CPT intestinal permeability. It was demonstrated that, with the HG increasing, the CPT permeability decreases and may be accumulated in the intestinal barrier. Although

nowadays the use of HG in the clinic is not a usual practice, it is known that in the future it can serve as a significant therapeutic approach. Therefore, this system can be triggered by HG and may be used in the future as a therapeutic approach for local CRC therapy.

8.2. Future perspectives

Science is constantly asking us new questions, and it appears that the work will never be completed because there is always room for improvement. As a result, there are several aspects of this PhD thesis that could be done/changed in order to improve the quality of this work.

Starting with the synthesis of the new chitosan derivatives, other fatty acids and mPEG ratios could be investigated in order to improve the loading capacity of the system. Furthermore, the production of micelles could be tested on an industrial scale to determine whether this system is capable of retaining the same characteristics when produced on a larger scale and whether the yield and time of production could be improved. Aside from the economic benefits of this process, it is a way to bring these micelles to clinics. The functionalization of this system with CRC-targeting ligands could be a promising approach to improving its therapeutic effect. Because these micelles are not receptor-targeted, incorporating a ligand could improve micelle accumulation in the tumor and, as a result, achieve a better therapeutic outcome. Another exciting option could be the co-encapsulation of other anticancer drugs, such as 5-FU, for CRC oral chemotherapy in order to achieve a more effective treatment, especially in more advanced cases of the disease. In addition, the encapsulation of other hydrophobic drugs could be done in order to address other diseases such as ulcerative colitis or IBD, which benefited from the local action of this system at the intestinal level.

During this thesis was suggested a potential anti-inflammatory effect of the micelles in the colitis-associated CRC mice model. It would be interesting to learn whether chitosan micelles have an anti-inflammatory effect or if it is due to the CPT action in slowing cancer progression and, as a result, reducing systemic and local inflammation as measured by intestine and colon length and the spleen index. This could be accomplished by characterizing immune cells in the intestine and spleen, as well as analyzing systemic inflammatory cytokines in the serum of the animals. And, because CPT-loaded micelles demonstrated tremendous potential in reducing locally CRC, it would be interesting to test other administration routes, particularly the rectal route, because micelles will be in direct contact with colon tumors. However, the system would need to be carefully designed in order to improve the retention time of the micelles in the mucosa, which may be associated with improved mucoadhesion and mucodiffusion of the micelles.

Finally, the mucoadhesive properties of the system should be investigated to supplement the data obtained in this thesis. It is critical to understand how mucoadhesive and mucodiffusive this system is and, based on the results, decide whether or not to change the formulation in order to improve mucus adherence and micelle diffusion.

Appendix 1

The effect of hypergravity in intestinal permeability of nanoformulations and molecules

The information provided in this section was based in the following publication:

Azevedo C.*, Macedo M.H.*, **Almeida A**.*, Pinto S.*, van Loon J. & Sarmento B, 2021. The effect of hypergravity in intestinal permeability of nanoformulations and molecules. *European Journal of Pharmaceutics and Biopharmaceutics*, 163: 38-48. (*equal contribution)

In this paper, I was responsible for the conception, execution and revision of the manuscript as Cláudia Azevedo, Maria Helena Macedo and Soraia Pinto. The supervisor was responsible for reviewing and submit the manuscript. This paper was previously included in Cláudia Azevedo's thesis and it is partially reproduced in this section.

A1.1. Abstract

The oral administration of drugs remains a challenge due to rapid enzymatic degradation and minimal absorption in the gastrointestinal tract. Mechanical forces, namely hypergravity, can interfere with cellular integrity and drug absorption, and there is no study describing its influence in the intestinal permeability. In this work, it was studied the effect of hypergravity on intestinal Caco-2 cells and its influence in the intestinal permeability of different nanoformulations and molecules. It was shown that the cellular metabolic activity and integrity were maintained after exposure to different gravity-levels (g-levels). Expression of important drug transporters and tight junctions' proteins was evaluated and, most proteins demonstrated a switch of behavior in their expression. Furthermore, paracellular transport of FITC-Dextran showed to significantly increase with hypergravity, which agrees with the decrease of transepithelial electrical resistance and the increase of claudin-2 at higher g-levels. The diffusion of camptothecin released from polymeric micelles revealed a significant decrease, which agrees with the increased expression of the P-gp observed with the increase in g-levels, responsible for pumping this drug out. Thus, this study supports the effect of hypergravity on intestinal permeability is dependent on the molecule studied and the mechanism by which it is absorbed in the intestine.

A1.2. Introduction

Oral administration is considered the preferred drug delivery route due to ease and patient compliance [1]. However, several drugs have limited bioavailability since they do not endure the harsh environment of gastrointestinal tract and poorly cross epithelial barriers [2]. In order to overcome the inefficient delivery, nanotechnology has been used as a promising strategy to overcome those biological barriers and to improve the intestinal absorption of drugs, which can be assessed by *in vitro* cellular models. In fact, nanosystems provide a stable biocompatible environment to encapsulate drugs, promote a controlled release and an efficient absorption [2, 3]. These nanosystems are also responsible to improve the therapeutic efficacy, increasing the residence time and minimizing the unwanted side effects by driving drugs towards the site of action and increasing the concentration of drug in the targeted site [1, 4]. After developing new drugs and incorporating them into nanosystems, it is important to evaluate their absorption profile in intestinal cellular models, such as the gold standard Caco-2 monoculture model [5]. The Caco-2 monoculture model relies on seeding Caco-2 cells in a semi-permeable support, Transwell® inserts, and culturing them to allow their differentiation into enterocyte-like cells, forming a monolayer that mimics the intestinal epithelium. Transwell® inserts membranes are very convenient to perform permeability assays, since they provide independent access to both sides of the

monolayer (apical and basolateral sides). Therefore, during the permeability assays, it is possible to measure the amount of drug that was capable of crossing the cellular membrane, enabling a correlation to the absorption that will occur *in vivo*. According to the literature, mechanical forces of strain and fluid shear can stimulate CYP3A4 activity, glucose reuptake and mucus production, which is known to be absent in static Caco-2 models [6]. Particularly, studies indicated that barrier function, namely downregulation of occludin expression, decrease of transepithelial electrical resistance (TEER) values and increase of paracellular transport can be altered, in endothelial cells, measured after a 1-3 g hypergravity (HG) rocket launch profile exposure [7], while an on-line measurements of the barrier integrity in endothelial cells exposed to 2-4 g HG showed an increase with increasing gravity levels (g-levels) [8]. However, a very limited set of studies has exploited the effect of HG on drug absorption, and none of them related with the intestinal permeability of orally delivered drugs. Here, it was intended to understand the impact of HG, as mechanical force, upon metabolic activity, integrity and expression of cellular components. Ultimately, it was evaluated how different transport vias, such as paracellular and diffusion were affected after HG exposure, in order to find a more advantageous strategy to enhance drug delivery. This innovative study will help researchers and pharmaceutical industries in oral drug development areas, since it may correlate more precisely the obtained results with the permeability in the human intestine. Although nowadays using HG in the clinic is not a usual practice, it is known that in the future it can serve as a significant therapeutic approach [9-11]. Therefore, it is important to understand its effects in different cells and systems and recognize the importance of developing new drugs that can be triggered by HG.

A1.3. Materials and methods

A1.3.1. Polymeric micelles production

Chitosan-based micelles were obtained by a dialysis method, as previously described [12, 13]. Shortly, 10 mg of *O*-methyl-*O'*-succinylpolyethylene glycol-chitosan-oleic acid (mPEG-CS-OA, all material purchased from Merck) were dissolved in 4 mL of dimethyl sulfoxide (DMSO):HCl 0.1 M (9:1) in a glass tube allowing its complete dissolution overnight at RT. Camptothecin (CPT, Hangzhou ROYAL Import & Export Co., Ltd.) was previously dissolved in DMSO at 1 mg/mL concentration and added to the polymer solution to perform a 5% drug loading (w/w). The mixture was left under stirring and dialyzed (3.5 kDa Mw cutoff, Fisher Scientific) against water with three-cycle renewal to remove the DMSO and the non-associated free drug. Micelles were collected from the dialysis bag and centrifuged at 3110 g for 20 min to remove the drug precipitate formed when dialyzing. The nanosystems were

frozen with 0.5% (w/v) trehalose as a cryoprotectant, to maintain the micelle architecture, and afterwards, freeze-dried to obtain the micellar powder [13].

A1.3.2. Cell culture

C2BBe1 [Caco-2 clone] (human colorectal adenocarcinoma) cells were acquired from ATCC and maintained in a complete medium consisting of Dulbecco's Modified Eagle's Medium (DMEM, ATCC) supplemented with 10% (v/v) Fetal Bovine Serum (FBS, Biochrom) and 1% (v/v) antibiotic-antimitotic mixture (final concentration of 100 U/mL penicillin and 100 U/mL streptomycin) in 75 cm^2 T-flasks, inside an incubator at 37 ºC and 5% CO_2 and 95% relative humidity. DMEM medium was changed three times per week. Caco-2 cells were used at passages 77 to 83. When confluence reached about 70% to 80%, cells were detached from the flasks by treating it with trypsin-EDTA at 37 ºC and transferred to another 75 cm^2 T-flasks or Transwell® and multiwell plates.

A1.3.3. Hypergravity exposure

Cells were exposed to HG in the LDC [14] at the TEC-MMG LIS Lab from ESTEC-ESA in Noordwijk, Netherlands. The LDC, with a diameter of 8 meters, allows for the application of up to 20 g. The four arms of the centrifuge hold at maximum six gondolas, plus one gondola in the center for a 1.0 g rotational control, if required (Figure A1.1A). The gondolas of the centrifuge swing out, resulting in an acceleration vector that is always perpendicular to the samples surface. Because of this and its size, the systems avoid inertial shear forces common in smaller centrifuges [15]. The Transwell® multiwell plates were placed in a 37 ºC incubator (Thermo Scientific Heratherm IMC-18 mini incubator) that were accommodated in one of the gondolas. Since multi g-levels can be created during one run the experiment was performed during 2 rounds.

A1.3.4. Metabolic activity studies

The influence of HG on the metabolic activity of Caco-2 cells was evaluated by resazurin and LDH assays. Caco-2 cells (4.0 x 10^4 cells per well) were seeded in 96-well plates in 200 µL of DMEM complete medium and were incubated for 24 h. Then, medium was removed, and cells were washed twice with 200 µL of fresh pre-heated Phosphate-Buffered Saline (PBS) 1X to remove cellular debris and 200 µL of fresh pre-heated DMEM without FBS was added to each well. Plates were then incubated for 4 h at 37 °C in an orbital shaker (Stuart S150 Orbital Incubator at 100 rpm) for the reference condition (1.0 g shaking), while plates at HG were placed in the LDC at 2.5 g, 5.0 g and 7.5 g at 37 °C.

Afterwards, the 96-well plates were centrifuged at 250 g for 10 min at RT to remove dead cells, and the supernatant was used to perform the LDH assay, while the remaining Caco-2 cells attached at the bottom of the plate were used for resazurin assay. For this, cells were washed twice with 200 µL PBS 1X and then treated with DMEM complete medium containing 20% resazurin (0.1 mg/mL; Merck) during 2 h at 37 °C, 5% CO_2 and 95% relative humidity, protected from light. After 2 h of incubation, 150 µL of each well was transferred to a black 96-well plate and the fluorescence was measured at 530/590 nm (excitation/emission wavelengths, respectively), using a plate reader (Victor NivoTM, PerkinElmer, Inc.). The negative control consisted in cells incubated with 1% (v/v) of Triton X-100 in complete medium and the positive control consisted in cells incubated with complete medium, both at reference conditions. A number of six replicates were performed for each group. The metabolic activity was expressed according to the following equation:

$$Cellular\ viability\ (\%) = \frac{Fluorescence\ (Experimental\ value) - Fluorescence\ (Positive\ control)}{Fluorescence\ (Negative\ control) - Fluorescence\ (Positive\ control)} \times 100 \quad \text{(A1.1)}$$

To the 100 µL of supernatant collected after centrifugation from 96-well plates, 100 µL of the reaction mixture composed by the catalyst solution and the dye solution (LDH Cytotoxicity Detection Kit, Takara Bio) were added to each well and incubated for 10 min at RT in the dark. The absorbance was measured at 492 nm and 690 nm, using a plate reader (Victor NivoTM, PerkinElmer, Inc.). The negative control was composed by cells incubated with complete medium only and the positive control was composed by cells incubated with 1% (v/v) of Triton X-100 in complete medium, both at reference conditions. A number of six replicates were performed for each group. The cellular cytotoxicity was expressed according to the following equation:

$$Cellular\ cytotoxicity\ (\%) = \frac{Absorbance\ (Experimental\ value) - Absorbance\ (Negative\ control)}{Absorbance\ (Positive\ control) - Absorbance\ (Negative\ control)} \times 100 \quad \text{(A1.2)}$$

A1.3.5. Tight junctions and drug transporters' expression by immunocytochemistry

To understand if HG could have an impact in TJs and drug transporters expression of cells, the models were subjected to different g-levels, without any treatment.

The TJ presence was assessed using claudin-1, claudin-2 and occludin, which are integral transmembrane proteins, and ZO-1, a peripheral TJ protein. The presence of the drug transporters P-gp, PEPT-1, and MRP2 was evaluated. MUC2 was chosen to evaluate mucin expression, since it is the mostly expressed mucin in the small intestine [16]. After 4 h of exposure to HG, samples were washed once with PBS 1X and fixed with 2%

paraformaldehyde (PFA) for 20 min. Then, cells were washed three times with PBS 1X. To stain with different antibodies, a permeabilization step using a solution of 0.2% (v/v) Triton X-100 in PBS 1X for 5 min at RT was performed. Afterward, cells were washed thrice with PBS 1X for 5 min. A blocking step was performed using a solution containing 1.5% Bovine Serum Albumin (BSA) and 5% FBS in PBS 1X for 1 h at RT. Inserts were incubated with the primary antibodies' solutions [rabbit anti-human occludin primary antibody (1:100; 701161, ThermoFisher Scientific) + mouse anti-human MRP2 primary antibody (1:100; MA1-26536, Invitrogen)], [rabbit anti-human P-gp primary antibody (1:250; PA5-61300, Thermofisher Scientific)], [rabbit anti-human Claudin-1 (1:200; SAB5500083-100, Sigma Aldrich) + mouse anti-human MUC2 primary antibody (1:50; ab118964, Abcam)] and [rabbit anti-human ZO-1 primary antibody conjugated with Alexa Fluor 488 (1:50, SC-33725, Santa Cruz Biotechnology) + mouse anti-human PEPT1 primary antibody (1:100; ab203043, Abcam)] overnight at 4 ºC in a humidified chamber protected from light. Inserts were washed three times for 5 min with PBST, composed by PBS 1X and 0.05% Tween® 20, and incubated with the secondary antibodies and 4', 6-diamidino-2-phenylindole (DAPI) to counterstain the nuclei (500 ng/mL; Sigma Aldrich). Depending on the primary antibodies used, Goat anti-Mouse Alexa Fluor 594 F(ab')2 fragment of immunoglobulin G (IgG) (H+L) (1:500; A11020, Invitrogen), Goat anti-Rabbit Alexa Fluor 488 F(ab') fragment of IgG (H+L) (1:500; A11070, Invitrogen) and Donkey anti-Rabbit IgG H&L Alexa Fluor 594 pre-adsorbed (1:500; Ab150064, Abcam) were used. Secondary antibodies were added to samples for 2 h at 4 ºC in a humidified chamber protected from light. Cells were then washed twice with PBST and once with PBS 1X, all for 5 min. Inserts were mounted in slices using fluorescent mounting medium (Dako). Samples were left to dry protected from light and were maintained at 4 °C until visualization by a spectral confocal laser scanning microscope TCS-SP5 AOBS (Leica). Since the aim was to compare the amount and localization of tight and adherens junctions between samples and also the expression of drug transporters, laser power and gain of each laser were maintained for all samples regarding each antibody. The expression signal was quantified by using the ImageJ and samples were normalized according the following expression:

$$Expression\ (\%) = \frac{Samples\ in\ HG}{Reference\ condition} \times 100 \quad \text{(A1.3)}$$

A1.3.6. Cellular integrity by hematoxylin and eosin staining

To assess cellular integrity after exposure to different g-levels, H&E staining was performed. Inserts with cells were washed once with PBS 1X for 5 min and fixed using 2% PFA in PBS

1X for 20 min at RT. Then, inserts were washed thrice with PBS 1X for 5 min and kept in PBS 1X at 4 ºC until further processing for paraffin embedding. Sections of 3 mm were obtained using an RM2255 microtome (Leica) and then stained for H&E. Briefly, sections were deparaffinized and rehydrated, stained for 3 min in Gil's Hematoxylin (Thermo Scientific), 6 min in running water, dehydrated, stained for 1 min in Eosin Y (Thermo Scientific), cleared, and mounted in Entellan (Merck). Representative images of each condition were obtained with a Light microscope Olympus DP 25 Camera Software Cell B.

A1.3.7. Intestinal permeability study

Caco-2 cells were seeded at a density of 1.0 x 10^5 cells per cm^2 onto 12-Transwell® cell culture inserts (surface area of 1.1 cm^2, inner diameter of 12 mm and pore size of 1 µm; Millicell) and were allowed to grow and differentiate for 21 days inside an incubator as previously described (Figure A1.1A). The medium was replaced every two/three days from the apical (0.5 mL) and basolateral (1.5 mL) sides. The permeability assays through the cell monolayers were performed in the apical-to-basolateral direction in Hank's Balanced Salt Solution (HBSS) buffer at reference conditions (1.0 g shaking) [17], 37 °C, in an orbital shaker and at 2.5 g, 5.0 g and 7.5 g, 37 ºC, in the LDC. Prior to the experiment, the cell culture medium was removed from both sides of the inserts and the monolayers were washed twice with pre-warmed HBSS. Then, the monolayers were allowed to equilibrate with 0.5 mL and 1.5 mL of HBSS in the apical and basolateral compartments, respectively, for 30 min at 37 ºC, 100 rpm (Stuart S150 Orbital Incubator), at reference conditions. Then, the HBSS of the apical compartment was removed and 0.5 mL of CPT-micelles (0.1 µg/mL CPT) in ddH_2O or fluorescein isothiocyanate–dextran (FITC-Dextran) 4 kDa (200 µg/mL; Sigma Aldrich) in HBSS (pH 7.4) were added to the apical side. At different time-points (0.5, 1, 2, 3 and 4 h), TEER values were measured using an EVOM2 epithelial voltohmmeter equipped with a STX2 electrode (World Precision Instruments, Inc.) and 200 µL of each sample was removed from the basolateral side of the inserts and replaced for the same volume of pre-warmed HBSS buffer (Figure A1.1B). The amount of albumin was quantified by enzyme linked immunosorbent assays (ELISA), as detailed elsewhere [18]. The permeated CPT was quantified by high-performance liquid chromatography (HPLC), as previously described [19]. Lastly, FITC-Dextran was measured by fluorescence at an excitation/emission wavelengths of 490/520 nm, respectively, using a plate reader (Victor NivoTM PerkinElmer, Inc.). The integrity of the cell monolayers was checked before and during the permeability experiment by measuring the TEER. The permeability percentage and apparent permeability coefficient (*Papp*) of each formulation after 240 min of experiment were determined by the following equations:

$$Drug\ permeated\ (\%) = \frac{total\ mass}{theoretic\ mass} \times 100 \quad \text{(A1.4)}$$

$$Papp = \frac{dQ}{A \times C_0 \times dt} \quad \text{(A1.5)}$$

where dQ (µg) is the total amount of compound in the basolateral side, A is the surface area of the insert (cm^2), C_0 is the initial concentration in the apical side (µg/mL) and dt (s) is the time of the experiment.

A.1.3.8. Statistical analysis

Statistical analysis was performed using the GraphPad Prism Software vs. 6.0 (GraphPad Software Inc). Statistical significance of the difference between two groups was evaluated by the Student's t-test. Differences between groups were compared using one-way or two-way analysis of variance (ANOVA) Dunnett's multiple comparison test. Results are expressed as mean ± standard deviation and geometric means with 95% confidence intervals. The level of significance was set at probabilities of ∗P < 0.05, ∗∗P < 0.001, and #P < 0.0001. N = 6 for all data points.

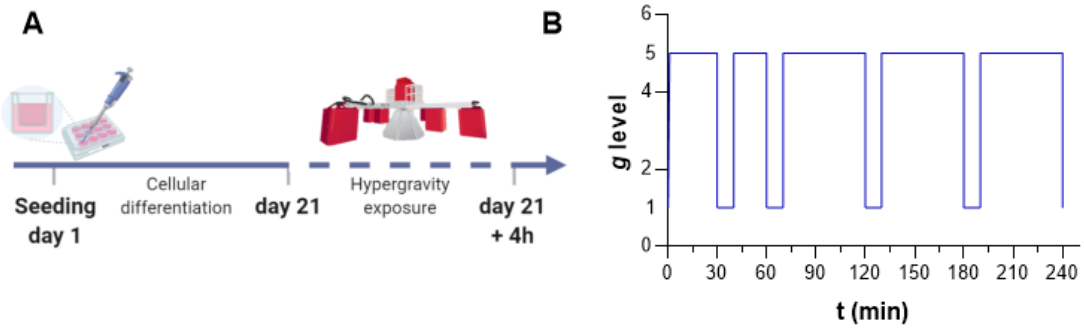

Figure A1.1. Experimental procedure of the intestinal permeability under different gravity levels (g-levels). (A) Schematic illustration of cell culture and HG exposure process: Caco-2 cells were cultured for 21 days, to allow their differentiation into enterocyte-like cells. After this, FITC-dextran, Ins-NPs-Alb and CPT-micelles were incubated for 4 h, at different g-levels; (B) Schematic diagram for an example of HG exposure, which entailed 10 min rest period at different time points (0.5, 1, 2, 3 and 4 h). During this rest period at 1.0 g, TEER was measured and samples were removed from the basolateral side, for further quantification. This set up was performed for 2.5 g, 5.0 g and 7.5 g using the LDC and for the reference using an orbital-shaker, as control.

A1.4. Results and discussion

A1.4.1. No influence of hypergravity in cellular metabolic activity

The *in vitro* metabolic activity studies (resazurin and lactate dehydrogenase (LDH) assays) were performed using an intestinal cell line, Caco-2 clone, in order to resemble the intestinal enterocytes (representing 90% of the total intestinal epithelial cells) [20, 21]. To assess the effect of HG on the cellular metabolism, viability and cytotoxicity were measured after exposure to different g-levels (2.5 g, 5.0 g and 7.5 g), for 4 h inside a large diameter centrifuge (LDC) from European Space Research and Technology Centre (ESTEC) of the European Space Agency (ESA) and compared to reference control. The obtained data showed similar cellular viability for nearly all the tested g-levels as compared with the reference conditions, of approximately 100% (Figure A1.2A). It was observed that at 2.5 g, cellular viability presented a statistically significant increase when compared to the reference. However, in biological terms, this difference is not relevant. These outcomes were in accordance with the values obtained in the cytotoxicity assay (Figure A1.2B), where no cytotoxicity was found. Despite there are no published studies reporting the influence of g-levels in the metabolism of intestinal epithelial cells, the obtained results are in line with the reported data using different cell lines. Previous studies on osteoblasts and human tendon cells demonstrated no significant influence on cellular viability after exposure to HG (5 g, 10 g, 15 g and 20 g) during 3 and 4 h, respectively [22, 23]. Additionally, the exposure of nasal epithelial cells to 10 g during three cycles of 20 min, with 20 min resting periods between each time, also did not cause significant loss of cellular metabolic activity [24].

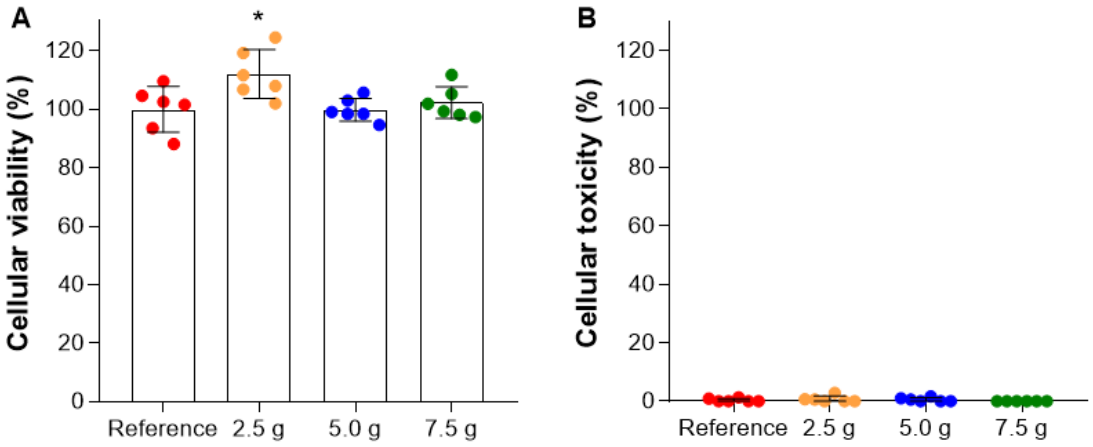

Figure A1.2. Evaluation of metabolic activity of Caco-2 cells after HG exposure. (A) Evaluation of cellular viability through resazurin assay; (B) Evaluation of cellular toxicity through LDH assay. Shown are the arithmetic means ± SD. *P<0.05 comparing with the reference, by one-way analysis of variance (ANOVA) Dunnett's multiple comparison test (*n* = 6).

A1.4.2. Hypergravity might induce a tipping point on the expression of cellular components

Before studying the effect of HG upon transport, it was crucial to understand how transporters and TJs proteins might be affected (Figure A1.3A).

Different TJs proteins were evaluated, namely occludin, claudin-1, claudin-2 and zona occludens-1 (ZO-1). Occludin and claudins are integral transmembrane proteins, whereas ZO-1 is a peripheral membrane adaptor, acting as a bridge between the integral membrane TJs [25-27]. Occludin is normally highly expressed at cell-cell contact sites, being essential to the assembly and maintenance of TJs and, when this protein is under expressed, it can lead to an increase in the paracellular permeability of macromolecules [26, 28]. Observing Figures A1.3B, this protein showed increased expression with the increase of the g-levels from reference conditions to 5.0 g, but a decrease was observed afterwards. Because of the lack of a trend, it was hard to conclude if this could have an impact in the permeability outcomes. When looking at claudin-1 (Figures A1.3C), its expression follows the opposite trend observed with occludin, with the decrease of the g-levels from reference conditions to 5.0 g and then, an increase. As for occludin, this change in behavior makes it hard to predict if it will have an impact in permeability. Claudins are the major determinant of the barrier function, defining the paracellular flux of small solutes [29]. There are two types of claudins: sealing and pore forming. Claudin-1 is a member of the sealing family, which means that if this protein is decreased, it results in a leakier barrier. On the other hand, claudin-2 belongs to the class of pore-forming claudins and an increase in these type of TJs means the selectivity for paracellular permeability is reduced [29]. In the specific case of claudin-2, it is capable of forming pores that are permeable to small cations and water, being size selective [30, 31].

When looking at the expression of claudin-2 (Figures A1.3D and Figure S3 from supplementary material), a decrease in its expression occurred from reference to 2.5 g, and then an increase was observed for the higher g-levels. Since claudin-2 is a pore forming TJ, these results may indicate an increase in permeability with the increase in g-force from 5.0 g to 7.5 g. Regarding ZO-1, although its role and importance is not yet clearly understood, some studies have been showing that cells with lower expression or absence of this protein present normal permeability, being more impactful in the assembly of other TJ proteins, as occludin and claudins [32]. Since it was not possible to observe major changes in the expression of ZO-1 between the different g-levels, it is likely that this protein had no impact in permeability outcomes (Figures A1.3E).

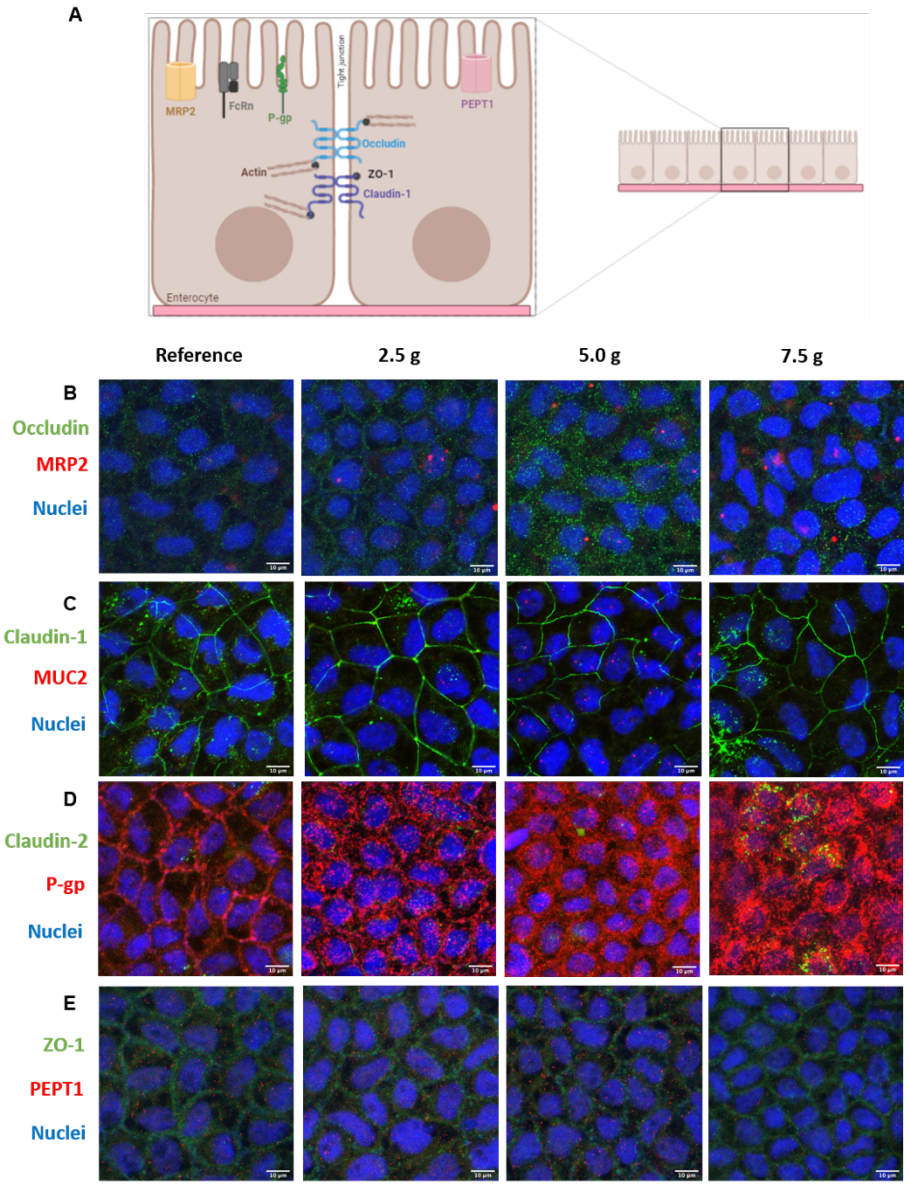

Figure A1.3. Assessment and comparison of different proteins at different g-levels. (A) Schematic illustration of the studied cellular components involved in different transport vias. Visualization of nuclei and (B) occludin and MRP2; (C) claudin-1 and MUC2; (D) claudin-2 and P-gp; (E) ZO-1 and PEPT1. Occludin, claudin-1, claudin-2 and ZO-1 are presented in green. MRP2, MUC2, P-gp and PEPT1 are presented in red. Nuclei are presented in blue.

There is no doubt that expression and assembly of TJs present a key role concerning the permeability outcomes of compounds that cross the intestinal barrier by the paracellular route. Nevertheless, when it comes to the transcellular pathway, the different drug transporters located in intestinal cells might have a wide impact on the permeability of compounds, mostly in the ones that are substrates of these transporters. Taking into consideration that CPT can suffer efflux by P-glycoprotein (P-gp) and multidrug resistance protein 2 (MRP2) [33], the expression of these transporters after the exposure to HG was

evaluated. Despite peptide transporter 1 (PEPT-1) not being directly linked to the drugs tested in this study, its expression was evaluated, since this is an important uptake transporter present in intestinal cells and it is considered highly attractive as a drug target [34]. When looking at the expression of PEPT1 (Figures A1.3E and Figure S4 from supplementary material), its expression was increased from reference to 2.5 g and then a decrease was observed for the higher g-levels. Looking at the efflux pump MRP2, a slight increase was observed with the increase in g-levels, but does not seem to be noteworthy and, therefore, most likely not capable of affecting permeability outcomes (Figures A1.3B and Figure S1). P-gp, the other efflux pump presents the same behavior, but much more pronounced (Figures A1.3D and Figure S3 from supplementary materials). In this case, this great increase from lower to higher g-levels can potentially lead to a greater efflux of drugs that are substrates of P-gp, such as CPT, which could translate in a decrease in the transport of these compounds through the intestinal barrier. Although one could have expected that 4 h would not be enough to observe differences in the expression of proteins, truth is that is possible to find reports in literature where changes in P-gp expression are observed in short timepoints. For example, in a work developed by Ye et al. [35], the use of the *Pseudomonas aeruginosa* toxin Cif was able to cause changes in P-gp expression in Caco-2 cells in the time course of 2 h. Besides, in a report by Herzog and colleagues [36], genetic expression of P-gp in LS180 cells was changed after treatment with P-gp antagonists for 8 h. So, it is reasonable to admit that exposing cells to different HG levels for 4 h is capable of altering the expression of some proteins, as observed in this work.

Mucin 2 (MUC2) was evaluated because this is the most expressed mucin in the small intestine and it is known that mechanical forces can interfere with the production of mucus, as previously stated [6, 16]. In this sense, it could be interesting to understand if HG might have an impact on its secretion. However, the change of MUC2 with the increase in g-levels seems to be negligible (Figures A1.3C and Figure S2 from supplementary material). Considering all these results, it is possible to conclude that HG affects protein expression in different ways. In some cases, like for the efflux pumps, a trend is observed, where protein expression increases with the increase in g-levels. However, it is interesting to see that for most proteins, this trend could not be observed. In fact, there seems to be a tipping point at 2.5 g or 5.0 g and proteins revert their behavior when reaching that point. For PEPT-1 and Claudin-2 this turning point occurs at 2.5 g, whether for Occludin and Claudin-1, this occurs at 5.0 g. Other interesting fact is that this change in behavior can occur in both directions, meaning protein expression can first increase and then decrease or the other way around, depending on the protein.

Regarding the localization of the transporters (Figure S5 of supplementary material), it was possible to observe that MRP2 was located at the apical side of the cells, confirming what

is described in the literature [37, 38]. P-gp is also known to be localized at the apical side of enterocytes, a perfect location to mediate the efflux of undesired compounds, like toxins, into the organism, but also to limit the entrance of drugs [39]. In this study, it was possible to confirm the apical localization of P-gp, although its presence was not only at the apical side, but extended into the basolateral part of the cells. In the case of PEPT1, its apical localization was also confirmed [40]. When it comes the localization of different transporters, it was possible to conclude that HG did not have an impact in this regard, being that no differences were observed between the localization of the different proteins when comparing the different g-levels.

A1.4.3. Barrier integrity is maintained after exposure to hypergravity

To assess the cellular integrity and morphology after exposure to HG, hematoxylin and eosin (H&E) staining was performed for each condition and nanoformulation/molecule (Figure A1.4). In this assay two dyes were used, hematoxylin and eosin, that work as basic and acidic dyes, respectively. Hematoxylin was used to stain acidic structures in purple, as the nucleus containing nucleic acids. On the other hand, eosin dyes basic structures in pink, so it was used to stain cytoplasm and extracellular matrix, by containing proteins [41]. Taking this in mind, it was possible to verify that the cellular membrane integrity was generally maintained and attached to the Transwell® membrane. Regarding the different compounds that were incubated, there was no significant difference between them, demonstrating an apparent resemblance with the reference group. Thus, the possibility of the effect be due to compounds and not due to the HG was discarded. Actually, the safety of camptothecin-associated polymeric micelles (CPT-micelles) was assessed, and the used concentrations are therefore compatible with the permeability model and quantifying methods (Figure S6 from supplementary material). However, some portions of the monolayer suffered membrane disruption and release of cytoplasm content, which could be due to handling procedure, as normally happens.

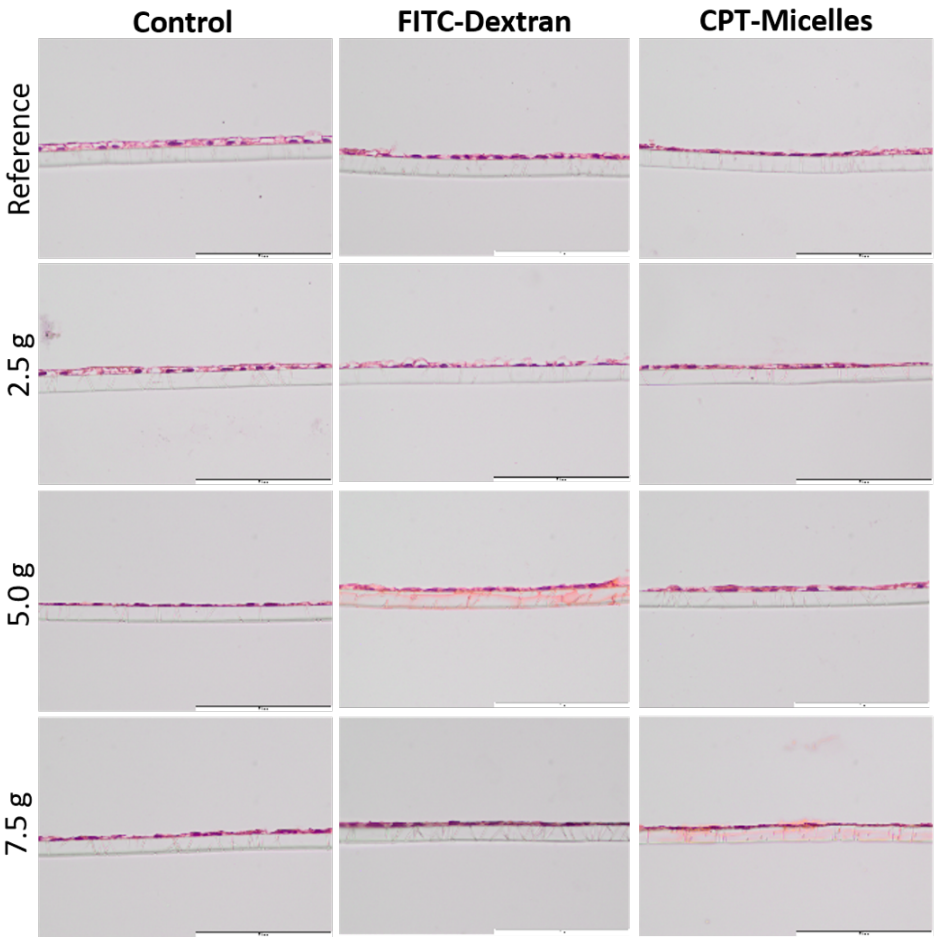

Figure A1.4. H&E staining to address the cellular integrity when cells were exposed to different compounds and g-levels. Dextran and CPT-micelles were exposed to different g-levels (2.5 g, 5.0 g and 7.5 g) for 4 h. Cells without samples and the reference (shaking at 1.0 g) were included as controls. Cytoplasm stained with pink and nucleus with purple. The Transwell® membrane is transparent and is right below the cellular monolayer. Scale bar = 100 µm.

A1.4.4. Hypergravity interfered differently among transport mechanisms

In this study, FITC-Dextran and CPT-micelles were used to evaluate the effect of HG upon paracellular, passive and transcellular transport (Figure A1.5). The different g-levels were compared to 1.0 g shaking reference, based on the permeability protocol established in our lab [12, 42-47].

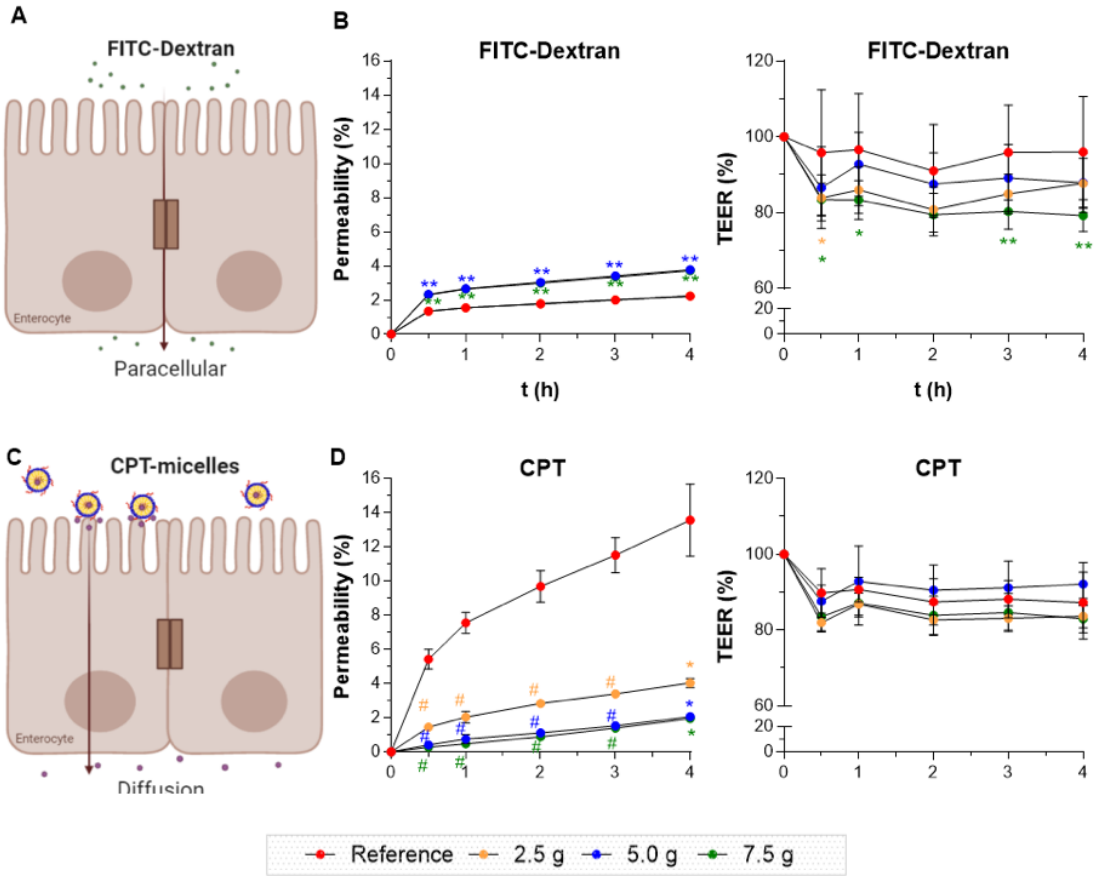

Figure A1.5. Intestinal permeability and respective TEER values of compounds with different pathways of internalization. (A) Schematic representation of the paracellular via used by FITC-Dextran; (B) Permeability percentage of FITC-Dextran quantified by fluorescence and respective TEER values; (C) Schematic representation of the CPT transport; (D) Permeability percentage of CPT from the micelles, quantified by HPLC, and respective TEER values during 4 h of incubation at different g-levels. Shown are the arithmetic means ± SD. ∗P < 0.05, ∗∗P < 0.001, and #P < 0.0001 comparing with the reference, by two-way analysis of variance (ANOVA) Dunnett's multiple comparison test, *n*=6).

FITC-Dextran, a hydrophilic compound that is known to cross the intestinal epithelium by the paracellular route (Figure A1.5A), with a molecular weight of 4 kDa, was used to measure the paracellular permeability and the possible impact of the different g-levels [47, 48]. When it comes to TEER values, it was observed that there was a significant decrease when cells where subjected to a force of 7.5 g (Figure A1.5B). Nevertheless, the TEER values were still high, having a decrease of around 20%, comparing to the initial value. When it comes to the other g-levels tested, only other significant decrease was observed for 2.5 g at 30 min, but the models were then able to recover and increase the TEER, getting close to the initial values. Looking at the permeability, FITC-Dextran showed significantly higher permeability at 5.0 and 7.5 g (Figure A1.5B). At the reference and 2.5 g, permeability

values were around 2%, translating in a *Papp* value of around 0.7 x 10^6 cm/s. On the other hand, in the case of 5.0 and 7.5 g, permeability increased to around 4%, which means *Papp* values were about 1.1 x 10^6 cm/s, as demonstrated in Table A1.1. When comparing the results obtained by the TEER values, the immunostaining performed on the models and the permeability outcomes, it is possible to correlate the results. In fact, as stated in Section 3.2. expression of claudin-2 was enhanced for the higher g-levels. These evidences could be translated in an increase in the permeability of paracellular compounds, as FITC-Dextran. Besides, TEER values are associated with the expression of TJs and a decrease in TEER can be associated with an under expression of sealing TJs, or an overexpression of pore-forming TJs, like of claudin-2 [49, 50], which was observed here. Nevertheless, it is important to state that although the increase in permeability had a statistical significance, in biological terms an increase from 2% to 4% is very low, suggesting that only a small fraction of the compound was able to pass, even at higher g-levels, and therefore, the barrier integrity was largely maintained. As already mentioned, the effect of HG in intestinal permeability was not reported in the literature, making it impossible to perform comparations. Nevertheless, FITC-Dextran with a molecular weight of 4 kDa was used to test the permeability of the nasal route under 10 g HG [24]. These authors observed that TEER significantly decreased and permeability was enhanced by 16%. The observed decrease in TEER values correlate with the results presented here and the increase in permeability too. In the case of the mentioned study, the increase was even higher, which could be derived from the fact that the applied force was greater or simply because other cell types were used that reacted in a different way. There are other studies that address permeability in the intestine and in the lung, but under the effect of microgravity and, in both studies, microgravity induces an increase in the permeability of FITC-Dextran [51, 52]. However, since applied forces are different, a direct comparison with the present study cannot be established.

Polymeric micelles based on chitosan were carefully thought out to improve the solubility and the bioavailability of CPT. Thus, the micellar system has a pegylated surface to improve the mucodiffusion and the micelle core is constituted by strong fatty acids, which maintain the drug encapsulated due to stablished hydrophobic interactions. These micelles are around 150 nm, have a positive superficial charge and an association efficiency of around 80% [13]. CPT is a substrate of some of the ABC (ATP-binding cassette) transporters, namely P-gp and MRP2 [33], which leads to resistance when it comes to absorption of this drug in the small intestine (Figure A1.5C). Looking for the permeability data, it was possible to observe a pattern where the intestinal permeability decreased as the g-level increased (Figure A1.5D). It was a very interesting fact since at reference conditions the CPT permeability, around 14%, achieved a *Papp* of 4.28 x 10^{-6} cm/s and, as the g-levels

increased, the CPT intestinal permeability decreased, reaching a *Papp* of 0.62 x 10^{-6} cm/s for the 7.5 g (Table A1.1). The increased P-gp expression with the increase in g-levels may have contributed for this outcome (Figures A1.3D), since with the increase in P-gp expression, the efflux suffered by the drug will be greater. In fact, many studies report differences in P-gp efflux ability when inhibiters of this transporter are used and the substrate is in contact with the monolayers for 2 h [53-55]. In this case, where the permeability assay was performed for 4 h, it is expectable that if a higher expression of P-gp is observed, this will reflect in higher efflux of compounds that are substrates of this protein, which is the case of CPT. Although the micellar system can protect the drug, with such a significant increase of the efflux pumps, it is expected that the permeability will not increase or be maintained, but decrease since the opposite path is much higher. At the same time, the TEER values were monitored at all different g-levels and were recorded steadily without significant decreases (Figure A1.5D), which was in line with no intestinal permeability increasing. In this sense, we can verify that the permeability of drugs mediated by efflux pumps, such as the case of CPT, tend to decrease their permeability with increasing HG. In any case, it is worth mentioning that the shear forces that are acting on the reference at 1.0 g, because it is at shaking conditions, can also have an impact on the permeability outcomes. In this case, the decrease in permeability may not only be related with the increase in g-levels, but it is possible that the absence of shear forces in HG conditions lead to lower permeability results. This evidence adds to our basic understanding of the impact of mechanical stimuli i.e. HG, on drug transportation processes and can bring new treatment strategies for subjects exposed to different gravity environments such as astronauts and pilots.

Table A1.1. Apparent permeability coefficients calculated after 4 h of incubation in Caco-2 cells (mean ± SD, n=3 (x 10^{-6} cm/s)).

P_{app}	Reference	2.5 g	5.0 g	7.5 g
FITC-Dextran	0.70 ± 0.07	0.71 ± 0.02	1.14 ± 0.04	1.18 ± 0.05
CPT	4.28 ± 0.66	1.27 ± 0.09	0.65 ± 0.06	0.62 ± 0.05

CPT – camptothecin; FITC-dextran – fluorescein isothiocyanate-dextran; Ins-NPs-Albumin – insulin-loaded nanoparticles conjugated with albumin; P_{app} – apparent permeability coefficient; SD – standard deviation.

A1.5. Conclusions

In this study, the effect of different HG levels (2.5 g, 5.0 g and 7.5 g) in the intestinal transport of nanoformulations and molecules for oral delivery, as well as the influence of HG in the

expression of TJs and drug transporters were evaluated. According to the results, the exposure to HG did not affect the metabolic activity and integrity of intestinal epithelial cells. Notwithstanding, the expression of TJs and transporters of Caco-2 cells, as well as the intestinal transport of molecules and nanoformulations by paracellular, passive and transcellular pathways were affected by the exposure to different g-levels. Regarding the paracellular transport, FITC-Dextran increased with the increase of g-levels. This can be also related with the increase of claudin-2 expression for higher g-levels. On the other side, the passive transport of CPT from micelles by diffusion decreased with the augment of g-levels, which is in line with the general increase of P-gp expression, responsible for CPT efflux. This pioneer study was important to understand biologic mechanisms and can be crucial when developing new formulations for oral delivery.

References

1. Sarmento, B., D. Ferreira, and T. Vasconcelos, *Polymer-Based Delivery Systems for Oral Delivery of Peptides and Proteins, in Delivery Technologies for Biopharmaceuticals: Peptides, Proteins, Nucleic Acids and Vaccines,* L. Jorgensen and H.M. Nielsen, Editors. 2009, John Wiley & Sons, Ltd. p. 207-227.
2. Araujo, F., et al., *Antihyperglycemic potential of incretins orally delivered via nano and microsystems and subsequent glucoregulatory effects.* Current Pharmaceutical Biotechnology, 2014. **15**(7): p. 609-19.
3. Pereira, C., et al., *Targeting membrane transporters and receptors as a mean to optimize orally delivered biotecnhological based drugs through nanoparticle delivery systems*. Current Pharmaceutical Biotechnology, 2014. **15**: p. 650-658.
4. Moulari, B., et al., *Nanoparticle targeting to inflamed tissues of gastrointestinal tract.* Current Drug Delivery, 2013. **10**: p. 9-17.
5. Hidalgo, I.J., T.J. Raub, and R.T. Borchardt, *Characterization of the human colon carcinoma cell line (Caco-2) as a model system for intestinal epithelial permeability*. Gastroenterology, 1989. **96**(3): p. 736-49.
6. Kim, H.J. and D.E. Ingber, *Gut-on-a-Chip microenvironment induces human intestinal cells to undergo villus differentiation*. Integrative Biology, 2013. **5**(9): p. 1130-40.
7. Sumanasekera, W.K., et al., *Estradiol and dihydrotestosterone regulate endothelial cell barrier function after hypergravity-induced alterations in MAPK activity*. American Journal of Physiology-Cell Physiology, 2007. **293**(2): p. C566-73.
8. Szulcek, R., et al., *Transient intervals of hyper-gravity enhance endothelial barrier integrity: impact of mechanical and gravitational forces measured electrically*. PLoS One, 2015. **10**(12): p. e0144269.
9. Genchi, G.G., et al., *Hypergravity as a tool for cell stimulation: implications in biomedicine*. Frontiers in Astronomy and Space Sciences, 2016. **3**: p. 26.
10. Dechaumet, B., et al., *Hypergravity as a gravitational therapy mitigates the effects of knee osteoarthritis on the musculoskeletal system in a murine model*. PLoS One, 2020. **15**(12): p. e0243098.
11. Jang, T.Y., et al., *Hypergravity enhances the therapeutic effect of dexamethasone in allergic asthma and rhinitis animal model*. PLoS One, 2018. **13**(5): p. e0197594.
12. Almeida, A., et al., *Synthesis and characterization of chitosan-grafted-polycaprolactone micelles for modulate intestinal paclitaxel delivery*. Drug Delivery and Translational Research, 2018. **8**(2): p. 387-397.

13. Almeida, A., et al., *Novel amphiphilic chitosan micelles as carriers for hydrophobic anticancer drugs*. Materials Science and Engineering: C, 2020. **112**: p. 110920.
14. Loon, J.J.W.A.v., et al. *The large diameter centrifuge, LDC, for life and physical sciences and technology*. 2008.
15. van Loon, J.J.W.A., et al., *Inertial shear forces and the use of centrifuges in gravity research. What is the proper control?* Journal of Biomechanical Engineering, 2003. **125**(3): p. 342-346.
16. Schneider, H., et al., *Study of mucin turnover in the small intestine by in vivo labeling*. Scientific Reports, 2018. **8**(1): p. 5760.
17. Hubatsch, I., E.G.E. Ragnarsson, and P. Artursson, *Determination of drug permeability and prediction of drug absorption in Caco-2 monolayers*. Nature Protocols, 2007. **2**(9): p. 2111-2119.
18. Azevedo, C., et al., *Engineered albumin-functionalized nanoparticles for improved FcRn binding enhances oral delivery of insulin.* Journal of Controlled Release, 2020. **327**: p. 161-173.
19. Martins, S.M., et al., *Development and validation of a simple reversed-phase HPLC method for the determination of camptothecin in animal organs following administration in solid lipid nanoparticles*. Journal of Chromatography B, 2012. **880**: p. 100-107.
20. Araújo, F. and B. Sarmento, *Towards the characterization of an in vitro triple co-culture intestine cell model for permeability studies*. International Journal of Pharmaceutics, 2013. **458**(1): p. 128-34.
21. Pereira, C., et al., *Cell-based in vitro models for intestinal permeability studies, in Concepts and Models for Drug Permeability Studies*, 2016, Woodhead Publishing. p. 57-81.
22. Searby, N.D., C.R. Steele, and R.K. Globus, *Influence of increased mechanical loading by hypergravity on the microtubule cytoskeleton and prostaglandin E2 release in primary osteoblasts*. American Journal of Physiology-Cell Physiology, 2005. **289**(1): p. C148-58.
23. Costa-Almeida, R., et al., *Continuous exposure to simulated hypergravity-induced changes in proliferation, morphology, and gene expression of human tendon cells*. Stem Cells and Development, 2018. **27**(12): p. 858-869.
24. Kim, D., Y.H. Kim, and S. Kwon, *Enhanced nasal drug delivery efficiency by increasing mechanical loading using hypergravity*. Scientific Reports, 2018. **8**(1): p. 168.
25. Gonzalez-Mariscal, L., et al., *Tight junction proteins*. Progress in Biophysics and Molecular Biology, 2003. **81**(1): p. 1-44.

26. Lee, B., K.M. Moon, and C.Y. Kim, *Tight junction in the intestinal epithelium: Its association with diseases and regulation by phytochemicals*. Journal of Immunology Research. 2018: p. 2645465.
27. Lee, S.H., *Intestinal permeability regulation by tight junction: implication on inflammatory bowel diseases*. Intestinal Research, 2015. **13**(1): p. 11-8.
28. Al-Sadi, R., et al., *Occludin regulates macromolecule flux across the intestinal epithelial tight junction barrier*. American Journal of Physiology-Gastrointestinal and Liver Physiology, 2011. **300**(6): p. G1054-64.
29. Gunzel, D. and A.S. Yu, *Claudins and the modulation of tight junction permeability*. Physiological Reviews, 2013. **93**(2): p. 525-69.
30. Van Itallie, C.M., A.S. Fanning, and J.M. Anderson, *Reversal of charge selectivity in cation or anion-selective epithelial lines by expression of different claudins*. American Journal of Physiology-Renal Physiology, 2003. **285**(6): p. F1078-84.
31. Rosenthal, R., et al., *Claudin-2, a component of the tight junction, forms a paracellular water channel*. Journal of Cell Science, 2010. **123**(Pt 11): p. 1913-21.
32. Umeda, K., et al., *Establishment and characterization of cultured epithelial cells lacking expression of ZO-1*. Journal of Biological Chemistry, 2004. **279**(43): p. 44785-94.
33. Lalloo, A.K., et al., *Membrane transport of camptothecin: facilitation by human P-glycoprotein (ABCB1) and multidrug resistance protein 2 (ABCC2)*. BMC Medicine, 2004. **2**(1): p. 16.
34. Estudante, M., et al., *Intestinal drug transporters: an overview*. Advanced Drug Deliv Reviews, 2013. **65**(10): p. 1340-56.
35. Ye, S., et al., *Chemotoxicity of doxorubicin and surface expression of P-glycoprotein (MDR1) is regulated by the Pseudomonas aeruginosa toxin Cif*. American Journal of Physiology-Cell Physiology, 2008. **295**(3): p. C807-C818.
36. Herzog, C.E., et al., *Increased mdr-1/P-glycoprotein expression after treatment of human colon carcinoma cells with P-glycoprotein antagonists.* Journal of Biological Chemistry, 1993. **268**(4): p. 2946-2952.
37. Liu, Y.H., et al., *Multidrug resistance-associated proteins and implications in drug development.* Clinical and Experimental Pharmacology and Physiology, 2010. **37**(1): p. 115-20.
38. Yu, X.Q., et al., *Multidrug resistance associated proteins as determining factors of pharmacokinetics and pharmacodynamics of drugs*. Current Drug Metabolism, 2007. **8**(8): p. 787-802.

39. Hediger, M.A., et al., *The ABCs of solute carriers: physiological, pathological and therapeutic implications of human membrane transport proteinsIntroduction*. Pflugers Arch, 2004. **447**(5): p. 465-8.
40. Shugarts, S. and L.Z. Benet, *The role of transporters in the pharmacokinetics of orally administered drugs*. Pharmaceutical Research, 2009. **26**(9): p. 2039-54.
41. Fischer, A.H., et al., *Hematoxylin and eosin staining of tissue and cell sections*. Cold Spring Harbor Protocols, 2008.
42. Silva, D.S., et al., *Self-aggregates of 3, 6-O, O'-dimyristoylchitosan derivative are effective in enhancing the solubility and intestinal permeability of camptothecin*. Carbohydrate Polymers, 2017. **177**: p. 178-186.
43. Silva, D.S., et al., *Synthesis and characterization of 3, 6-O, O'-dimyristoyl chitosan micelles for oral delivery of paclitaxel*. Colloids and Surfaces B: Biointerfaces, 2017. **152**: p. 220-228.
44. Silva, D.S., et al., *N-(2-hydroxy)-propyl-3-trimethylammonium, o-mysristoyl chitosan enhances the solubility and intestinal permeability of anticancer curcumin*. Pharmaceutics, 2018. **10**(4): p. 245.
45. Sgorla, D., et al., *Development and characterization of lipid-polymeric nanoparticles for oral insulin delivery*. Expert Opinion on Drug Delivery, 2018. **15**(3): p. 213-222.
46. Heep, G., et al., *Zein-casein-lysine multicomposite nanoparticles are effective in modulate the intestinal permeability of ferulic acid*. International Journal of Biological Macromolecules, 2019. **138**: p. 244-251.
47. Macedo, M.H., et al., *Development of an improved 3D in vitro intestinal model to perform permeability studies of paracellular compounds*. Frontiers in Bioengineering and Biotechnology, 2020. **8**(1076).
48. Woting, A. and M. Blaut, *Small intestinal permeability and gut-transit time determined with low and high molecular weight fluorescein isothiocyanate-dextrans in C3H mice*. Nutrients, 2018. **10**(6): p. 685.
49. Li, N., et al., *Development of an improved three-dimensional in vitro intestinal mucosa model for drug absorption evaluation*. Tissue Engineering Part C: Methods, 2013. **19**(9): p. 708-719.
50. Yi, B., et al., *Three-dimensional in vitro gut model on a villi-shaped collagen scaffold*. Biochip Journal, 2017. **11**(3): p. 219-232.
51. Alvarez, R., et al., *A simulated microgravity environment causes a sustained defect in epithelial barrier function*. Scientific Reports, 2019. **9**(1): p. 17531.
52. dos Santos, M.A., et al., *Modelling the effects of microgravity on the permeability of air interface respiratory epithelial cell layers*. Advances in Space Research, 2010. **46**(6): p. 712-718.

53. Balimane, P.V., A. Marino, and S. Chong, *P-gp inhibition potential in cell-based models: which "calculation" method is the most accurate?* AAPS PharmSciTech, 2008. **10**(4): p. 577-586.
54. Madden, L.R., et al., *Bioprinted 3D primary human intestinal tissues model aspects of native physiology and ADME/Tox functions*. IScience, 2018. **2**: p. 156-167.
55. Ohashi, R., et al., *Development of simplified in vitro P-glycoprotein substrate assay and in silico prediction models to evaluate transport potential of P-glycoprotein*. Molecular Pharmaceutics, 2019. **16**(5): p. 1851-1863.

Supplementary Material for Supporting the Appendix 1

The effect of hypergravity in intestinal permeability of nanoformulations and molecules

Section 1 | Hypergravity effect on the expression of junctional proteins and drug transporters

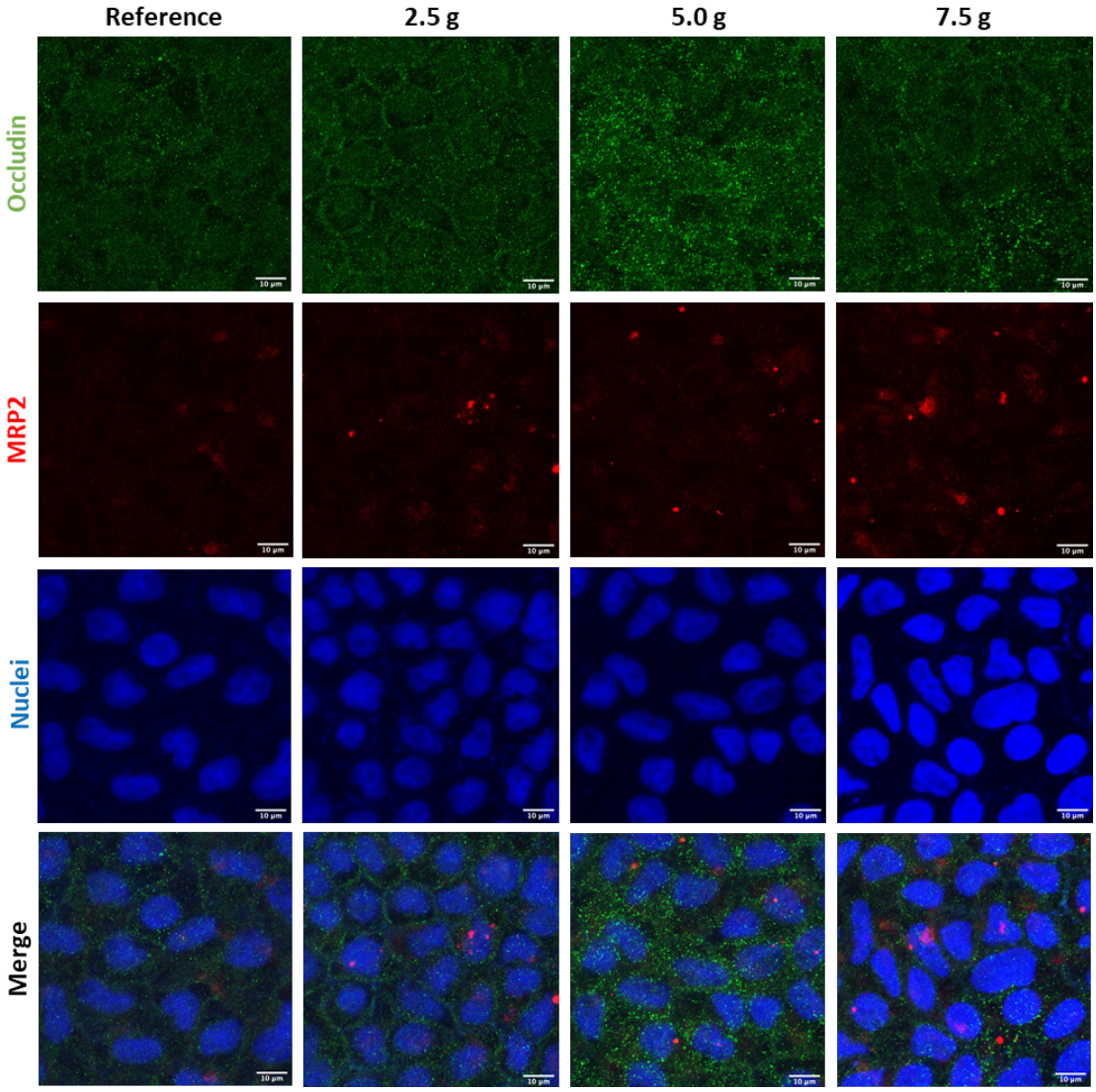

Figure S1. Visualization of occludin and MRP2 at different g-levels. Occludin is presented in **green**, MRP2 in **red** and nuclei in **blue.**

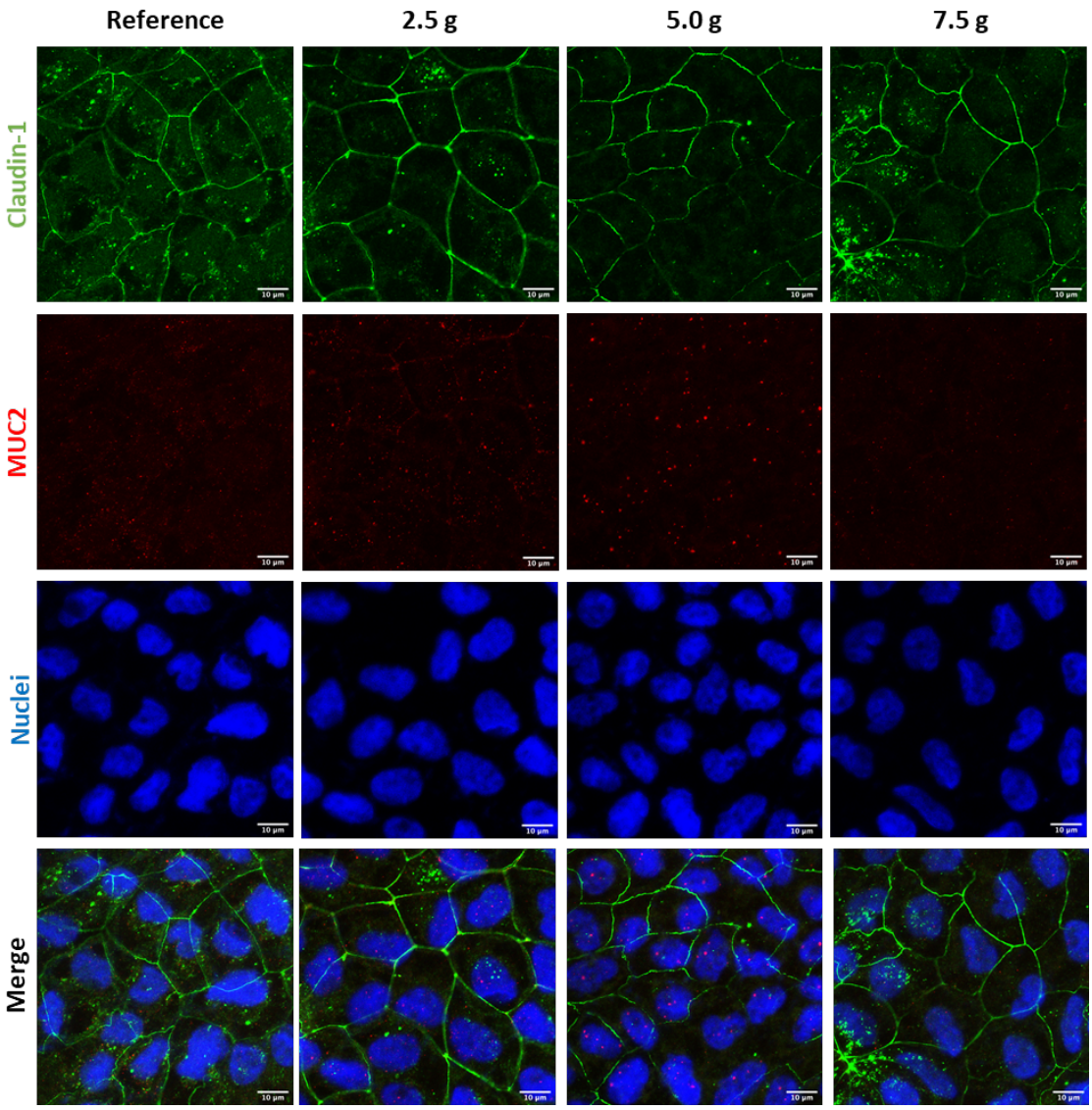

Figure S2. Visualization of claudin-1 and MUC2 at different g-levels. Claudin-1 is presented in **green**, MUC2 in **red** and nuclei in **blue**.

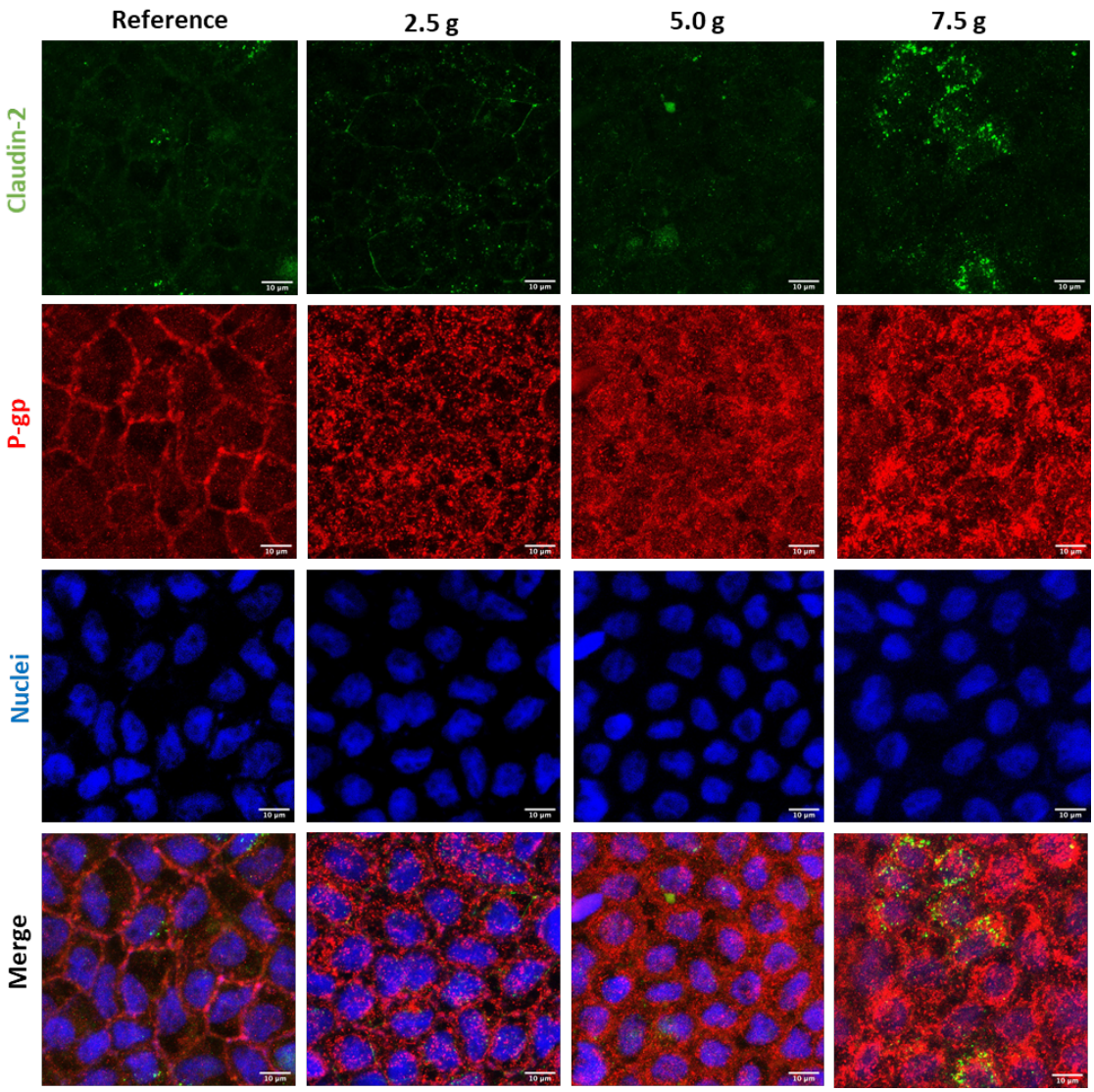

Figure S3. Visualization of claudin-2 and P-gp at different g-levels. Claudin-2 is presented in **green**, P-gp in **red** and nuclei in **blue**.

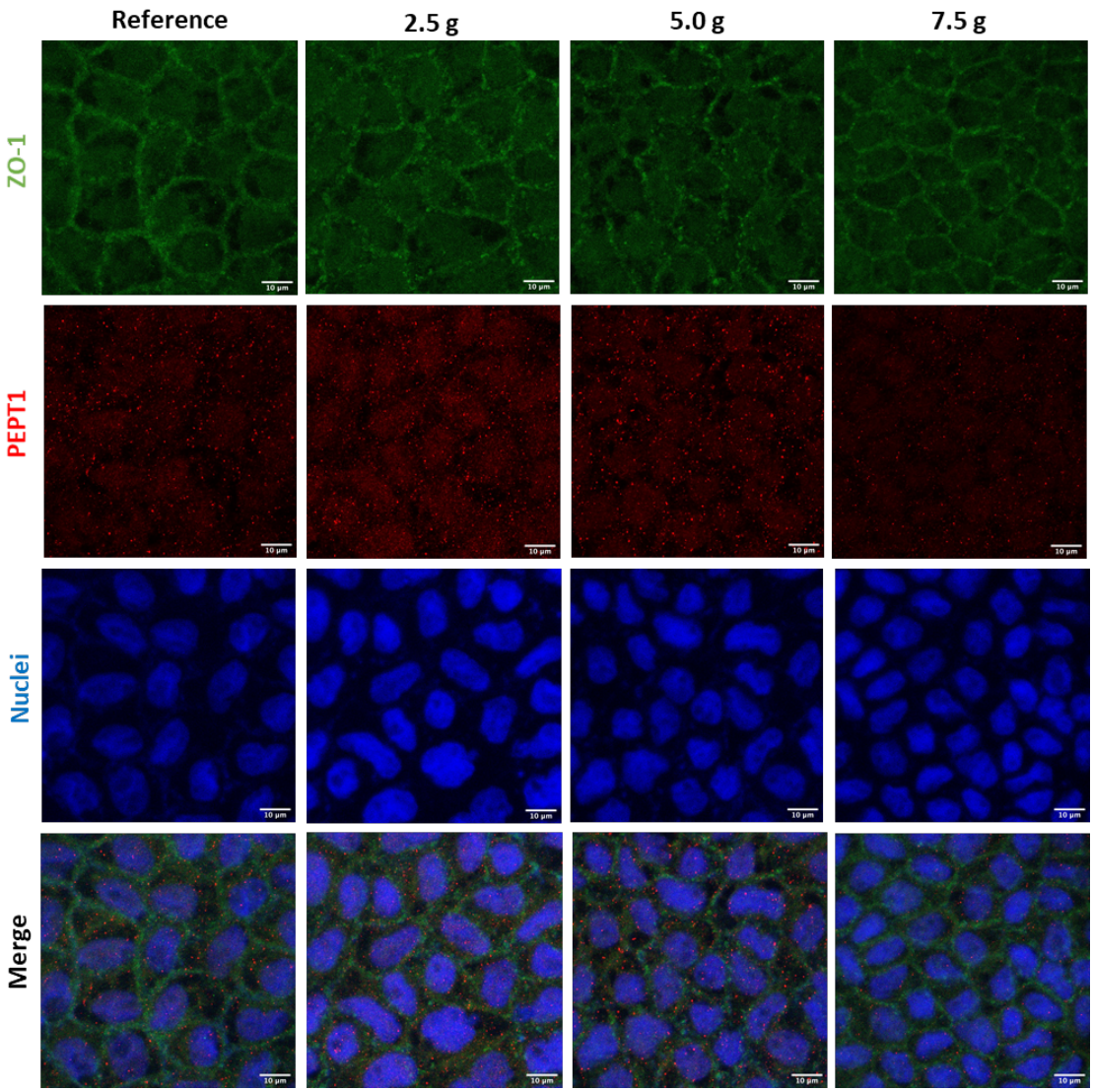

Figure S4. Visualization of ZO-1 and PEPT1 at different g-levels. ZO-1 is presented in **green**, PEPT1 in **red** and nuclei in **blue**.

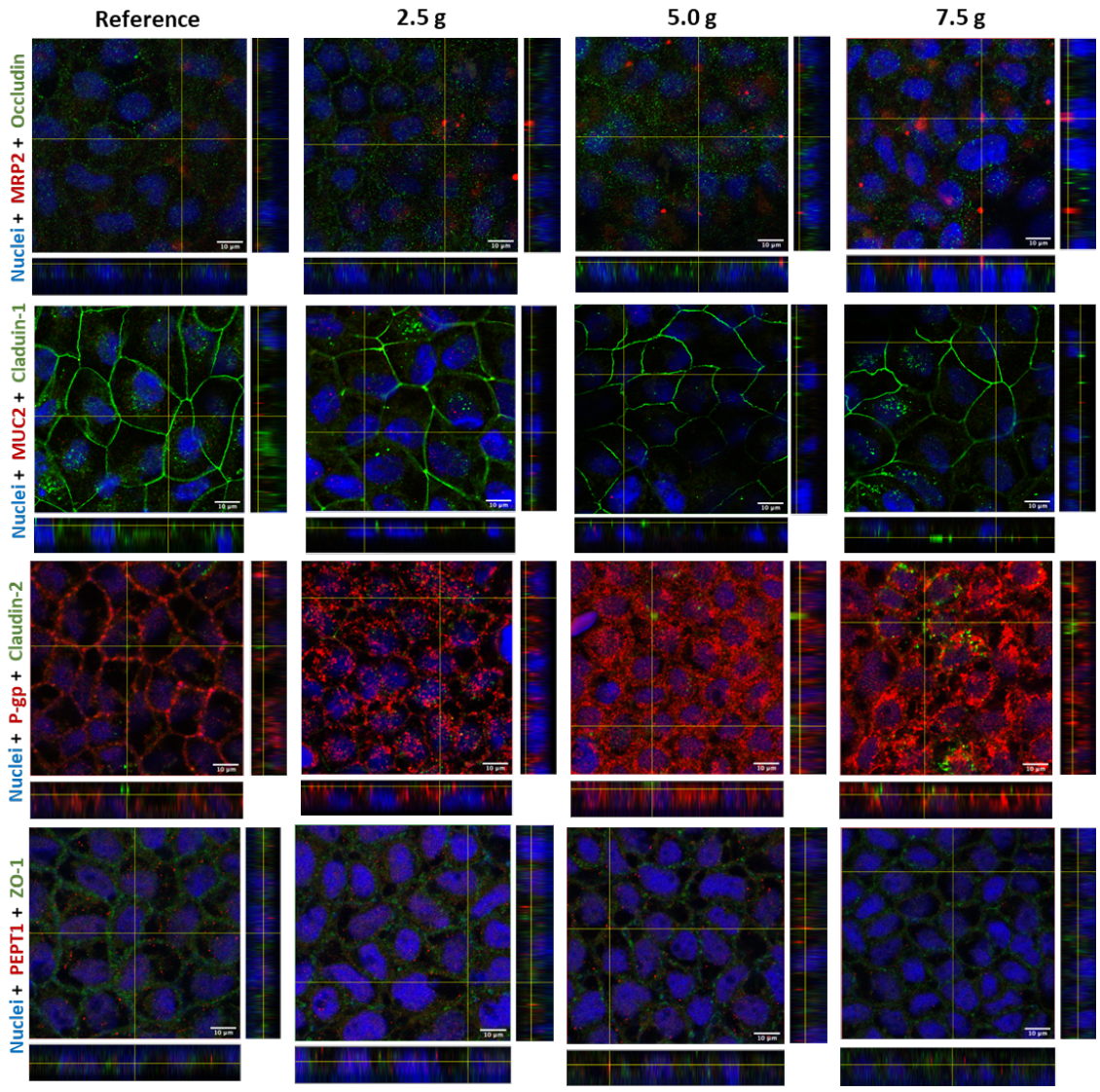

Figure S5. ORTO visualization of cellular components at different g-levels. Occludin, claudin-1, claudin-2 and ZO-1 are presented in **green**. MRP2, MUC2, P-gp and PEPT1 are presented in **red**. Nuclei are **blue**.

Section 2 | Safety of CPT-micelles

Caco-2 monoculture was seeded at a density of 10 000 cells/well in 200 µL per well and incubated during 4 hours. After that, the medium was aspirated and the wells were washed twice with 100 µL of fresh pre-heated HBSS buffer (pH 7.4). After washing, 200 µL of the micelles solutions corresponding to CPT amounts of 0.78, 1.56, 3.12 and 6.25 µg/mL were added to each well and the plates were incubated for a period of 4 and 24 h at 37°C. After the incubation period, the media was removed, and 150 µL of 0.5 mg/mL MTT solution was added at each well, followed by incubation of the plates at 37°C during 4 h. The reaction was terminated by removal of the media and addition of 150 µL of DMSO. The levels of

reduced MTT were determined by measuring the absorbance at 470 nm and 630 nm using a microtiter plate reader (Biotek-Synergy H1 Hibrid reader, using the Gen5 2.01 program). The % of MTT reduction was calculated as follows:

$$MTT\ reduction\ (\%) = \frac{absorbance\ of\ treated\ cells}{absorbance\ of\ untreated\ cells} \times 100 \qquad \text{(S1)}$$

The final results of MTT reduction, are expressed as the percentage of the absorbance of control cells.

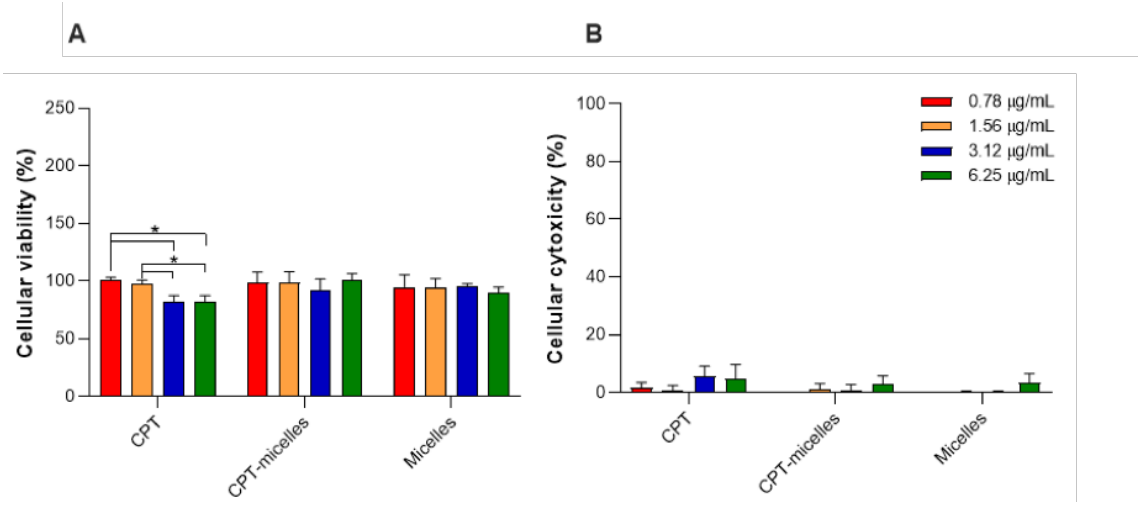

Figure S6. Evaluation of the safety of nanosystems. (A) Cellular viability, assessed by the MTT assay and (B) cellular cytotoxicity assessed by the LDH assay, of micelles loaded with CPT or not. Free CPT was included as control. Shown are the arithmetic means ± SD. ∗P < 0.05, comparing with the control, by two-way analysis of variance (ANOVA) Tukey's multiple comparison test, *n*=4).

Appendix 2

Supplementary information for supporting the Chapter 4

Novel chitosan modification into an amphiphilic polymer as micellar carrier of hydrophobic anticancer drugs for oral administration

A2.1. Chemical chitosan modification

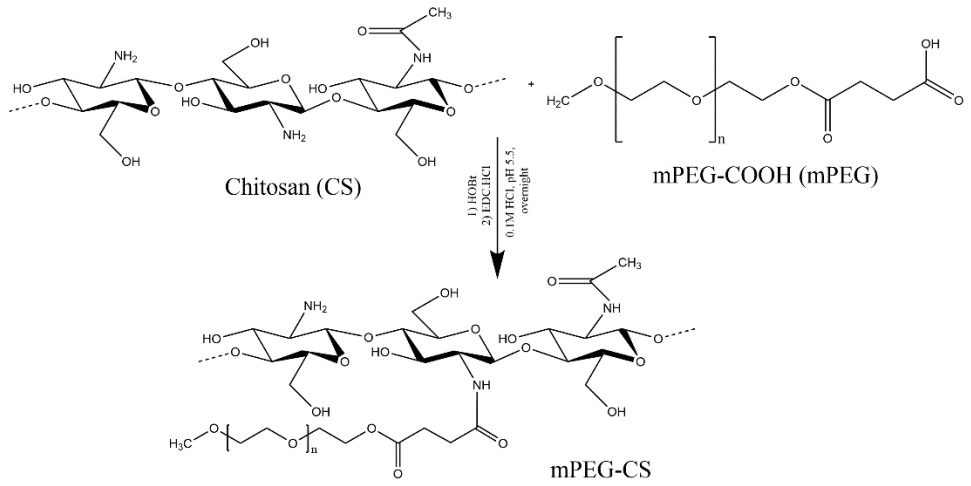

Figure A2.1. Schematic representation of the mPEG-CS synthesis by a carbodiimide amidation.

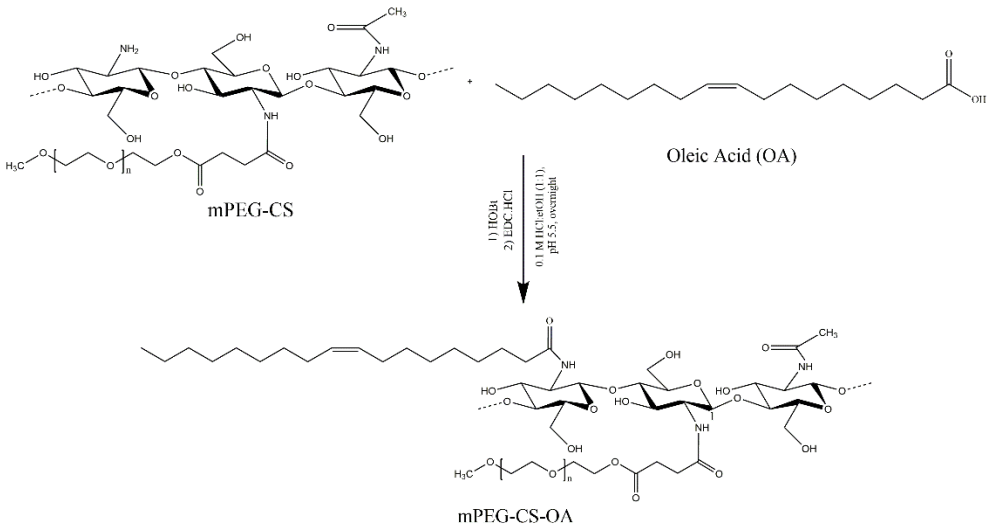

Figure A2.2. Schematic representation of the mPEG-CS-OA synthesis by a carbodiimide amidation.

A2.2. Physicochemical characterization of the new chitosan derivatives

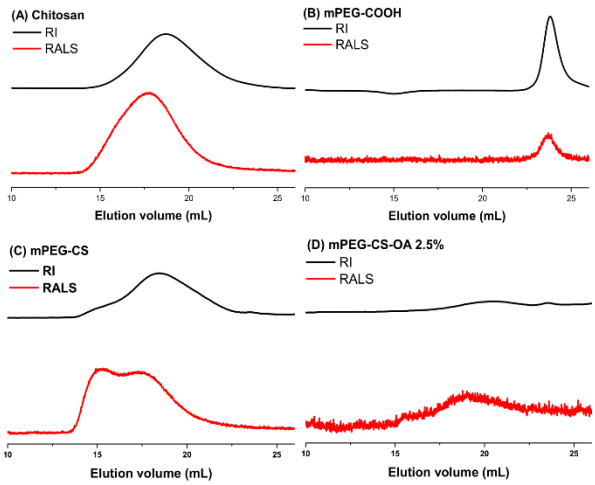

Figure A2.3. GPC chromatograms of (A) chitosan, (B) mPEG-COOH, (C) mPEG-CS and (D) mPEG-CS-OA2.5%.

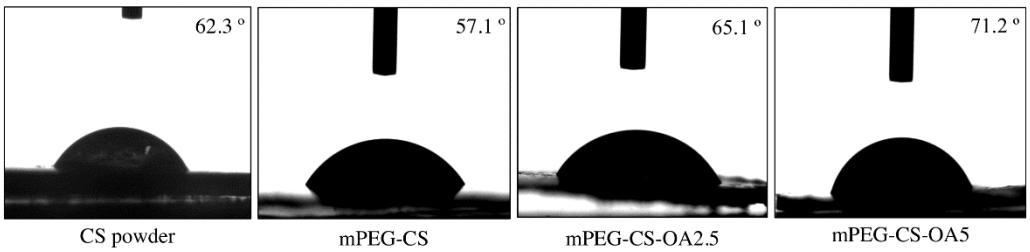

Figure A2.4 – From the left to the right, chitosan, mPEG-chitosan, mPEG-chitosan-oleic acid 2.5% and mPEG-chitosan-oleic acid 5% contact angle.

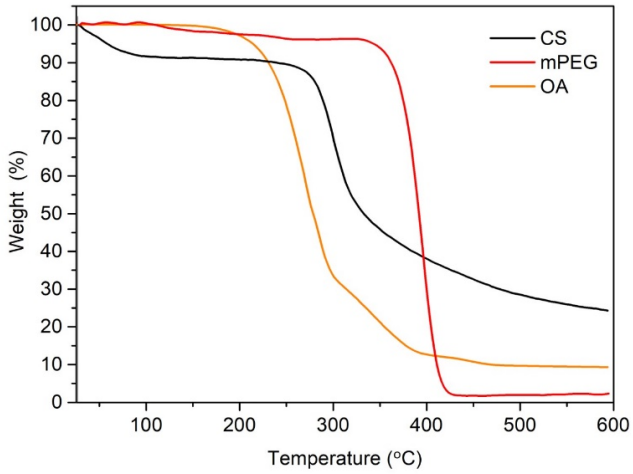

Figure A2.5. Thermogravimetric curves of the raw material: chitosan (CS), mPEG and oleic acid (OA).

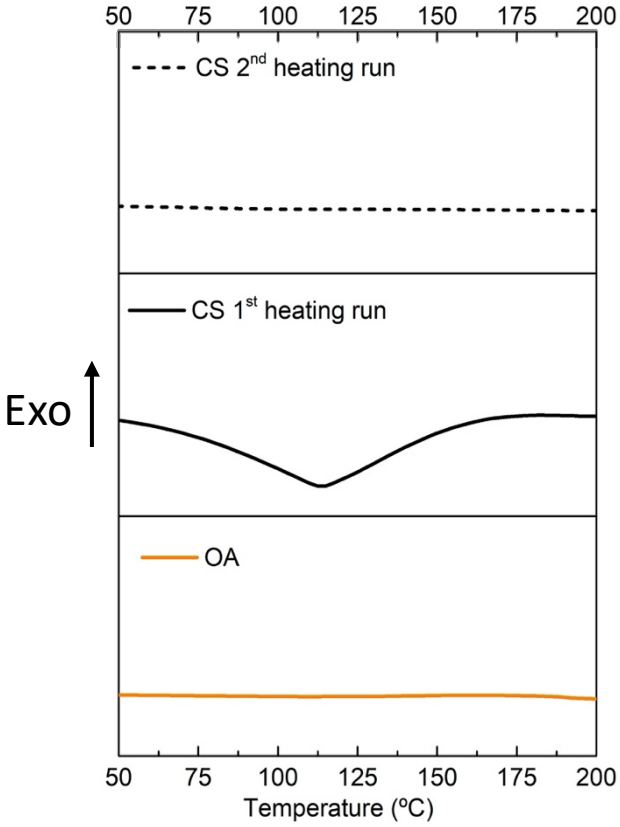

Figure A2.6 - DSC thermograms for raw materials: chitosan (CS) and oleic acid (OA). In the case of CS first and second run curves are different.

Table A2.1. XRD peak positions of mPEG, CS, mPEG+CS, mPEG-CS, mPEG-CS-OA2.5 and mPEG-CS-OA5.

2θ (º)					
mPEG	**CS**	**mPEG+CS**	**mPEG-CS**	**mPEG-CS-OA2.5**	**mPEG-CS-OA5**
	10.75				
19.09	19.91	17.25/21.33	19.37	19.22	19.27
23.33	23.70	24.17	23.35	23.30	23.31
26.11		28.42	26.71	27.42	27.45
30.81		29.75		31.75	31.79
35.59	35.60	35.52			
45.04		42.50		45.08	45.02
53.48		43.29		53.89	53.93

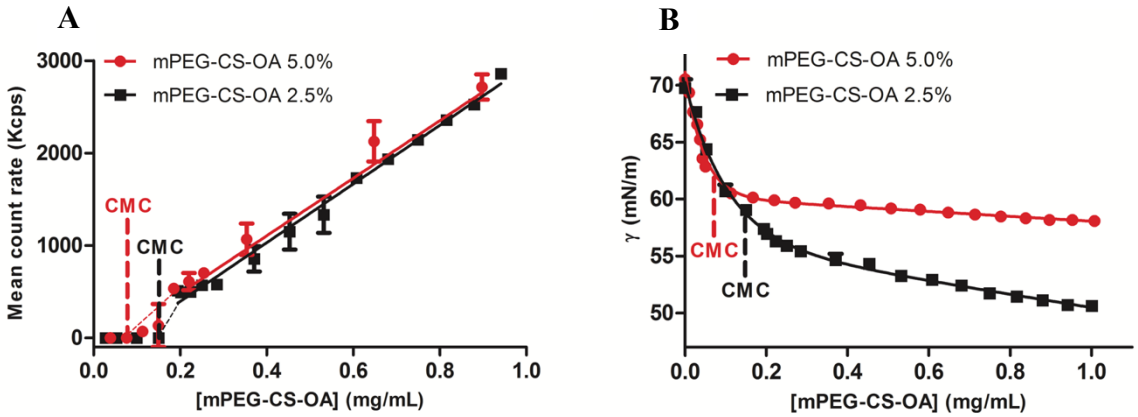

Figure A2.7. Critical micelle concentration determined by (A) Rayleigh scattering measured by DLS and by (B) surface tension method. Graphs are plotted in function of polymer concentration.

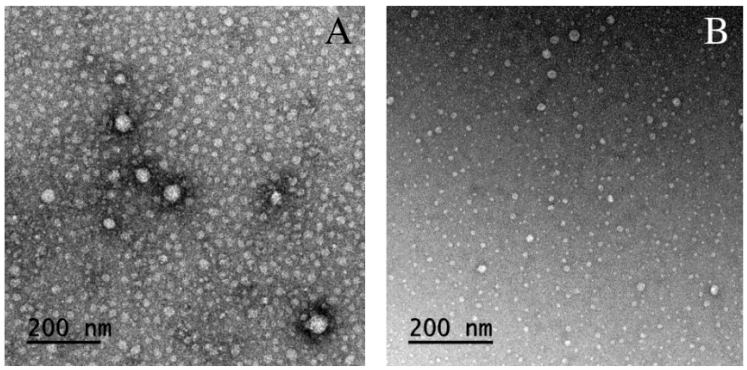

Figure A2.8. TEM images of empty (A) and CPT-loaded micelles (B).

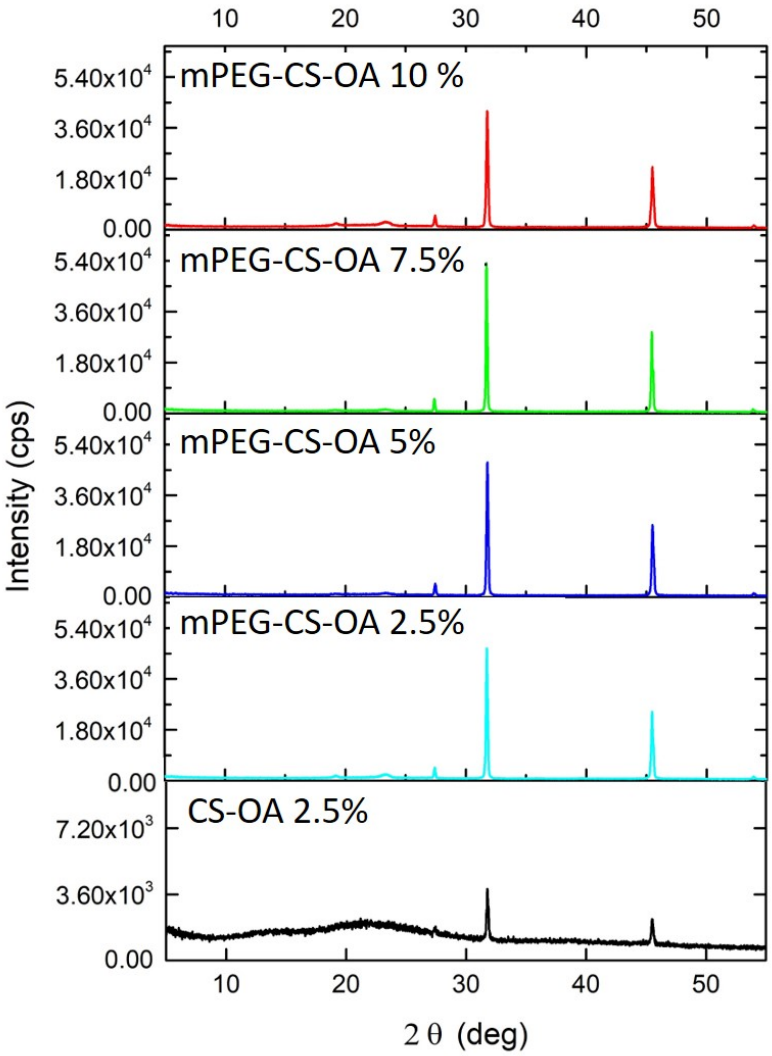

Figure A2.9. XRD diffraction patterns of CS-OA 2.5%, mPEG-CS-OA 2.5%, mPEG-CS-OA 5.0%, mPEG-CS-OA 7.5% and mPEG-CS-OA 10.0%.

Appendix 3

Supplementary information for supporting the Chapter 6

3D printed systems for specific colonic delivery of camptothecin-loaded chitosan micelles

A3.1. Material and methods

Table A3.1. FDM settings for batches with free CTP and CPT-loaded micelles.

	Layer thickness (mm)	Perimeter speed (mm/s)	Infill speed (mm/s)	Feeding rate (mm/s)	Height (mm)	Diameter (mm)
Free CPT	0.35	8	8	1.12	7.35	12
CPT-loaded micelles	0.35	8	8	1.12	8.35	13

Table A3.2. IVF settings for every printable ink injected (free drug, delaying polymer, micelles) corresponding to both batches.

		Deposit speed (µL/s)	Retract speed (µL/s)	Purge (µL)	Volume (µL)
Free CPT	**Drug**	7	1	0	200
	Eudragit FS 30D	1	1	50	350
CPT-loaded micelles	**Micelles**	4	1	0	200
	Eudragit FS 30D	1	1	50	500

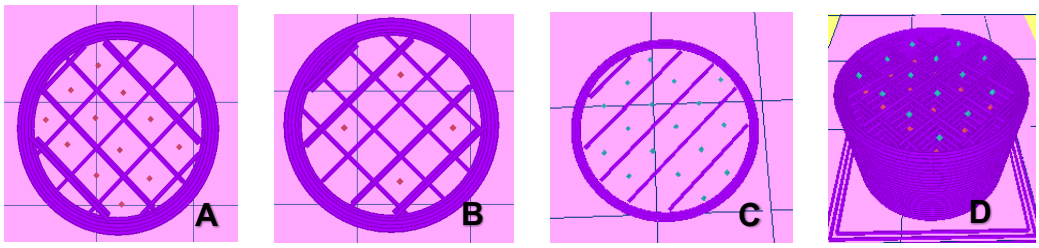

Figure A3.1. Digital design of printfills: (A) injection points for micelles; (B) injection points for free drug; (C) injection points of Eudragit FS30D for both batches; and (D) general design of the printfill.

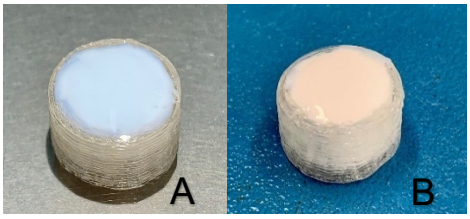

Figure A3.2. Printfill before (A) and after drying step (B).

Table A3.3. Details of the four phases of the intestinal transit for drug release test.

Phase	Intestinal segment	Volume (mL)*	Residence time (h)	pH
1	Stomach	500	2	1.2 ± 0.1
2	Jejunum	585	2	6.8 ± 0.2
3	Ileum (distal)	785	0.5	7.5 ± 0.2
4	Colon (proximal)	832	3.5	6.0 ± 0.2

*Approximate values

Table A3.4. Switch solution compositions used in the dissolution assay.

Switch solution	Phase	Composition for one vessel
I	1 → 2	4.08 g potassium dihydrogenphosphate, 30 mL sodium hydroxide 2.0 M (80 g/L), demineralized water of 129 mL
II	2 → 3	2.04 g potassium dihydrogenphosphate, 12.0 mL sodium hydroxide 2.0 M (80 g/L), demineralized water of 311 mL
III	3 → 4	9 mL hydrochloric acid 3.0 M, demineralized water of 60 mL

A3.2. Results and discussion

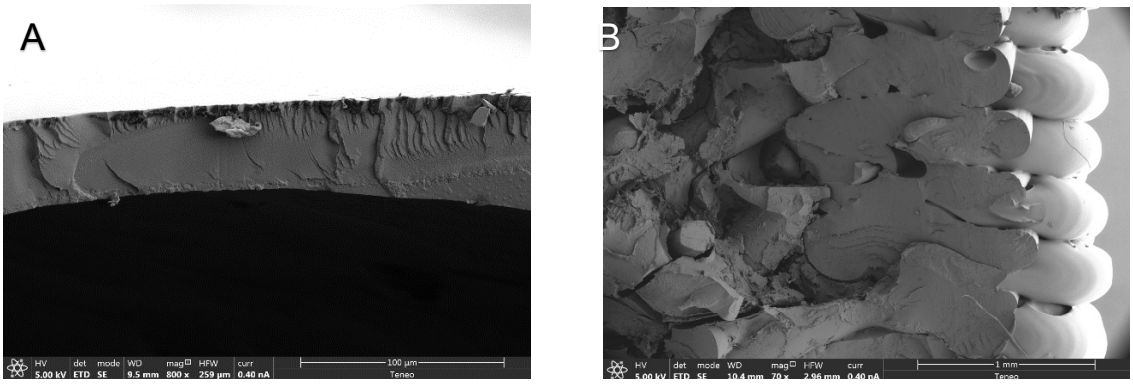

Figure A3.3. SEM images of top film of Eudragit FS30D (A) and sealed PLA perimeter (B).

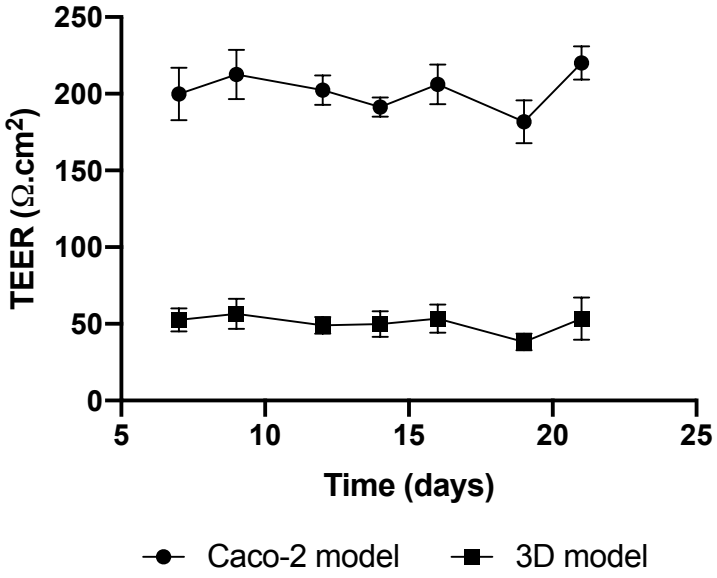

Figure A3.4. TEER values of Caco-2 and 3D models during 21 days of culture. Error bars represent mean ± SD (*n* = 6).

Appendix 4

Supplementary information for supporting the Chapter 7

Oral delivery of camptothecin-loaded in chitosan-based micelles is effective in reducing colorectal cancer

A4.1: Characterization of camptothecin-loaded polymeric micelles

Morphological analysis CPT-loaded mPEG-CS-OA micelles was assessed by transmission electron microscopy (TEM). Micelles were prepared on a grid treated with uranyl acetate and then examined in a JEM-1210 Transmission Electron Microscope (JEOL Ltd., Tokyo, Japan) operating at 120 kV.

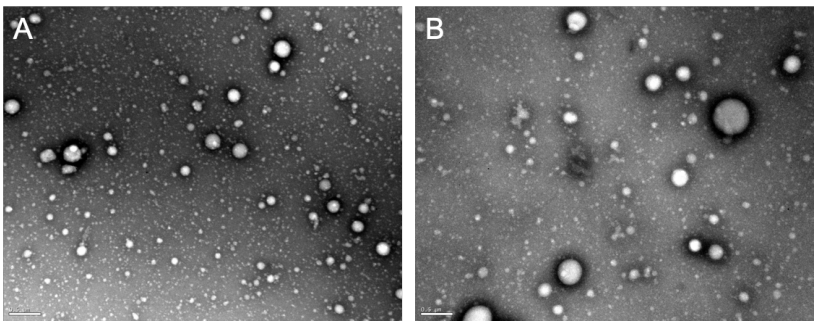

Figure A4.1. Transmission electron microscopy images of (A) unloaded chitosan micelles and (B) CPT-loaded chitosan micelles. Scale bar corresponding to 0.5 μm.

A4.2: *In vitro* antitumor efficacy studies

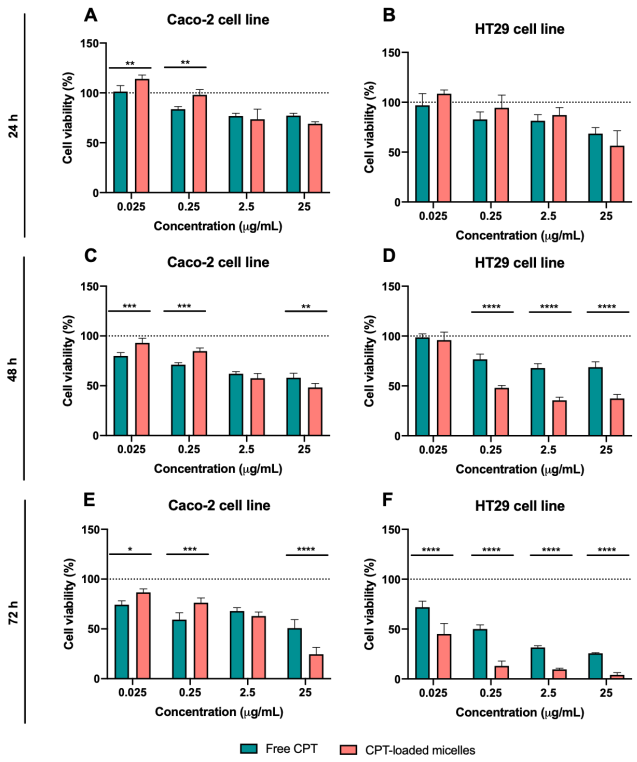

Figure A4.2. Anticancer activity of free CPT and CPT-loaded micelles against Caco-2 (A, C and E) and HT29 (B, D and F) colorectal cancer cell lines during 24 h (A and B), 48 h (C and D) and 72 h

(E and F) of incubation. Concentration is represented in function of CPT. Error bars represent mean ± SD (n = 3). *p<0.05, **p<0.01, ***p<0.001 and ****p<0.0001 denotes a significant difference by two-way analysis of variance (ANOVA) Sidak's multiple comparison test.

A4.3: Wound healing migration assay

HCT226 cells were culture without FBS one day before the seeding. Then, $6x10^5$ cells/well were seeded in 24-well plates until its complete confluency. The 'wound' was performed in the middle of the well by scraping it with a sterile tip and the wells were washed twice with medium without serum to remove the detached cells. Empty and CPT-loaded micelles and free CPT were incubated at CPT concentration of 0.25, 2.5 and 25 µg/mL (equivalent polymer mass for the empty micelles) and, wells without any treatment were used as control. Plates were left incubated a 37 ºC and 5% CO_2 and 95% relative humidity and, the healing process was observed through an optical microscope and microphotographs were taken at time 0, 1 and 2 days. The 'wound' area was measured with ImageJ software and, the relative wound closure was evaluated in comparison with the wound area at time 0.

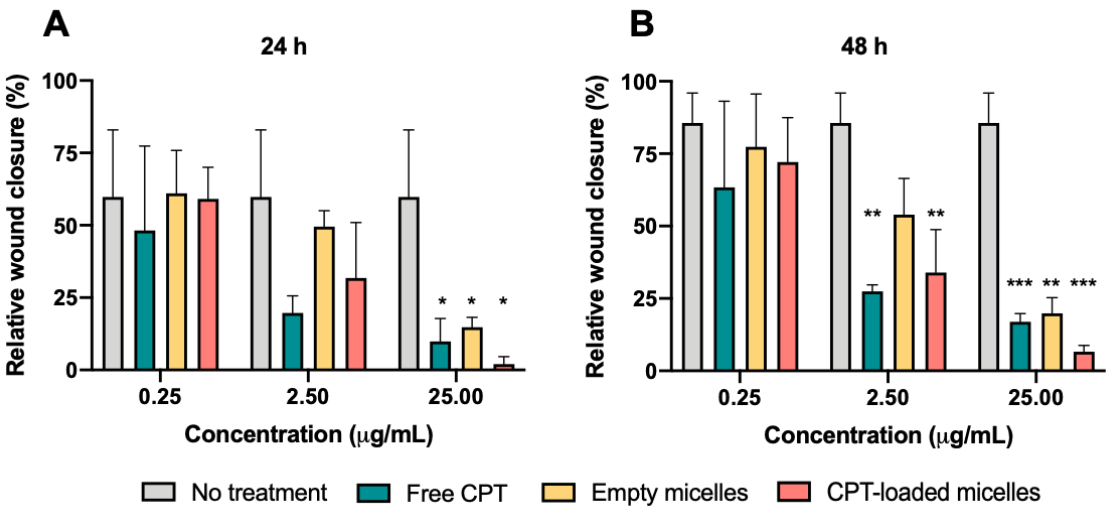

Figure A4.3. Wound healing assay performed in HCT116 cells incubated with complete DMEM (control) or with different CPT concentrations of free CPT or CPT-loaded micelles and empty micelles after (A) 24 h and (B) 48 h of incubation. Concentration is represented in function of CPT. Error bars represent mean ± SD (n = 3). *p<0.05, **p<0.01 and ***p<0.001 denotes a significant difference when compared with the control (no treatment) by two-way analysis of variance (ANOVA) Dunnett's multiple comparison test.

A4.4: Assessment of monolayer integrity by immunocytochemistry

Inserts from the intestinal permeability were washed once with PBS and fixed with 2% paraformaldehyde (PFA) in PBS during 30 min at RT. After, samples were washed thrice with PBS during 5 min and then, cells were permeabilized with 0.2% (v/v) Triton X-100 in PBS for 10 min at RT. The inserts were washed thrice with PBS during 5 min and, a blocking step was performed using a blocking solution (BS) constituted by 1.5% bovine serum albumin (BSA) and 5.0% FBS in PBS during 1 h at RT. Inserts were then placed in a humidified chamber and were incubated with rabbit anti-human EpCAM primary antibody (1:250) (10694-R028, Sino Biological) overnight at 4 ºC. Afterwards, inserts were washed thrice during 5 min with 0.05% Tween-20 in PBS (PBST) and, incubated with the secondary antibody goat anti-rabbit IgG (H+L) cross-adsorbed, Alexa Fluor 488 (A-11008, Invitrogen) (1:500). At the same time, cell nuclei were counterstained with DRAQ5™ Fluorescent Probe Solution (Thermo Fisher Scientific) (5 µM) during 2 h. At the end, inserts were washed twice with PBST and once with PBS during 5 min and stored at 4 ºC in PBS until visualization by a spectral confocal laser scanning microscope TCS-SP5 AOBS (Leica).

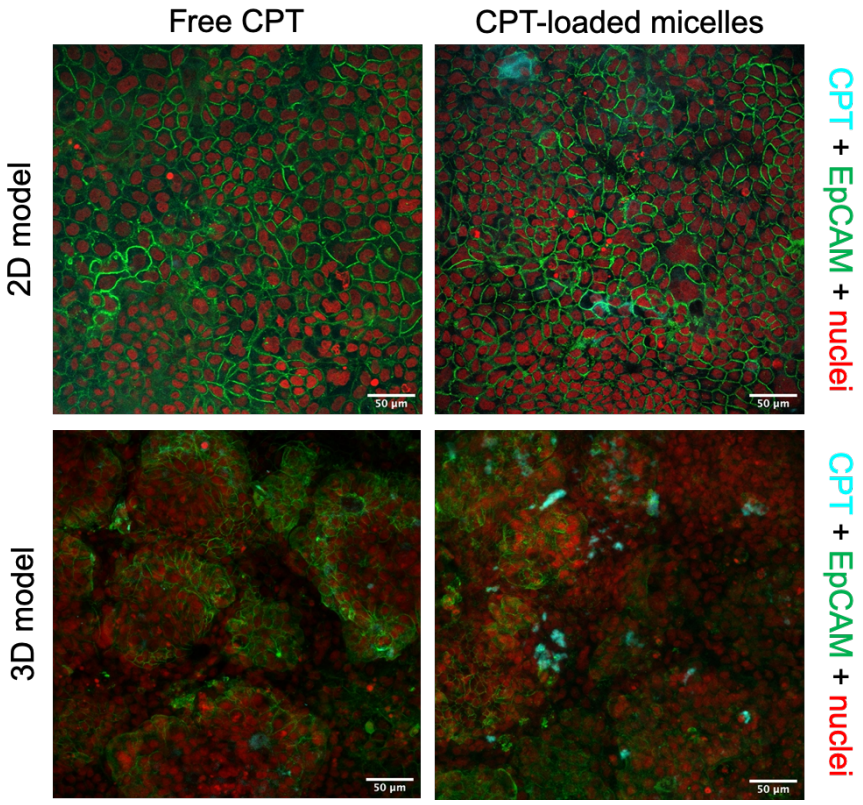

Figure A4.4. Visualization of CPT, EpCAM and nuclei of the 2D and 3D intestinal monolayers after permeability tested with free CPT, CPT-loaded mPEG-CS-OA micelles and CPT-loaded CS-OA micelles. EpCAM is present in **green**, nuclei in **red** and CPT in **blue**. Scale bar represents 50 µm.

A4.5: CRC induction by AOM/DSS

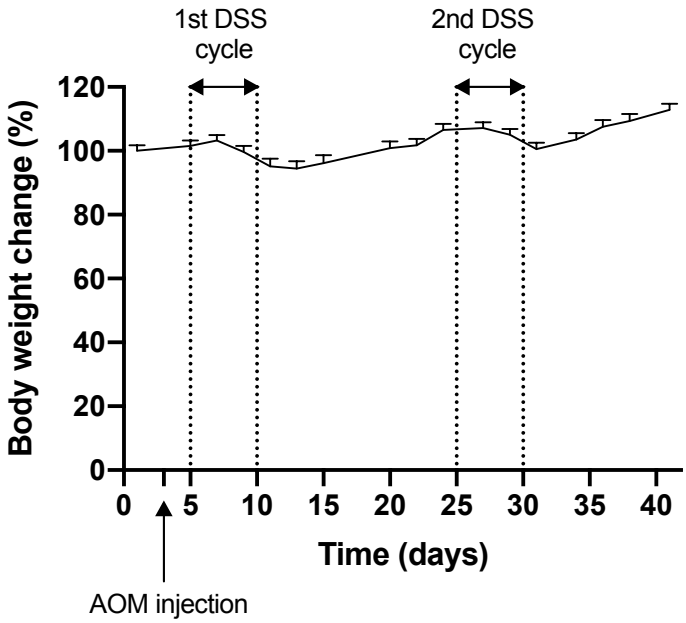

Figure A4.5. Animal body weight change during chemical CRC induction.

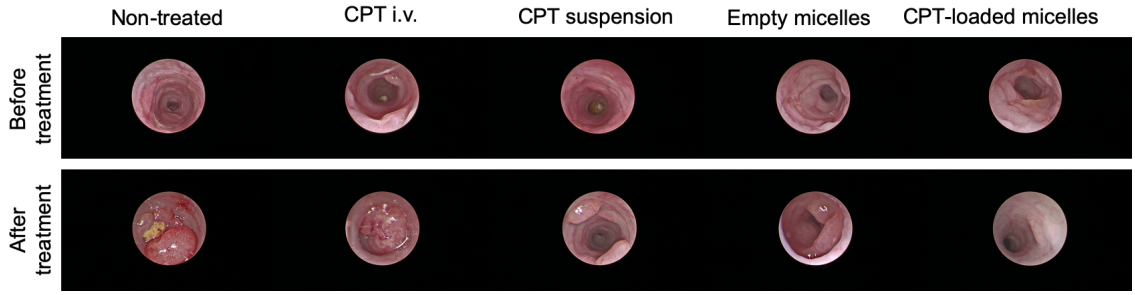

Figure A4.6. Images acquired by colonoscopy before and after the treatment started. Saline (non-treated), CPT suspension, empty micelles and CPT-loaded micelles were administered orally, while CPT i.v. was administered intravenously.

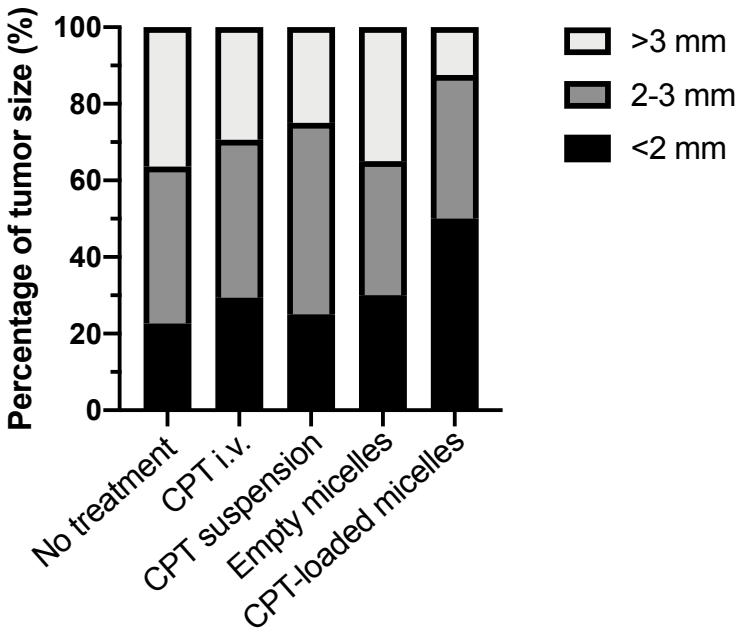

Figure A4.7. Percentage of tumor size distribution expressed in millimeters (mm).

BIBLIOGRAPHIC NOTE

Andreia Almeida was born on June 01, 1993 in Paredes, Porto, Portugal. She obtained her Bachelor in Biomedical Engineering in 2014 at University of Trás-os-Montes e Alto Douro (UTAD), Vila Real, Portugal. Later, she obtained her Master in Biomedical Engineering at Faculty of Engineering, University of Porto (FEUP), Porto, Portugal. Since 2017, she has been developing her PhD thesis in Biomedical Sciences, PhD program from Instituto de Ciências Biomédicas de Abel Salazar (ICBAS), at Instituto de Investigação e Inovação em Saúde (I3S) / Instituto de Engenharia Biomédica (INEB), Porto, Portugal. Her research is mainly focused on the development of polymeric micelles to improve the solubility of hydrophobic anticancer drugs. Her current interest is also focused on oral delivery of pharmaceutical dosage forms, new chitosan derivatives for polymeric micelles production, drug delivery across biological barriers and *in vitro/in vivo* correlation of drug absorption. She developed several skills as polymer synthesis and characterization, 3D printing techniques, a solid knowledge in cell culture techniques and cell-based assays, as well as, conducting *in vivo* experiments in mice models. Her research work resulted in 6 peer-reviewed articles (two published and four submitted for publication), 3 book chapters, 17 peer reviewed publications as result of the collaboration with other projects, 9 oral and 12 poster presentations in international and national meetings or conferences.

During her PhD, Andreia was able to improve her expertise in creativity, planning, technology transfer, and entrepreneurship by engaging in a startup acceleration program with a business idea and, participated in European Space Agency (ESA) Spin Your Thesis! program. Moreover, Andreia worked in collaboration with Vall d'Hebron Research Institute (Spain), Centro de Física das Universidades do Minho e Porto (Portugal) and, conducted three short term scientific missions at Technion - Israel Institute of Technology (Israel), University of Seville (Spain) and MyBiotech GmbH Industry (Germany) sponsored by European Cooperation in Science & Technology (COST). She also demonstrated proactivity and initiative by attending several courses, workshops or training schools to complement her knowledge in health science.

As result of her work, Andreia was also awarded with the “Norte Empreendedor” prize by Associação Empresarial de Portugal (AEP), an ITC conference grant by COST and with the Pharmaceutics 2020 Travel Award. Currently, Andreia is Ambassador at the Young Scientist Committee of the Controlled Release Society (CRS) and board member of the Transdermal and Mucosal Delivery focus group of CRS as Social Media Representative.